Theory and computation of line defect fields in solids and liquid crystals

Submitted in partial fulfillment of the requirements for

the degree of

Doctor of Philosophy
in
Civil Engineering

Chiqun Zhang
B.S., Civil Engineering, Tianjin University
M.S., Civil and Environmental Engineering, Carnegie Mellon University

Carnegie Mellon University
Pittsburgh, PA
Sepetember, 2017

Keywords: generalized disclination, dislocation, disclination, phase boundary, nematic liquid crystal, phase transition

Dedicated to

my father

Mr. Jianguo Zhang

and my mother

Ms. Zhongyun Liu

Abstract

Theory and computation of line defect fields in solids and liquid crystals

The theory and computation of line defects are discussed in the context of both solids and liquid crystals. This dissertation includes four parts. The Generalized Disclination theory is discussed and applied to numerous interfacial and bulk line defect problems. An augmented Oseen-Frank energy as well as a novel 2D-model is proposed and demonstrated for disclination dynamics in liquid crystal. A model based on kinematics and thermodynamics is devised to predict tactoid dynamics during the process of the isotropic-nematic phase transition in LCLC.

In the first part of the thesis, the utility of the notion of generalized disclinations in materials science is discussed within the physical context of modeling interfacial and bulk line defects. The Burgers vector of a disclination dipole in linear elasticity is derived, clearly demonstrating the equivalence of its stress field to that of an edge dislocation. An explicit formula for the displacement jump of a single localized composite defect line in terms of given g.disclination and dislocation strengths is deduced based on the Weingarten theorem for g.disclination theory at finite deformation. The Burgers vector of a g.disclination dipole at finite deformation is also derived.

In the second part, a numerical method is developed to solve for the stress and distortion fields of g.disclination systems. Problems of small and finite deformation theory are considered. The fields of various line defects and grain/phase boundary problems are approximated. It is demonstrated that while the far-field topological identity of a dislocation of appropriate strength and a disclination-dipole plus a slip dislocation comprising a disconnection are the same, the latter microstructure is energetically favorable. This underscores the complementary

importance of *all* of topology, geometry, and energetics (plus kinetics) in understanding defect mechanics. It is established that finite element approximations of fields of interfacial and bulk line defects can be achieved in a systematic and routine manner, thus contributing to the study of intricate defect microstructures in the scientific understanding and predictive design of materials.

In the third part, nonsingular disclination dynamics in a uniaxial nematic liquid crystal is modeled within a mathematical framework where the kinematics is a direct extension of the classical way of identifying these line defects with singularities of a unit vector field representing the nematic director. We devise a natural augmentation of the Oseen-Frank energy to account for physical situations where infinite director gradients have zero associated energy cost, as would be necessary for modeling half-integer strength disclinations within the framework of the director theory. A novel 2D-model of disclination dynamics in nematics is proposed, which is based on the extended Oseen-Frank energy and takes into account thermodynamics and the kinematics of conservation of defect topological charge. We validate this model through computations of disclination equilibria, annihilation, repulsion, and splitting.

In the fourth part, the isotropic-nematic phase transition in chromonic liquid crystals is studied. We simulate such tactoid equilibria and dynamics with a model using degree of order, a variable length director as state descriptors, and an interfacial descriptor. We introduce an augmented Oseen-Frank energy, with non-convexity in both interfacial energy and the dependence of the energy on the degree of order. A strategy is devised based on continuum kinematics and thermodynamics. The model is used to predict tactoid dynamics during the process of phase transition. We reproduce observed behaviors in experiments and perform an experimentally testable parametric study of the effect of bulk elastic and tactoid interfacial energy constants on the interaction of interfacial

and bulk fields in the tactoids.

Acknowledgments

I would like to express my sincere gratitude to all the individuals who helped me during the course of my studies. My deepest thanks go to my family, especially my parents and my wife for the continuous support and encouragement.

I would like to thank my advisor, Prof. Amit Acharya, not only for providing me opportunities to work on challenging problems, but also for his patience, motivation and immense knowledge. He is one of the most knowledgeable person that I have had the pleasure of their acquaintance. I would especially like to thank him for teaching me how to study complicated problems from both the mathematical theories and the numerical calculations. It was really an honor working with him.

I want to thank Prof. Noel Walkington, who helped me on the isotropic-nematic phase transition project. I appreciate all his effort in investing time and energy to answer my questions. His coding skills inspired me a lot. I thank Prof. Dmitry Golovaty and Prof. Oleg Lavrentovich for the helpful technical discussions. I would also like to thank Prof. Jacobo Bielak for guiding me into the finite element method and vibration analysis. My thanks also go to Prof. Robert Suter for his time and agreeing to be on my thesis committee.

I would like to thank my colleagues, Dr. Xiaohan Zhang, Dr. Saurabh Puri, Mr. Rajat Arora and Mr. Sabyasachi Chatterjee, for their valuable inputs and interesting discussions. My special thanks go to Maxine Leffard for her effort in making my graduate life in CEE rich and wonderful.

The funding of Dean's Fellowship provided by Civil and Environmental Engineering Department is highly appreciated. I also acknowledge support from grants NSF-DMS-1434734.

Contents

List of Figures

Chapter 1

Motivation and overview

1.1 Line defects in crystalline solid

Crystalline materials have been widely applied in information technology, astronomy, medicine, manufacture and other sectors. With the increasing demand for thinner and smaller devices, understanding defects in crystalline structures is of great significance. Two commonly observed line defects are dislocations and disclinations. Weingarten's theorem was introduced in 1901 [Wei01]. Dislocations and disclinations in crystalline solid were introduced by Volterra [Vol07], motivated by Weingarten's theorem. A dislocation is a defect within a crystal structure representing the displacement jump. Two primary types of dislocations are edge dislocations and screw dislocations. The magnitude and the direction of the lattice displacement jump resulting from a dislocation is measured by Burgers vector. A disclination is a kind of defects originating from the rotation incompatibility, whose magnitude and direction are represented by the Frank vector [DeW73a]. Dislocations and disclinations are used to study various interfaces, such as high-angle boundary, grain boundary ledges, twin boundary, etc. [KF08]. In particular, dislocations are widely accepted for modeling low angle boundaries, such as tilt grain boundaries and twist grain boundaries, by employing the Frank-Bilby equation [Fra50, Bil55]. However, the dislocation model cannot deal with high angle boundaries since the packed dislocations are too close to identify a corresponding Burgers vector. Also, modeling boundaries as infinite dislocation walls makes the application of 3d grain boundary network difficult. On the other hand, disclinations can be used to model both the low angle and high angle boundaries, while accounting for the fine structure of the boundaries [Li72, GNR$^+$89, HES$^+$95].

In addition to dislocations and disclinations, [AF12, AF15] introduce the concept of generalized disclination (g.disclination), accounting for the distortion incompatibility. The distortion is a deformation gradient for a defect-free crystal. In many circumstances with defects, the distortion is not the gradient of a vector field. The surface of a distortion discontinuity is called a phase boundary (including a grain boundary as a special case).

The g.disclination is defined as the discontinuity of the distortion discontinuity, namely the tips of terminating phase boundaries. When the distortions involved in the discontinuity are pure rotations, g.disclinations become conventional disclinations.

The static theories of dislocation fields and of disclination fields are discussed in [Krö81, DeW71, DeW73a]. The theory of the crystal defects (dislocations and disclinations) proposed in [DeW73a] will reduce to the dislocation theory in [Krö81] when the disclination vanishes. A mechanical theory of dislocation fields is proposed in [Ach01], dealing with crystal plasticity. The notation and theory of g.disclination is proposed in [AF12, AF15]. In the absence of g.disclinations, the g.disclination theory becomes the dislocation theory in [Ach01]. In [Ach03], it shows that the dislocation field theory will give a unique displacement field when the dislocation velocity is assumed as data as well as constitutive elasticity. The dislocation-disclination statics is generalized in [FTC11] and the application of dislocation and disclination fields on grain boundary plasticity is discussed in [TCF$^+$13, FTC14]. The concept and the statics as well as dynamics of g.disclinations are proposed in [AF12, AF15], which extends the pioneering work of DeWit [DeW73a]. In this work, an extension of g.disclination theory is proposed by introducing an additional field $\boldsymbol{H}^s$ that is discussed in details in Chapter 3. The proposed model can reproduce the stress free equilibria of twin boundaries when the eigenwall field $\boldsymbol{S}$ is prescribed as data. Weingarten theorem for g.disclinations at finite deformation is interpreted in terms of g.disclination kinematics. A numerical scheme considering both the small deformation and finite deformation are proposed and applied to solve numerous problems involving bulk and interfacial line defects.

1.2 Disclinations in nematic liquid crystal and isotropic-nematic phase transition

With the increasing applications in material science, biological systems, and industrial engineering such as display technologies and nanofluidic devices, researches on liquid crystals have gained great interest and have advanced quite rapidly. With properties between liquids and solids, liquid crystals may flow as liquids while keeping some crystalline attributes of solids. Depending on the amount of order in the material, there are many types of liquid crystal phases.

In this work, we are primarily interested in uniaxial nematic liquid crystals (NLC), which consists of rod-like molecules with no positional order but retaining some long-range orientational order. The orientational order is characterized by the director and is represented by a unit vector field in classical models [Ste04].

Another interest of this work concerns nematic inclusions in an isotropic matrix, namely a nematic liquid crystal undergoing an isotropic-nematic phase transition. The isotropic-nematic phase transition in Lyotropic Chromonic Liquid Crystals (LCLC) happens when temperature changes, which is observed in the novel experiments of Lavrentovich and co-workers [KL07, Lav14, VPSL02, KSL13]. LCLC molecules are aggregates of plank-like or disc-like unites with an aromatic flat core and peripheral polar groups. The isotropic-nematic phase transition in defect-free problem is first order. As temperature decreases, chromonic inclusions nucleate, grow and coalesce, giving rise to tactoid microstructures. Nematic symmetry allows for two types of topologically defects: disclinations in the bulk and point defects on the surfaces (cusps).

For the sake of completeness, three classical mathematical models of nematic liquid crystals are reviewed below. In all models, we denote Ω as an open domain enclosed by the boundary $\partial\Omega$.

1. The Oseen-Frank model. In the Oseen-Frank model [Fra58, Ose33], the elastic energy of the director distortion is given by $E_{OF} = \frac{1}{2}\int_\Omega F_{OF}(\boldsymbol{n}, \nabla \boldsymbol{n}) d\boldsymbol{x}$, with the energy density

$$F_{OF} = K_1(\nabla \cdot \boldsymbol{n})^2 + K_2((\nabla \times \boldsymbol{n}) \cdot \boldsymbol{n})^2 + K_3|(\nabla \times \boldsymbol{n}) \times \boldsymbol{n}|^2 + K_{24}((\nabla \cdot \boldsymbol{n})^2 - \mathrm{tr}(\nabla \boldsymbol{n})^2).$$

K_i are material dependent Frank elastic constants satisfying appropriate inequalities [HKL88] so that energy-minimizing configuration exists. To describe the interaction between the nematic directors and the nematic particle interfaces, the Oseen-Frank energy can be augmented by introducing the Rapini-Papoular surface energy $E_{RP} = \int_{\partial\Omega} F_{RP} dS$ with $F_{RP} = (1 - \alpha(\boldsymbol{n} \cdot \nu)^2)$, where $\boldsymbol{\nu}$ is the unit vector normal to the interface $\partial\Omega$ and α is a material dependent constant between -1 and 1. One limitation of the Oseen-Frank model is that it cannot deal with certain types of defects, such as disclinations, because the constraint on $\boldsymbol{n}$ ($|\boldsymbol{n}| = 1$) is too rigid. The Oseen-Frank model is extended in [Eri91] for disclinations by introducing an additional scalar field describing the degree of local orientational order. However, neither model can describe biaxial configurations which are conjectured to exist at the core of a nematic defect. In [BZ07, BB15], it also suggests the use of discontinuous order parameter fields.

2. The Ericksen-Leslie model and its augmentation with degree of order. Motivated by the hydrostatic theory of liquid crystals, Ericksen[Eri61] proposed conservation laws for the dynamical behavior of anisotropic liquids. Constitutive equations for anisotropic fluids was proposed by Leslie in [Les66]. The dynamic theory for nematic liquid crystals was completed by Leslie in [Les68], now considered as the Ericksen-Leslie theory for the dynamics of nematic liquid crystals. In addition to the constraints $|\boldsymbol{n}| = 1$ and $div(\boldsymbol{v}) = 0$, the Ericksen-Leslie model consists of the balance laws arising from linear and angular momentum, that resulting in the evolution equa-

tions for $\boldsymbol{n}$ and $\boldsymbol{v}$. To deal with the defects, [Eri91] augmented the Ericksen-Leslie model with an additional scalar degree of order beyond the director. The Ericksen-Leslie model for nematic liquid crystals with variable degree of orientation is also discussed in [BBCH92, Vir95, Wal11a]. One limitation of the augmented Ericksen-Leslie mode is cannot deal with half integer defects that predicting unbounded energy in a finite body.

3. The Landau-de Gennes model. The Landau-de Gennes theory introduces a tensor-valued order parameter to incorporate biaxiality of nematic liquid crystals [BZ07, MN14, MZ10]. The order parameter is a second order tensor $\boldsymbol{Q}$ that is traceless and the nematic free energy is given as

$$F_{LdG}(\boldsymbol{Q}) = a\,\mathrm{tr}(\boldsymbol{Q}^2) + b\,\mathrm{tr}(\boldsymbol{Q}^3) + c\,\mathrm{tr}(\boldsymbol{Q}^4),$$

where a, b and c are temperature or material dependent parameters. At temperatures below the supercooling temperature, tensor fields that minimize the Landau-de Gennes free energy do not have isotropic cores [GJ15]. The order parameter becomes biaxial inside cores and is uniaxial at core centers [SS87, KL07]. When the director is constrained in plane, namely the director can be parametrized by an angle field, and the temperature is below the supercooling temperature, the Landau-de Gennes energy with half strength line defects is infinite.

A model dealing with nematic defects dynamics is proposed in [AD13], which introduces an augmented Oseen-Frank kinematics and defines a director distortion field and an director incompatible field in analogy with plasticity theories. The director incompatibility field is non-vanishing in the presence of defects. The evolution equations of the director field and the director incompatibility field are motivated from geometric conservation laws. In [PAD15], the static equilibrium of director fields of prescribed disclinations are solved with a finite element based numerical scheme. In addition, the comparison and connections

between modeling liquid crystal disclinations and modeling solid dislocations with the eigendeformation method is discussed in [PAD15].

In this work, we study the equilibria and dynamics of liquid crystal disclination based on an augmented Oseen-Frank energy and show that the gradient flow dynamics for this energy is not suitable for modeling the defect evolution problem. Then a 2D model based on thermodynamics and defect topological conservation law is constructed and applied to analyze nematic disclination dynamics. This work also proposes a dynamic model derived from the kinematic flux and thermodynamics, which is capable to deal with tactoid dynamics and isotropic-nematic phase transitions.

1.3 Terminology

The condition that a is defined to be b is indicated by the statement $a := b$. The Einstein summation convention is implied unless otherwise specified. $\boldsymbol{Ab}$ is denoted as the action of a tensor $\boldsymbol{A}$ on a vector $\boldsymbol{b}$, producing a vector. A $\cdot$ represents the inner product of two vectors; the symbol $\boldsymbol{AD}$ represents tensor multiplication of the second-order tensors $\boldsymbol{A}$ and $\boldsymbol{D}$. A third-order tensor is treated as a linear transformation on vectors to a second-order tensors.

We employ rectangular Cartesian coordinates and components in this paper; all tensor and vector components are written with respect to a rectangular Cartesian basis $(\boldsymbol{e}_i)$, i=1 to 3. The symbol *div* represents the divergence, *grad* represents the gradient on the body

(assumed to be a domain in ambient space). In component form,

$$
\begin{aligned}
(\boldsymbol{A} \times \boldsymbol{v})_{im} &= e_{mjk} A_{ij} v_k \\
(\boldsymbol{B} \times \boldsymbol{v})_{irm} &= e_{mjk} B_{irj} v_k \\
(\operatorname{div} \boldsymbol{A})_i &= A_{ij,j} \\
(\operatorname{div} \boldsymbol{B})_{ij} &= B_{ijk,k} \\
(\operatorname{curl} \boldsymbol{A})_{im} &= e_{mjk} A_{ik,j} \\
(\operatorname{curl} \boldsymbol{B})_{irm} &= e_{mjk} B_{irk,j}, \\
(\boldsymbol{A} : \boldsymbol{B})_{ir} &= A_{imn} B_{mnr},
\end{aligned}
$$

where e_{mjk} is a component of the alternating tensor $\boldsymbol{X}$.

1.4 Dissertation outline

This dissertation involves the modeling and understanding of defects in solids with g.disclination theory, the static equilibrium and dynamics of disclinations in nematic liquid crystals, and the modeling of isotropic-nematic phase transition in LCLC. Specifically, this dissertation is organized as follows.

1. Chapter 2 discusses physical situations that may be associated with the mathematical concept of g.disclinations. The interpretation of the Weingarten theorem for g.disclination in terms of g.disclination kinematics is proposed. The connection between the topological properties of a g.disclination dipole and a dislocation is established in Chapter 2. The Burgers vector of a g.disclination dipole at finite deformation is also deduced. The work in Chapter 2 was done in collaboration with Prof. Amit Acharya. The content of this chapter forms the manuscript of a paper co-authored with Amit Acharya.
2. Chapter 3 reviews the static theory of g.disclinations and proposes numerical schemes

for the small and finite deformation settings. Numerous calculations of line defects in the bulk and interfaces are performed with the g.disclination model. Results of some cases, such as a single disclination, a single dislocation, and a twin boundary, are discussed and compared with classical results where available. Chapter 3 shows the capacity of the g.disclination model in studying various defect problems. The theoretical part of the work in Chapter 3 was done in collaboration with Prof. Amit Acharya. The numerical scheme of finite deformation is an adaptation from Dr. Saurubh Puri's thesis [Pur09]. The content of this chapter forms the manuscript of a paper co-authored with Amit Acharya, and Saurabh Puri.

3. Chapter 4 shows the work on disclination static equilibria and dynamics of nematic liquid crystals. An augmentation of the Oseen-Frank energy is proposed to account for physical situations where infinite director gradients have zero associated energy. Equilibria and dynamics of disclinations in nematic liquid crystals are studied within the proposed framework. Chapter 4 also demonstrates that the gradient flow dynamics for this energy, that is perfectly adequate for predicting defect equilibria, is not able to describe defect evolution. A 2D-model of disclination dynamics in nematics is proposed, and various problems, such as disclination equilibria, annihilation, repulsion, and splitting are computed with the proposed model. The work in Chapter 4 shows that the energy function we devise can serve as well for the modeling of equilibria and dynamics of screw dislocation line defects in solids, making the conclusions of the work in Chapter 4 relevant to mechanics of both solids and liquid crystals. The theoretical part of Chapter 4 was done in collaboration with Prof. Amit Acharya, being an adaptation of the model for dislocation dynamics presented in [AZ15]. The wave-propagative aspects of the numerical algorithm is based on work of [TAS05, DAZM13] adapted in [ZAWB15]. This is coupled to a standard Galerkin framework for the director equilibrium equation. This algorithm was implemented

in a general code framework developed by Prof. Noel Walkington. Technical discussions with Prof. Dmitry Golovaty are also acknowledged. This chapter forms the content of a published paper co-authored with Xiaohan Zhang, Amit Acharya, Dmitry Golovaty, and Noel J. Walkington [ZZA+16].

4. Chapter 5 studies the isotropic-nematic phase transition in chromonic liquid crystals. In the work of Chapter 5, the nematic tactoid equilibria and dynamics are modeled by degree of order, a variable length director as state descriptors, and an interface normal field. An augmented Oseen-Frank energy is proposed with non-convexity in both interfacial energy and the dependence of the energy on the degree of order. Based on kinematics and thermodynamics, a strategy is devised in Chapter 5 to represent phase transition dynamics. The model is used to predict tactoid nucleation, expansion, and coalescence during the process of the isotropic-nematic phase transition. A preliminary parametric study is performed on the effect of nematic elastic constants and the tactoid interfacial energy parameters on the interaction between tactoid interface and bulk director fields. Prof. Oleg Lavrentovich introduced us to the topic of chromonic liquid crystals and provided technical guidance on key experimental observations that have been modeled. Prof. Noel Walkington developed the theory and implementation of the Ericksen-Leslie model with variable degree of order and interfacial energy. The modification of this model to incorporate a separate interfacial normal field and the derivation of the level-set based kinematic evolution, both of which enabled the prediction of tactoid dynamics, was done by me in collaboration with Prof. Amit Acharya. The implementation of this modified model was my work. The content of this chapter forms the manuscript of a paper co-authored with Amit Acharya, Noel J. Walkington, and Oleg D. Lavrentovich.

For the entire work reported in this thesis, all numerical implementations, verifications and validations were carried out by me. All scientific explorations were done by me with

guidance, when necessary, from Prof. Amit Acharya.

Chapter 2

On the relevance of generalized disclinations in defect mechanics

2.1 Introduction

While the mechanics of disclinations has been studied [WIT70, DeW71, DeW73a, DeW73b, Nab87, HPL06, Zub97, RK09, FTC11], there appears to be a significant barrier to the adoption of disclination concepts in the practical modeling of physical problems in the mechanics of materials, perhaps due to the strong similarities between the fields of a disclination dipole and a dislocation [RK09]. Furthermore, the finite deformation version of disclination theory is mathematically intricate [Zub97, DZ11], and does not lend itself in a natural way to the definition of the strength of a disclination purely in terms of any candidate field that may be defined to be a disclination density. This has prevented the introduction of a useful notion of a disclination density field [Zub97, DZ11], thereby hindering the development of a finite deformation theory of disclination fields and its computational implementation to generate approximate solutions for addressing practical problems in the mechanics of materials and materials science.

A recent development in this regard is the development of g.disclination theory (generalized disclination theory) [AF12, AF15], that alleviates the significant road-block in the finite deformation setting mentioned above. It does so by adopting a different conceptual standpoint in defining the notion of g.disclinations than what arose in the works of Weingarten and Volterra (as described by Nabarro [Nab87]). This new standpoint also allows the consideration of phase and grain-boundaries and their terminating line defects within a common framework. Briefly, Weingarten asked a question adapted to the theory of linear elasticity which requires the construction of a displacement field on a multiply-connected[1] body with a single hole, and the characterization of its jumps across any surface that renders the body simply-connected when 'cut' by it. An important constraint of the construction is that the strain of the displacement match a given symmetric second-order tensor field on the simply-connected body induced by the cut; the given symmetric

[1]We refer to any non simply-connected body as multiply-connected or multi-connected.

second-order tensor field is assumed twice-differentiable on the original multiply-connected domain and to satisfy the St.-Venant compatibility conditions. There is a well defined analogous question at finite deformations [Cas04]. The constructed displacement field on the simply-connected domain will in general have a jump (i.e. difference) in the values of its rotation field at corresponding points across the surface but the jump in its strain (similarly defined) necessarily vanishes by definition. However, when viewed from this perspective and keeping physically abundant objects like (incoherent) phase boundaries in mind across which strains are discontinuous as well, there seems to be no reason to begin from a starting point involving a continuous strain field; it is just as reasonable to ask that one is given a smooth third-order tensor field that is curl-free on a multiply-connected domain with a hole (this condition replacing the given strain field satisfying the St.-Venant compatibility condition), and then ask for the construction of a displacement field whose second gradient matches the given third-order tensor field on a cut-surface induced simply-connected domain, and the characterization of the jump of the displacement field across the surface. This allows the whole first gradient of the deformation/displacement field (constructed on the simply-connected domain) to exhibit jumps across the surface, instead of only the rotation. Moreover, this whole argument goes through seamlessly in the context of geometrically nonlinear kinematics; the g.disclination strength is defined as a standard contour integral of the given third order tensor field. The framework naturally allows the calculation of fields of a purely rotational disclination specified as a g.disclination density distribution.

The principal objectives of this cahper are to

- review the physical situations that may be associated with the mathematical concept of disclinations (considered as a special case of g.disclinations). Much is known in this regard amongst specialists (cf. [RK09]), and we hope to provide complementary, and on occasion new, perspective to what is known to set the stage for solving physical

problems related to disclination mechanics in Chapter 3 within the framework of g.disclinations.

- Establish the connection between the topological properties of a g.disclination dipole and a dislocation at finite strains by deducing the formula for the Burgers vector of the g.disclination dipole.
- Interpret the Weingarten theorem for g.disclinations at finite deformation [AF15] in terms of g.disclination kinematics.

This paper is organized as follows. Section 2.2 provides a review of related prior literature. A brief Section 5.2 introduces the notation utilized in the paper. In Section 2.4 we discuss various physical descriptions for disclinations, dislocations, and grain boundaries as well as the interrelations between them. In Section 2.5 we derive the Burgers vector of a disclination dipole within classical elasticity theory, making a direct connection with the stress field of an edge dislocation. Section 2.6 provides an overview of generalized disclination statics from [AF15]. In Section 2.6.1, the Weingarten theorem for generalized disclination theory from [AF15] is recalled for completeness and a new result proving that the displacement jump is independent of the cut-surface under appropriate special conditions is deduced. In this paper, we refer the Weingarten theorem for generalized disclination theory from [AF15] as the Weingarten-gd theorem. In Section 2.7 the Weingarten-gd theorem for g.disclinations is interpreted in the context of g.disclination kinematics, providing an explicit formula for the displacement jump of a single g.disclination in terms of data prescribed to define the two defect densities (g.disclination and dislocation densities) in g.disclination theory. Finally, in Section 2.8 we derive the Burgers vector for a g.disclination dipole.

2.2 A brief review of prior work

In this section we briefly review some of the vast literature on the mathematical modeling of disclinations and grain boundaries. An exhaustive review of the subject is beyond the scope of this paper.

The definition of the dislocation and the disclination in *solids*[2] was first introduced by Volterra (as described by Nabarro [Nab87]). Nabarro [Nab87] studied geometrical aspects of disclinations and Li [Li72] presented microscopic interpretations of a grain boundary in terms of a dislocation and a disclination model. The static fields of dislocations and disclinations along with applications have been studied extensively within linear elasticity by DeWit [WIT70, DeW71, DeW73b, DeW72], as well as in 2-d nonlinear elasticity by Zubov [Zub97] and the school of study led by Romanov [RK09]. In [RK09], the elastic fields and energies of the disclination are reviewed and the disclination concept is applied to explaining several observed microstructures in crystalline materials. In [RV92], the expression for the Burgers vector for a single-line, two-rotation-axes disclination dipole appropriate for geometrically linear kinematics is motivated from a physical perspective without dealing with questions of invariance of the physical argument w.r.t different cut-surfaces or the topological nature of the displacement jump of a disclination-dipole in contrast to that of a single disclination.

In Fressengeas et al. [FTC11], the elasto-plastic theory of dislocation fields [Ach01] is non-trivially extended to formulate and study time-dependent problems of defect dynamics including both disclination and dislocation fields. Nonlinear elasticity of disclinations and dislocations in 2-d elastic bodies is discussed in [Zub97, DZ11]. Dislocations and disclinations are studied within Riemannian geometry in [KMS15]; Cartan's geometric method to study Riemannian geometry is deployed in [YG12] to determine the nonlinear residual stress for 2-d disclination distributions. Similar ideas are also reviewed in [CMB06], in a

[2]There is a difference in meaning between disclinations in solids and in nematic liquid crystals as explained in [RK09, KF08, PAD15].

different degree of mathematical detail and without any explicit calculations, in an effort to develop a time-dependent model of mesoscale plasticity based on disclination-dislocation concepts. Another interesting recent work along these lines is the one in [RG17] that discusses 'metrical disclinations' (among other things) that are related to our g.disclinations. The concerns of classical, nonlinear disclination theory related to defining the strength of a single disclination in a practically applicable manner, and therefore studying the mechanics of interactions of collections of individual such defects, remains in this theory and the authors promote the viewpoint of avoiding any type of curvature line-defects altogether.

From the materials science perspective, extensive studies have been conducted on grain boundary structure, kinetics, and mechanics from the atomistic [SV83a, SV83b] as well as from more macroscopic points of view [Mul56, CMS06, Cah82]. In [KRR06, SElDRR04, Roh10, Roh11], the grain boundary character distribution is studied from the point of view of grain boundary microstructure evolution. In [KLT06, EES$^+$09], a widely used framework for grain boundary network evolution, which involves the variation of the boundary energy density based on misorientation, is proposed. In most cases, these approaches do not establish an explicit connection with the stress and elastic deformation fields caused by the grain boundary [HHM01]. Phase boundary mechanics considering effects of stress is considered in [PL13, AD15], strictly within the confines of compatible elastic deformations.

One approach to study a low angle grain boundary is to model it as a series of dislocations along the boundary [RS50, SV83a, SV83b]. In [DXS13], a systematic numerical study is conducted of the structure and energy of low angle twist boundaries based on a generalized Peierls-Nabarro model. The dislocation model has also been applied to study grain boundaries with disconnections [HP96, HH98, HPL06, HPL07, HPH09, HP11, HPH$^+$13]. In these work, disconnections are modeled as dislocations at a step and the grain boundaries are represented as a series of coherency dislocations. Long-range stress fields for disconnections in tilt walls are discussed from both the discrete dislocations and the disclination dipole perspectives in [AZH08]. In [VD13, VAKD14, VD15] a combination of the

Frank-Bilby equation [Fra50, Fra53, BBS55, SB95, BB56] and anisotropic elasticity theory is employed to formulate a computational method for describing interface dislocations. In [DSSS98] atomic-level mechanisms of dislocation nucleation is examined by dynamic simulations of the growth of misfitting films.

Although low angle grain boundaries can be modeled by dislocations, the dislocation model is no longer satisfactory for describing high-angle boundaries because the larger misorientations require introducing more dislocations along the boundary interface which shortens the distance between dislocations [BAC05]. Thus, it is difficult to identify the Burgers vectors of grain boundary dislocations in high angle grain boundaries. Alternatively, a grain boundary can also be modeled as an array of disclination dipoles [RK09, NSB00]. In [FTC14], the crossover between the atomistic description and the continuous representation is demonstrated for a tilt grain boundary by designing a specific array of disclination dipoles. Unlike the dislocation model for a grain boundary, the disclination model is applicable to the modeling of both low and high angle grain boundaries.

2.3 Notation and terminology

$\boldsymbol{F}^e$ is the elastic distortion tensor; $\boldsymbol{W} := (\boldsymbol{F}^e)^{-1}$ is the inverse-elastic 1-distortion tensor; $\boldsymbol{S}$ is the eigenwall tensor (3^{rd}-order); $\boldsymbol{Y}$ is the inverse-elastic 2-distortion tensor (3^{rd}-order); $\boldsymbol{\alpha}$ is the dislocation density tensor (2^{nd}-order) and $\boldsymbol{\Pi}$ is the generalized disclination density tensor (3^{rd}-order). The physical and mathematical meanings of these symbols will be discussed subsequently in Section 2.6.

In dealing with questions related to the Weingarten-gd theorem, we will often have to talk about a vector field $\boldsymbol{y}$ which will generically define an inverse elastic deformation from the current deformed configuration of the body.

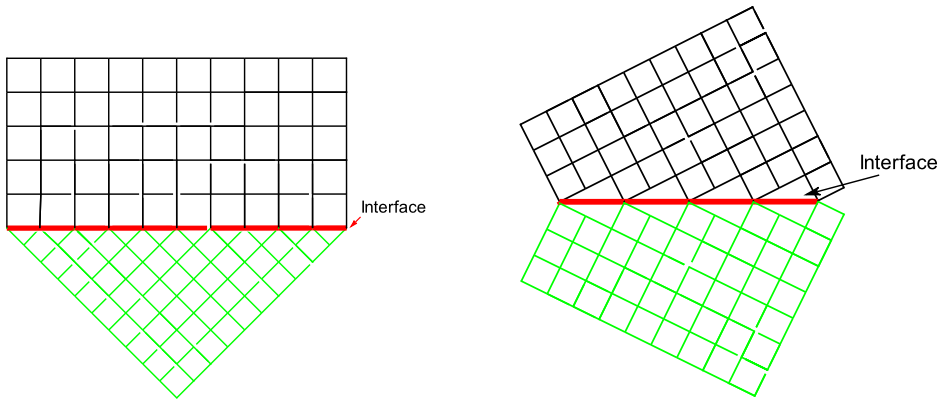

(a) A compatible/coherent phase boundary, where all atomic planes from either side match along the interface.

(b) An incompatible/incoherent phase boundary. There are some mismatches of the atomic planes along the interfaces.

Figure 2.1: *Illustration of a compatible/coherent and an incompatible/incoherent phase boundary.*

2.4 Basic ideas for the description of g.disclinations, dislocations, and grain boundaries

In this section we will discuss various aspects of modeling g.disclinations and their relationship to dislocations, mostly from a physical perspective and through examples. Beginning from a geometric visualization of single disclinations, we will motivate the physical interpretation of such in lattice structures. The formation and movement of a disclination dipole through a lattice will be motivated. Descriptions of a dislocation in terms of a disclination dipole will be discussed. Finally, we will demonstrate how the description of a low-angle boundary in terms of disclination dipoles may be understood as a dislocated grain-boundary in a qualitative manner.

In many situations in solid mechanics it is necessary to consider a 2-D surface where a distortion measure is discontinuous. In elasticity a distortion corresponds to the deformation gradient; in linear elasticity the distortion will be grad $\boldsymbol{u}$, where $\boldsymbol{u}$ is the displacement. However, there are many cases where the distortion field cannot be interpreted as a gradient

of a vector field on the whole body. In such cases, the distortion will have an incompatible part that is not curl-free. One familiar situation is to consider the presence of dislocations modeled by the elastic theory of dislocations [Krö81, Wil67]. A 2-d surface of discontinuity of the elastic distortion is referred to as a phase boundary, of which the grain boundary is a particular case. Based on whether atomic planes from either side of the interface can match with each other at the interface or not, a phase boundary is categorized into a compatible/coherent or an incompatible/incoherent boundary, as shown in Figure 2.1. A special compatible phase boundary is called a twin boundary with a highly symmetrical interface, where one crystal is the mirror image of the other, also obtained by a combination of shearing and rotation of one side of the interface with respect to the other. A grain boundary is an interface between two grains with different orientations. The orientation difference between the two grains comprising a grain boundary is called the misorientation at the interface, and it is conventional to categorize grain boundaries based on the misorientation angle. Low angle grain boundaries (LAGBs) are defined as those whose misorientations are less than 11 degrees and high angle grain boundaries (HAGBs) are those with greater misorientations. In the situation that the phase boundary discontinuity shows gradients along the surface, we will consider the presence of line defects. Following [AF12, AF15], the terminating tip-curves of phase boundary discontinuities are called generalized disclinations or g.disclinations.

The classical singular solutions for defect fields contain interesting subtleties. For instance, the normal strain e_{11} in dimension two for a straight dislocation and of a straight

disclination in linear elasticity are [DeW71, DeW73b]:

Straight Dislocation

$$e_{11} = -\frac{b_1}{4\pi\,(1-\nu)}[(1-2\nu)\,\frac{x_2}{\rho^2} + 2\frac{x_1^2 x_2}{\rho^4}] + \frac{b_2}{4\pi\,(1-\nu)}[(1-2\nu)\,\frac{x_1}{\rho^2} - 2\frac{x_1 x_2^2}{\rho^4}],$$

Straight Disclination

$$e_{11} = \frac{\Omega_3}{4\pi(1-\nu)}[(1-2\nu)\ln\rho + \frac{x_2^2}{\rho^2}].$$

The strain fields blow up in both the dislocation and the disclination cases. In addition, on approaching the core (i.e. the coordinate origin in the above expressions) in dislocation solutions, the elastic strain blows up as $\frac{1}{\rho}$, ρ being the distance from the dislocation core. Thus the linear elastic energy density diverges as $\frac{1}{\rho^2}$, causing unbounded total energy for a finite body for the dislocation whereas the total energy of a disclination is bounded. The disclination, however, has more energy stored in the far-field (w.r.t the core) than the dislocation, and this is believed to be the reason for a single disclination being rarely observed as opposed to a dislocation. Our modeling philosophy and approach enables defects to be represented as non-singular defect lines and surfaces, always with bounded total energy (and even local stress fields).

2.4.1 Disclinations

Volterra [Nab85] described dislocations and disclinations by considering a cylinder with a small inner hole along the axis, as shown in Figure 2.2 (the hole is exaggerated in the figure). Figure 2.2(e)(f)(g) show configurations of disclinations. Imagine cutting the cylinder with a half plane, rotating the cut surfaces by a vector $\boldsymbol{\omega}$, welding the cut surfaces together and relaxing (i.e. letting the body attain force equilibrium). Then a rotation discontinuity occurs on the cut surface and the vector $\boldsymbol{\omega}$ is called the Frank vector. If the Frank vector is parallel to the cylinder's axis, the disclination is called a wedge disclination; if the Frank

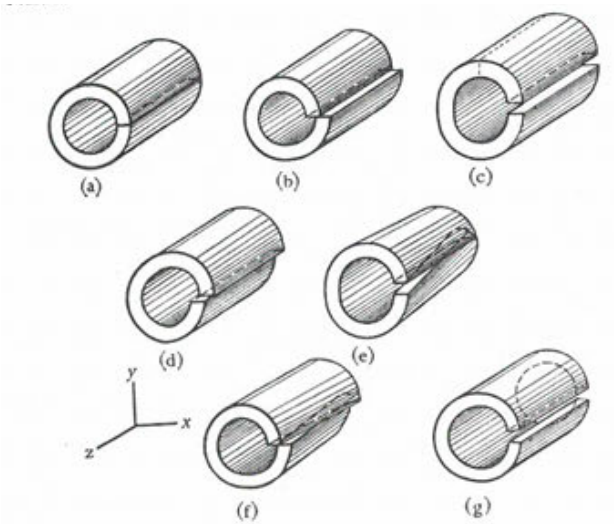

Figure 2.2: *Descriptions of Volterra dislocations and disclinations . Figure (a) is a cylinder with an inner hole along the axis. Figure (b) and (c) are the edge dislocations. Figure (d) is the screw dislocation. Figure (e) and (f) are twist disclinations and Figure (g) is the wedge disclination. (Figure reprinted from [Nab87] with permission from Dover Publications).*

vector is normal to the cylinder's axis, the line defect is called a twist disclination. In the following, we will mostly focus on wedge disclinations.

A wedge disclination can be visualized easily [Naz13], as shown in Figure 2.3. By taking away or inserting a wedge of an angle ω, a positive or negative wedge disclination is formed. In Figure 2.3(a) is a negative wedge disclination and (b) is a positive wedge disclination in a cylindrical body. After eliminating the overlap/gap-wedge and welding and letting the body relax, the body is in a state of internal stress corresponding to that of the wedge disclination (of corresponding sign).

In this work, we introduce a description for the disclination configuration based on the elastic distortion field, as shown in Figure 2.4. In Figure 2.4, red lines represent one elastic distortion field (possibly represented by the Identity tensor); black lines represent another distortion field. Thus, there is a surface of discontinuity between these two distortion fields and a terminating line (which is a point on the 2-d plane) on the interface is called a disclination. Also, there is a gap-wedge between the red part and the black part as shown in Figure 2.4(a), indicating it as a positive disclination; an overlap-wedge in Figure 2.4(b)

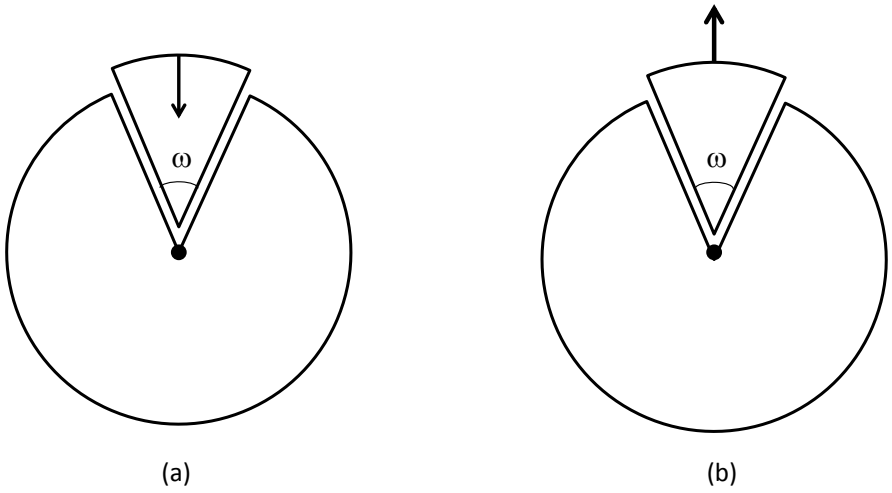

Figure 2.3: *A planar illustration for wedge disclinations. Figure (a) is a negative wedge disclination, where a wedge is inserted into a vertical cut causing compressive circumferential stress after 'welding' the wedge to the body. Figure (b) is a positive wedge disclination, where the wedge is taken out of the original structure and the exposed faces welded together. ω is the wedge angle as well as the magnitude of the Frank vector. (Figure reproduced from [Naz13] with permission from publisher of article under an open-access Creative Commons license).*

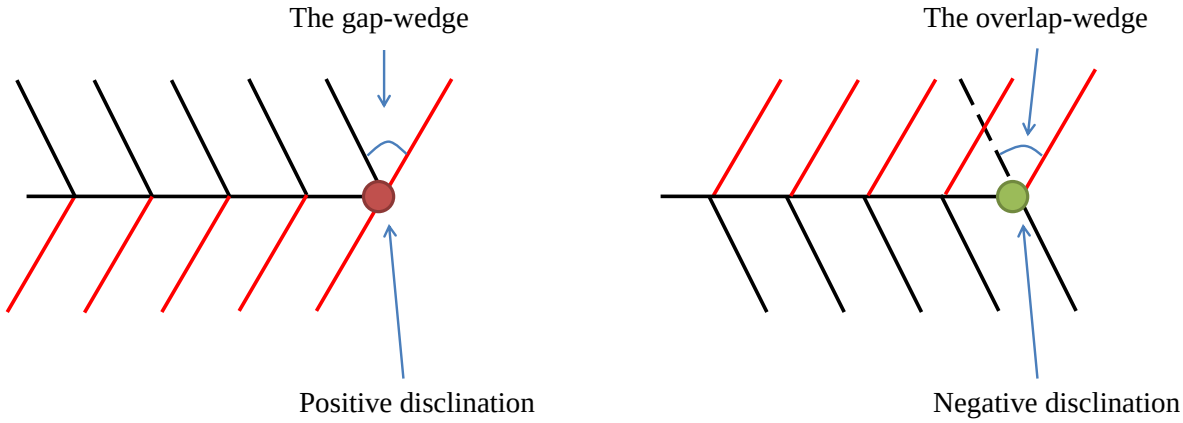

(a) A positive wedge disclination with a gap-wedge between two orientations. The red dot is the positive wedge disclination core where the interface of the orientation-discontinuity terminates.

(b) A negative wedge disclination with an overlap-wedge between two orientations. The green dot is the negative wedge disclination core where the interface of the orientation-discontinuity terminates.

Figure 2.4: *An elastic distortion based description of wedge disclinations.*

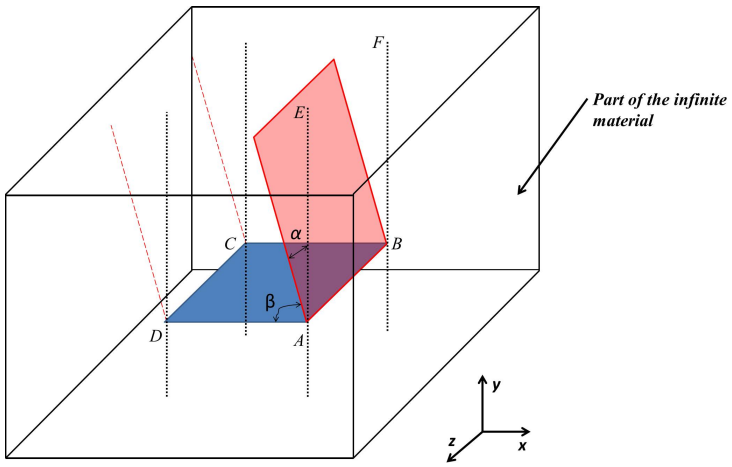

Figure 2.5: *A 3D description for a disclination loop in an infinite block. ABCD is the disclination loop in a parallelepiped. Wedge disclinations exist along AB and CD while twist disclinations exist along AD and BC.*

corresponds to a negative disclination. Since a gap-wedge is eliminated for a positive disclination, there is circumferential tension around the core. Similarly, there is circumferential compression around the core for the negative disclination because of the inserted wedge. These physical arguments allow the inference of some features of the internal state of stress around disclination defects without further calculation.

A disclination loop is formed if an inclusion of a crystal with one orientation, and in the shape of a parallelepiped with infinite length, is inserted in another infinite crystal of a different orientation, as shown in Figure 2.5. Focusing on the bottom surface of the parallelepiped, we consider the 'exterior' crystal as having one set of atomic planes parallel to the $y-z$ plane bounded by unbounded black rectangles in Figure 2.5. The interior crystal has one set of planes at an angle of α to the $y-z$ plane. The line of intersection AB represents a termination of a gap-wedge formed by the red plane of the interior crystal and the plane $ABFE$ of the exterior crystal. Because the misorientation vector is directed along line AB (z axis), the latter serves as a wedge disclination. Similarly, there is a wedge disclination along intersection line CD of opposite sign to AB. For intersection lines BC and DA, the misorientation vector is perpendicular to the direction of intersection lines

and twist disclinations of opposite signs are formed along BC and DA. The curve $ABCD$ forms a disclination loop in the body (on elimination of the gap and overlap wedges).

2.4.2 Disclination dipole formation and movement in a lattice

Due to the addition and subtraction of matter over large distances involved in the definition of a disclination in the interior of a body, it is intuitively clear that a single disclination should cause long-range elastic stresses, which can also be seen from the analytical solution given in Section 2.2. Thus, a disclination rarely exists alone. Instead, usually, disclinations appear in pairs in the form of dipoles, namely a pair(s) of disclinations with opposite signs. Figure 2.6 shows a schematic of how a disclination dipole can form in a hexagonally coordinated structure. Figure 2.6(a) is the original structure with a hexagonal lattice; Figure 2.6(b) shows how bonds can be broken and rebuilt to transform a hexagon pair to a pentagon-heptagon pair in a topological sense (this may be thought of as a situation before relaxation); Figure 2.6(c) presents the relaxed configuration with a disclination dipole (the penta-hepta pair) after the transformation.

In a stress-free hexagonal lattice, removing an edge of a regular hexagon to form a pentagon can be associated with forming a positive wedge disclination at the center of the regular polygon (due to the tensile stress created in the circumferential direction); similarly, adding an edge to form a heptagon may be considered the equivalent of forming a negative wedge disclination. Hence, a heptagon-pentagon pair in a nominally hexagonal lattice is associated with a disclination dipole. It should be clear by the same logic that in a lattice with regular n-sided repeat units, an $(n-1)-(n+1)$ polygon pair may be viewed as a disclination dipole.

Figure 2.7 shows how a disclination dipole moves by local crystal rearrangement under some external force. Figure 2.7(a) shows the configuration for a hexagonal lattice with a disclination dipole; then some atomic bonds nearby are broken and rebuilt in Figure 2.7(b);

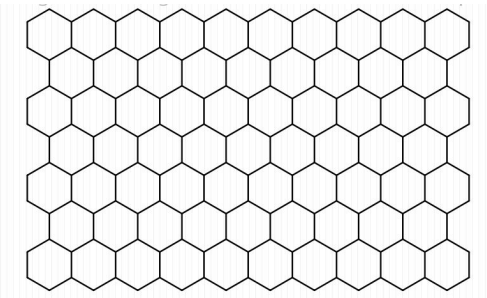

(a) Structure of a hexagonal lattice.

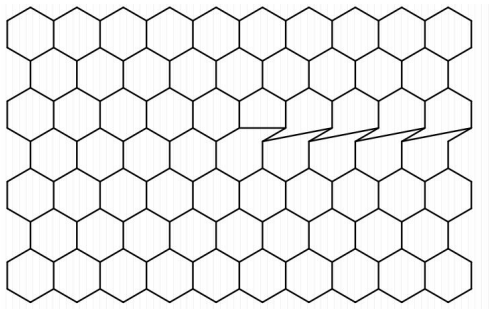

(b) Break and rebuild atomic bonds to form a disclination dipole (pentagon-heptagon pair).

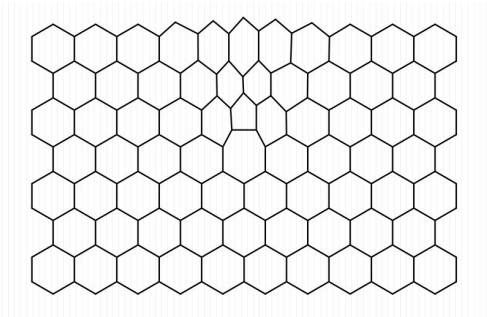

(c) Relaxed configuration with a disclination dipole.

Figure 2.6: *Kinematics of formation of a disclination-dipole in a hexagonal lattice. Figures constructed with Chemdoodle[che].*

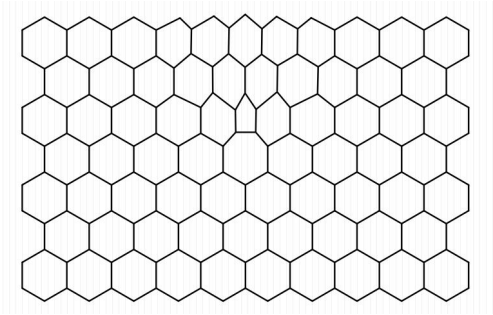

(a) Structure of a hexagonal lattice with a disclination dipole.

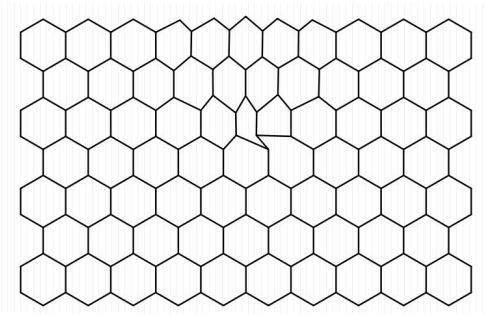

(b) Break and rebuild atomic bonds to move a disclination dipole.

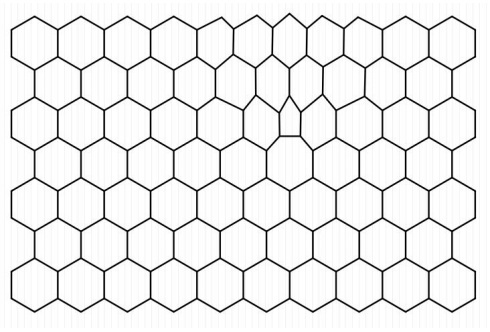

(c) Relaxed configuration with disclination dipole having moved through the material to the right.

Figure 2.7: *Kinematics of motion of a disclination dipole. Figures constructed with Chemdoodle[che].*

Figure 2.7(c) shows the relaxed configuration, where the disclination dipole has moved the right. The movement of a disclination dipole is a local rearrangement instead of a global rearrangement required to move a single disclination.

2.4.3 Descriptions of a dislocation by a (g.)disclination dipole

In this section we consider two physically distinct constructions that motivate why a straight edge dislocation may be thought of as being closely related to a (g.)disclination dipole. Figure 2.8(a) is a perfect crystal structure. Black lines represent atomic planes and red lines are the atomic bonds between two horizontal atomic planes. We apply a shear on the top and the bottom of this body along the blue arrows shown in Figure 2.8(a).

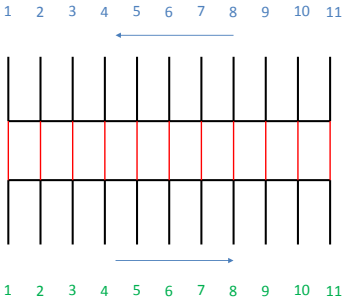

(a) A perfect crystal structure, where the black lines represent atomic planes.

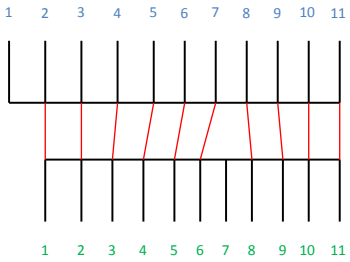

(b) Half-planes of atoms $(1-7)$ in the top-block change topological connections to their counterparts in the bottom block on shearing, resulting in the appearance of an 'extra' half-plane in the bottom block. No extra atoms are introduced in the structure.

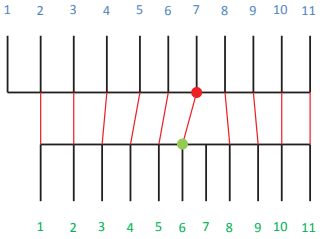

(c) Interpretation of defected structure as a disclination dipole. The red and green dots represent positive and negative wedge disclinations, respectively.

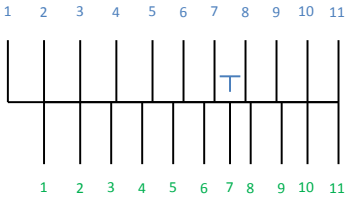

(d) Disclination dipole in (c) viewed at a larger length scale (weaker resolution). The disclination dipole appears as an edge dislocation.

Figure 2.8: *Interpretation of a wedge disclination dipole as an edge dislocation.*

After shearing, an extra half plane is introduced in the bottom part, as shown in Figure 2.8(b). This dislocation can as well be interpreted as a disclination dipole; a positive disclination (the red dot in Figure 2.8(c)) exists in the top part and a negative disclination (the green dot in Figure 2.8(c)) exists in the bottom part. Figure 2.8(d) shows a zoomed-out macroscopic view of the final configuration with an extra half-plane (of course obtained by a process where no new atoms have been introduced). Thus, a dislocation can be represented as a disclination dipole with very small separation distance. The Burgers vector of the dislocation is determined by the misorientation of the disclinations as well as the interval distance, as discussed in detail in Section 2.8. The upper disclination has a gap-wedge, namely a positive disclination, while the lower disclination has an overlap-wedge which is a negative disclination. Thus, the upper part is under tension and the bottom part under compression, consistent with the dislocation description with an 'extra' half-plane in the bottom part. Our rendition here is a way of understanding how a two-line, two-rotation axes disclination dipole [RK09] results in an edge dislocation in the limit of the distance between the two planes vanishing.

Another way in which a dislocation can be associated with a disclination dipole is one that is related to the description of incoherent grain boundaries. Figure 2.9(a) is an incompatible grain boundary represented by orientation fields, where black and red lines represent two different orientations. In Figure 2.9(b), the grain boundary interface is cut in two parts and the cut points are treated as a disclination dipole; the red dot is the positive disclination and the green dot is the negative disclination. In contrast to the description in Fig. 2.8, here the discontinuity surfaces being terminated by the disclinations are coplanar. In Figure 2.9(b), the disclination on the left is of negative strength while the disclination on the right is positive. It is to be physically expected that the disclination on the left of the dipole produces a compressive stress field in the region to the left of the dipole. Similarly, the disclination on the right of the pair should produce a tensile stress field to the right of the dipole. Figure 2.9(c) is the stress field for the grain boundary in Figure 2.9(a)

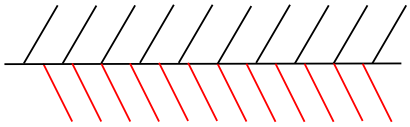

(a) A defected grain boundary.

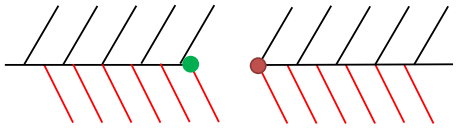

(b) A disclination dipole representing one defect of the grain boundary.

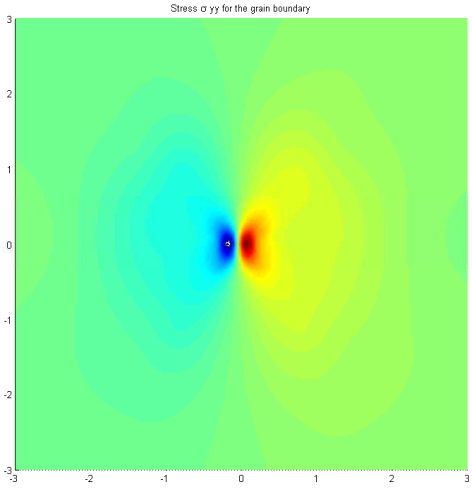

(c) Stress σ_{yy} around a single defect in the grain boundary, calculated from the (g.)disclination dipole model.

Figure 2.9: *The disclination dipole description of a defect in the grain boundary.*

modeled by a single disclination dipole through a numerical approximation of a theory to be described in Section 2.6. Indeed, the calculation bears out the physical expectation - the blue part represents a region with compressive stress and the red part a region with tensile stress. The stress field may be associated with that of an edge dislocation with Burgers vector in the vertical direction with an extra half plane of atoms in the right-half plane of the figure. This description of a dislocation by a disclination dipole is a way of understanding a single-line, two-rotation-axes dipole [RK09].

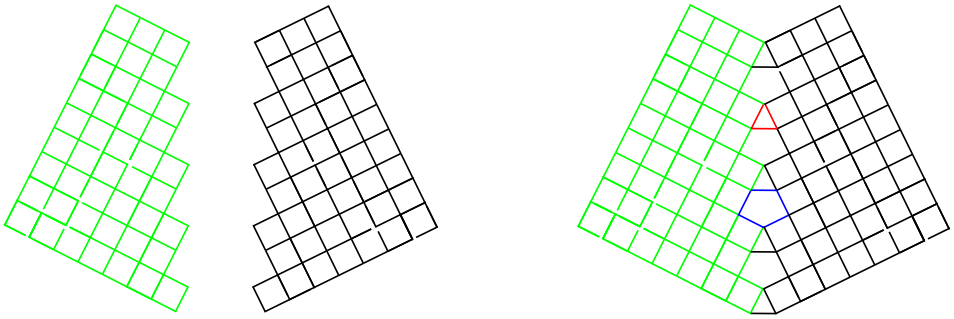

(a) Two grains with different crystal structures.

(b) Bi-crystal after merging two grains together.

Figure 2.10: *Schematic of forming a series of disclination dipoles in a grain boundary. The red triangle is a positive disclination while the blue pentagon is a negative disclination. The pentagon-triangle disclination dipoles (in a 4-coordinated medium) exist along the interface.*

2.4.4 Grain boundaries via (g.)disclinations

We have already seen in the last section that a disclination-dipole model can be relevant to modeling the geometry and mechanics of grain boundaries. Figure 2.10 motivates how disclination dipoles arise naturally in the idealized description of a grain boundary from a microscopic view. In Figure 2.10(a), there are two grains with different orientations. After putting these two grains together and connecting the adjacent atomic bonds, we form a grain boundary, as shown in Figure 2.10(b). There exists a series of disclination dipoles along the boundary, as shown in Figure 2.10(b) where a blue pentagon is a negative disclination while a red triangle is a positive disclination.

In some cases, grain boundaries involve other types of defects beyond disclination dipoles, such as dislocations. Figure 2.11 is an example of a vicinal crystal interface [BAC05], which consists of a combination of dislocations and disclinations along the interface. In Figure 2.11(a) a high-angle tilt boundary with a tilt of 53.1° is viewed along the $< 100 >$ tilt axis. If we slightly increase the tilt angle while keeping the topology of bond connections near the boundary fixed, high elastic deformations are generated, as shown in the Figure 2.11(b). Instead, an array of dislocations is often observed along the boundary

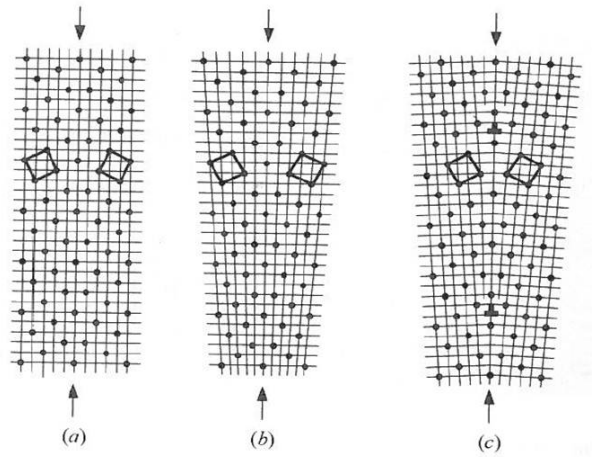

Figure 2.11: *(a) A common tilt grain boundary with 53.1 degree misorientation. (b) The configuration after applying additional tilt angle without any rearrangement. (c) The configuration with some dislocations introduced along the interface to eliminate far field deformation. (Figures reproduced from [BAC05] with permission from John Wiley and Sons).*

as shown in the configuration Figure 2.11(c), presumably to eliminate long-range elastic deformations. In Chapter 3, we calculate the elastic fields of such boundaries utilizing both g.disclinations and dislocations.

2.4.4.1 Relationship between the disclination and dislocation models of a low-angle grain boundary

Normally, a grain boundary is modeled by an array of dislocations. As discussed in Section 2.2, a dislocation model cannot deal with a high-angle grain boundary. An alternative is to interpret the grain boundary through a disclination model as we discussed above. In this section, the relation between the disclination and dislocation models for a low-angle grain boundary is explained.

Consider a defect-free crystal as shown in Figure 2.12(a). First, we horizontally cut the material into four parts, as shown in the upper configuration in Figure 2.12(b). Now, for every part, we cut the material along its center surface (the dashed line in Figure 2.12(b)), insert one atom at the top and take away one atom from the bottom, weld the two half parts

together again and relax the material. Then the configuration for every part will become the configuration at the bottom in Figure 2.12(b). By inserting and taking away atoms, we generate a negative disclination at the top and a positive disclination at the bottom. Repeating the same procedure for the remaining three parts, we finally obtain four parts with configurations as in Figure 2.12(c). The blue pentagons are negative disclinations while the red triangles are positive disclinations; a pair of a blue pentagon and an adjacent red triangle forms a disclination dipole. Next, we weld back these four parts and relax the whole material. Finally, a crystal configuration as in Figure 2.12(d) is generated, which is a grain boundary with the boundary interface shown as the blue dashed line. Along the grain boundary, dislocations exist along the interface with extra atomic planes shown as red lines in Figure 2.12(d). When the pentagon-triangle (5-3) disclination dipole is brought together to form a dislocation, the pentagon-triangle structure actually disintegrates and becomes a pentagon-square-square (5-4-4) object. Thus, a grain boundary can be constructed from a series of disclination dipoles; at the same time, we can see dislocation structures at the grain boundary interface. It is as if the 5-3 disclination dipole structure fades into the dislocation structure on coalescing the two disclinations in a dipole.

A comparison between the dislocation model and the disclination model has also been discussed in [Li72] where the possibility of modeling a dislocation by a disclination dipole is proposed within the context of the theory of linear elasticity. In this paper, we have elucidated the physical picture of forming a dislocation from a disclination dipole and, in subsequent sections, we also derive the general relationship between the Burgers vector of a dislocation and the disclination dipole for both the small and finite deformation cases, capitalizing crucially on a g.disclination formulation of a disclination dipole.

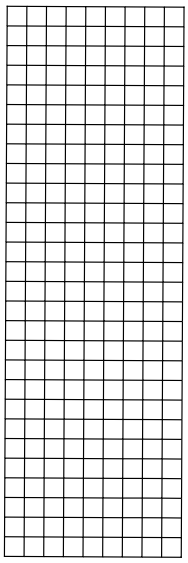

(a) The perfect crystal configuration.

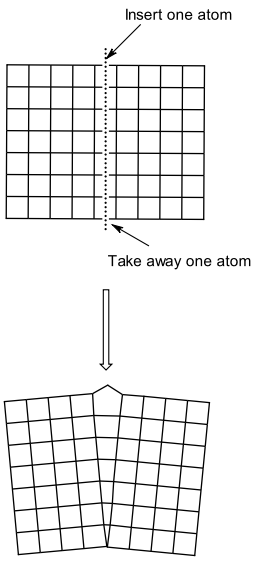

(b) Cut the material into four parts; introduce a positive disclination at the top and a negative disclination at the bottom.

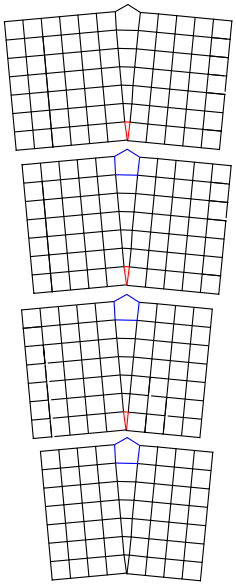

(c) Repeat the same procedure for all four parts.

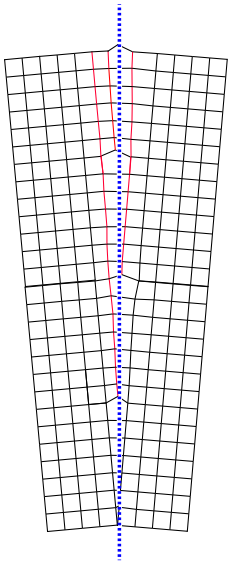

(d) Weld four parts together and form a grain boundary whose interface is shown as the dotted blue line.

Figure 2.12: *Schematic of how disclination dipoles may fade into dislocations along a grain boundary.*

2.5 The Burgers vector of a disclination dipole in linear elasticity

We derive a formula for the Burgers vector of a wedge disclination dipole utilizing the linear theory of plane isotropic elasticity. Consider a positive disclination located at the origin O, as shown in Figure 2.13(a). We denote the stress at point $\boldsymbol{c}$ of a single disclination located at $\boldsymbol{a}$ with Frank vector $\boldsymbol{\Omega}$ as $\boldsymbol{\sigma}(\boldsymbol{c}; \boldsymbol{a}, \boldsymbol{\Omega})$. Thus, the stress field at $\boldsymbol{r}$ in Figure 2.13(a) is $\boldsymbol{\sigma}(\boldsymbol{r}; \boldsymbol{0}, \boldsymbol{\Omega})$. Next we consider the field point $\boldsymbol{r} + \delta\boldsymbol{r}$ marked by the green point as in Figure 2.13(b), with the disclination kept at the origin O. The stress tensor at this point is given by $\boldsymbol{\sigma}(\boldsymbol{r} + \delta\boldsymbol{r}; \boldsymbol{0}, \boldsymbol{\Omega})$.

Instead of moving the field point in Figure 2.13(b), we next consider the field point as fixed at $\boldsymbol{r}$ with the disclination moved from $\boldsymbol{0}$ to $-\delta\boldsymbol{r}$ as shown in Figure 2.13(c). The value of the stress at $\boldsymbol{r}$ now is $\boldsymbol{\sigma}(\boldsymbol{r}; -\delta\boldsymbol{r}, \boldsymbol{\Omega})$. Utilizing the results in [DeW73a], the stress of a disclination, of fixed strength $\boldsymbol{\Omega}$ and located at $\boldsymbol{a} = a_1\boldsymbol{e}_1 + a_2\boldsymbol{e}_2 + a_3\boldsymbol{e}_3$, at the field

point $\boldsymbol{c} = c_1\boldsymbol{e}_1 + c_2\boldsymbol{e}_2 + c_3\boldsymbol{e}_3$ is given by

$$
\begin{aligned}
\sigma_{11}(\boldsymbol{c};\boldsymbol{a},\boldsymbol{\Omega}) =& -\frac{G\Omega_1(c_3-a_3)}{2\pi(1-\nu)}\left[\frac{c_1-a_1}{\rho^2} - 2\frac{(c_1-a_1)(c_2-a_2)^2}{\rho^4}\right] \\
& -\frac{G\Omega_2(c_3-a_3)}{2\pi(1-\nu)}\left[\frac{c_2-a_2}{\rho^2} + 2\frac{(c_1-a_1)^2(c_2-a_2)}{\rho^4}\right] \\
& +\frac{G\Omega_3}{2\pi(1-\nu)}\left[\ln\rho + \frac{(c_2-a_2)^2}{\rho^2} + \frac{\nu}{1-2\nu}\right] \\
\sigma_{22}(\boldsymbol{c};\boldsymbol{a},\boldsymbol{\Omega}) =& -\frac{G\Omega_2(c_3-a_3)}{2\pi(1-\nu)}\left[\frac{c_1-a_1}{\rho^2} + 2\frac{(c_1-a_1)(c_2-a_2)^2}{\rho^4}\right] \\
& -\frac{G\Omega_2(c_3-a_3)}{2\pi(1-\nu)}\left[\frac{c_2-a_2}{\rho^2} - 2\frac{(c_1-a_1)^2(c_2-a_2)}{\rho^4}\right] \\
& +\frac{G\Omega_3}{2\pi(1-\nu)}\left[\ln\rho + \frac{(c_1-a_1)^2}{\rho^2} + \frac{\nu}{1-2\nu}\right] \\
\sigma_{33}(\boldsymbol{c};\boldsymbol{a},\boldsymbol{\Omega}) =& -\frac{G\nu(c_3-a_3)}{\pi(1-\nu)\rho^2}(\Omega_1(c_1-a_1)+\Omega_2(c_2-a_2)) + \frac{G\Omega_3}{2\pi(1-\nu)}\left[2\nu\ln\rho + \frac{\nu}{1-2\nu}\right] \\
\sigma_{12}(\boldsymbol{c};\boldsymbol{a},\boldsymbol{\Omega}) =& \frac{G\Omega_1(c_3-a_3)}{2\pi(1-\nu)}\left[\frac{c_2-a_2}{\rho^2} - 2\frac{(c_1-a_1)^2(c_2-a_2)}{\rho^4}\right] \\
& +\frac{G\Omega_2(c_3-a_3)}{2\pi(1-\nu)}\left[\frac{c_1-a_1}{\rho^2} - 2\frac{(c_1-a_1)^2(c_2-a_2)}{\rho^4}\right] - \frac{G\Omega_3(c_1-a_1)(c_2-a_2)}{2\pi(1-\nu)\rho^2} \\
\sigma_{23}(\boldsymbol{c};\boldsymbol{a},\boldsymbol{\Omega}) =& \frac{G\Omega_1(c_1-a_1)(c_2-a_2)}{2\pi(1-\nu)\rho^2} - \frac{G\Omega_2}{2\pi(1-\nu)}\left[(1-2\nu)\ln\rho + \frac{(c_1-a_1)^2}{\rho^2}\right] \\
\sigma_{13}(\boldsymbol{c};\boldsymbol{a},\boldsymbol{\Omega}) =& -\frac{G\Omega_1}{2\pi(1-\nu)}\left[(1-2\nu)\ln\rho + \frac{(c_2-a_2)^2}{\rho^2}\right] + \frac{G\Omega_2(c_1-a_1)(c_2-a_2)}{2\pi(1-\nu)\rho^2},
\end{aligned}
\tag{2.1}
$$

where ρ is the distance between the field point $\boldsymbol{c}$ and the source point $\boldsymbol{a}$, $\rho = |\boldsymbol{c}-\boldsymbol{a}|$. Equation (2.1) shows that the stress fields only depend on the relative location of the field and disclination source points. In other words, given a disclination at $\boldsymbol{a}$ with Frank vector $\boldsymbol{\Omega}$, the stress field at point $\boldsymbol{c}$ can be expressed as

$$\boldsymbol{\sigma}(\boldsymbol{c};\boldsymbol{a},\boldsymbol{\Omega}) = \boldsymbol{f}(\boldsymbol{c}-\boldsymbol{a};\boldsymbol{\Omega}),$$

where $\boldsymbol{f}$ is the formula for the stress field of the wedge disclination in linear isotropic elasticity whose explicit expression in Cartesian coordinates is given in (2.1). From (2.1),

we have

$$\boldsymbol{f}(\boldsymbol{x};\boldsymbol{\Omega}) = -\boldsymbol{f}(\boldsymbol{x};-\boldsymbol{\Omega}), \tag{2.2}$$

for any given $\boldsymbol{x}$. Thus, for the stress fields, we have

$$\boldsymbol{\sigma}(\boldsymbol{c};\boldsymbol{a},\boldsymbol{\Omega}) = -\boldsymbol{\sigma}(\boldsymbol{c};\boldsymbol{a},-\boldsymbol{\Omega}).$$

Hence, the stress field in Figure 2.13(a) can be written as

$$\boldsymbol{\sigma}(\boldsymbol{r};\boldsymbol{0},\boldsymbol{\Omega}) = \boldsymbol{f}(\boldsymbol{r};\boldsymbol{\Omega}).$$

The stress field corresponding to Figure 2.13(b) is

$$\boldsymbol{\sigma}(\boldsymbol{r}+\delta\boldsymbol{r};\boldsymbol{0},\boldsymbol{\Omega}) = \boldsymbol{f}(\boldsymbol{r}+\delta\boldsymbol{r};\boldsymbol{\Omega}).$$

Also, the stress field in Figure 2.13(c) is

$$\boldsymbol{\sigma}(\boldsymbol{r};-\delta\boldsymbol{r},\boldsymbol{\Omega}) = \boldsymbol{f}(\boldsymbol{r}-(-\delta\boldsymbol{r});\boldsymbol{\Omega}) = \boldsymbol{f}(\boldsymbol{r}+\delta\boldsymbol{r};\boldsymbol{\Omega}).$$

In Figure 2.13(d), a disclination dipole is introduced. A negative disclination with Frank vector $-\boldsymbol{\Omega}$ is at $\boldsymbol{0}$ and the positive disclination with Frank vector $\boldsymbol{\Omega}$ is at $-\delta\boldsymbol{r}$. Thus, $\delta\boldsymbol{r}$ is the separation vector of the dipole, pointing from the positive disclination to the negative disclination and we are interested in calculating the stress at $\boldsymbol{r}$, represented as the red dot. Let the stress field for the disclination configuration in Figure 2.13(d) be denoted as $\hat{\boldsymbol{\sigma}}$. Due to superposition in linear elasticity, the stress field of Figure 2.13(d)

can be written as

$$\hat{\boldsymbol{\sigma}}(\boldsymbol{r};\delta\boldsymbol{r},\boldsymbol{\Omega}) := \boldsymbol{\sigma}(\boldsymbol{r};-\delta\boldsymbol{r},\boldsymbol{\Omega}) + \boldsymbol{\sigma}(\boldsymbol{r};\boldsymbol{0},-\boldsymbol{\Omega})$$
$$\Rightarrow \hat{\boldsymbol{\sigma}}(\boldsymbol{r};\delta\boldsymbol{r},\boldsymbol{\Omega}) = \boldsymbol{f}(\boldsymbol{r}+\delta\boldsymbol{r};\boldsymbol{\Omega}) + \boldsymbol{f}(\boldsymbol{r};-\boldsymbol{\Omega}).$$

On applying (2.2), we have

$$\hat{\boldsymbol{\sigma}}(\boldsymbol{r};\delta\boldsymbol{r},\boldsymbol{\Omega}) = \boldsymbol{f}(\boldsymbol{r}+\delta\boldsymbol{r};\boldsymbol{\Omega}) - \boldsymbol{f}(\boldsymbol{r};\boldsymbol{\Omega})$$
$$\Rightarrow \hat{\boldsymbol{\sigma}}(\boldsymbol{r};\delta\boldsymbol{r},\boldsymbol{\Omega}) = \boldsymbol{\sigma}(\boldsymbol{r}+\delta\boldsymbol{r};\boldsymbol{0},\boldsymbol{\Omega}) - \boldsymbol{\sigma}(\boldsymbol{r};\boldsymbol{0},\boldsymbol{\Omega}). \tag{2.3}$$

Therefore, we have shown that the stress field in Figure 2.13(d) equals the difference between the stress fields in Figure 2.13(b) and the one in Figure 2.13(a).

Specializing to the plane case with $\boldsymbol{r} = x_1\boldsymbol{e}_1 + x_2\boldsymbol{e}_2$, the stress field corresponding to Figure 2.13(a) , given the Frank vector $\boldsymbol{\Omega} = \Omega_3\boldsymbol{e}_3$, is

$$\sigma_{11}(\boldsymbol{r};\boldsymbol{0},\boldsymbol{\Omega}) = f_{11}(x_1,x_2;\Omega_3) = \frac{G\Omega_3}{2\pi(1-\nu)}\left[\ln r + \frac{x_2^2}{r^2} + \frac{\nu}{1-2\nu}\right]$$
$$\sigma_{22}(\boldsymbol{r};\boldsymbol{0},\boldsymbol{\Omega}) = f_{22}(x_1,x_2;\Omega_3) = \frac{G\Omega_3}{2\pi(1-\nu)}\left[\ln r + \frac{x_1^2}{r^2} + \frac{\nu}{1-2\nu}\right]$$
$$\sigma_{12}(\boldsymbol{r};\boldsymbol{0},\boldsymbol{\Omega}) = f_{12}(x_1,x_2;\Omega_3) = -\frac{G\Omega_3 x_1 x_2}{2\pi(1-\nu)r^2},$$

where r is the norm of $\boldsymbol{r}$, G is the shear modulus and ν is the Poisson ratio. Assuming

$$\delta\boldsymbol{r} := \delta x_1\boldsymbol{e}_1 + \delta x_2\boldsymbol{e}_2 \tag{2.4}$$

to be small, the Taylor expansion of $\boldsymbol{\sigma}(\boldsymbol{r}+\delta\boldsymbol{r};\boldsymbol{0},\boldsymbol{\Omega})$ is

$$\boldsymbol{\sigma}(\boldsymbol{r}+\delta\boldsymbol{r};\boldsymbol{0},\boldsymbol{\Omega}) = \boldsymbol{f}(\boldsymbol{r};\boldsymbol{\Omega}) + \frac{\partial\boldsymbol{f}(\boldsymbol{r};\boldsymbol{\Omega})}{\partial\boldsymbol{r}}\delta\boldsymbol{r} + O(\delta\boldsymbol{r}^2).$$

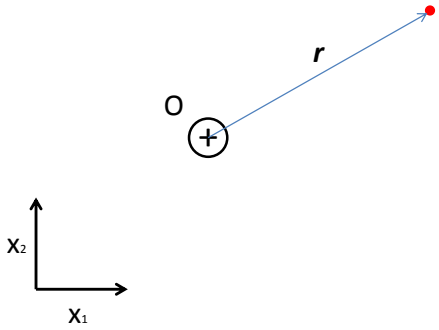

(a) A positive disclination located at the coordinate origin with a field point located at $\boldsymbol{r}$.

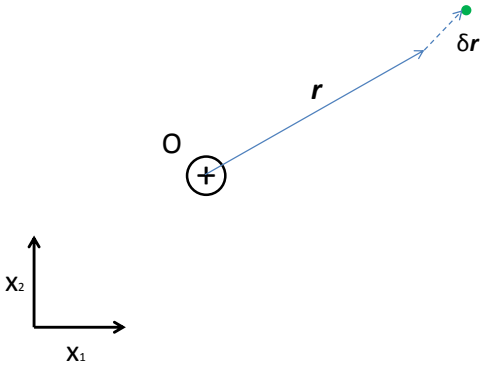

(b) Move the field point to $\boldsymbol{r} + \delta\boldsymbol{r}$.

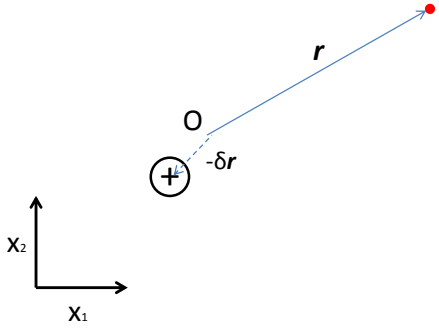

(c) The configuration with disclination source moved to $-\delta\boldsymbol{r}$.

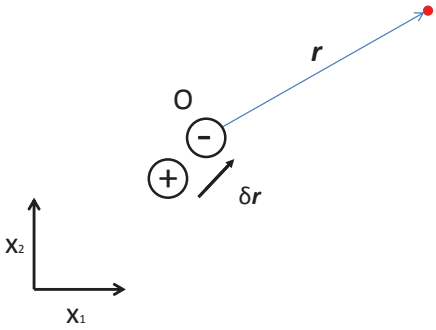

(d) Place a disclination dipole with the separation vector $\delta\boldsymbol{r}$ and keep the field point at $\boldsymbol{r}$.

Figure 2.13: *Schematic in support of calculation of stress field of a wedge-disclination dipole in linear, plane, isotropic elasticity.*

After substituting $\boldsymbol{r} = x_1\boldsymbol{e}_1 + x_2\boldsymbol{e}_2$ and $\delta\boldsymbol{r} = \delta x_1\boldsymbol{e}_1 + \delta x_2\boldsymbol{e}_2$, we have

$$\begin{aligned}
\sigma_{11}(\boldsymbol{r}+\delta\boldsymbol{r};\boldsymbol{0},\boldsymbol{\Omega}) &= f_{11}(x_1,x_2;\Omega_3) + \frac{\partial f_{11}(x_1,x_2;\Omega_3)}{\partial x_1}\delta x_1 + \frac{\partial f_{11}(x_1,x_2;\Omega_3)}{\partial x_2}\delta x_2 + O(\delta\boldsymbol{r}^2)\\
\sigma_{22}(\boldsymbol{r}+\delta\boldsymbol{r};\boldsymbol{0},\boldsymbol{\Omega}) &= f_{22}(x_1,x_2;\Omega_3) + \frac{\partial f_{22}(x_1,x_2;\Omega_3)}{\partial x_1}\delta x_1 + \frac{\partial f_{22}(x_1,x_2;\Omega_3)}{\partial x_2}\delta x_2 + O(\delta\boldsymbol{r}^2)\\
\sigma_{12}(\boldsymbol{r}+\delta\boldsymbol{r};\boldsymbol{0},\boldsymbol{\Omega}) &= f_{12}(x_1,x_2;\Omega_3) + \frac{\partial f_{12}(x_1,x_2;\Omega_3)}{\partial x_1}\delta x_1 + \frac{\partial f_{12}(x_1,x_2;\Omega_3)}{\partial x_2}\delta x_2 + O(\delta\boldsymbol{r}^2).;
\end{aligned}$$

After substituting $\boldsymbol{\sigma}(\boldsymbol{r};\boldsymbol{0},\boldsymbol{\Omega})$ and $\boldsymbol{\sigma}(\boldsymbol{r}+\delta\boldsymbol{r};\boldsymbol{0},\boldsymbol{\Omega})$ into (2.3) and omitting the higher order terms, we get

$$\begin{aligned}
\hat{\sigma}_{11}(x_1,x_2;\delta x_1,\delta x_2,\Omega_3) &= \frac{G\Omega_3\delta x_2}{2\pi(1-\nu)}\left[\frac{x_2}{r^2} + 2\frac{x_1^2x_2}{r^4}\right] + \frac{G\Omega_3\delta x_1}{2\pi(1-\nu)}\left[\frac{x_1}{r^2} - 2\frac{x_1x_2^2}{r^4}\right]\\
\hat{\sigma}_{22}(x_1,x_2;\delta x_1,\delta x_2,\Omega_3) &= \frac{G\Omega_3\delta x_2}{2\pi(1-\nu)}\left[\frac{x_2}{r^2} - 2\frac{x_1^2x_2}{r^4}\right] + \frac{G\Omega_3\delta x_1}{2\pi(1-\nu)}\left[\frac{x_1}{r^2} + 2\frac{x_1x_2^2}{r^4}\right]\\
\hat{\sigma}_{12}(x_1,x_2;\delta x_1,\delta x_2,\Omega_3) &= -\frac{G\Omega_3\delta x_2}{2\pi(1-\nu)}\left[\frac{x_2}{r^2} - 2\frac{x_1x_2^2}{r^4}\right] - \frac{G\Omega_3\delta x_1}{2\pi(1-\nu)}\left[\frac{x_2}{r^2} - 2\frac{x_1^2x_2}{r^4}\right].
\end{aligned} \tag{2.5}$$

The stress field of the single edge dislocation in 2-D, isotropic elasticity is [DeW73b]

$$\begin{aligned}
\sigma^b_{11}(x_1,x_2;b_1,b_2) &= -\frac{Gb_1}{2\pi(1-\nu)}\left[\frac{x_2}{r^2} + 2\frac{x_1^2x_2}{r^4}\right] + \frac{Gb_2}{2\pi(1-\nu)}\left[\frac{x_1}{r^2} - 2\frac{x_1x_2^2}{r^4}\right]\\
\sigma^b_{22}(x_1,x_2;b_1,b_2) &= -\frac{Gb_1}{2\pi(1-\nu)}\left[\frac{x_2}{r^2} - 2\frac{x_1^2x_2}{r^4}\right] + \frac{Gb_2}{2\pi(1-\nu)}\left[\frac{x_1}{r^2} + 2\frac{x_1x_2^2}{r^4}\right]\\
\sigma^b_{12}(x_1,x_2;b_1,b_2) &= \frac{Gb_1}{2\pi(1-\nu)}\left[\frac{x_2}{r^2} - 2\frac{x_1x_2^2}{r^4}\right] - \frac{Gb_2}{2\pi(1-\nu)}\left[\frac{x_2}{r^2} - 2\frac{x_1^2x_2}{r^4}\right].
\end{aligned} \tag{2.6}$$

On defining the Burgers vector of a disclination dipole with separation vector $\delta\boldsymbol{r}$ (2.4) and strength $\boldsymbol{\Omega}$ as

$$\boldsymbol{b} := -\Omega_3\delta r_2\boldsymbol{e}_1 + \Omega_3\delta r_1\boldsymbol{e}_2 = \boldsymbol{\Omega}\times\delta\boldsymbol{r}, \tag{2.7}$$

we see that the stress field of the disclination dipole (2.5) exactly matches that of the single edge dislocation (2.6).

This establishes the correspondence between the Burgers vector of the wedge disclina-

tion dipole and the edge dislocation in 2-d, isotropic, plane, linear elasticity. In Section 2.8 we establish the general form of this geometric relationship in the context of exact kinematics, valid for any type of material (i.e. without reference to material response).

2.6 Generalized disclination theory and associated Weingarten's theorem

The connection between g.disclinations (and dislocations) represented as fields and their more classical representation following Weingarten's pioneering work is established in Sections 2.7 and 2.8. In this Section we briefly review the defect kinematics of g.disclination theory and a corresponding Weingarten-gd theorem developed in [AF15] that are necessary prerequisites for the arguments in the aforementioned sections. We also develop a new result in Section 2.6.2 related to the Weingarten-gd theorem, proving that the inverse deformation jump across the cut-surface is independent of the surface when the g.disclination density vanishes.

As defined in Section 2.2, a single g.disclination is a line defect terminating a distortion discontinuity. Developed as a generalization of eigendeformation theory of Kroner, Mura and deWit, the generalized disclination has a core and the discontinuity is modeled by an eigenwall field with support in a layer [AF15], as shown in Figure 3.1. The representation of a discrete g.disclination involves a continuous elastic 2-distortion field $\boldsymbol{Y}$, assumed to be irrotational outside the generalized disclination core ($\boldsymbol{Y} = \operatorname{grad}\operatorname{grad}(\boldsymbol{x}^{-1})$ in the case without defects, where $\boldsymbol{x}$ is the deformation map). The *strength of the discrete generalized disclination is given by the second order tensor obtained by integrating the 2-distortion field along any closed curve encircling the core; when defined from a terminating distortion discontinuity, it is simply the difference of the two distortions involved in defining the discontinuity.* One way of setting up the generalized disclination density tensor field,

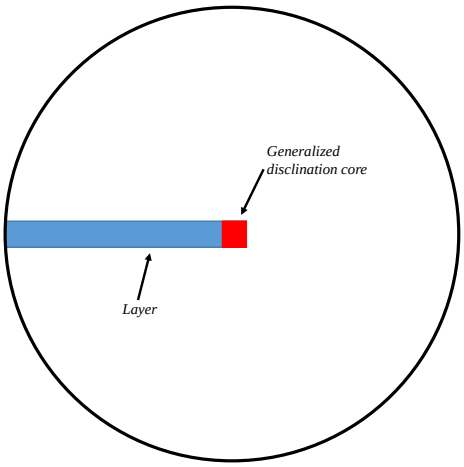

Figure 2.14: *Physical regularization of classical terminating discontinuity. Treat the distortion discontinuity as the eigenwall field* $\boldsymbol{S}$ *with support in a layer.*

which is a third order tensor, is to assign the tensor product of the strength tensor and the core line direction vector as a uniformly distributed field within the generalized disclination core, and zero outside it. In the case of a disclination, the strength tensor is necessarily the difference of two orthogonal tensors.

The fundamental kinematic decomposition of generalized disclination theory [AF15] is to write

$$\boldsymbol{Y} = \operatorname{grad} \boldsymbol{W} + \boldsymbol{S}, \tag{2.8}$$

where $\boldsymbol{W}$ is the i-elastic 1-distortion ($\boldsymbol{F}^{-1}$ in the defect-free case, where $\boldsymbol{F}$ is the deformation gradient) and $\boldsymbol{S}$ (3^{rd}-order tensor) is the eigenwall field.

With this decomposition of $\boldsymbol{Y}$, it is natural to measure the generalized disclination density as

$$\operatorname{curl}(\boldsymbol{Y} - \operatorname{grad} \boldsymbol{W}) = \operatorname{curl} \boldsymbol{S} =: \boldsymbol{\Pi}. \tag{2.9}$$

It characterizes the closure failure of integrating $\boldsymbol{Y}$ on closed contours in the body:

$$\int_a \boldsymbol{\Pi} \boldsymbol{n} da = \int_c \boldsymbol{Y} d\boldsymbol{x} \tag{2.10}$$

where a is any area patch with closed boundary contour c in the body. Physically, it is to be interpreted as a density of lines (threading areas) in the current configuration, carrying a tensorial attribute that reflects a jump in $\boldsymbol{W}$.

The dislocation density is defined as [AF15]

$$\boldsymbol{\alpha} := \boldsymbol{Y} : \boldsymbol{X} = (\boldsymbol{S} + \operatorname{grad} \boldsymbol{W}) : \boldsymbol{X}. \tag{2.11}$$

In the case that there is no distortion discontinuity, namely $\boldsymbol{S} = \boldsymbol{0}$, (3.4) becomes $\boldsymbol{\alpha} = -\operatorname{curl} \boldsymbol{W}$, since $\operatorname{curl} \boldsymbol{A} = -\operatorname{grad} \boldsymbol{A} : \boldsymbol{X}$ for any smooth tensor field $\boldsymbol{A}$. The definition of the dislocation density (3.4) is motivated by the displacement-jump formula (2.16) / [AF15] corresponding to a single, isolated defect line terminating an i-elastic distortion jump in the body. In this situation, the displacement jump for an isolated defect line, measured by integrating $\boldsymbol{W}$ along any closed curve encircling the defect core cylinder[3], is no longer a topological object independent of the curve (in the class of curves encircling the core) due to the fact that in the presence of a g.disclination density localized in the core cylinder the field $\boldsymbol{S}$ cannot be localized in the core - it is, at the very least, supported in a layer extending to the boundary from the core, or, when $div\, \boldsymbol{S} = \boldsymbol{0}$, completely delocalized over the entire domain.

Now we apply a Stokes-Helmholtz-like orthogonal decomposition of the field $\boldsymbol{S}$ into a compatible part and an incompatible part:

$$\begin{aligned} \boldsymbol{S} &= \boldsymbol{S}^{\perp} + \operatorname{grad} \boldsymbol{Z}^{s} \\ \operatorname{curl} \boldsymbol{S}^{\perp} &= \boldsymbol{\Pi} \\ \operatorname{div} \boldsymbol{S}^{\perp} &= \boldsymbol{0} \\ \text{with} \quad \boldsymbol{S}^{\perp}\boldsymbol{n} &= \boldsymbol{0} \quad \text{on the boundary.} \end{aligned} \tag{2.12}$$

[3]In [AF15] a typographical error suggests that the displacement jump is obtained by integrating $\boldsymbol{\alpha}$ on area patches; $\boldsymbol{\alpha}$ there should have been replaced by curl $\boldsymbol{W}$.

It is clear that when $\boldsymbol{\Pi} = \mathbf{0}$ then $\boldsymbol{S}^{\perp} = \mathbf{0}$.

In summary, the governing equations for computing the elastic fields for static generalized disclination theory (i.e. when the disclination and dislocation fields are specified) are

$$\begin{aligned} &\operatorname{curl} \boldsymbol{S} = \boldsymbol{\Pi} \\ &\boldsymbol{S} = \boldsymbol{S}^{\perp} + grad\, \boldsymbol{Z}^{s} \\ &\operatorname{div} \boldsymbol{S}^{\perp} = \mathbf{0} \quad \text{ with } \boldsymbol{S}^{\perp}\boldsymbol{n} = \mathbf{0} \text{ on the boundary} \\ &\boldsymbol{\alpha} = (\boldsymbol{S} + grad \boldsymbol{W}) : \boldsymbol{X}, \end{aligned} \tag{2.13}$$

where $\boldsymbol{\Pi}$ and $\boldsymbol{\alpha}$ are specified from physical considerations. These equations are solved along with balance of linear and angular momentum involving Cauchy stresses and couple-stresses (with constitutive assumptions) to obtain g.disclination and dislocation stress and couple stress fields. In Chapter 3 we solve these equations along with

$$\operatorname{div} \boldsymbol{T} = \mathbf{0}$$

with $\boldsymbol{T}$ representing the Cauchy stress as a function of $\boldsymbol{W}$, and we ignore couple stresses for simplicity.

2.6.1 Review of Weingarten theorem associated with g.disclinations

In this section we provide an overview of the Weingarten-gd theorem for g.disclinations introduced in [AF15]. Figure 2.15 shows cross-sections of three dimensional multi-connected bodies with toroidal (Figure 2.15(a)) and through holes (Figure 2.15(d)). In both cases, the multi-connected body can be transformed into a simply-connected one by introducing a cut-surface. For the toroidal case, putting the cut-surface either from a curve on the external surface to a curve on the exterior surface of the torus (Figure 2.15(b)) or putting

the cut-surface with bounding curve along the interior surface of the torus (Figure 2.15(c)) will make the multi-connected domain into a simply-connected domain. Similarly, the body with the through-hole can be cut by a surface extending from a curve on the external surface to the surface of the hole. Figures 2.15(b) and 2.15(e) result in topological spheres while Fig. 2.15(c) results in a topological sphere with a contained interior cavity. In terms of g.disclination theory, the holes are associated with the cores of the defect lines.

Given a continuously differentiable 3-order tensor field $\tilde{\boldsymbol{Y}}$ on the multi-connected domain such that $\tilde{\boldsymbol{Y}}$ is symmetric in the last two indices and curl $\tilde{\boldsymbol{Y}} = \boldsymbol{0}$, the Weingarten-gd problem asks if there exists a vector field $\boldsymbol{y}$ on the cut-induced simply-connected domain such that

$$\operatorname{grad}\operatorname{grad}\boldsymbol{y} = \tilde{\boldsymbol{Y}},$$

and a formula for the possible jump $[\![\boldsymbol{y}]\!]$ of $\boldsymbol{y}$ across the cut-surface. Also, since $\tilde{\boldsymbol{Y}}$ is curl-free and continuously differentiable on the multi-connected domain, we can defined a field $\tilde{\boldsymbol{W}}$ such that

$$\operatorname{grad}\tilde{\boldsymbol{W}} = \tilde{\boldsymbol{Y}}$$

on the corresponding simply-connected domain.

In the following, we will assign a unit normal field to any cut-surface. For any point on the cut-surface, say $\boldsymbol{A}$, we will denote by $\boldsymbol{A}^+$ a point arbitrarily close to $\boldsymbol{A}$ from the region into which the normal at $\boldsymbol{A}$ points and as $\boldsymbol{A}^-$ a similar point from the region into which the negative normal points. For any smooth function, say $\boldsymbol{f}$, defined on the (multi)-connected domain, we will define

$$\boldsymbol{f}^+(\boldsymbol{A}) := \lim_{\boldsymbol{A}^+\to\boldsymbol{A}} \boldsymbol{f}(\boldsymbol{A}^+) \quad \text{and} \quad \boldsymbol{f}^-(\boldsymbol{A}) := \lim_{\boldsymbol{A}^-\to\boldsymbol{A}} \boldsymbol{f}(\boldsymbol{A}^-). \tag{2.14}$$

Consider a closed contour in Fig. 2.16 in the multi-connected domain starting and ending at $\boldsymbol{A}$ and passing through $\boldsymbol{B}$ as shown. In addition, also consider as the 'inner' and

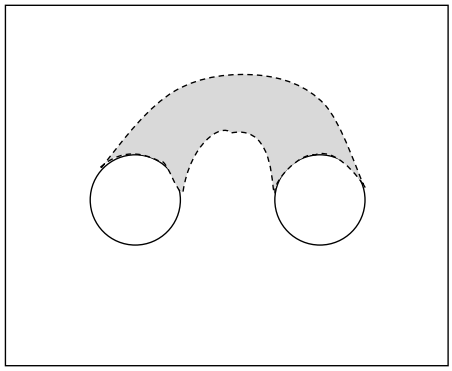

(a) The cross-section of a multi-connected body with a toroidal hole. The shaded gray area is the 'half-toroid'. The half-toroid is not shown in Figures 2.15(b) and 2.15(c).

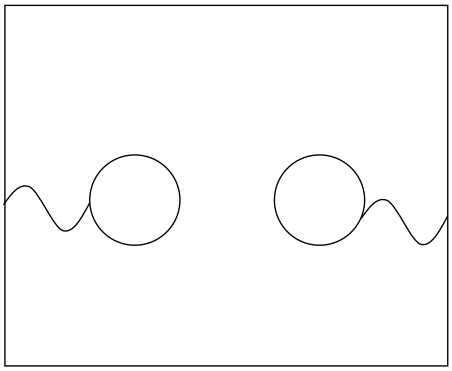

(b) The multi-connected body becomes simply-connected after introducing the cut-surface.

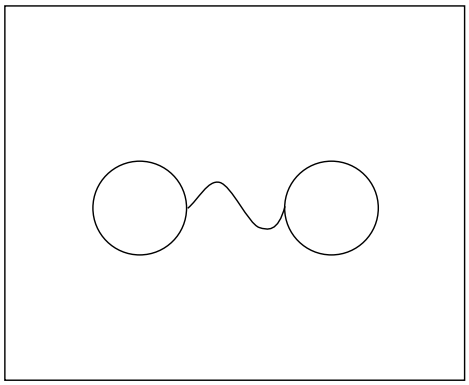

(c) Another method to introduce the cut surface to make the multi-connected body simply-connected.

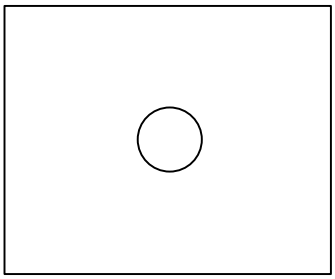

(d) The cross-section of a multi-connected body with a through hole.

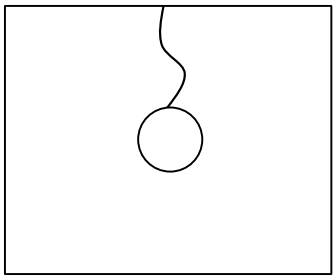

(e) The cross-section of a simply-connected body with a through hole and a cut surface.

Figure 2.15: *The cross-sections of multi-connected bodies with a toroidal hole or a through hole, and their corresponding simply-connected bodies by introducing cut-surfaces.*

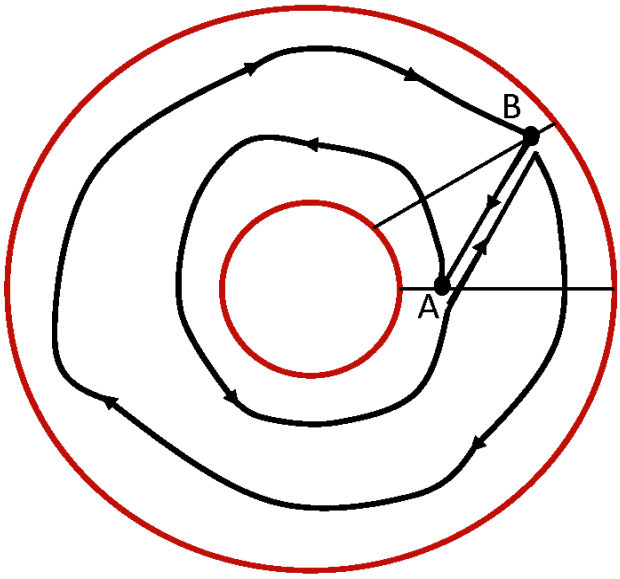

Figure 2.16: *A contour enclosing the core on the cross-section of the multi-connected domain. The contour passes through points* $\boldsymbol{A}$ *and* $\boldsymbol{B}$*. (Figure reproduced from [AF15] with permission from Springer).*

'outer' closed contours the closed curves that remain by ignoring the overlapping segments, the inner closed contour passing through $\boldsymbol{A}$ and the outer through $\boldsymbol{B}$. Then, because of the continuity of $\tilde{\boldsymbol{Y}}$ and its vanishing *curl*, the line integral of $\tilde{\boldsymbol{Y}}$ on the inner and outer closed contours must be equal and this statement holds for any closed contour enclosing the hole. The line integral of $\tilde{\boldsymbol{Y}}$ on the closed contour is defined as

$$\int_C \tilde{\boldsymbol{Y}}\, d\boldsymbol{x} =: \boldsymbol{\Delta}.$$

Now, considering the cut-surface passing through $\boldsymbol{A}$, if we construct the corresponding $\tilde{\boldsymbol{W}}$, say $\tilde{\boldsymbol{W}}_1$, then the jump of $\tilde{\boldsymbol{W}}_1$ is given by

$$[\![\tilde{\boldsymbol{W}}_1]\!](\boldsymbol{A}) = \int\limits_{C(A^-,A^+)} \tilde{\boldsymbol{Y}}\, d\boldsymbol{x} = \boldsymbol{\Delta},$$

where $C(A^-, A^+)$ is the curve from the inner closed contour with the point $\boldsymbol{A}$ taken out and with start-point $\boldsymbol{A}^-$ and the end-point $\boldsymbol{A}^+$, as shown in Figure 2.16. Similarly, a different

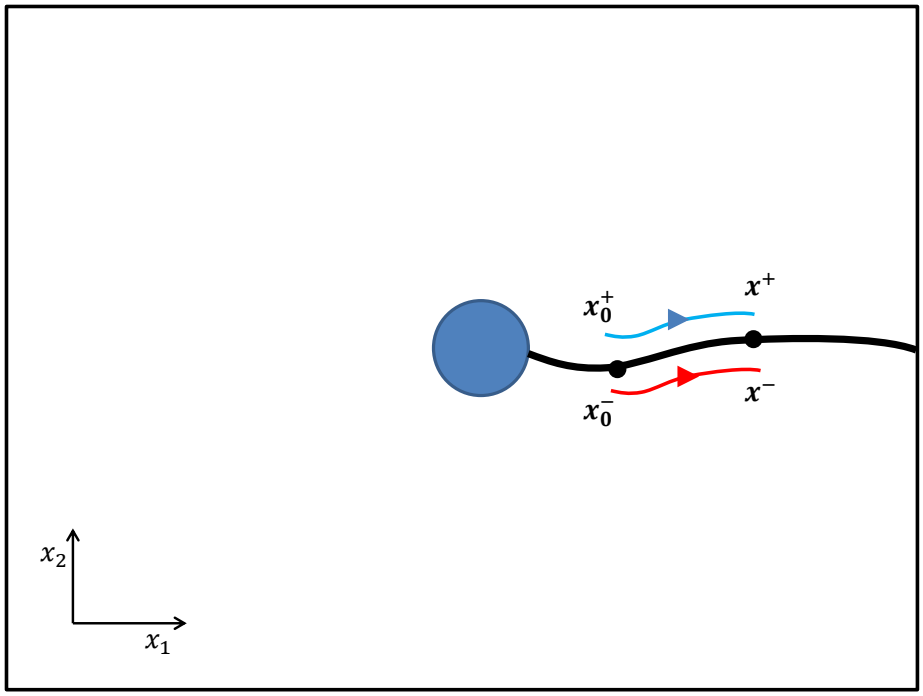

Figure 2.17: *Cross-section of a simply-connected domain induced by a cut-surface. The red path is from $\boldsymbol{x}_0^-$ to $\boldsymbol{x}^-$ and the blue path is from $\boldsymbol{x}_0^+$ to $\boldsymbol{x}^+$.*

cut-surface passing through another point $\boldsymbol{B}$ can be introduced and the corresponding $\tilde{\boldsymbol{W}}_2$ can be constructed with $[\![\tilde{\boldsymbol{W}}_2]\!](\boldsymbol{B}) = \boldsymbol{\Delta}$. Since $\boldsymbol{A}$, $\boldsymbol{B}$ and the cut surfaces are chosen arbitrarily, the jump of any of the functions $[\![\tilde{\boldsymbol{W}}]\!]$ across their corresponding cut-surface takes the same value, independent of the invoked cut-surface and the point on the surface.

In addition, due to the symmetry in the last two indices of $\tilde{\boldsymbol{Y}}$, curl $\tilde{\boldsymbol{W}}$ vanishes. Thus, a vector field $\boldsymbol{y}$ can be defined, on the relevant cut-induced simply-connected domain associated with the construction of $\tilde{\boldsymbol{W}}$, such that

$$\operatorname{grad} \boldsymbol{y} = \tilde{\boldsymbol{W}}. \tag{2.15}$$

Now choose a point $\boldsymbol{x}_0$ arbitrarily on the cut-surface. Let $\boldsymbol{x}$ be any other point on this cut-surface, as shown in Figure 2.17.

Since

$$\tilde{\boldsymbol{W}}^- = (\operatorname{grad} \boldsymbol{y})^-$$
$$\tilde{\boldsymbol{W}}^+ = (\operatorname{grad} \boldsymbol{y})^+,$$

then $\boldsymbol{y}$ at $\boldsymbol{x}$ across the cut-surface is

$$\boldsymbol{y}^+(\boldsymbol{x}) = \boldsymbol{y}^+(\boldsymbol{x}_0) + \int_{\boldsymbol{x}_0^+}^{\boldsymbol{x}^+} \tilde{\boldsymbol{W}}^+(\boldsymbol{x}')d\boldsymbol{x}'$$
$$\boldsymbol{y}^-(\boldsymbol{x}) = \boldsymbol{y}^-(\boldsymbol{x}_0) + \int_{\boldsymbol{x}_0^-}^{\boldsymbol{x}^-} \tilde{\boldsymbol{W}}^-(\boldsymbol{x}')d\boldsymbol{x}'$$

(by working on paths from $\boldsymbol{x}_0^{+/-}$ to $\boldsymbol{x}^{+/-}$ and then taking limits as the paths approach the cut-surface). Then the jump of $\boldsymbol{y}$, $[\![\boldsymbol{y}]\!]$ can be derived as

$$[\![\boldsymbol{y}]\!](\boldsymbol{x}) = \boldsymbol{y}^+(\boldsymbol{x}) - \boldsymbol{y}^-(\boldsymbol{x}) = [\![\boldsymbol{y}]\!](\boldsymbol{x}_0) + \int_{\boldsymbol{x}_0}^{\boldsymbol{x}} [\![\tilde{\boldsymbol{W}}]\!](\boldsymbol{x}')d\boldsymbol{x}'.$$

Recall that $[\![\tilde{\boldsymbol{W}}]\!](\boldsymbol{x}') = \boldsymbol{\Delta}$, which is independent of the cut-surface and the point $\boldsymbol{x}'$ on it.

Therefore,

$$[\![\boldsymbol{y}]\!](\boldsymbol{x}) = [\![\boldsymbol{y}]\!](\boldsymbol{x}_0) + \boldsymbol{\Delta}(\boldsymbol{x} - \boldsymbol{x}_0). \tag{2.16}$$

Furthermore, it can be shown that the jump at any point $\boldsymbol{x}$ on the cut-surface is independent of the choice of the base point $\boldsymbol{x}_0$ (on the cut-surface).

In addition, consider the case where $[\![\tilde{\boldsymbol{W}}]\!] = \boldsymbol{0}$ - i.e. the defect line is a pure dislocation. Then the Burgers vector is defined as

$$\boldsymbol{b}(\boldsymbol{x}) := [\![\boldsymbol{y}]\!](\boldsymbol{x}),$$

and from Eqn 2.16, given an arbitrarily fixed cut-surface, we have

$$[\![\boldsymbol{y}]\!](\boldsymbol{x}) = [\![\boldsymbol{y}]\!](\boldsymbol{x}_0) \tag{2.17}$$

where $\boldsymbol{x}$ and $\boldsymbol{x}_0$ are arbitrarily chosen points on the cut-surface. Thus, it has been shown that for $\boldsymbol{\Delta} = \boldsymbol{0}$, the displacement jump is independent of location on a given cut-surface.

In the next Section 2.6.2, we furthermore show that the Burgers vector is independent of the choice of the cut-surface as well when $\boldsymbol{\Delta} = \boldsymbol{0}$ and $\boldsymbol{\alpha}$ is localized in the core.

2.6.2 Cut-surface independence in the Weingarten-gd theorem for $\boldsymbol{\Delta} = \boldsymbol{0}$

We now prove that the jump (2.17) across a cut-surface in the Weingarten-gd theorem is independent of the choice of the surface when $\boldsymbol{\Delta} = \boldsymbol{0}$.

By hypothesis, there is a continuous field $\tilde{\boldsymbol{Y}}$ in the multi-connected body with $\operatorname{curl} \tilde{\boldsymbol{Y}} = \boldsymbol{0}$ and $\tilde{Y}_{ijk} = \tilde{Y}_{ikj}$. Also, after introducing an arbitrary cut-surface, as in Figure 2.15(e), we can construct fields $\tilde{\boldsymbol{W}}$ and $\tilde{\boldsymbol{y}}$ such that $\operatorname{grad}(\operatorname{grad} \tilde{\boldsymbol{y}}) = \tilde{\boldsymbol{Y}}$ and $\operatorname{grad} \tilde{\boldsymbol{W}} = \tilde{\boldsymbol{Y}}$. Based on the Weingarten-gd theorem, we have on this arbitrary chosen cut-surface

$$[\![\tilde{\boldsymbol{y}}(\boldsymbol{x})]\!] = [\![\tilde{\boldsymbol{y}}(\boldsymbol{x}_0)]\!] + \boldsymbol{\Delta}(\boldsymbol{x} - \boldsymbol{x}_0),$$

where $\boldsymbol{\Delta} = \oint \tilde{\boldsymbol{Y}} d\boldsymbol{x}$. Since $\boldsymbol{\Delta} = \boldsymbol{0}$, it is clear that

$$[\![\tilde{\boldsymbol{y}}(\boldsymbol{x})]\!] = [\![\tilde{\boldsymbol{y}}(\boldsymbol{x}_0)]\!].$$

The goal now is to prove that

$$[\![\tilde{\boldsymbol{y}}(\boldsymbol{x})]\!] =: \boldsymbol{b}$$

where the vector $\boldsymbol{b}$ is independent of the choice of the cut-surface and, hence, independent

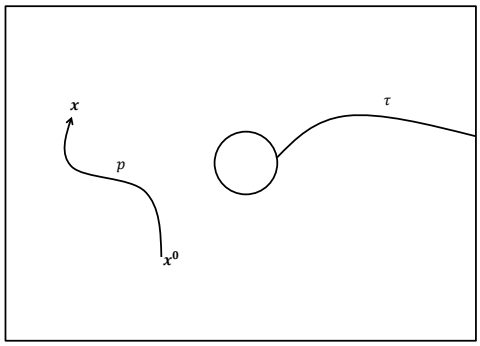

Figure 2.18: *Arbitrary path (shown on the cross-section) for construction of a continuous field* $\boldsymbol{W}^\tau$ *on the simply-connected domain induced by a cut-surface* τ *when* $\boldsymbol{\Delta} = \mathbf{0}$.

of $\boldsymbol{x}$ on the cut-surface as well using results of Section 2.6.1.

Since the definition of $\tilde{\boldsymbol{W}}$ depends on the cut-surface, given a simply-connected domain induced by a cut-surface τ, we can express any such $\tilde{\boldsymbol{W}}$, say $\boldsymbol{W}^\tau$, on the simply-connected domain as

$$W_{ij}^\tau(\boldsymbol{x}, \boldsymbol{x}^0, p) := \int_{\substack{\boldsymbol{x}^0 \\ p}}^{\boldsymbol{x}} E_{ijk}\, dx_k + W_{ij}^\tau(\boldsymbol{x}^0) \tag{2.18}$$

where p is a curve from $\boldsymbol{x}^0$ to $\boldsymbol{x}$ as shown in Figure 2.18, and $\boldsymbol{E} := \tilde{\boldsymbol{Y}}$ with the field $\tilde{\boldsymbol{Y}}$ satisfying the constraint $\oint \tilde{\boldsymbol{Y}}\, d\mathbf{x} = \boldsymbol{\Delta} = \mathbf{0}$. Since the line integral of $\boldsymbol{E}$ on any closed loop is zero, $\boldsymbol{W}^\tau$ as defined is independent of path on the original multi-connected domain and hence thinking of the constructed $\boldsymbol{W}^\tau$ as a continuous function on it makes sense.

Now with the constructed $\boldsymbol{W}^\tau$, we can define the line integral

$$\boldsymbol{b}^{\tau,p} := \oint_p \boldsymbol{W}^\tau d\boldsymbol{x}$$

on a closed loop p enclosing the core.

We now show first that $\boldsymbol{b}^{\tau,p}$ is independent of the loop used to define it. Since grad $\boldsymbol{W}^\tau =$

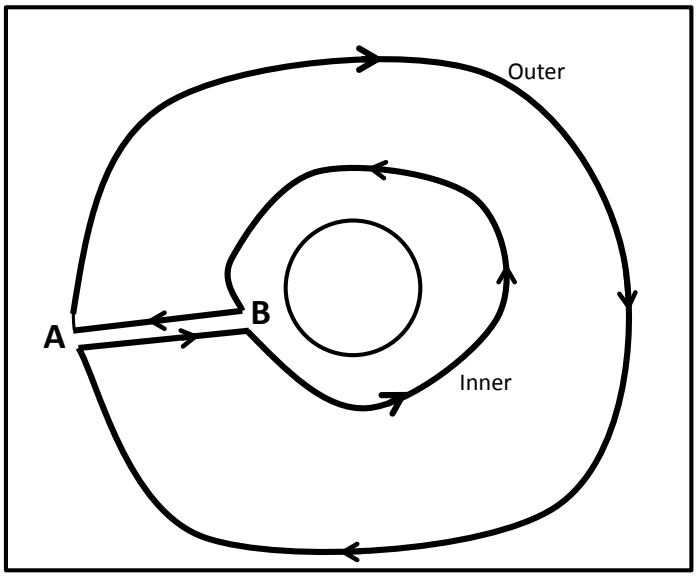

Figure 2.19: *A closed loop in the cross-section of a multi-connected domain to justify independence of the Burgers vector from the circuit used to evaluate it for* $\boldsymbol{\Delta} = \mathbf{0}$.

$\boldsymbol{E}$ from the definition (2.18) and $\boldsymbol{E}$ is symmetric in the last two indices by hypothesis,

$$\begin{aligned} & E_{ijk} = W^{\tau}_{ij,k} \\ & \Rightarrow E_{ijk} - E_{ikj} = W^{\tau}_{ij,k} - W^{\tau}_{ik,j} = 0 \\ & \Rightarrow e_{mkj}(W^{\tau}_{ij,k} - W^{\tau}_{ik,j}) = 0 \\ & \Rightarrow \operatorname{curl} \boldsymbol{W}^{\tau} = \mathbf{0} \end{aligned}$$

Thus, on the multi-connected domain, given any arbitrary closed loop as in Figure 2.19,

$$\oint \boldsymbol{W}^{\tau} d\boldsymbol{x} = \mathbf{0}$$

$$\int_{\text{inner}} \boldsymbol{W}^{\tau} d\boldsymbol{x} - \int_{\text{outer}} \boldsymbol{W}^{\tau} d\boldsymbol{x} + \int_{B}^{A} \boldsymbol{W}^{\tau} d\boldsymbol{x} + \int_{A}^{B} \boldsymbol{W}^{\tau} d\boldsymbol{x} = \mathbf{0}$$

where $\int_{inner} \boldsymbol{W}^{\tau} d\boldsymbol{x}$ is the integral along the inner loop anti-clockwise and $\int_{outer} \boldsymbol{W}^{\tau} d\boldsymbol{x}$ is the

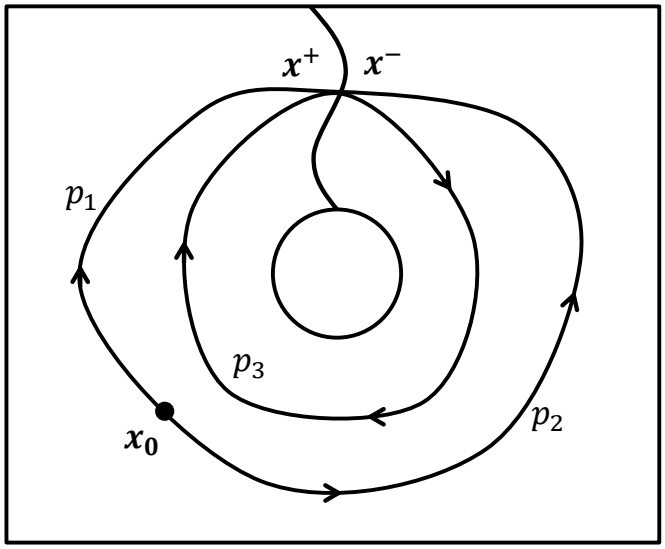

Figure 2.20: *The integration path on the cross-section of a simply-connected domain to calculate the jump* $[\![\boldsymbol{y}]\!]$ *at* $\boldsymbol{x}$.

integral along the outer loop anti-clockwise. Therefore, since $\int_B^A \boldsymbol{W}^\tau d\boldsymbol{x} + \int_A^B \boldsymbol{W}^\tau d\boldsymbol{x} = \boldsymbol{0}$,

$$\int_{\text{inner}} \boldsymbol{W}^\tau d\boldsymbol{x} = \int_{\text{outer}} \boldsymbol{W}^\tau d\boldsymbol{x}.$$

Thus, $\boldsymbol{b}^{\tau,p}$ is independent of the loop path p and we will denote it as $\boldsymbol{b}^\tau$.

Now for a simply-connected domain induced by the cut-surface τ, given a $\boldsymbol{W}^\tau$, there exists (many) $\boldsymbol{y}^\tau$ satisfying $grad\boldsymbol{y}^\tau = \boldsymbol{W}^\tau$; any such $\boldsymbol{y}^\tau$ may be expressed as

$$\boldsymbol{y}^\tau(\boldsymbol{x};\boldsymbol{x}_0) = \int_{\boldsymbol{x}_0}^{\boldsymbol{x}} \boldsymbol{W}^\tau d\boldsymbol{x} + \boldsymbol{y}^\tau(\boldsymbol{x}_0).$$

Then, with reference to Fig. 2.20, we have

$$\boldsymbol{y}^\tau(\boldsymbol{x}^+) = \boldsymbol{y}^\tau(\boldsymbol{x}_0) + \int_{\substack{\boldsymbol{x}_0 \\ p_1}}^{\boldsymbol{x}^+} \boldsymbol{W}^\tau d\boldsymbol{x}$$

$$\Rightarrow \boldsymbol{y}^\tau(\boldsymbol{x}^+) = \boldsymbol{y}^\tau(\boldsymbol{x}_0) + \int_{\substack{\boldsymbol{x}_0 \\ p_2}}^{\boldsymbol{x}^-} \boldsymbol{W}^\tau d\boldsymbol{x} + \int_{\substack{\boldsymbol{x}^- \\ p_3}}^{\boldsymbol{x}^+} \boldsymbol{W}^\tau d\boldsymbol{x}$$

and

$$\boldsymbol{y}^{\tau}(\boldsymbol{x}^{-}) = \boldsymbol{y}^{\tau}(\boldsymbol{x}_0) + \int_{\substack{\boldsymbol{x}_0 \\ p_2}}^{\boldsymbol{x}^{-}} \boldsymbol{W}^{\tau} d\boldsymbol{x}.$$

Thus,

$$[\![\boldsymbol{y}^{\tau}]\!] = \int_{\substack{\boldsymbol{x}^{-} \\ p_3}}^{\boldsymbol{x}^{+}} \boldsymbol{W}^{\tau} d\boldsymbol{x} = \boldsymbol{b}^{\tau}. \tag{2.19}$$

We note next that if τ and τ' are two cut-surfaces, (2.18) and the continuity of $\boldsymbol{W}^{\tau}, \boldsymbol{W}^{\tau'}$ imply that $\boldsymbol{W}^{\tau} - \boldsymbol{W}^{\tau'}$ is a constant tensor on the original multi-connected domain, and therefore (2.19) implies that $\boldsymbol{b}^{\tau} = \boldsymbol{b}^{\tau'} =: \boldsymbol{b}$, a constant vector independent of the cut-surface.

Therefore, we have shown that when $\boldsymbol{\Delta} = \boldsymbol{0}$, the Burgers vector is cut-surface independent.

2.7 Interpretation of the Weingarten theorem in terms of g.disclination kinematics

The Weingarten-gd theorem for generalized disclinations (2.16) was reviewed in Section 2.6.1. We recall that the jump of the inverse-deformation $\boldsymbol{y}$ across a cut-surface is characterized, in general, by the jump at an arbitrarily chosen point on the surface, $[\![\boldsymbol{y}(\boldsymbol{x}_0)]\!]$, and $\boldsymbol{\Delta} = [\![\tilde{\boldsymbol{W}}]\!]$, and all of these quantities are defined from the knowledge of the field $\tilde{\boldsymbol{Y}}$. However, given a g.disclination and a dislocation distribution $\boldsymbol{\Pi}$ and $\boldsymbol{\alpha}$, respectively, on the body, it is natural to ask as to what ingredients of g.disclination theory correspond to a candidate $\tilde{\boldsymbol{Y}}$ field. A consistency condition we impose is that in the absence of a g.disclination density, the jump of the inverse deformation field should be characterized by the Burgers vector of the given dislocation density field.

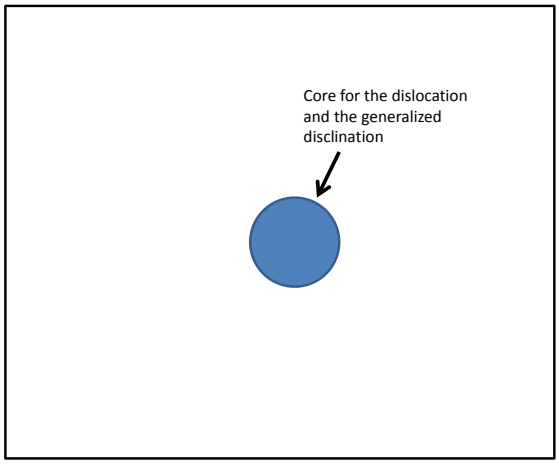

Figure 2.21: *The dislocation and the generalized disclination densities are localized in a defect core.*

2.7.1 Derivation of $\tilde{\boldsymbol{Y}}$ in g.disclination theory

Let $\boldsymbol{\Pi}$ and $\boldsymbol{\alpha}$ be localized in a core as shown in the Figure 2.21. In g.disclination theory,

$$\boldsymbol{Y} = \boldsymbol{S} + \operatorname{grad} \boldsymbol{W}$$

$$\boldsymbol{\alpha} := \boldsymbol{S} : \boldsymbol{X} + \operatorname{grad} \boldsymbol{W} : \boldsymbol{X}$$

with

$$\operatorname{curl} \boldsymbol{Y} = \operatorname{curl} \boldsymbol{S} = \boldsymbol{\Pi}.$$

From the definition of $\boldsymbol{\alpha}$, we have

$$\begin{aligned} & \alpha_{ij} = S_{imn} e_{jmn} + W_{im,n} e_{jmn} \\ \Rightarrow\ & \alpha_{ij} e_{jrs} = (S_{imn} + W_{im,n}) (\delta_{mr}\delta_{ns} - \delta_{ms}\delta_{nr}) \\ \Rightarrow\ & \left(Y_{irs} - \frac{1}{2}\alpha_{ij} e_{jrs}\right) - \left(Y_{isr} - \frac{1}{2}\alpha_{ij} e_{jsr}\right) = 0. \end{aligned}$$

Now, we *define* $\tilde{\boldsymbol{Y}}$*, in terms of ingredients of g.disclination theory,* as

$$\tilde{Y}_{imn} := Y_{imn} - \frac{1}{2}\alpha_{ij}e_{jmn} = S_{imn} + W_{im,n} - \frac{1}{2}\alpha_{ij}e_{jmn} \tag{2.20}$$

and verify that

$$\tilde{Y}_{imn} = \tilde{Y}_{inm}.$$

Therefore, $\tilde{\boldsymbol{Y}}$ is symmetric in the last two indices. In addition,

$$\begin{aligned}(\text{curl } \tilde{\boldsymbol{Y}})_{imr} &= e_{rpn}\tilde{Y}_{imn,p} = S_{imn,p}e_{rpn} - W_{im,np}e_{rpn} - \frac{1}{2}\alpha_{il,p}e_{lmn}e_{rpn} \\ \Rightarrow (\text{curl } \tilde{\boldsymbol{Y}})_{imr} &= \Pi_{imr} - \frac{1}{2}\alpha_{il,p}e_{lmn}e_{rpn}.\end{aligned}$$

Since $\boldsymbol{\Pi}$ and $\boldsymbol{\alpha}$ are localized in the core, curl $\tilde{\boldsymbol{Y}}$ is localized in the core and curl $\tilde{\boldsymbol{Y}} = \boldsymbol{0}$ outside the core.

2.7.2 Jump of inverse deformation in terms of defect strengths in g.disclination theory

With the definition of $\tilde{\boldsymbol{Y}}$ in terms of g.disclination theory (2.20), we will now identify $\boldsymbol{\Delta}$ and the jump of the inverse deformation across a cut-surface in a canonical example in terms of prescribed data used to define an isolated defect line (i.e. the strengths of the g.disclination and dislocation contained in it) and location on the surface.

A g.disclination in a thick infinite plate in the $x_1 - x_2$ plane is considered, with the g.disclination line in the positive x_3 direction. Assume the strength of the g.disclination to be $\boldsymbol{\Delta}^F$ (cf. Sec. 2.6 for definition of the strength). Based on the characterization of $\boldsymbol{\Pi}$ in (2.10), a candidate for the localized and smooth generalized disclination density $\boldsymbol{\Pi}$ is assumed to only have non-zero components Π_{ij3}, namely $\boldsymbol{\Pi} = \Pi_{ij3}\boldsymbol{e}_i \otimes \boldsymbol{e}_j \otimes \boldsymbol{e}_3$, with Π_{ij3}

given as (cf. [Ach01])

$$\Pi_{ij3} = \psi_{ij}(r) = \begin{cases} \frac{\Delta_{ij}^F}{\pi r_0}\left(\frac{1}{r} - \frac{1}{r_0}\right) & r < r_0 \\ 0 \quad r \geq r_0, \end{cases}$$

where $r = \sqrt{x_1^2 + x_2^2}$. It is easy to verify that $\boldsymbol{\Pi}$ is a smooth field and

$$\int_{core} \boldsymbol{\Pi} \boldsymbol{e}_3 da = \boldsymbol{\Delta}^F.$$

Similarly, the localized and smooth dislocation density $\boldsymbol{\alpha}$ is assumed as

$$\alpha_{i3} = \begin{cases} \frac{b_i}{\pi r_0}\left(\frac{1}{r} - \frac{1}{r_0}\right) & r < r_0 \\ 0 & r \geq r_0, \end{cases}$$

where $\boldsymbol{b}$ is the Burgers vector with

$$\int_{core} \boldsymbol{\alpha} \boldsymbol{e}_3 da = \boldsymbol{b}.$$

Recall that

$$\begin{aligned} &\tilde{Y}_{irs} = Y_{irs} - \frac{1}{2}\alpha_{ij} e_{rsj} \\ &\Rightarrow \tilde{Y}_{irs} = S^{\perp}_{irs} + Z^s_{ir,s} + W_{ir,s} - \frac{1}{2}\alpha_{ij} e_{rsj} \\ &\Rightarrow \tilde{\boldsymbol{Y}} = \boldsymbol{S}^{\perp} + \operatorname{grad} \boldsymbol{Z}^s + \operatorname{grad} \boldsymbol{W} - \frac{1}{2}\boldsymbol{\alpha} : \boldsymbol{X}, \end{aligned} \tag{2.21}$$

where $\boldsymbol{Z}^s$ is the compatible part of $\boldsymbol{S}$ and $\boldsymbol{S}^{\perp}$ is incompatible part of $\boldsymbol{S}$ that cannot be

represented as the gradient, satisfying the equations

$$\begin{aligned} \operatorname{curl} \boldsymbol{S}^{\perp} &= \boldsymbol{\Pi} \\ \operatorname{div} \boldsymbol{S}^{\perp} &= \mathbf{0} \\ \boldsymbol{S}^{\perp}\boldsymbol{n} &= \mathbf{0} \qquad \text{on the boundary.} \end{aligned}$$

One way to get the solution of $\boldsymbol{S}^{\perp}$ from the above equations is to decompose $\boldsymbol{S}^{\perp}$ as $\boldsymbol{S}^{\perp} = \boldsymbol{S}^{*} + \operatorname{grad} \boldsymbol{Z}^{*}$, where $\boldsymbol{S}^{*}$ satisfies

$$\begin{aligned} \operatorname{curl} \boldsymbol{S}^{*} &= \boldsymbol{\Pi} \\ \operatorname{div} \boldsymbol{S}^{*} &= \mathbf{0} \end{aligned} \tag{2.22}$$

and $\boldsymbol{Z}^{*}$ satisfies

$$\begin{aligned} &\operatorname{div}(\operatorname{grad} \boldsymbol{Z}^{*}) = \mathbf{0} \\ &(\operatorname{grad} \boldsymbol{Z}^{*})\boldsymbol{n} = -\boldsymbol{S}^{*}\boldsymbol{n} \qquad \text{on the boundary.} \end{aligned} \tag{2.23}$$

The solution of (2.22) can be acquired from the Riemann-Graves operator as shown in Appendix A. Furthermore, since $\int_{\partial V} \boldsymbol{S}^{*}\boldsymbol{n} da = \int_{V} \operatorname{div} \boldsymbol{S}^{*} dv = \mathbf{0}$, where ∂V is the boundary of V, a unique solution for $\operatorname{grad} \boldsymbol{Z}^{*}$ from (2.23), which is the (component-wise) Laplace equation for $\boldsymbol{Z}^{*}$ with Neumann boundary conditions, exists. Substituting $\boldsymbol{S}^{\perp}$ into Eqn (2.21), we have

$$\begin{aligned} &\tilde{\boldsymbol{Y}} = \boldsymbol{S}^{\perp} + \operatorname{grad} \boldsymbol{Z}^{s} + \operatorname{grad} \boldsymbol{W} - \frac{1}{2}\boldsymbol{\alpha} : \boldsymbol{X} \\ &\Rightarrow \tilde{\boldsymbol{Y}} = \boldsymbol{S}^{*} + \operatorname{grad} \boldsymbol{Z}^{*} + \operatorname{grad} \boldsymbol{Z}^{s} + \operatorname{grad} \boldsymbol{W} - \frac{1}{2}\boldsymbol{\alpha} : \boldsymbol{X} \\ &\Rightarrow \tilde{\boldsymbol{Y}} := \boldsymbol{S}^{*} + \operatorname{grad} \boldsymbol{A} - \frac{1}{2}\boldsymbol{\alpha} : \boldsymbol{X}, \end{aligned} \tag{2.24}$$

where $\boldsymbol{A}$ is defined as $\boldsymbol{A} := \boldsymbol{Z}^{*} + \boldsymbol{Z}^{s} + \boldsymbol{W}$.

In addition, we have

$$\alpha_{ij} = S_{imn}e_{jmn} + W_{im,n}e_{jmn}$$

$$\alpha_{ij} = S^*_{imn}e_{jmn} + Z^*_{im,n}e_{jmn} + Z^s_{im,n}e_{jmn} + W_{im,n}e_{jmn}$$

$$\alpha_{ij} - S^*_{imn}e_{jmn} = -(\operatorname{curl} \boldsymbol{A})_{ij}. \tag{2.25}$$

Denoting $B_{ij} = S^*_{imn}e_{jmn} - \alpha_{ij}$, we have

$$(\operatorname{curl} \boldsymbol{A})_{ij} = B_{ij}.$$

As given in Appendix A, we obtain $\boldsymbol{S}^*$ as

$$S^*_{ij1} = \begin{cases} \frac{\Delta^F_{ij}}{2\pi}(-\frac{x_2}{r^2}) & r > r_0 \\ \frac{-x_2\Delta^F_{ij}}{\pi r^2 r_0}(r - \frac{r^2}{2r_0}) & r \le r_0 \end{cases}$$

$$S^*_{ij2} = \begin{cases} \frac{\Delta^F_{ij}}{2\pi}(\frac{x_1}{r^2}) & r > r_0 \\ \frac{x_1\Delta^F_{ij}}{\pi r^2 r_0}(r - \frac{r^2}{2r_0}) & r \le r_0. \end{cases}$$

Also, following similar arguments as in Appendix A, in Appendix B we obtain $\boldsymbol{A}^*$ with

$\boldsymbol{A} = \boldsymbol{A}^* + \operatorname{grad} \boldsymbol{z}^A$,[4] where $\boldsymbol{A}^*$ is given by

$$A^*_{11} = \begin{cases} C_1 \left(-\Delta^F_{12} x_2^2 - \Delta^F_{11} x_1 x_2\right) + \frac{x_2}{r^2}\left[\frac{b_1}{\pi r_0}\left(r - \frac{r^2}{2r_0}\right)\right] & r < r_0 \\ C_2 \left(-\Delta^F_{12} x_2^2 - \Delta^F_{11} x_1 x_2\right) + \frac{x_2}{r^2}\frac{b_1}{2\pi} & r \geq r_0 \end{cases}$$

$$A^*_{12} = \begin{cases} C_1 \left(\Delta^F_{12} x_2 x_1 + \Delta^F_{11} x_1^2\right) - \frac{x_1}{r^2}\left[\frac{b_1}{\pi r_0}\left(r - \frac{r^2}{2r_0}\right)\right] & r < r_0 \\ C_2 \left(\Delta^F_{12} x_2 x_1 + \Delta^F_{11} x_1^2\right) - \frac{x_1}{r^2}\frac{b_1}{2\pi} & r \geq r_0 \end{cases}$$

$$A^*_{21} = \begin{cases} C_1 \left(-\Delta^F_{22} x_2^2 - \Delta^F_{21} x_1 x_2\right) + \frac{x_2}{r^2}\left[\frac{b_2}{\pi r_0}\left(r - \frac{r^2}{2r_0}\right)\right] & r < r_0 \\ C_2 \left(-\Delta^F_{22} x_2^2 - \Delta^F_{21} x_1 x_2\right) + \frac{x_2}{r^2}\frac{b_2}{2\pi} & r \geq r_0 \end{cases}$$

$$A^*_{22} = \begin{cases} C_1 \left(\Delta^F_{22} x_2 x_1 + \Delta^F_{21} x_1^2\right) - \frac{x_1}{r^2}\left[\frac{b_2}{\pi r_0}\left(r - \frac{r^2}{2r_0}\right)\right] & r < r_0 \\ C_2 \left(\Delta^F_{22} x_2 x_1 + \Delta^F_{21} x_1^2\right) - \frac{x_1}{r^2}\frac{b_2}{2\pi} & r \geq r_0 \end{cases}$$

and $C_1 = \frac{1}{2\pi r_0 r} - \frac{1}{6\pi r_0^2}$ and $C_2 = \frac{1}{3\pi r_0 r} + \frac{r - r_0}{2\pi r^3}$. $\boldsymbol{A}^*$ can be decomposed into two parts. The first part is the terms associated with C_1 and C_2, denoted as $\boldsymbol{A}^o$; the other part is the remaining terms associated with $\boldsymbol{b}$, denoted as $\boldsymbol{A}^\alpha$. Thus, $\boldsymbol{A} = \boldsymbol{A}^o + \boldsymbol{A}^\alpha + \operatorname{grad} \boldsymbol{z}^A$. $\boldsymbol{A}^o$ and $\boldsymbol{A}^\alpha$ are given as

[4] While not relevant for the essentially topological arguments here, we note that it is in the field grad $\boldsymbol{z}^A$ that the compatible part of $\boldsymbol{W}$ resides which helps in satisfaction of force equilibrium.

$$A^o_{11} = \begin{cases} \left(\frac{1}{2\pi r_0 r} - \frac{1}{6\pi r_0^2}\right)\left(-\Delta^F_{12}x_2^2 - \Delta^F_{11}x_1x_2\right) & r < r_0 \\ \left(\frac{1}{3\pi r_0 r} + \frac{r-r_0}{2\pi r^3}\right)\left(-\Delta^F_{12}x_2^2 - \Delta^F_{11}x_1x_2\right) & r \geq r_0 \end{cases}$$

$$A^o_{12} = \begin{cases} \left(\frac{1}{2\pi r_0 r} - \frac{1}{6\pi r_0^2}\right)\left(\Delta^F_{12}x_2x_1 + \Delta^F_{11}x_1^2\right) & r < r_0 \\ \left(\frac{1}{3\pi r_0 r} + \frac{r-r_0}{2\pi r^3}\right)\left(\Delta^F_{12}x_2x_1 + \Delta^F_{11}x_1^2\right) & r \geq r_0 \end{cases}$$

$$A^o_{21} = \begin{cases} \left(\frac{1}{2\pi r_0 r} - \frac{1}{6\pi r_0^2}\right)\left(-\Delta^F_{22}x_2^2 - \Delta^F_{21}x_1x_2\right) & r < r_0 \\ \left(\frac{1}{3\pi r_0 r} + \frac{r-r_0}{2\pi r^3}\right)\left(-\Delta^F_{22}x_2^2 - \Delta^F_{21}x_1x_2\right) & r \geq r_0 \end{cases}$$

$$A^o_{22} = \begin{cases} \left(\frac{1}{2\pi r_0 r} - \frac{1}{6\pi r_0^2}\right)\left(\Delta^F_{22}x_2x_1 + \Delta^F_{21}x_1^2\right) & r < r_0 \\ \left(\frac{1}{3\pi r_0 r} + \frac{r-r_0}{2\pi r^3}\right)\left(\Delta^F_{22}x_2x_1 + \Delta^F_{21}x_1^2\right) & r \geq r_0 \end{cases}$$

$$A^\alpha_{11} = \begin{cases} \frac{x_2}{r^2}\left[\frac{b_1}{\pi r_0}\left(r - \frac{r^2}{2r_0}\right)\right] & r < r_0 \\ \frac{x_2}{r^2}\frac{b_1}{2\pi} & r \geq r_0 \end{cases}$$

$$A^\alpha_{12} = \begin{cases} \frac{x_1}{r^2}\left[\frac{b_1}{\pi r_0}\left(r - \frac{r^2}{2r_0}\right)\right] & r < r_0 \\ \frac{x_1}{r^2}\frac{b_1}{2\pi} & r \geq r_0 \end{cases}$$

$$A^\alpha_{21} = \begin{cases} \frac{x_2}{r^2}\left[\frac{b_2}{\pi r_0}\left(r - \frac{r^2}{2r_0}\right)\right] & r < r_0 \\ \frac{x_2}{r^2}\frac{b_2}{2\pi} & r \geq r_0 \end{cases}$$

$$A^\alpha_{22} = \begin{cases} \frac{x_1}{r^2}\left[\frac{b_2}{\pi r_0}\left(r - \frac{r^2}{2r_0}\right)\right] & r < r_0 \\ \frac{x_1}{r^2}\frac{b_2}{2\pi} & r \geq r_0. \end{cases}$$

We now consider a multiply connected domain by thinking of the cylinder with the core region excluded and introduce a simply-connected domain by a cut-surface. On this simply-connected domain we define a $\tilde{\boldsymbol{W}}$ satisfying grad $\tilde{\boldsymbol{W}} = \tilde{\boldsymbol{Y}}$ and recall that $\tilde{\boldsymbol{Y}} =$

$\boldsymbol{S}^* + \operatorname{grad}\boldsymbol{A} - \frac{1}{2}\boldsymbol{\alpha} : \boldsymbol{X}$. Then

$$\tilde{\boldsymbol{W}}(\boldsymbol{x}) = \int_{\boldsymbol{x}_r}^{\boldsymbol{x}} \tilde{\boldsymbol{Y}}(\boldsymbol{s})d\boldsymbol{s} + \tilde{\boldsymbol{W}}(\boldsymbol{x}_r) \tag{2.26}$$

$$\tilde{\boldsymbol{W}}(\boldsymbol{x}) = \int_{\boldsymbol{x}_r}^{\boldsymbol{x}} [\boldsymbol{S}^* + \operatorname{grad}\boldsymbol{A} - \tfrac{1}{2}\boldsymbol{\alpha} : \boldsymbol{X}](\boldsymbol{s})d\boldsymbol{s} + \tilde{\boldsymbol{W}}(\boldsymbol{x}_r) \tag{2.27}$$

$$\tilde{\boldsymbol{W}}(\boldsymbol{x}) = \int_{\boldsymbol{x}_r}^{\boldsymbol{x}} \boldsymbol{S}^*(\boldsymbol{s})d\boldsymbol{s} - \tfrac{1}{2}\int_{\boldsymbol{x}_r}^{\boldsymbol{x}} (\boldsymbol{\alpha} : \boldsymbol{X})(\boldsymbol{s})d\boldsymbol{s} + \boldsymbol{A}(\boldsymbol{x}) + const, \tag{2.28}$$

where $\boldsymbol{x}_r$ is a given point and *const* is the constant $\tilde{\boldsymbol{W}}(\boldsymbol{x}_r) - \boldsymbol{A}(\boldsymbol{x}_r)$, with $\tilde{\boldsymbol{W}}(\boldsymbol{x}_r)$ being arbitrarily assignable.

Consider a path p from $\boldsymbol{z}^-$ to $\boldsymbol{z}^+$, both points arbitrarily close to $\boldsymbol{z} \in S$, on opposite sides of S (see (2.14) for notation) and define

$$[\![\boldsymbol{y}(\boldsymbol{z})]\!] = \lim_{\substack{\boldsymbol{z}^+ \to \boldsymbol{z} \\ \boldsymbol{z}^- \to \boldsymbol{z}}} \int_p \tilde{\boldsymbol{W}}(\boldsymbol{x})d\boldsymbol{x}$$

for any $\boldsymbol{z}$ on the cut-surface.

After substituting $\tilde{\boldsymbol{W}}$ and noticing $\oint_p const\, d\boldsymbol{x} = \boldsymbol{0}$ and $\oint_p \operatorname{grad}\boldsymbol{z}^A\, d\boldsymbol{x} = \boldsymbol{0}$, the jump at $\boldsymbol{x}$ can be further written as

$$\begin{aligned}[\![\boldsymbol{y}]\!] &= \int_p \int_{\boldsymbol{x}_r}^{\boldsymbol{x}} \boldsymbol{S}^*(\boldsymbol{s})d\boldsymbol{s}d\boldsymbol{x} + \int_p \boldsymbol{A}(\boldsymbol{x})d\boldsymbol{x} - \frac{1}{2}\int_p \int_{\boldsymbol{x}_r}^{\boldsymbol{x}} (\boldsymbol{\alpha} : \boldsymbol{X})(\boldsymbol{s})d\boldsymbol{s}d\boldsymbol{x} \\ &= \int_p \int_{\boldsymbol{x}_r}^{\boldsymbol{x}} \boldsymbol{S}^*(\boldsymbol{s})d\boldsymbol{s}d\boldsymbol{x} + \int_p \boldsymbol{A}^o(\boldsymbol{x})d\boldsymbol{x} + \int_p \boldsymbol{A}^\alpha(\boldsymbol{x})d\boldsymbol{x} - \frac{1}{2}\int_p \int_{\boldsymbol{x}_r}^{\boldsymbol{x}} (\boldsymbol{\alpha} : \boldsymbol{X})(\boldsymbol{s})d\boldsymbol{s}d\boldsymbol{x}. \end{aligned} \tag{2.29}$$

Now suppose $\boldsymbol{x}$ located as $(R, 0)$ and p is given as a circle with radius $r = R$, where $R \geq r_0$. Clearly, this circle encloses the whole disclination core. Also, since $A^o_{ij}(x_1, x_2) = A^o_{ij}(-x_1, -x_2)$, then

$$\int_p \boldsymbol{A}^o(\boldsymbol{x})d\boldsymbol{x} = \boldsymbol{0}.$$

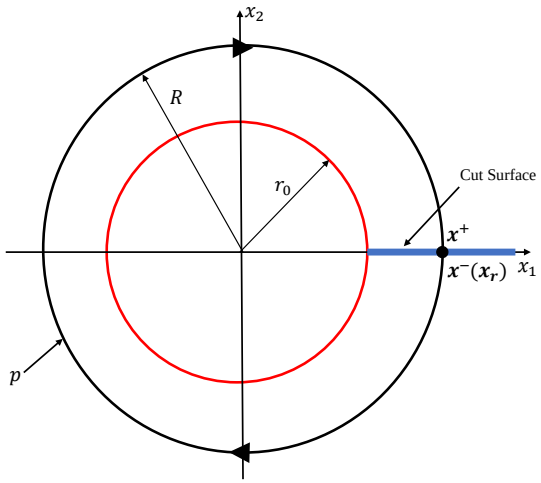

Figure 2.22: *Configuration of a closed contour enclosing the disclination and passing through* $\boldsymbol{x}$.

Also, for any loop enclosing the core, $\boldsymbol{\alpha} = \mathbf{0}$ along the loop and thus,

$$\int_p \int_{\boldsymbol{x}_r}^{\boldsymbol{x}} (\boldsymbol{\alpha} : \boldsymbol{X})(\boldsymbol{s}) d\boldsymbol{s} d\boldsymbol{x} = \mathbf{0}.$$

Therefore, the jump $[\![\boldsymbol{y}]\!] = [\![\boldsymbol{y}]\!]^s + [\![\boldsymbol{y}]\!]^\alpha$, where $[\![\boldsymbol{y}]\!]^s = \oint_p \int_{\boldsymbol{x}_r}^{\boldsymbol{x}} \boldsymbol{S}^*(\boldsymbol{s}) d\boldsymbol{s} d\boldsymbol{x}$ and $[\![\boldsymbol{y}]\!]^\alpha = \oint_p \boldsymbol{A}^\alpha(\boldsymbol{x}) d\boldsymbol{x}$. With reference to Figure 2.22 and choose $\boldsymbol{x}_r$ as $\boldsymbol{x}^-$, $[\![\boldsymbol{y}]\!]^s$ evaluates to

$$\begin{aligned} [\![\boldsymbol{y}]\!]_1^s &= R\Delta_{11}^F \\ [\![\boldsymbol{y}]\!]_2^s &= R\Delta_{21}^F. \end{aligned} \tag{2.30}$$

$[\![\boldsymbol{y}]\!]^\alpha = \oint_p \boldsymbol{A}^\alpha(\boldsymbol{x}) d\boldsymbol{x}$ can be obtained as follows:

$$\begin{aligned} [\![\boldsymbol{y}]\!]_1^\alpha &= \oint_{2\pi}^0 \left[-A_{11}^\alpha R \sin\beta + A_{12}^\alpha R(\cos\beta)\right] d\beta \\ \Rightarrow [\![\boldsymbol{y}]\!]_1^\alpha &= \oint_{2\pi}^0 -\tfrac{b_1}{2\pi} d\beta = b_1 \\ [\![\boldsymbol{y}]\!]_2^\alpha &= \oint_{2\pi}^0 \left[-A_{21}^\alpha R \sin\beta + A_{22}^\alpha R(\cos\beta)\right] d\beta \\ \Rightarrow [\![\boldsymbol{y}]\!]_2^\alpha &= \oint_{2\pi}^0 -\tfrac{b_2}{2\pi} d\beta = b_2 \end{aligned}$$

Thus, the jump at point $\boldsymbol{x}$, $(R, 0)$, is

$$[\![\boldsymbol{y}]\!]_1 = R\Delta^F_{11} + b_1$$
$$[\![\boldsymbol{y}]\!]_2 = R\Delta^F_{21} + b_2,$$

which can be written in the form

$$[\![\boldsymbol{y}]\!](\boldsymbol{x}) = \boldsymbol{\Delta}^F\boldsymbol{x} + \boldsymbol{b} = \boldsymbol{\Delta}^F(\boldsymbol{x} - \boldsymbol{x}_0) + [\![\boldsymbol{y}]\!](\boldsymbol{x}_0), \tag{2.31}$$

where

$$\boldsymbol{\Delta}^F = \begin{bmatrix} \Delta^F_{11} & \Delta^F_{12} \\ \Delta^F_{21} & \Delta^F_{22} \end{bmatrix}$$

and

$$[\![\boldsymbol{y}]\!](\boldsymbol{x}_0) = \boldsymbol{\Delta}^F\boldsymbol{x}_0 + \boldsymbol{b}.$$

for an arbitrarily chosen base-point $\boldsymbol{x}_0$ on the cut-surface.

For $\boldsymbol{\Pi} = \boldsymbol{0}$ (i.e. no generalized disclination in the defect), given a localized dislocation density $\boldsymbol{\alpha}$, the jump in the inverse deformation should be the same as the integral of $\boldsymbol{\alpha}$ over any arbitrary area threaded by the core, denoted as $\boldsymbol{b}$. Since $\boldsymbol{\Pi} = \boldsymbol{0}$, then $\boldsymbol{\Delta}^F = \boldsymbol{0}$ and (2.31) implies,

$$[\![\boldsymbol{y}]\!] = \boldsymbol{b}.$$

Thus, in this special, but canonical, example, we have characterized the jump in the inverse deformation due to a defect line in terms of data characterizing the g.disclination and dislocation densities of g.disclination theory and shown that the result is consistent with what is expected in the simpler case when the g.disclination density vanishes.

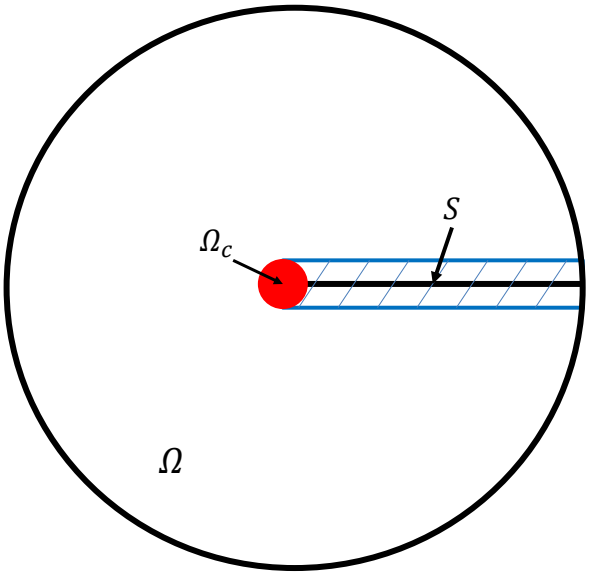

Figure 2.23: *The cross-section of a simply-connected domain Ω with a cut-surface S and a core Ω_c. The blue shaded area is the layer S_l which includes the core.*

2.7.3 The connection between $\boldsymbol{W}$ and $\boldsymbol{y}$

We now deal with the question of how the inverse deformation field $\boldsymbol{y}$ defined on a cut-surface induced simply-connected domain defined from the field $\tilde{\boldsymbol{Y}}$ may be related to the i-elastic 1-distortion field $\boldsymbol{W}$ of g.disclination theory. The setting we have in mind is as follows: with reference to Fig. 2.23, we consider the domain Ω with the core comprising the region $\Omega_c \subset \Omega$. Let the cut-surface be S, connecting a curve on the boundary of Ω_c to a curve on the boundary of Ω so that $(\Omega \backslash \Omega_c) \backslash S$ is simply-connected. Also consider a 'layer' region $S_l \subset \Omega$ such that $S \subset S_l$ as well as $\Omega_c \subset S_l$, as shown in Figure 2.23. We assume that $\boldsymbol{S}$ has support in S_l. We now think that a problem of g.disclination theory has been solved with $\boldsymbol{S}$, $\boldsymbol{\Pi}$, and $\boldsymbol{\alpha}$ as given data on Ω satisfying the constraint curl $\boldsymbol{S} = \boldsymbol{\Pi}$.

From (2.20) and (2.26), we have

$$\operatorname{grad}(\tilde{\boldsymbol{W}} - \boldsymbol{W}) = \boldsymbol{S} - \frac{1}{2}\boldsymbol{\alpha}\boldsymbol{X} \quad \text{on } (\Omega \backslash \Omega_c) \backslash S.$$

We then have

$$[\![\boldsymbol{W}]\!] = [\![\text{grad } \boldsymbol{y}]\!] - \boldsymbol{\Delta}^F = \boldsymbol{0} \quad \text{on } \mathbf{S},$$

since the dislocation density $\boldsymbol{\alpha}$ is localized in the core, an expected result since $\boldsymbol{W}$ is a continuous field on Ω. Moreover, we have

$$\boldsymbol{W} = \text{grad } \boldsymbol{y} + \boldsymbol{W}^* \quad \text{on } \Omega \backslash S_l,$$

where $\boldsymbol{W}^*$ is a constant second-order tensor. Thus, when S_l is truly in the shape of a layer around S (including the core as defined), $\boldsymbol{W}$ can indeed be viewed as the gradient of the deformation $\boldsymbol{y}$ constructed from $\tilde{\boldsymbol{Y}}$, up to a constant second-order tensor, in most of the domain. On the other hand, when $S_l = \Omega \backslash \Omega_c$ as e.g. when curl $\boldsymbol{S} = \boldsymbol{\Pi}$ with div $\boldsymbol{S} = \boldsymbol{0}$ on Ω with $\boldsymbol{\Pi}$ still supported in the core, such an identification is not possible.

2.8 Burgers vector of a g.disclination dipole

We will derive the Burgers vector for a given g.disclination dipole with separation vector $\boldsymbol{d}$. In Figure 2.24, the red circle is the (cross-section of the) positive g.disclination while the blue circle is that of the negative g.disclination. The separation vector between these two disclination is $\boldsymbol{d}$. For the calculations in this section, we assume Cartesian coordinates whose origin is at the positive g.disclination core and the x and y axes are shown as in Figure 2.24. The boundary of the positive g.disclination core is the circle with center at $(0, 0)$ and radius r_0; the boundary of the negative disclination core is the circle with center at $(d, 0)$ and radius r_0. Denote the strength of the positive disclination as $\boldsymbol{\Delta}^F$ (see Sec. 2.6 for the definition of the strength). We denote the whole domain as Ω and the boundary of the domain as $\partial\Omega$. The positive g.disclination density field $\boldsymbol{\Pi}^+$ and the negative g.disclination density field $\boldsymbol{\Pi}^-$ are both localized inside the cores (while being defined in all of Ω). We define the core of the g.disclination dipole, Ω_c, as a patch including the positive and

negative g.disclinations enclosed by the black contour C in Figure 2.24. In the following calculation, the core is referred as the g.disclination dipole core. Also, let the cut-surface be S, which is along the positive x axis connecting the boundary of Ω to the curve C at $\boldsymbol{x}_c$ shown as the green line in Figure 2.24. Namely, $S = \{(x, y) \in \Omega | y = 0, x \geq x_c\}$. In addition, the cut-induced simply-connected domain is denoted as $(\Omega \backslash \Omega_c) \backslash S$.

We denote the defect density field for the g.disclination dipole as $\boldsymbol{\Pi}$. Clearly, $\boldsymbol{\Pi}$ is localized within the g.disclination core, given as $\boldsymbol{\Pi} = \boldsymbol{\Pi}^+ + \boldsymbol{\Pi}^-$ on Ω. Based on the Weingarten-gd theorem, given $\boldsymbol{S}^*$, $\boldsymbol{\alpha}$, and $\boldsymbol{A}$, $\tilde{\boldsymbol{Y}}$ is defined as in (2.21) and (2.24):

$$\tilde{\boldsymbol{Y}} := \boldsymbol{S}^* + \operatorname{grad} \boldsymbol{A} - \frac{1}{2} \boldsymbol{\alpha} : \boldsymbol{X} \qquad \text{in } \Omega.$$

In this case, $\boldsymbol{\alpha} = \boldsymbol{0}$, thus

$$\tilde{\boldsymbol{Y}} = \boldsymbol{S}^* + \operatorname{grad} \boldsymbol{A}. \tag{2.32}$$

Recall that given the g.disclination density $\boldsymbol{\Pi}$, $\boldsymbol{S}^*$ is calculated from

$$\left.\begin{aligned} \operatorname{curl} \boldsymbol{S}^* = \boldsymbol{\Pi} = \boldsymbol{\Pi}^+ + \boldsymbol{\Pi} - \\ \operatorname{div} \boldsymbol{S}^* = \boldsymbol{0} \end{aligned}\right\} \qquad \text{in } \Omega.$$

Since $\boldsymbol{S}^*$ is a solution to linear equations, $\boldsymbol{S}^*$ can be written as

$$\boldsymbol{S}^* = \boldsymbol{S}^{*+} + \boldsymbol{S}^{*-},$$

with $\boldsymbol{S}^{*+}$ and $\boldsymbol{S}^{*-}$ calculated from

$$\left.\begin{aligned} \operatorname{curl} \boldsymbol{S}^{*+} &= \boldsymbol{\Pi}^{+} \\ \operatorname{div} \boldsymbol{S}^{*+} &= \boldsymbol{0} \end{aligned}\right\} \quad \text{in } \Omega$$

$$\left.\begin{aligned} \operatorname{curl} \boldsymbol{S}^{*-} &= \boldsymbol{\Pi}^{-} \\ \operatorname{div} \boldsymbol{S}^{*-} &= \boldsymbol{0} \end{aligned}\right\} \quad \text{in } \Omega.$$

Similarly, given $\boldsymbol{S}^{*}$, $\boldsymbol{A} = \boldsymbol{A}^{*} + \operatorname{grad} \boldsymbol{z}^{A}$, where $\boldsymbol{A}^{*}$ satisfies (2.25)

$$\left.\begin{aligned} \operatorname{curl} \boldsymbol{A}^{*} &= \boldsymbol{S}^{*} : \boldsymbol{X} \\ \operatorname{div} \boldsymbol{A}^{*} &= \boldsymbol{0} \end{aligned}\right\} \quad \text{in } \Omega.$$

Therefore, $\boldsymbol{A}$ can be written as $\boldsymbol{A} = \boldsymbol{A}^{*+} + \boldsymbol{A}^{*-} + \operatorname{grad} \boldsymbol{z}^{A}$, where $\boldsymbol{A}^{*+}$ and $\boldsymbol{A}^{*-}$ are calculated from

$$\left.\begin{aligned} \operatorname{curl} \boldsymbol{A}^{*+} &= \boldsymbol{S}^{*+} : \boldsymbol{X} \\ \operatorname{div} \boldsymbol{A}^{*+} &= \boldsymbol{0} \end{aligned}\right\} \quad \text{in } \Omega$$

$$\left.\begin{aligned} \operatorname{curl} \boldsymbol{A}^{*-} &= \boldsymbol{S}^{*-} : \boldsymbol{X} \\ \operatorname{div} \boldsymbol{A}^{*-} &= \boldsymbol{0} \end{aligned}\right\} \quad \text{in } \Omega.$$

After substituting $\boldsymbol{S}^{*}$ and $\boldsymbol{A}$, $\tilde{\boldsymbol{Y}}$ can be written as

$$\tilde{\boldsymbol{Y}} = \boldsymbol{S}^{*+} + \boldsymbol{S}^{*-} + \operatorname{grad} \boldsymbol{A}^{*+} + \operatorname{grad} \boldsymbol{A}^{*-} + \operatorname{grad} \operatorname{grad} \boldsymbol{z}^{A} \quad \text{on} \quad \Omega.$$

In the cut-induced simply-connected domain $(\Omega \backslash \Omega_c) \backslash S$, given the core Ω_c and cut-surface S shown in Figure 2.24, $\tilde{\boldsymbol{W}}$ is defined as (2.26)

$$\tilde{\boldsymbol{W}}(\boldsymbol{x}) := \int_{\boldsymbol{x}_r}^{\boldsymbol{x}} \tilde{\boldsymbol{Y}}(\boldsymbol{s}) d\boldsymbol{s} + \tilde{\boldsymbol{W}}(\boldsymbol{x}_r)$$

where $\boldsymbol{x}_r$ is a fixed point and $\tilde{\boldsymbol{W}}(\boldsymbol{x}_r)$ is an arbitrary constant. After substituting $\tilde{\boldsymbol{Y}}$, we have

$$\tilde{\boldsymbol{W}}(\boldsymbol{x}) = \int_{\boldsymbol{x}_r}^{\boldsymbol{x}} \boldsymbol{S}^{*+}(\boldsymbol{s})d\boldsymbol{s} + \int_{\boldsymbol{x}_r}^{\boldsymbol{x}} \boldsymbol{S}^{*-}(\boldsymbol{s})d\boldsymbol{s} + \boldsymbol{A}^{*+}(\boldsymbol{x}) + \boldsymbol{A}^{*-}(\boldsymbol{x}) + \operatorname{grad} \boldsymbol{z}^A(\boldsymbol{x}) + const,$$

where *const* is the constant equal to $\tilde{\boldsymbol{W}}(\boldsymbol{x}_r) - \boldsymbol{A}^{*+}(\boldsymbol{x}_r) - \boldsymbol{A}^{*-}(\boldsymbol{x}_r) - \operatorname{grad} \boldsymbol{z}^A(\boldsymbol{x}_r)$. Write $\tilde{\boldsymbol{W}}(\boldsymbol{x})$ as

$$\tilde{\boldsymbol{W}}(\boldsymbol{x}) = \tilde{\boldsymbol{T}}^{+}(\boldsymbol{x};\boldsymbol{x}_r) + \tilde{\boldsymbol{T}}^{-}(\boldsymbol{x};\boldsymbol{x}_r) + \operatorname{grad} \boldsymbol{z}^A(\boldsymbol{x}) + const,$$

where

$$\tilde{\boldsymbol{T}}^{+}(\boldsymbol{x};\boldsymbol{x}_r) := \int_{\boldsymbol{x}_r}^{\boldsymbol{x}} \boldsymbol{S}^{*+}(\boldsymbol{s})d\boldsymbol{s} + \boldsymbol{A}^{*+}(\boldsymbol{x})$$
$$\tilde{\boldsymbol{T}}^{-}(\boldsymbol{x};\boldsymbol{x}_r) := \int_{\boldsymbol{x}_r}^{\boldsymbol{x}} \boldsymbol{S}^{*-}(\boldsymbol{s})d\boldsymbol{s} + \boldsymbol{A}^{*-}(\boldsymbol{x})$$

With reference to Fig. 2.24, it follows from (2.15) that the jump of $\boldsymbol{y}$ at $\boldsymbol{x}_0$ is

$$[\![\boldsymbol{y}]\!](\boldsymbol{x}_0) = \int_p \tilde{\boldsymbol{W}}(\boldsymbol{x})d\boldsymbol{x},$$

where p is a path shown in Fig. 2.24 from $\boldsymbol{x}_0^-$ to $\boldsymbol{x}_0^+$. Since $\boldsymbol{z}$ is continuous on Ω, $\int_p \operatorname{grad} \boldsymbol{z}(\boldsymbol{x})d\boldsymbol{x} = \boldsymbol{0}$. Also, with $\int_p const d\boldsymbol{x} = \boldsymbol{0}$, we have

$$[\![\boldsymbol{y}]\!](\boldsymbol{x}_0) = \int_p \tilde{\boldsymbol{T}}^{+}(\boldsymbol{x};\boldsymbol{x}_r)d\boldsymbol{x} + \int_p \tilde{\boldsymbol{T}}^{-}(\boldsymbol{x};\boldsymbol{x}_r)d\boldsymbol{x},$$

Let $\boldsymbol{x}_0$ be the point located at $(x_0, 0)$ and denote p^+ as a clockwise circle centered at $(0, 0)$ with radius x_0 and p^- as a clockwise circle centered at $(d, 0)$ with radius $x_0 - d$. Also, we choose $\boldsymbol{x}_0$ big enough so that p^+ and p^- enclose the g.disclination core - this induces no loss in generality for our final result, as we show in the discussion surrounding (2.33)

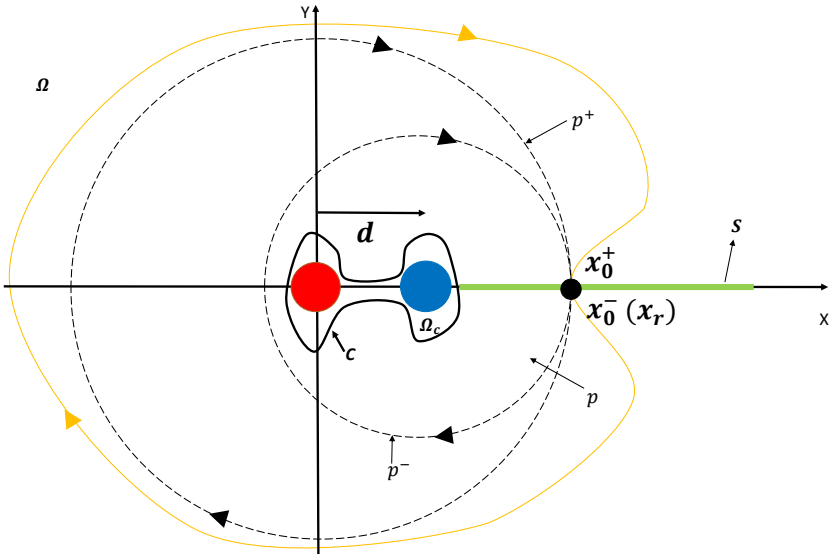

Figure 2.24: *Configuration for a disclination dipole with separation vector* $\boldsymbol{d}$ *and an introduced cut-surface.*

and (2.34). Also, let $\boldsymbol{x}_r$ be $\boldsymbol{x}_0^-$. Based on the argument in Appendix C,

$$\oint_p \tilde{\boldsymbol{T}}^+(\boldsymbol{x};\boldsymbol{x}_r)d\boldsymbol{x} = \oint_{p^+} \tilde{\boldsymbol{T}}^+(\boldsymbol{x};\boldsymbol{x}_0^-)d\boldsymbol{x} =: \boldsymbol{I}^+$$
$$\oint_p \tilde{\boldsymbol{T}}^-(\boldsymbol{x};\boldsymbol{x}_r)d\boldsymbol{x} = \oint_{p^-} \tilde{\boldsymbol{T}}^-(\boldsymbol{x};\boldsymbol{x}_0^-)d\boldsymbol{x} =: \boldsymbol{I}^-$$

(This step is utilized to facilitate the computation of the line integrals, which are most conveniently calculated on circular paths).

Given the $\boldsymbol{\Pi}^+$ and $\boldsymbol{\Pi}^-$ fields, based on the calculation in Appendix D, we have

$$I_1^+ = x_0\Delta_{11}^F$$
$$I_2^+ = x_0\Delta_{21}^F$$
$$I_1^- = -(x_0-d)\Delta_{11}^F$$
$$I_2^- = -(x_0-d)\Delta_{21}^F.$$

Thus, the jump $[\![\boldsymbol{y}]\!]$ at $\boldsymbol{x}_0$ is

$$[\![y]\!]_1(\boldsymbol{x}_0) = x_0\Delta^F_{11} - (x_0 - d)\Delta^F_{11} = d\Delta^F_{11}$$
$$[\![y]\!]_2(\boldsymbol{x}_0) = x_0\Delta^F_{21} - (x_0 - d)\Delta^F_{21} = d\Delta^F_{21}$$

Therefore, the jump at $\boldsymbol{x}_0$ is

$$[\![\boldsymbol{y}]\!](\boldsymbol{x}_0) = \boldsymbol{\Delta}^F\boldsymbol{d}$$

Recall from (2.32) that

$$\tilde{\boldsymbol{Y}} = \boldsymbol{S}^* + \operatorname{grad}\boldsymbol{A},$$

so that

$$\operatorname{curl}\tilde{\boldsymbol{Y}} = \operatorname{curl}\boldsymbol{S}^* = \boldsymbol{\Pi}.$$

Therefore,

$$\boldsymbol{\Delta} = \int_C \tilde{\boldsymbol{Y}}d\boldsymbol{x} = \int_{\Omega_c} \operatorname{curl}\tilde{\boldsymbol{Y}}\boldsymbol{n}da = \int_{\Omega_c} (\boldsymbol{\Pi}^+ + \boldsymbol{\Pi}^-)\boldsymbol{n}da$$

where C is the boundary of the g.disclination core and Ω_c is the area of the core enclosed by C. Because $\boldsymbol{\Pi}^+$ and $\boldsymbol{\Pi}^-$ have opposite signs but are otherwise identical (shifted) fields,

$$\boldsymbol{\Delta} = \int_{\Omega_c} (\boldsymbol{\Pi}^+ + \boldsymbol{\Pi}^-)\boldsymbol{n}da = \boldsymbol{0}.$$

Then, invoking (2.17), the jump of $\boldsymbol{y}$ satisfies

$$[\![\boldsymbol{y}]\!](\boldsymbol{x}) = [\![\boldsymbol{y}]\!](\boldsymbol{x}_0) = \boldsymbol{\Delta}^F\boldsymbol{d} \quad \text{for} \quad \boldsymbol{x} \in S. \tag{2.33}$$

In addition, as proved in Section 2.6.2, the jump $[\![\boldsymbol{y}]\!]$ is independent of the cut-surface when $\boldsymbol{\Delta} = \boldsymbol{0}$. Therefore, defining the Burgers vector $\boldsymbol{b}$ of the g.disclination dipole as the

jump $[\![\boldsymbol{y}]\!]$ across *any* arbitrary cut-surface rendering $\Omega \backslash \Omega_c$ simply-connected, we have

$$\boldsymbol{b} = \boldsymbol{\Delta}^F \boldsymbol{d}. \tag{2.34}$$

Now, considering a disclination dipole with separation vector $\boldsymbol{d} = \delta \boldsymbol{r}$, where the Frank vector for the positive disclination is given as $\boldsymbol{\Omega} = \Omega_3 \boldsymbol{e}_3$, $\boldsymbol{\Delta}^F$ is given by the difference of two inverse rotation tensors, written as

$$\left[\boldsymbol{\Delta}^F\right] = \begin{bmatrix} cos\Omega_3 - 1 & -sin\Omega_3 \\ sin\Omega_3 & cos\Omega_3 - 1 \end{bmatrix}.$$

When the strength of the disclination is low, $|\Omega_3| \ll 1$, $cos\Omega_3 - 1 \approx 0$ and $sin\Omega_3 \approx \Omega_3$, and we have

$$\boldsymbol{\Delta}^F = \begin{bmatrix} 0 & -\Omega_3 \\ \Omega_3 & 0 \end{bmatrix},$$

a skew symmetric tensor.

From (2.34), the components of the Burgers vector $\boldsymbol{b}$ are given as

$$b_1 = -\Omega_3 \delta r_2, \quad b_2 = \Omega_3 \delta r_1$$

which matches the result (2.7) from linear elasticity.

Chapter 3

Finite element approximation of the fields of bulk and interfacial line defects

3.1 Introduction

In the context of continuum mechanics, the distortion measure is similar to a deformation or a displacement gradient, except such a measure is not the gradient of a vector field in many situations involving material defects. Such a situation arises when the distortion represents, through a non-singular field, the 'gradient' of a field that contains a terminating discontinuity on a surface. If the discontinuity is in the displacement field, the terminating curve is called a dislocation; if the discontinuity is in the rotation field, the terminating curve is called a disclination. In some cases, the discontinuity can arise in the strain field as well, as for instance in the solid-to-solid phase transformation between austenite and martensite. In [AF12, AF15], the concept of the disclination is extended to the generalized disclination (g.disclination) to deal with general distortion-discontinuity problems. The g.disclination can be thought of as a discontinuity (along a curve or loop) of a distortion discontinuity (along a surface).

The strain and stress fields of dislocations and disclinations in a linear elastic isotropic body have been studied in [Nab85, Nab67, DeW73a]. However, in classical linear elasticity, the stress and strain fields for these defects have singularities at the defect cores, often predicting infinite energies for finite bodies. In [AF12, AF15], a continuum model is introduced for the g.disclination static equilibrium as well as dynamic behaviors, where the singularities are well-handled. The Weingarten theorem for g.disclinations established in [AF15] is characterized further in Chapter 2, with the derivation of explicit formula for important topological properties of canonical g.disclination configurations. Relationships between the representations of the dislocation, disclination, and the g.disclination from the Weingarten point of view and in g.disclination theory are established therein. Concrete connections are also established between g.disclinations as mathematical objects and the physical ideas of interfacial and bulk line defects like defected grain and phase boundaries, dislocations, and disclinations. The papers [AF12, AF15] and Chapter 2 explain the

theoretical and physical basis for the results obtained in the present work.

This paper focuses on the applications of the g.disclination model through computation. The goal is to show that the g.disclination model is capable of solving various material-defect problems, within both the small and finite deformation settings. Finite element schemes to solve for the stress and energy density fields of g.disclination distributions are proposed, implemented, and verified for the small and finite deformation settings, for a 'canonical' class of defect configurations (mentioned in the abstract).

The paper is organized as follows. Section 5.2 contains notation and terminology. In Section 3.3, we briefly review elements of g.disclination theory from [AF12, AF15] that provide the governing equations for this work, rationalize a procedure for defining a g.disclination as data for computation of stress fields, and discuss the stress field of a disclination viewed as an Eshelby cut and weld problem. Section 3.4 proposes numerical schemes based on the Galerkin and Least Squares Finite Element methods to solve for the fields of g.disclinations at small and finite deformations. Section 3.5 contains results pertaining to twelve illustrative problems (with sub-cases), all modeled by appropriate combinations of g.disclinations, eigenwall fields, and dislocations as data. Section 3.6 makes contact between the g.disclination model and classical disclination theory of DeWit [DeW73a], under appropriate restriction on specified data. It is also shown here that for identical specified data, g.disclination theory predicts essentially the entire elastic distortion uniquely, while the classical theory uniquely predicts only the elastic strain field, a particularly clear distinction for the special case of both models in which the data specified is only a dislocation density field. Section 5.5 contains concluding remarks.

3.2 Notation and terminology

The following list describes some of the mathematical symbols we use in this work:

$\boldsymbol{U}^e$: the elastic strain tensor (2^{nd}-order).

$\boldsymbol{F}^e$: the elastic distortion tensor. In small deformation, $\boldsymbol{F}^e = \boldsymbol{I} + \boldsymbol{U}^e$ (2^{nd}-order).

$\boldsymbol{W}$: the inverse-elastic (i-elastic) 1-distortion tensor. $\boldsymbol{W} = (\boldsymbol{F}^e)^{-1}$ (2^{nd}-order).

$\hat{\boldsymbol{F}}^e$: the closest-well elastic distortion tensor (2^{nd}-order).

$\hat{\boldsymbol{W}}$: the closest-well-inverse-elastic (cwi-elastic) 1-distortion tensor. $\hat{\boldsymbol{W}} = \left(\hat{\boldsymbol{F}}^e\right)^{-1}$ (2^{nd}-order).

$\boldsymbol{S}$: the eigenwall tensor (3^{rd}-order).

$\boldsymbol{Y}$: the i-elastic 2-distortion tensor (3^{rd}-order).

$\boldsymbol{\alpha}$: the dislocation density tensor (2^{nd}-order).

$\boldsymbol{\Pi}$: the g.disclination density tensor (3^{rd}-order).

The normalized difference between two stress fields $\boldsymbol{\sigma}_A$ and $\boldsymbol{\sigma}_B$ is denoted as $\delta\sigma_{A,B}$, defined as

$$\delta\sigma_{A,B} = \frac{|\boldsymbol{\sigma}_A - \boldsymbol{\sigma}_B|}{|\boldsymbol{\sigma}_A|}, \tag{3.1}$$

where $|\cdot|$ represents the l^2-norm of a matrix. The mean of $\delta\sigma_{A,B}$ is defined as the volume average of the field $\delta\sigma_{A,B}$ over the entire body. *Note that, by definition, whenever such comparisons are presented, they represent differences between the tensors involved and not that of any specific components.*

In Sec. 3.5.9.4 and 3.5.10, repeated indices represent discrete forms rather than Einstein summation.

3.3 Elements of g.disclination theory

We recapitulate the basic theory for g.disclination statics from [AF12, AF15] for the sake of completeness and provide the arguments for defining individual g.disclination cores for work in subsequent sections.

Developed as a generalization of eigenstrain theory of Kröner, Mura, and deWit, an individual g.disclination is a curve that terminates a discontinuity of elastic distortion on

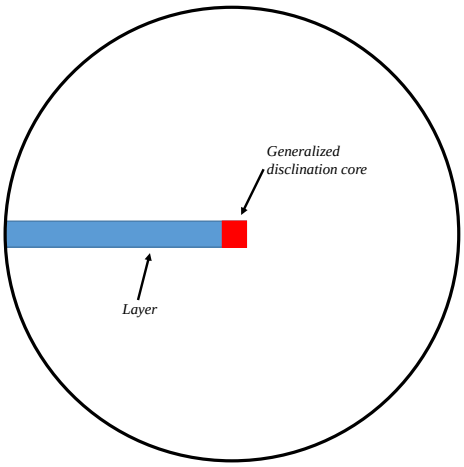

Figure 3.1: *Physical regularization of a classical terminating discontinuity of a vector/tensor field. Treat its distortion discontinuity as a smooth field localized inside the layer.*

a surface. The distortion discontinuity is modeled by a field with support within a layer [AF15], as shown in Figure 3.1. The termination is considered as continuous over the core within the layer. The core is the support of the g.disclination density field. The strength of an individual g.disclination is simply the difference of the distortions forming the distortion discontinuity terminated by it. One way of setting up the 3-order g.disclination density tensor is to assign the tensor product of the strength tensor and the tangent direction vector of the g.disclination curve as a uniformly distributed field within the g.disclination core, and zero outside it - further details are provided below in (3.13)-(3.18).

The fundamental kinematic decomposition of g.disclination theory is

$$\boldsymbol{Y} = \operatorname{grad} \boldsymbol{W} + \boldsymbol{S}, \tag{3.2}$$

where $\boldsymbol{W}$ is the i-elastic 1-distortion and $\boldsymbol{S}$ is the eigenwall field.

With this decomposition of $\boldsymbol{Y}$, a natural measure of the g.disclination density is

$$\operatorname{curl}(\boldsymbol{Y} - \operatorname{grad} \boldsymbol{W}) = \operatorname{curl} \boldsymbol{S} =: \boldsymbol{\Pi}, \tag{3.3}$$

since it characterizes the closure failure of integrating $\boldsymbol{Y}$ on closed contours in the body:

$$\int_A \boldsymbol{\Pi}\boldsymbol{n}da = \int_C \boldsymbol{Y}d\boldsymbol{x},$$

where A is any area patch with closed boundary contour C. Physically, it is to be interpreted as a density of lines (threading areas) in the current configuration, carrying a tensorial attribute that reflects a jump in the values of $\boldsymbol{W}$ across the layer representing a phase/grain boundary.

The dislocation density is defined as

$$\boldsymbol{\alpha} := \boldsymbol{Y} : \boldsymbol{X} = (\boldsymbol{S} + \operatorname{grad}\boldsymbol{W}) : \boldsymbol{X}. \tag{3.4}$$

When there is no discontinuity of elastic distortion across a layer, namely $\boldsymbol{S} = \boldsymbol{0}$, (3.4) becomes $\boldsymbol{\alpha} = -\operatorname{curl}\boldsymbol{W}$, since $\operatorname{curl}\boldsymbol{A} = -\operatorname{grad}\boldsymbol{A} : \boldsymbol{X}$ for any smooth tensor field $\boldsymbol{A}$. We utilize a Stokes-Helmholtz-like orthogonal decomposition of the field $\boldsymbol{S}$ into compatible and incompatible parts,

$$\boldsymbol{S} = \boldsymbol{S}^{\perp} + \operatorname{grad}\boldsymbol{Z}^s. \tag{3.5}$$

For the problems of g.disclination statics considered in this paper, $\boldsymbol{\alpha}$ and either $\boldsymbol{\Pi}$ or $\boldsymbol{S}$ need to be prescribed as data. In the case where $\boldsymbol{\alpha}$ and $\boldsymbol{\Pi}$ are prescribed, we take $\boldsymbol{Z}^s = -\boldsymbol{I}$ and $\boldsymbol{S} = \boldsymbol{S}^{\perp}$ with $\boldsymbol{S}^{\perp}$ determined by the system

$$\begin{aligned} \operatorname{curl}\boldsymbol{S}^{\perp} &= \boldsymbol{\Pi} \\ \operatorname{div}\boldsymbol{S}^{\perp} &= \boldsymbol{0} \\ \text{with}\quad \boldsymbol{S}^{\perp}\boldsymbol{n} &= \boldsymbol{0} \quad \text{on boundary of the body,} \end{aligned} \tag{3.6}$$

which guarantees that the field $\boldsymbol{S}^{\perp}$ is vanishing if and only if $\boldsymbol{\Pi} = \boldsymbol{0}$.

Defining a new field $\boldsymbol{H}^s$ as the deviation of $-\boldsymbol{Z}^s$ from the identity so that

$$\boldsymbol{H}^s := -(\boldsymbol{Z}^s + \boldsymbol{I}) \quad \text{and} \quad \boldsymbol{S} = \boldsymbol{S}^{\perp} - \operatorname{grad} \boldsymbol{H}^s, \tag{3.7}$$

when $\boldsymbol{\alpha}$ and $\boldsymbol{S}$ are prescribed, $\boldsymbol{Z}^s$ is determined from

$$\operatorname{div}(\boldsymbol{S}) = \operatorname{div}(\operatorname{grad} \boldsymbol{Z}^s) = -\operatorname{div}(\operatorname{grad} \boldsymbol{H}^s) \tag{3.8}$$

with the value of $\boldsymbol{H}^s = \boldsymbol{0}$ at a single point of the body.

Then, given $\boldsymbol{\alpha}$, $\boldsymbol{S}$, and $\boldsymbol{H}^s$, the i-elastic distortion field $\boldsymbol{W}$ is determined from the system

$$\begin{aligned} \boldsymbol{\alpha} &= (\boldsymbol{S} + \operatorname{grad} \boldsymbol{W}) : \boldsymbol{X} \\ \hat{\boldsymbol{W}} &= \boldsymbol{W} - \boldsymbol{H}^s \\ \operatorname{div}[\boldsymbol{T}(\hat{\boldsymbol{W}})] &= \boldsymbol{0} \\ \boldsymbol{T}\boldsymbol{n} &= \boldsymbol{t} \quad \text{on the boundary,} \end{aligned} \tag{3.9}$$

where $\boldsymbol{T}$ (symmetric) is the stress field depending on $\hat{\boldsymbol{W}}$ (and the unstressed elastic reference from which $\hat{\boldsymbol{W}}$ is measured). $\boldsymbol{t}$ is a prescribed, statically consistent traction field on the boundary of the body. *For all computations in this chapter we will assume* $\boldsymbol{t} = \boldsymbol{0}$*, unless otherwise specified*, but this implies no loss of essential generality in the formulation or in the computational work.

We view the i-elastic distortion $\boldsymbol{W}(\boldsymbol{x})$ as a mapping between a local configuration, around the generic point $\boldsymbol{x}$ in the generally stressed configuration, and a fixed (over all $\boldsymbol{x}$) local stress-free configuration; how the local configuration around each point $\boldsymbol{x}$ of the current configuration is to be understood, at least in principle, is described in Appendix E. In our model there is some freedom in making the choice of the fixed local stress-free configuration; for instance, it may be associated with the stress-free state of a particular

phase of the material, e.g. the high-temperature/symmetry austenite phase. In this paper, we associate it with the stress-free local configuration of a particular point in the body (that would represent one of the phases of the material, say a martensite variant); the point is the one where $\boldsymbol{H}^s$ is specified (see the discussion surrounding (3.8)). The cwi-elastic distortion, $\hat{\boldsymbol{W}}(\boldsymbol{x})$, on the other hand represents the mapping between a local configuration around the generic point $\boldsymbol{x}$ in the stressed configuration and the unstressed configuration it would attain when (conceptually) released from all loads on it. The motivation and detailed discussions for the dependency of $\boldsymbol{T}$ on $\hat{\boldsymbol{W}}$ are presented in Sections 3.5.9 and 3.6. An example for developing intuition for some qualitative differences between these fields in the context of a through and terminating twin boundary is also provided in Appendix E.

We obtain the governing equations for the small deformation case by defining the tensors $\boldsymbol{U}^e$ and $\hat{\boldsymbol{U}}^e$ through the approximations $\boldsymbol{W} = \boldsymbol{I} - \boldsymbol{U}^e$ and $\hat{\boldsymbol{U}}^e := \boldsymbol{I} - \hat{\boldsymbol{W}} = \boldsymbol{U}^e + \boldsymbol{H}^s$ with $\boldsymbol{T} = \boldsymbol{C} : \hat{\boldsymbol{U}}^e$. Substituting in (3.9) and using (3.7) we have

$$\begin{aligned} \operatorname{curl} \hat{\boldsymbol{U}}^e &= \boldsymbol{\alpha} - \boldsymbol{S}^{\perp} : \boldsymbol{X} \\ \operatorname{div}[\boldsymbol{C} : \hat{\boldsymbol{U}}^e] &= \boldsymbol{0} \\ [\boldsymbol{C} : \hat{\boldsymbol{U}}^e]\boldsymbol{n} &= \boldsymbol{t} \ \text{ on the boundary.} \end{aligned} \tag{3.10}$$

with $\boldsymbol{S}^{\perp}$ satisfying (3.6). We refer to the symmetric part of $\hat{\boldsymbol{U}}^e$, $\hat{\boldsymbol{U}}^e_{sym} =: \hat{\boldsymbol{\epsilon}}^e$, as the closest-well elastic strain and the skew-symmetric part, $\hat{\boldsymbol{U}}^e_{skw} =: \hat{\boldsymbol{\Omega}}^e$, as the closest-well elastic rotation tensor. We similarly define the elastic strain $\boldsymbol{\epsilon}^e$ and the elastic rotation $\boldsymbol{\Omega}^e$ tensor fields from $\boldsymbol{U}^e$.

It is important to note that if the defect fields $\boldsymbol{\Pi}$, $\boldsymbol{\alpha}$, and $\boldsymbol{Z}^s$ transform to $\boldsymbol{R\Pi}$, $\boldsymbol{R\alpha}$, and $\boldsymbol{R}\,\boldsymbol{Z}^s$ for a spatially constant (on the current configuration), rotation field $\boldsymbol{R}$ representing a change in the point-wise unstressed elastic reference, then the solution $\boldsymbol{W}$ to $(3.9)_1$ transforms as $\boldsymbol{RW}$ and hence $\hat{\boldsymbol{W}}$ transforms as $\boldsymbol{R}\hat{\boldsymbol{W}}$. The corresponding closest-well elastic distortion field is $\hat{\boldsymbol{F}}^e\boldsymbol{R}^T$ measured from the point-wise rotated, closest-well, unstressed

reference. Since elastic constitutive equations for stress from two different reference configurations, say 1 and 2, necessarily have the property that $\boldsymbol{T}^{(2)}\left(\boldsymbol{F}^{(2)}\right)=\boldsymbol{T}^{(1)}\left(\boldsymbol{F}^{(1)}\right)$, where $\boldsymbol{F}^{(2)}\boldsymbol{G}=\boldsymbol{F}^{(1)}$ and $\boldsymbol{G}$ is the invertible tensor mapping reference 1 to 2 (pointwise), we have $\boldsymbol{T}^{(2)}\left(\boldsymbol{F}^{(2)}\right)=\boldsymbol{T}^{(1)}\left(\boldsymbol{F}^{(2)}\boldsymbol{G}\right)$ $\forall$ invertible $\boldsymbol{F}^{(2)}$, and this implies that, for $\boldsymbol{G}=\boldsymbol{R}$ and 2 representing the rotated unstressed reference, $\boldsymbol{T}^{(2)}\left(\hat{\boldsymbol{W}}^{-1}\boldsymbol{R}^{T}\right)=\boldsymbol{T}^{(1)}\left(\hat{\boldsymbol{W}}^{-1}\right)=:\boldsymbol{T}(\hat{\boldsymbol{W}})$ and therefore the stress prediction on the current configuration from (3.9) is invariant to the choice of unstressed elastic reference.

We will assume $\boldsymbol{Z}^{s}=-\boldsymbol{I}$ for many problems considered in this paper where $\boldsymbol{\alpha}$ and $\boldsymbol{\Pi}$ are prescribed as data. Sections 3.5.9-3.6 are exceptions where $\boldsymbol{\alpha}$ and $\boldsymbol{S}$ are specified. Our model ensures that, at least with respect to the l^2-norm on the space of third-order tensor fields, the stresses generated are only in response to the prescribed g.disclination (and dislocation) density fields, with no other sources involved. It also allows the realistic representation of terminating grain/phase boundaries with an eigenwall field $\boldsymbol{S}$ specified in a layer as in Fig. 3.1, with the concomitant recovery of classical results of defect theory related to dislocation and disclination stress fields. The use of the field $\boldsymbol{Z}^{s}$ ($\boldsymbol{H}^{s}$) is essential for this purpose, as it is impossible to represent a through or terminating grain/phase boundary interface by setting $\boldsymbol{S}=\boldsymbol{S}^{\perp}$, with $\boldsymbol{S}^{\perp}$ determined from the g.disclination density field (possibly vanishing). Details of these situations are discussed in Sections 3.5.9 and 3.6.

3.3.1 Modeling a $\boldsymbol{\Pi}$ field representing an individual g.disclination core

The tensor $\boldsymbol{\Pi}$ for a discrete g.disclination can be defined for prescription as given data as follows. Figure 3.2 shows an eigenwall field $\boldsymbol{S}$ supported in a layer, whose termination represents the g.disclination core. The layer is, in general, 'non-planar' and its termination

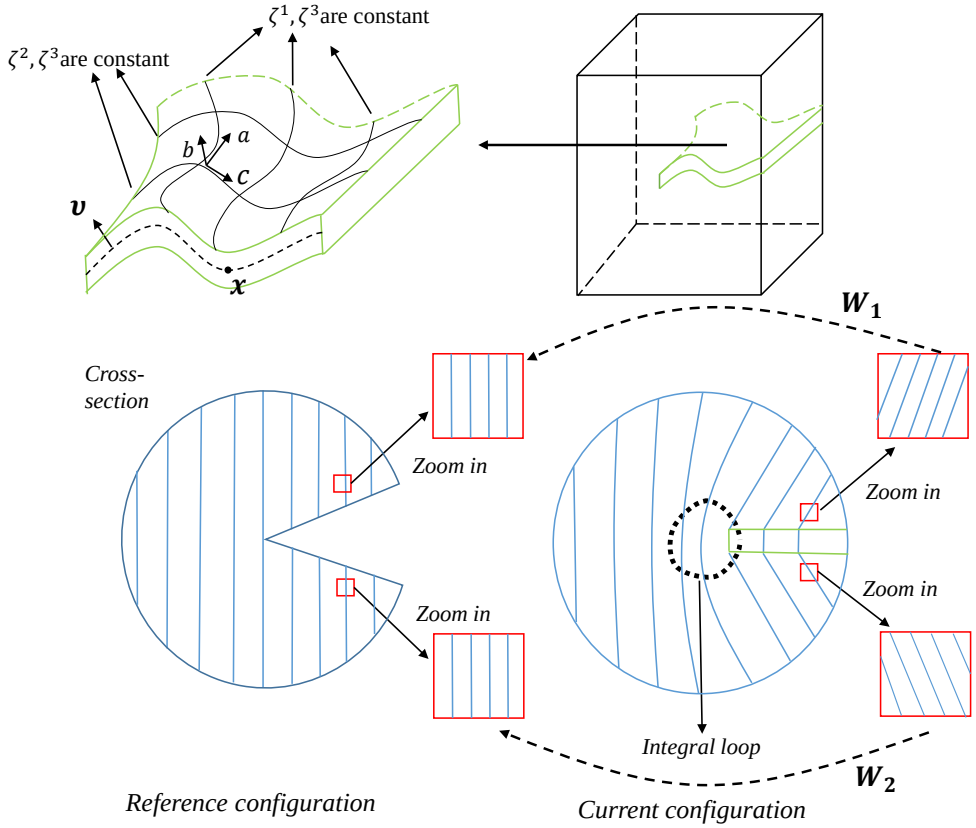

Figure 3.2: *The geometric definition of the layer.* $\boldsymbol{a}$, $\boldsymbol{b}$ *and* $\boldsymbol{c}$ *are natural basis vectors for a parametrization of the layer by coordinates* ξ^2, ξ^3, ξ^1. *The two lower sketches conceptualize the formation of a wedge disclination by the closing and welding of the gap in the unstretched reference configuration to form the stressed current configuration.*

not a straight 'line'. We assume the layer to be amenable to the description

$$\boldsymbol{s}(\xi^1, \xi^2, \xi^3) = \boldsymbol{x}(\xi^1, \xi^2) + \xi^3 \boldsymbol{\nu}(\xi^1, \xi^2), \tag{3.11}$$

where $\boldsymbol{x}$ is the 'mid-surface' of the layer, parametrized by curvilinear coordinates (ξ^1, ξ^2), and $\boldsymbol{\nu}$, the unit normal field to the mid-surface, is defined as

$$\boldsymbol{\nu}(\xi^1, \xi^2) = \frac{\frac{\partial \boldsymbol{x}}{\partial \xi^1} \times \frac{\partial \boldsymbol{x}}{\partial \xi^2}}{\left| \frac{\partial \boldsymbol{x}}{\partial \xi^1} \times \frac{\partial \boldsymbol{x}}{\partial \xi^2} \right|}. \tag{3.12}$$

ξ^3 serves as the remaining coordinate parametrizing the 3-dimensional layer. The parametriza-

tion (in the vicinity of the g.disclination core) is such that the surface $\xi^1 = 0, -\frac{t}{2} \leq \xi^3 \leq \frac{t}{2}$ coincides with the layer termination within the body, and the surfaces $\xi^3 = \pm\frac{t}{2}$ are the top and bottom surfaces of the layer, respectively. The layer mid-surface (and therefore the $\boldsymbol{\nu}$ field), is assumed known (e.g. from observations) for the definition of the $\boldsymbol{S}$ and $\boldsymbol{\Pi}$ fields in this static setting. Denote the i-elastic distortion field (the inverse rotation field in the disclination case) of the upper part as $\boldsymbol{W}_1$; the i-elastic distortion of the lower part is denoted as $\boldsymbol{W}_2$. The thickness of the layer is t in the normal direction to the layer. The eigenwall field $\boldsymbol{S}$ in the layer is defined as

$$\boldsymbol{S} = a(\xi^1)\frac{(\boldsymbol{W}_1 - \boldsymbol{W}_2)}{t} \otimes \boldsymbol{\nu}, \tag{3.13}$$

where $a(\xi^1)$ is a scalar function indicating the longitudinal extent of the core of the g.disclination; a candidate we utilize is

$$a(\xi^1) = \begin{cases} 0 & \xi^1 < 0 \\ \frac{1}{c}\xi^1 & 0 \leq \xi^1 < c \\ 1 & \xi^1 \geq c, \end{cases} \tag{3.14}$$

with c being the core width. The field $\boldsymbol{S}$ is assumed to vanish outside the layer. In general, $\boldsymbol{W}_1$ and $\boldsymbol{W}_2$ could be spatially varying along the longitudinal directions of the layer, while being always uniform in the transverse direction. Here we assume that $\boldsymbol{W}_1$ and $\boldsymbol{W}_2$, viewed as fields in the layer, are constant (In Section 3.5.12.2 we encounter a curved twin boundary of a lenticular inclusion where this is not the case; we comment on this after (3.18)). Then $\boldsymbol{\Pi} = \operatorname{curl} \boldsymbol{S}$ and is nonzero only in the core, given from Appendix F as

$$\boldsymbol{\Pi} = \frac{(\boldsymbol{W}_1 - \boldsymbol{W}_2)}{t} \otimes (\operatorname{grad} a \times \boldsymbol{\nu}) \qquad \text{in the core.} \tag{3.15}$$

As discussed in Appendix F, $\boldsymbol{\Pi}$ has support only in the layer and for a single g.disclination, only in the core.

We note here that defining $\boldsymbol{\Pi}$ is essential for many problems where the notion of a g.disclination with a prescribed strength makes sense without the notion of a corresponding physical interface, e.g. a pentagon-heptagon pair in a graphene monolayer, where the strength can be inferred without recourse to a distortion discontinuity. In situations where the axis of a g.disclination core cylinder is a general space curve, the procedure we have outlined above involving a layer field is still useful for defining the corresponding $\boldsymbol{\Pi}$ field.

The strength of a single disclination defined by $\boldsymbol{\Pi}$ given in (3.15) is obtained by integrating $\boldsymbol{\Pi}$ over any area patch A enclosing the core, such as any whose bounding curve is given by the black dashed line in Figure 3.2:

$$\boldsymbol{D} := \int_A \boldsymbol{\Pi} d\boldsymbol{a} = \int_{core} \boldsymbol{\Pi} d\boldsymbol{a}, \tag{3.16}$$

and as shown in Appendix F this is given by $\boldsymbol{W}_1 - \boldsymbol{W}_2$, which also corresponds to the line integral of $\boldsymbol{Y}$ on any circuit encircling the core cylinder, since $curl\boldsymbol{Y} = \boldsymbol{\Pi}$. For a planar layer with $\boldsymbol{\nu} = \boldsymbol{e}_2$ and $\xi^1 = x_1$,

$$\boldsymbol{\Pi} = \frac{\boldsymbol{W}_1 - \boldsymbol{W}_2}{ct} \otimes \boldsymbol{e}_3, \tag{3.17}$$

and choosing the area patch to be one with normal in the $\boldsymbol{e}_3$ direction, we have

$$D_{ij} = ct\frac{(W_1 - W_2)_{ij}}{ct} = (W_1 - W_2)_{ij}, \tag{3.18}$$

on the orthonormal basis $(\boldsymbol{e}_i), i = 1, 2, 3$.

If $(\boldsymbol{W}_1 - \boldsymbol{W}_2)$ is not a constant along the interface, then there is an additional contribution to $\boldsymbol{\Pi}$, as can be seen from the derivation of (F.1).

3.3.2 Disclinations in small and finite deformation theory

Consider an interface across which $\boldsymbol{W}_1 = \boldsymbol{R}_1$ and $\boldsymbol{W}_2 = \boldsymbol{R}_2$ are rotation tensors. For a given rotation tensor $\boldsymbol{R}$ corresponding to a rotation by an angle θ about an axis $\boldsymbol{l}$, one associates a skew tensor $\mathbb{W}$, which we shall refer to as the spin of the rotation in this paper, and its axial vector $\boldsymbol{w}$ such that

$$\boldsymbol{R}\boldsymbol{a} \approx \boldsymbol{a} + \mathbb{W}\boldsymbol{a} = \boldsymbol{a} + \boldsymbol{w} \times \boldsymbol{a}$$

for all vectors $\boldsymbol{a}$ in the plane normal to $\boldsymbol{l}$ when θ is small, as shown in Fig. 3.3.

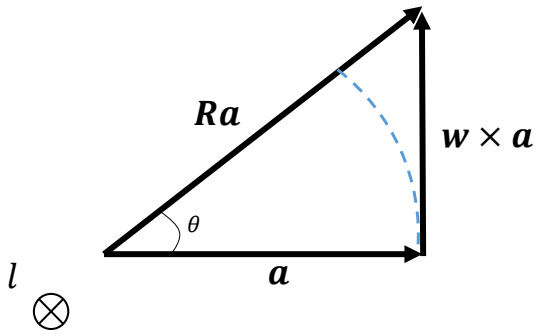

Figure 3.3: *The difference in the action of a finite rotation, $\boldsymbol{R}$, and its spin, $\boldsymbol{w}$, with axis $\boldsymbol{l}$ on a vector $\boldsymbol{a}$.*

The axial vector $\boldsymbol{w}$ is given by

$$\boldsymbol{w} = \tan\theta\, \boldsymbol{l},$$

and it follows that in an orthonormal basis

$$\mathbb{W}_{ij} = e_{imj} l_m \tan\theta.$$

For $\boldsymbol{l} = \boldsymbol{e}_3$, the only non-zero components of $\mathbb{W}$ are $\mathbb{W}_{21} = \tan\theta = -\mathbb{W}_{12}$.

Thus the small deformation approximation of the difference of two rotation tensors $\boldsymbol{R}_1$

and $\boldsymbol{R}_2$ corresponding to angles and axes of rotation $(\theta_1, \boldsymbol{l}_1)$ and $(\theta_2, \boldsymbol{l}_2)$ is given, in the first instance, by $\mathbb{W}_1 - \mathbb{W}_2$ with components

$$(\mathbb{W}_1)_{ij} - (\mathbb{W}_2)_{ij} = e_{imj} \left[(l_1)_m \tan\theta_1 - (l_2)_m \tan\theta_2 \right].$$

In linear disclination theory [DeW73a], the plastic bend-twist tensor arises when the skew-symmetric part of the plastic distortion tensor $\mathbb{W}^p$, which we shall refer to here as the plastic spin, exhibits discontinuities such that its gradient field is not well-defined in the whole body as integrable functions. DeWit [DeW73a] replaces the gradient of the axial vector of the plastic spin in such circumstances by the *plastic bend-twist* tensor, $\boldsymbol{\kappa}^P$, which is not irrotational (i.e. *curl*-free) in the whole domain to reflect the possibility of the singularities of the plastic spin field, even when $\boldsymbol{\kappa}^P$ is smooth. DeWit further defines the *Frank vector* of a closed curve ∂A to be

$$\Omega_q = -\int_{\partial A} \kappa^P_{kq} dx_k = -\int_A \epsilon_{pmk} \kappa^P_{kq,m} n_p da,$$

where A is any area patch whose boundary is ∂A, and $\boldsymbol{n}$ is the unit normal field on A.

For a single disclination, $\boldsymbol{\Omega} \neq \boldsymbol{0}$ in the core. Following the arguments in Chapter 2, one can create a non-simply connected domain by excluding the core cylinder/curve from the overall simply-connected body. By making an appropriate cut one can then render the body without the core simply-connected again (but not continuously deformable to the original body with the core). On this cut-induced simply connected domain one can construct a spin field $\mathbb{W}$, the gradient of whose axial vector field matches the given plastic bend-twist field, even though every cut-surface corresponds, in general, to a different spin field. However, for $\boldsymbol{\Omega} \neq \boldsymbol{0}$, each such spin field displays a *constant* jump (discontinuity) across its corresponding cut-surface and, moreover, this jump is constant regardless of the spin field (and corresponding cut-surface) involved. Let us denote this constant jump for

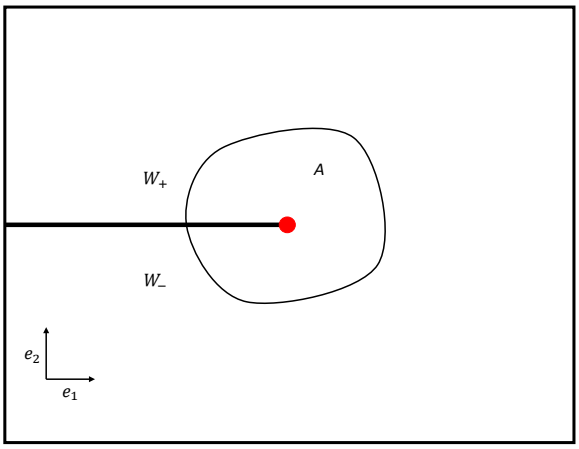

Figure 3.4: *A single disclination in the body with two different rotation skew matrices,* $\boldsymbol{W}_+$ *and* $\boldsymbol{W}_-$*. 'A' is an area patch enclosing the core.*

a single disclination as $[\![\mathbb{W}]\!]$ and it can be shown, following the arguments in Chapter 2, that

$$\Omega_q = -\frac{1}{2}\epsilon_{lqr}[\![\mathbb{W}]\!]_{rl}. \tag{3.19}$$

As illustration of these concepts, consider a single, straight, disclination through the plane of the paper as shown in Figure 3.4. The red point is the disclination core. For the cut-surface shown, $\mathbb{W}_+$ and $\mathbb{W}_-$ represent the limiting values, from the top and bottom respectively, of the constructed spin field $\mathbb{W}$ on the surface and they have the same rotation axis ($\boldsymbol{e}_3$). Assuming the Frank vector is specified as $|\boldsymbol{\Omega}|\boldsymbol{e}_3$, (3.19) implies

$$|\boldsymbol{\Omega}| = \tan\theta_1 - \tan\theta_2 \approx \tan(\theta_1 - \theta_2) \approx \theta_1 - \theta_2, \quad \text{when} \quad |\theta_1| \ll 1, |\theta_2| \ll 1. \tag{3.20}$$

Thus, when the angles θ_1 and θ_2 are small, then the magnitude of DeWit's Frank vector may be interpreted as the *misorientation* across any interface terminated by the disclination.

Finally, an observation on stress fields of single disclinations (involving large rotations, in general) is in order. Due to the lack of full rotational invariance of the linear elastic stress constitutive assumption, it is natural to expect large differences between results of

small and finite deformation theory for single disclinations with large misorientations. This can be appreciated by noting that if $\boldsymbol{T}$ is the nonlinear elastic stress response function out of some reference configuration

$$\boldsymbol{T}(\boldsymbol{F}) = \boldsymbol{T}(\boldsymbol{I}) + D\boldsymbol{T}(\boldsymbol{I})[\boldsymbol{F} - \boldsymbol{I}] + H.O.T,$$

where $H.O.T$ stands for higher order terms and $D\boldsymbol{T}$ is the derivative of the stress function, and we assume that $\boldsymbol{F}$ is measured from a stress-free reference. Let $D\boldsymbol{T}(I) = \boldsymbol{C}$, the 4^{th}-order tensor of elastic moduli (with minor symmetries). Frame-indifference implies that $\boldsymbol{T}(\boldsymbol{R}) = \boldsymbol{0}$ for all rotations $\boldsymbol{R}$. Then it is valid to write

$$\boldsymbol{0} = \boldsymbol{T}(\boldsymbol{R}) = \boldsymbol{C}[\boldsymbol{R} - \boldsymbol{I} - \mathbb{W}] + \mathbf{H.O.T.}, \tag{3.21}$$

where $\mathbb{W}$ is the spin of $\boldsymbol{R}$. In problems where the elastic distortion field attempts to attain locally large rotations (e.g. the field of a single disclination), it is clear that the linear elastic stress-approximation to such deformations, given by the first term on the rhs of (3.21), degrades as the angle of rotation increases. This is so since the argument involves (spurious) stretching of vectors (see Fig. 3.3) and therefore, strain, and this is sensed by the linear elastic moduli.

3.4 Numerical scheme

The standard Galerkin method is not adequate for solving the div-curl system (3.6) [Jia98]. Instead, we utilize the Least Squares Finite Element Method [Jia98] adapting the ideas in [RA05] for calculating fields of line defects in solids. The scheme for solving the entire system (3.9) is divided into three steps.

If $\boldsymbol{\Pi}$ is prescribed as data, the first step is to solve for the incompatible part $\boldsymbol{S}^{\perp}$ given

the g.disclination density field $\boldsymbol{\Pi}$. If $\boldsymbol{S}$ is prescribed as data, the first step is to solve for the compatible part $\boldsymbol{Z}^s$ given the eigenwall field $\boldsymbol{S}$. The second step is to solve for the i-elastic 1-distortion tensor $\boldsymbol{W}$ from (3.9), with $\boldsymbol{H}^s = \boldsymbol{0}$ and $\boldsymbol{S} := \boldsymbol{S}^\perp$ from the first step substituted in $(3.9)_1$ if $\boldsymbol{\Pi}$ is data. In the second step, different numerical schemes are applied to solve for force equilibrium $(3.9)_{3,4}$ depending on whether a 'small' or 'finite' deformation result is desired. In the following, the symbol $\boldsymbol{\delta}(\cdot)$ represents a variation associated with the field $(\cdot)$ in a class of functions.

When $\boldsymbol{\Pi}$ is prescribed, the equations to be solved for calculating $\boldsymbol{S}^\perp$ are

$$\begin{aligned} \operatorname{curl} \boldsymbol{S}^\perp &= \boldsymbol{\Pi} \\ \operatorname{div} \boldsymbol{S}^\perp &= \boldsymbol{0} \\ \text{with } \boldsymbol{S}^\perp \boldsymbol{n} &= \boldsymbol{0} \text{ on the boundary,} \end{aligned}$$

where $\boldsymbol{\Pi}$ is a given 3rd-order tensor field. In an orthonormal basis, the weak form for the above equations is given by

$$\int_V e_{ijk} \delta S^\perp_{rsk,j} \left(e_{imn} S^\perp_{rsn,m} - \pi_{rsi} \right) dv + \int_V \delta S^\perp_{isj,j} S^\perp_{ism,m} dv = 0. \tag{3.22}$$

The essential boundary condition $\boldsymbol{S}^\perp \boldsymbol{n} = \boldsymbol{0}$ needs to be imposed. Also, (3.22) should hold for all possible variations $\boldsymbol{\delta S}^\perp$ satisfying the essential boundary condition. The variational statement is obtained by looking for critical points of the least squares functional

$$\int_V \left(\frac{1}{2} \left\| \operatorname{curl} \boldsymbol{S}^\perp - \boldsymbol{\Pi} \right\|^2 + \frac{1}{2} \left\| \operatorname{div} \boldsymbol{S}^\perp \right\|^2 \right) dv.$$

When $\boldsymbol{S}$ is prescribed, the equation for calculating $\boldsymbol{H}^s$ is

$$-\operatorname{div}(\operatorname{grad} \boldsymbol{H}^s) = \operatorname{div}(\boldsymbol{S}),$$

where $\boldsymbol{S}$ is the prescribed eigenwall field and with $\boldsymbol{H}^s = \boldsymbol{0}$ prescribed at one point of the body. The weak form for the above equation is given by

$$\int_V \delta H^s_{ij,k} \left(H^s_{ij,k} + S_{ijk} \right) dv = \boldsymbol{0}. \tag{3.23}$$

Noting that regardless of the prescribed data we now have $\boldsymbol{S}$ and $\boldsymbol{H}^s$ defined by the above rules, the following equations need to be solved in the second step:

$$\begin{aligned} \boldsymbol{A} &:= \boldsymbol{S} : \boldsymbol{X} - \boldsymbol{\alpha} \\ \operatorname{curl} \boldsymbol{W} &= \boldsymbol{A} \\ \operatorname{div} \left[\boldsymbol{T} \left(\hat{\boldsymbol{W}} \right) \right] &= \boldsymbol{0}. \end{aligned}$$

where $\boldsymbol{T}(\hat{\boldsymbol{W}})$ represents the stress response with $\hat{\boldsymbol{W}} = \boldsymbol{W} - \boldsymbol{H}^s$. To solve this system, the small and finite deformation cases are separately dealt with.

3.4.1 Small deformation

On writing $\boldsymbol{W} \approx \boldsymbol{I} - \boldsymbol{U}^e$ and expressing $\boldsymbol{U}^e = \boldsymbol{\chi} + \operatorname{grad} \boldsymbol{f}$ and $\boldsymbol{T} = \boldsymbol{C}(\boldsymbol{U}^e + \boldsymbol{H}^s)$, $\boldsymbol{\chi}$ is solved from the following equations:

$$\begin{aligned} \operatorname{curl} \boldsymbol{\chi} &= -\boldsymbol{A} \\ \operatorname{div} \boldsymbol{\chi} &= \boldsymbol{0} \\ \boldsymbol{\chi} \boldsymbol{n} &= \boldsymbol{0} \quad \text{on the boundary,} \end{aligned}$$

where $\boldsymbol{n}$ is the unit normal vector on the boundary. The weak form of these equations is

$$\int_V e_{ijk} \delta \chi_{rk,j} \left(e_{imn} \chi_{rn,m} + A_{ri} \right) dv + \int_V \delta \chi_{ij,j} \chi_{im,m} dv = 0, \tag{3.24}$$

with boundary condition $\chi_{ij}n_j = 0$. In the small deformation case, the governing equation for $\boldsymbol{f}$ is given by

$$\operatorname{div}\left[\boldsymbol{C} : (\operatorname{grad}\boldsymbol{f} + \boldsymbol{\chi} + \boldsymbol{H}^s)\right] = \boldsymbol{0}, \tag{3.25}$$

where $\boldsymbol{C}$ is the possibly anisotropic, 4-order tensor of linear elastic moduli. Its corresponding weak form is

$$\int_V \delta f_{i,j}\left(C_{ijkl}f_{k.l} + C_{ijkl}\chi_{kl} + C_{ijkl}H^s_{kl}\right) dv - \int_{\partial V_t} \delta f_i t_i da = 0 \tag{3.26}$$

where ∂V_t represents the set of point on the boundary where the tractions t_i are specified. Also, the standard essential boundary condition on $\boldsymbol{f}$ are implemented to remove the rigid deformation mode. Given the generalized disclination density $\boldsymbol{\Pi}$ and the dislocation density $\boldsymbol{\alpha}$, the discretized weak forms (3.22), (3.24), and (3.26) yield the static solutions of a g.disclination problem for the small deformation case. When $\boldsymbol{S}$ and $\boldsymbol{\alpha}$ are prescribed, (3.23), (3.24), and (3.26) form the corresponding governing equations.

3.4.2 Finite deformation

In the finite deformation case one needs to solve $\hat{\boldsymbol{\chi}}$ from

$$\begin{aligned} \operatorname{curl}\hat{\boldsymbol{\chi}} &= \boldsymbol{A} \\ \operatorname{div}\hat{\boldsymbol{\chi}} &= \boldsymbol{0} \\ \hat{\boldsymbol{\chi}}\boldsymbol{n} &= \boldsymbol{0} \qquad \text{on the boundary,} \end{aligned}$$

see [AR06]. The corresponding weak form is [Pur09]

$$\int_B e_{ijk}\delta\hat{\chi}_{rk,j}\left(e_{imn}\hat{\chi}_{rn,m} - A_{ri}\right) dv + \int_B \delta\hat{\chi}_{ij,j}\hat{\chi}_{im,m} dv = 0, \tag{3.27}$$

and the boundary condition $\hat{\chi}_{ij} n_j = 0$ for all $i = 1, 2, 3$ on the boundary, $\boldsymbol{n}$ being the normal vector on the boundary. In addition, we need to solve the following equations:

$$\begin{aligned} \boldsymbol{W} &= \hat{\boldsymbol{\chi}} + \operatorname{grad} \hat{\boldsymbol{f}} \\ \hat{\boldsymbol{W}} &= \boldsymbol{W} - \boldsymbol{H}^s \\ \boldsymbol{E}^e &= \frac{1}{2}\left(\hat{\boldsymbol{W}}^{-T}\hat{\boldsymbol{W}}^{-1} - \boldsymbol{I}\right) \\ \boldsymbol{T} &= \hat{\boldsymbol{W}}^{-1}\left[\boldsymbol{C} : \boldsymbol{E}^e\right]\hat{\boldsymbol{W}}^{-T} \\ \operatorname{div} \boldsymbol{T} &= \boldsymbol{0}, \end{aligned} \tag{3.28}$$

where $(3.28)_3$ represents a St. Venant-Kirchhoff constitutive assumption for the stress, with $\boldsymbol{C}$ being the linear elastic moduli for the material(our basic methodology is, of course, not restricted to this choice). Also, essential boundary conditions on $\hat{\boldsymbol{f}}$ are required to eliminate the rigid deformation mode.

Since the governing equation div $\boldsymbol{T} = \boldsymbol{0}$ is nonlinear in $\hat{\boldsymbol{f}}$, we apply the Newton Raphson method to solve the problem utilizing the scheme in [Pur09]. We find that the initial guess for $\hat{\boldsymbol{f}}$ is crucial for success in solving problems of g.disclination theory. One contribution of this work is the development of a systematic strategy for generating this initial guess, as described in the following.

The initial guess for $\hat{\boldsymbol{f}}$ is denoted as $\hat{\boldsymbol{f}}_0$. A good candidate for $\hat{\boldsymbol{f}}_0$ is based on the solution $\boldsymbol{f}$ from the small deformation theory. Namely, to obtain $\hat{\boldsymbol{f}}_0$, we solve $\boldsymbol{f}$ from the small deformation theory equations exactly as given in Section 3.4.1. Then we set

$$\hat{\boldsymbol{f}}_0 = \boldsymbol{X} - \boldsymbol{f} \quad \text{as the initial guess for } \hat{\boldsymbol{f}} \text{ in the finite deformation theory,}$$

following the justification in [AR06, Sec. 5, p.1707].

With this initial guess for $\hat{\boldsymbol{f}}_0$ and the solution for $\hat{\boldsymbol{\chi}}$ obtained from solving (3.27), we solve the weak form of $(3.28)_4$ for $\hat{\boldsymbol{f}}$. The discrete residual is formed from the variational

statement for $(3.28)_4$,

$$\int_B \delta \hat{f}_{i,j} T_{ij} dv = 0, \tag{3.29}$$

and is given by

$$R_i^A = \int_B T_{ij} \frac{\partial N^A}{\partial x_j} dv,$$

where N^A is the shape function corresponding to the finite element mesh node A, and R_i^A is the discrete residual for the (A, i) degree of freedom.

The tangent stiffness for the problem is obtained by taking a variation of the residual (3.29) in a direction $d\hat{\boldsymbol{f}}$; the discrete form of the Jacobian matrix corresponding to the degree-of-freedom pair $\{(A, a), (B, b)\}$ is

$$J_{ab}^{AB} = \int_B \frac{\partial N^A}{\partial x_j} \frac{\partial T_{aj}}{\partial F_{mn}^e} \frac{\partial F_{mn}^e}{\partial \hat{W}_{ru}} \frac{\partial \hat{W}_{ru}}{\partial (grad \hat{f})_{bc}} \frac{\partial N^B}{\partial x_c} dv.$$

To summarize, the algorithm for the finite deformation scheme is

- Make a guess for $\hat{\boldsymbol{f}}_0$. $\hat{\boldsymbol{f}}_0$ is based on the solution $\boldsymbol{f}$ from small deformation theory, given as $\hat{\boldsymbol{f}}_0 = \boldsymbol{X} - \boldsymbol{f}$.
- Solve for $\hat{\boldsymbol{\chi}}$.
- Solve for $\hat{\boldsymbol{f}}$ using the equilibrium equation, div $\boldsymbol{T} = \boldsymbol{0}$. This equation is nonlinear, and solved using the Newton-Raphson method.
- Obtain $\hat{\boldsymbol{W}} = \hat{\boldsymbol{\chi}} + \text{grad}\, \hat{\boldsymbol{f}} - \boldsymbol{H}^s$; $\boldsymbol{E}^e = \frac{1}{2}(\hat{\boldsymbol{W}}^{-T}\hat{\boldsymbol{W}}^{-1} - \boldsymbol{I})$; $\boldsymbol{T} = \hat{\boldsymbol{W}}^{-1}[\boldsymbol{C} : \boldsymbol{E}^e]\hat{\boldsymbol{W}}^{-T}$.

3.5 Applications

In this section, an extensive list of model problems are solved to demonstrate the capability and features of our theoretical-computational model. Most problems are solved within both the small and finite deformation settings. In all 2D problems, the body is meshed with quadriltateral, bilinear elements. In this work, all stress fields are non-dimensionalized

by the shear modulus G. All length variables are non-dimensionalized by the core/layer height t. Unless otherwise specified, the elasticity tensor $\boldsymbol{C}$ is assumed to be isotropic with $E = 2.6G$, $\nu = 0.3$, where E is the Young's Modulus, G is shear modulus and ν is the Poisson's ratio. For all but two of the problems dealt with in this work, $\boldsymbol{\alpha}$ is set zero; the use of dislocations is explicitly mentioned, when it arises. The calculations in this section are conducted within the PETSc package on a 16-core computer.

In all figures in this work the horizontal axis represents the $\boldsymbol{e}_1$ direction and the vertical axis represents the $\boldsymbol{e}_2$ direction, unless otherwise specified. For all disclination problems treated here, given the misorientation angle θ, the eigenwall field $\boldsymbol{S}$ and the g.disclination density field $\boldsymbol{\Pi}$ are defined from (3.13) and (3.15) in Section 3.3.1, with $\boldsymbol{W}_2$ assumed as $\boldsymbol{I}$ and $\boldsymbol{W}_1$ to be

- $$\begin{bmatrix} 1 & tan\theta \\ -tan\theta & 1 \end{bmatrix}$$

  for the small deformation case and

- $$\begin{bmatrix} cos\theta & sin\theta \\ -sin\theta & cos\theta \end{bmatrix}$$

  for finite deformation.

We discuss a further point related to the definitions of $\boldsymbol{S}$ and $\boldsymbol{\Pi}$ in Sec. 3.5.2 after the discussion of the Eshelby cut-weld problem.

The stress comparisons between the small deformation and the finite deformation settings in this section are for all stress components followed the identical definition of the stress difference given in (3.1). Denoting $\boldsymbol{\sigma}_s$ as the stress field from the small deformation setting and $\boldsymbol{\sigma}_f$ as the stress field from the finite deformation setting, the difference of the stress fields between the small deformation setting and the finite deformation setting is

denoted as $\delta\sigma_{s,f}$.

3.5.1 A single disclination viewed as an Eshelby cut-and-weld problem

The stress field of a single disclination can be interpreted as a non-standard problem of nonlinear elasticity by adapting Eshelby's cut-and-weld procedures [Esh57, Esh56]. As will be evident, this is certainly not the most efficient methodology for dealing with disclinations, in particular, when they appear in collections of more than one; nevertheless, the example helps to develop intuition and we describe below the basis of our computation of the analogy.

With reference to Fig. 3.5 we first consider the following thought experiment. In Step 1 the edges of a gap wedge (the green lines in Figure 3.5(a)) in $C1$, a stress-free configuration, are brought together to close the gap, resulting in the configuration $C2$ (Figure 3.5(b)). This is achieved by applying appropriate displacement boundary conditions to the edges of the gap wedge. Clearly, non-zero (reaction) tractions exist along both adjoining edges on $C2$. In Step 2, imagine welding the edges to generate the configuration $\widetilde{C2}$ and removing from them the reaction tractions generated in Step 1, letting the welded body relax to the configuration $C3$. Concretely, the act of welding generating $\widetilde{C2}$ amounts to thinking that all further deformations of $C2$ are continuous on the surface in it along which the adjoining edges overlap. $C2$ has 'two additional' boundary surfaces than $\widetilde{C2}$. The act of relaxation implies that the stressed configuration $\widetilde{C2}$, now connected along the surface formed by the overlapping edges, is subjected to no internal, singular body force fields. Due to the removal of the reaction tractions on the edges, the stress field arising from the deformation in Step 1 no longer satisfies equilibrium on $\widetilde{C2}$, but the body now can only deform through a compatible deformation of $\widetilde{C2}$ to achieve the configuration $C3$ where it is in (force) equilibrium with no applied tractions or body forces.

We approximate the solution of the above problem with the algorithms described in Section 3.4 as follows. We assume the configuration $\widetilde{C2}$ as known (the domain in Fig. 3.6(a)) and first determine the stress-free configuration $C1$. This is done by viewing the intersection of the positive x-axis and the body as two surfaces on which are applied appropriate Dirichlet boundary conditions to represent the (inverse) deformation of these surfaces to their positions on the otherwise unknown unstressed reference configuration $C1$. On the rest of the boundary, traction-free boundary conditions are imposed. The solution is obtained by solving (3.28) for $\hat{\boldsymbol{f}}$ with $\hat{\boldsymbol{\chi}} = \boldsymbol{0}$ and $\boldsymbol{H}^s = \boldsymbol{0}$. Let the deformation gradient of $C1$ with respect to $C2$, the latter with the slit, be denoted as $\boldsymbol{W}^{(1)}$. Let the continuous deformation from $\widetilde{C2}$ to the unknown configuration $C3$ be denoted as $\boldsymbol{g}$ and the inverse of its deformation gradient as $\boldsymbol{W}^{(2)}$. Then, defining grad $\hat{\boldsymbol{f}}$ as $\text{grad}_3\ \hat{\boldsymbol{f}} = \boldsymbol{W}^{(1)}(\text{grad}_2\ \boldsymbol{g})^{-1} = \boldsymbol{W}^{(1)}\boldsymbol{W}^{(2)}$, we solve (3.28) for $\boldsymbol{g}$ with $\hat{\boldsymbol{\chi}} = \boldsymbol{0}$ and $\boldsymbol{H}^s = \boldsymbol{0}$; the subscripts 3 and 2 are included to indicate the fact that the spatial derivatives are w.r.t the configurations $C3$ and $\widetilde{C2}$, respectively, and the div in (3.28) is to be understood as div_3 as well. As this is simply a motivational example, in the solutions shown in Fig. 3.6(a), we assume for simplicity that $div_3 \approx div_2$ which may be justified for $|grad_2\, \boldsymbol{g} - \boldsymbol{I}| \ll 1$ (in the context of nonlinear finite element computations, this approximation is not essential in any way).

Figure 3.6(a) shows the σ_{11} field of a 45° positive disclination computed from the Eshelby process described above; the Dirichlet b.c. in Step 1 corresponds to the geometry of setting up a 45° gap-wedge between C1 and C2. The stress field σ_{11} of a disclination of the same strength on the configuration C2 is computed by setting up the g.disclination density field according to (3.18).

The system (3.28) is solved with $\boldsymbol{Z}^s = \boldsymbol{0}$ and $div = div_2$ and the result is shown in Figure 3.8(b). Figure 3.6(b) shows the difference $\delta\sigma_{e,g}$ following the definition in (3.1), where the subscript e denotes the stress field from the Eshelby process and the subscript g denotes the stress field from g.disclination model. The maximum of $\delta\sigma_{e,g}$ is less than 5%.

We note here that both the Eshelby cut-weld problem and the g.disclination problem

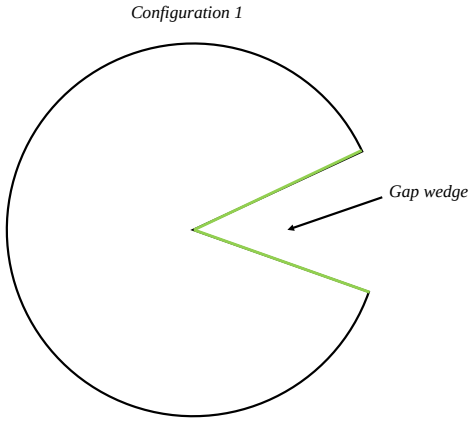

(a) Configuration C1 with a gap wedge.

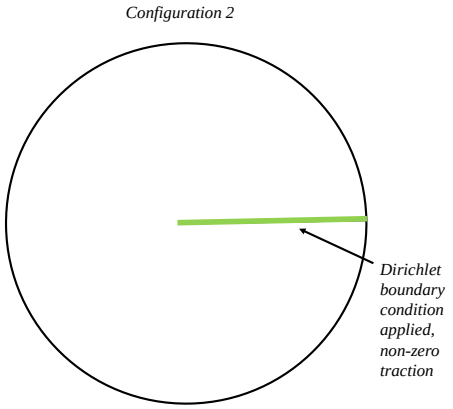

(b) Configuration C2 with a closed wedge. The configuration after welding the two edges is denoted as $\widetilde{C2}$.

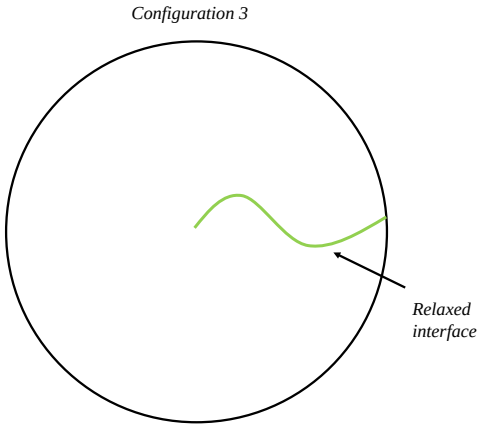

(c) Schematic of possible configuration C3 after welding the wedge and relaxing the body.

Figure 3.5: *An Eshelby cut-weld process to form a single positive disclination. After applying Dirichlet boundary conditions, the gap wedge in* $C1$ *is closed and the resultant traction along the interface in* $C2$ *is non-zero. The two edges are welded to generate the configuration* $\widetilde{C2}$*.* $C3$ *is attained by applying the negative of the obtained resultant traction along the interface on* $\widetilde{C2}$ *and solving for equilibrium of forces.*

are solved on a FE mesh with the same refinement and cannot represent singularities. It is most likely that the exact solution for the Eshelby cut-weld problem actually has a stress singularity at the origin which would be evident with mesh refinement. On the other hand, the g.disclination problem of the same strength does not have a singularity due to the definition of a well-defined core defined by the parameter c (that is expected to emerge in more comprehensive modeling from energetics). The far-field correspondence of the results however is expected to remain as shown in Fig. 3.6(b).

3.5.2 Approximation in $\boldsymbol{S}$ prescription

The considerations above related to the Eshelby cut-weld problem also make clear an important issue in the definition of the strength of a disclination; namely, that the definition of the difference $(\boldsymbol{W}_1 - \boldsymbol{W}_2)$ in the strength of a g.disclination in (3.15), (3.18), strictly speaking, cannot simply be achieved from the knowledge of the geometry of the gap/overlap wedge to be eliminated. Instead, it also requires knowledge of the additional tensor field $\boldsymbol{W}^{(2)}$ along the 'weld' surface. In principle, this is not a problem when physical observations are at hand defining the details of the interface and the question is to compute the elastic fields on the whole body, or when a full problem of evolution is solved, in which case the g.disclination density $\boldsymbol{\Pi}$, the eigenwall field $\boldsymbol{S}$, and their elastic fields are predicted quantities. Denote the (geometrically, or otherwise) inferred i-elastic distortion fields across the interface as $\boldsymbol{W}_1^i$ and $\boldsymbol{W}_2^i$. Then we have

$$\boldsymbol{W}_1 - \boldsymbol{W}_2 = (\boldsymbol{W}_1^i - \boldsymbol{W}_2^i)\boldsymbol{W}^{(2)}.$$

On defining $\varDelta\boldsymbol{W} := \boldsymbol{W}_1 - \boldsymbol{W}_2$ and $\varDelta\boldsymbol{W}^i := \boldsymbol{W}_1^i - \boldsymbol{W}_2^i$, we have

$$\varDelta\boldsymbol{W} - \varDelta\boldsymbol{W}^i = \varDelta\boldsymbol{W}^i(\boldsymbol{W}^{(2)} - \boldsymbol{I}).$$

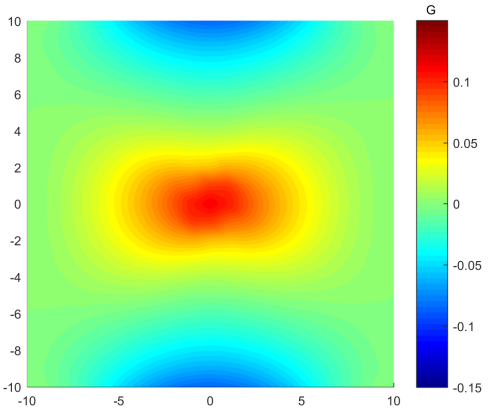

(a) Stress field of the 'Eshelby disclination' in the finite deformation setting.

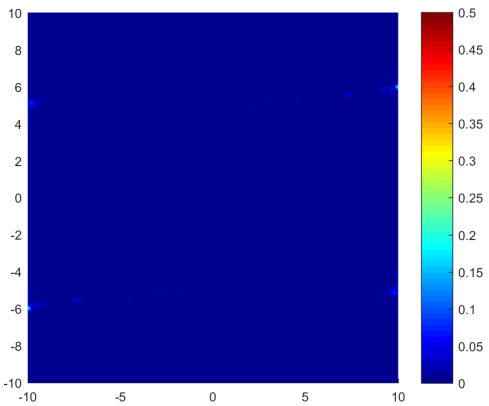

(b) $\delta\sigma_{e,g}$ between Eshelby process and the g.disclination model.

Figure 3.6: *Stress field σ_{11} for a single disclination viewed as an Eshelby process in the finite deformation setting. The maximum of $\delta\sigma_{e,g}$ is less than 5%.*

In most problems solved in this paper, we assume the $\boldsymbol{W}^{(2)}$ field to be approximately the identity tensor for the purpose of *defining* the g.disclination strength, the eigenwall fields and the dislocation density along interfaces (that serves as specified data), and approximate $\Delta\boldsymbol{W}$ as $\Delta\boldsymbol{W}^i$.

3.5.3 Field of a single disclination: comparison with the classical theory

In the linear elastic, small deformation theory [DeW73c], the 2-d stress field at $\boldsymbol{x}$ for a straight disclination along the x_3 direction passing through the coordinate origin is given as

$$\begin{aligned}
\sigma_{11} =& \frac{G\Omega_3}{2\pi(1-\nu)}\left[\ln\rho + \frac{x_2^2}{\rho^2} + \frac{\nu}{1-2\nu}\right] \\
\sigma_{22} =& \frac{G\Omega_3}{2\pi(1-\nu)}\left[\ln\rho + \frac{x_1^2}{\rho^2} + \frac{\nu}{1-2\nu}\right] \\
\sigma_{12} =& -\frac{G\Omega_3 x_1 x_2}{2\pi(1-\nu)\rho^2},
\end{aligned}$$

where $\rho = \sqrt{x_1^2 + x_2^2}$. With reference to Figure 3.4, and a misorientation angle θ of 5° , we have

$$\boldsymbol{\Omega} = 0.0875\boldsymbol{e}_3, \tag{3.30}$$

from (3.20).

The g.disclination density is defined from (3.17) as

$$\boldsymbol{\Pi} = \begin{cases} \frac{\Delta W_{ij}}{ct}\boldsymbol{e}_i \otimes \boldsymbol{e}_j \otimes \boldsymbol{e}_3 & \text{where } |x_1| \leq \frac{c}{2} \text{ and } |x_2| \leq \frac{t}{2} \\ \mathbf{0} & \text{otherwise,} \end{cases} \tag{3.31}$$

where $i, j = 1, 2$, c is the core width, t is the layer thickness and ΔW is given as

$$\begin{bmatrix} 0 & 0.0875 \\ -0.0875 & 0 \end{bmatrix}.$$

The size of the body is 10×10 and the size of the disclination core is 0.5×0.5 (in units of t, the core height). To compare our numerical solution with DeWit's infinite-medium solutions, the following Neumann boundary conditions are utilized. Considering the body in our model as a patch in an infinite domain, the traction field on the boundary of the corresponding patch from the infinite-medium solution is applied. Figure 3.7(a) is the stress field σ_{11} from the DeWit solution with Frank vector (3.30) and Figure 3.7(b) is the stress field σ_{11} from small deformation g.disclination theory with the g.disclination density (3.31). Here, we denote $\boldsymbol{\sigma}_a$ as the stress field from the analytical solution and $\boldsymbol{\sigma}_g$ as the stress field from the g.disclination model. The difference between the analytical solution and the g.disclination solution is denoted as $\delta\sigma_{a,g}$ following the definition (3.1).

Figure 3.7(c) shows the defined difference of the stress field; the computed stress field from g.disclination theory matches with the DeWit solution very well. Outside the core, the defined difference is less than 1%.

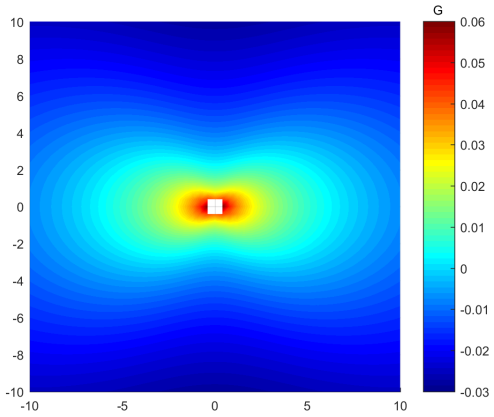

(a) σ_{11} for a single disclination from classical linear elasticity.

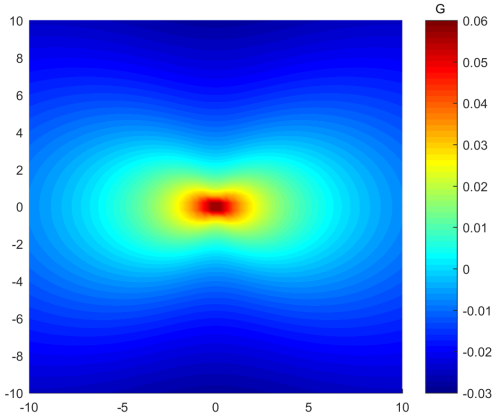

(b) σ_{11} for a single disclination from the g.disclination model.

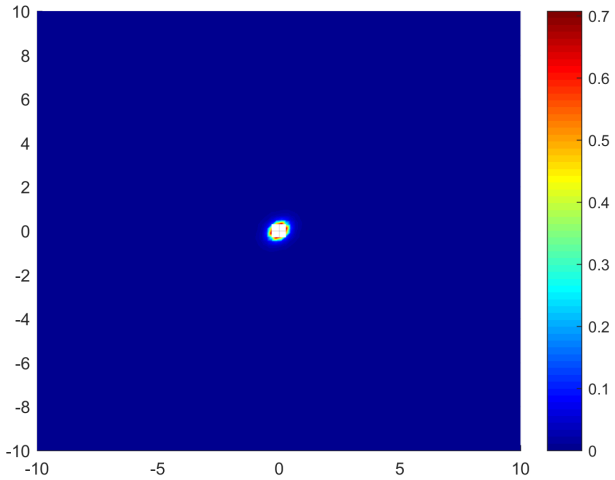

(c) $\delta\sigma_{a,g}$ between classical linear elasticity and the g.disclination model.

Figure 3.7: *The stress field σ_{11} and the comparison $\delta\sigma_{a,g}$ for a single disclination. The result from the g.disclination model matches well with the linear elasticity solution, with the $\delta\sigma_{a,g}$ maximum outside the core being less than* 1%.

3.5.4 A single disclination with large misorientation

We examine the difference between the stress fields from the small and finite deformation settings arising from a single disclination representing a high misorientation. For the small deformation problem, we assume the misorientation magnitude to be represented by $\tan\theta$, where θ is the misorientation, following (3.20). We set up a single disclination with a 45°

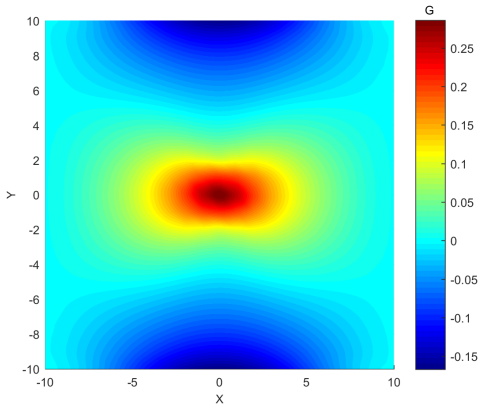

(a) Stress field σ_{11} from small deformation setting.

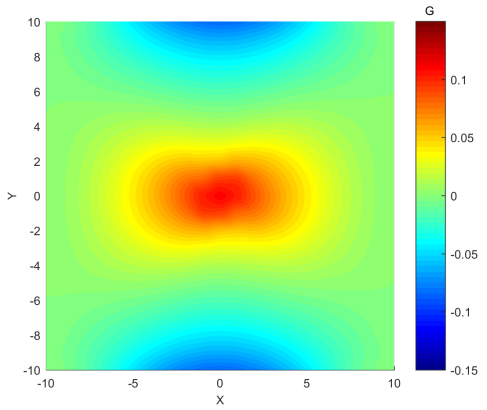

(b) Stress field σ_{11} from finite deformation setting.

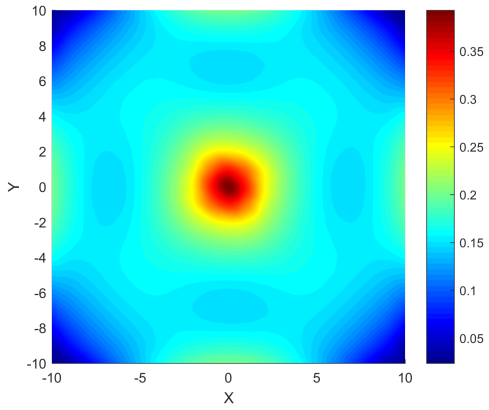

(c) $\delta\sigma_{s,f}$ between the small and finite deformation settings.

Figure 3.8: *Stress field σ_{11} for a single disclination from both the small and finite deformation settings. The maximum of $\delta\sigma_{s,f}$ is about* 40% *and the mean of $\delta\sigma_{s,f}$ is* 1.39%.

misorientation and apply traction-free boundary conditions. Figure 3.8(a) is the stress field from the small deformation setting and Figure 3.8(b) is that from the finite deformation setting. Figure 3.8(c) is the plot of the difference $\delta\sigma_{s,f}$, whose maximum is about 40% and the mean of $\delta\sigma_{s,f}$ is 1.39%. It is clear that for large misorientations like the one shown (which is more than the commonly believed threshold of $> 11°$), there are significant differences between the small and finite deformation results.

3.5.5 Single dislocation

Here we solve an edge dislocation problem, interpreted as a g.disclination dipole, as discussed in Chapter 2 [Sec. 4.3]. In this context, two opposite-sign g.disclinations are prescribed with the distortion differences as pure rotation differences (g.disclinations become pure disclinations), with Frank vector $\boldsymbol{\Omega}$ and $-\boldsymbol{\Omega}$ respectively. Based on the results in Chapter 2, the Burgers vector $\boldsymbol{b}$ for this disclination dipole in small deformation theory is given as $\boldsymbol{b} = \boldsymbol{\Omega} \times \delta\boldsymbol{r}$, where $\delta\boldsymbol{r}$ is the dipole vector (the vector that separates the two disclinations in the dipole).

Figure 3.9(a) is the stress field σ_{11} from the g.disclination dipole model and Figure 3.9(b) is the stress field σ_{11} for the classical linear elastic dislocation with the corresponding Burgers vector $\boldsymbol{b} = \boldsymbol{\Omega} \times \delta\boldsymbol{r}$. The traction boundary condition in the g.disclination dipole model is set to be that arising from the stress field of the corresponding classical linear elastic dislocation, following identical logic as in Section 3.5.3. $\boldsymbol{\sigma}_a$ denotes the stress field of the classical linear elastic edge dislocation and $\boldsymbol{\sigma}_d$ is the stress field from the g.disclination dipole model. The difference between the classical linear elasticity and the g.disclination dipole model is denoted as $\delta\sigma_{a,d}$ following definition (3.1). Figure 3.9(c) shows $\delta\sigma_{a,d}$. Outside the core, the stress fields from the g.disclination model match the one from the classical linear elastic dislocation very well.

3.5.6 High-angle grain boundaries

As discussed in Chapter 2, a grain boundary can be interpreted as a series of disclination dipoles. The elastic field of such a high-angle grain boundary is computed in this section. Also computed are the fields of a tilt grain boundary with disclination dipoles as well as with additional dislocations.

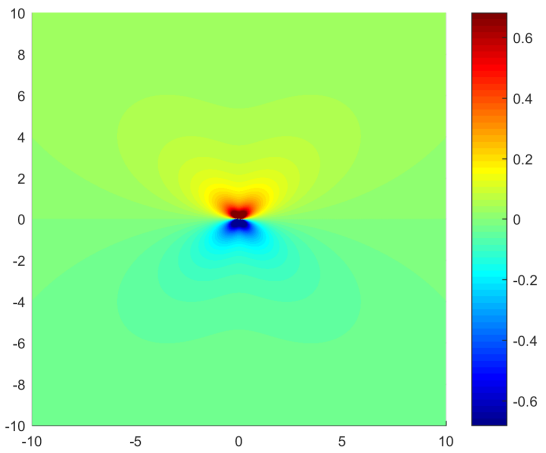

(a) Stress field σ_{11} from the g.disclination dipole model.

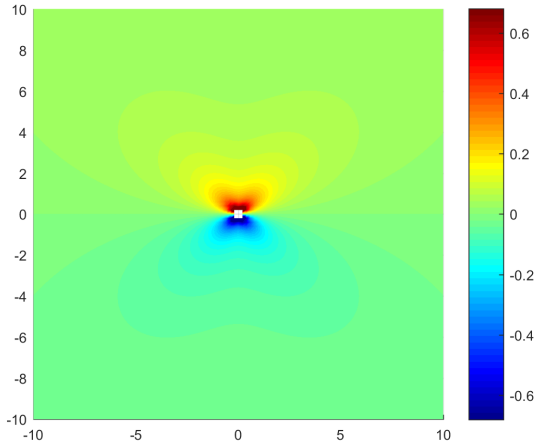

(b) Stress field σ_{11} from linear elasticity.

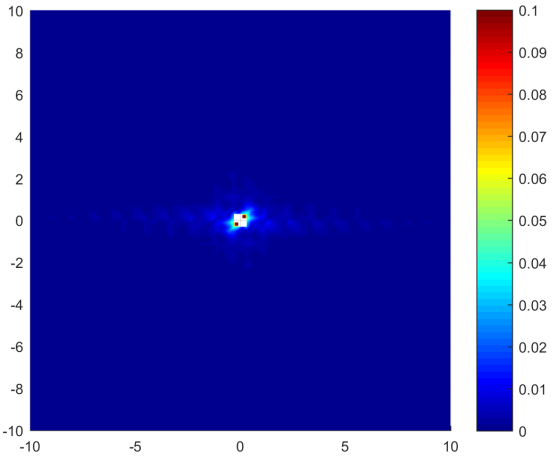

(c) $\delta\sigma_{a,d}$ between the g.disclination dipole model and linear elasticity.

Figure 3.9: *Stress fields σ_{11} of a single dislocation from the g.disclination dipole model and linear elasticity, respectively. Outside the core, the difference $\delta\sigma_{a,d}$ is less than 3%. Inside core, the stress field from linear elasticity blows up.*

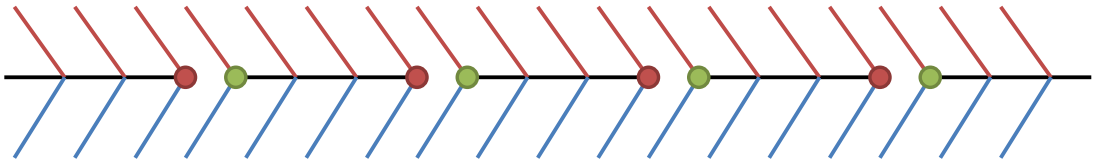

Figure 3.10: *A grain boundary interpreted as disclination dipoles equally spaced along the boundary interface. The red lines represent one grain while the blue lines represent another grain. Red points are positive disclinations and green points are negative disclinations.*

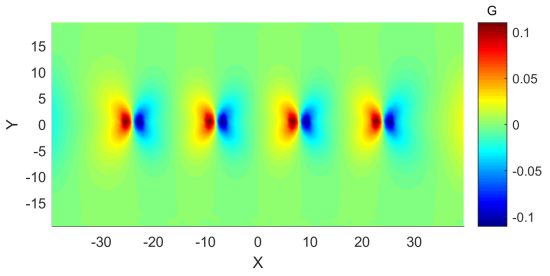

(a) Stress field σ_{22} for a grain boundary wall from the small deformation setting.

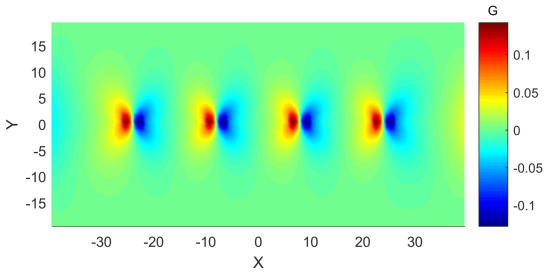

(b) Stress field σ_{22} for grain boundary wall from the finite deformation setting.

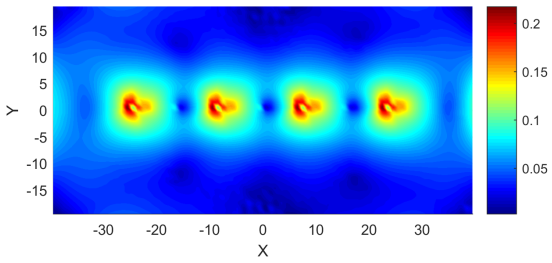

(c) $\delta\sigma_{s,f}$ between the small and finite deformation settings.

Figure 3.11: *Stress field σ_{22} for a grain boundary represented by a series of disclination dipoles. The maximum of $\delta\sigma_{s,f}$ is about 20% and the mean of $\delta\sigma_{s,f}$ is 0.57%.*

3.5.6.1 High-angle grain boundary modeled by g.disclination dipoles

Consider a grain boundary interpreted as four disclination dipoles equally spaced along the boundary interface, as illustrated in Figure 3.10. The individual misorientation magnitude of the disclinations involved in each dipole is 45°. The resulting grain boundary has the same misorientation magnitude.

Figure 3.11(a) and Figure 3.11(b) show the σ_{22} stress fields for the grain boundary in Figure 3.10 from the small and finite deformation settings, respectively. Figure 3.11(c) is the plot of the defined difference between the two deformation settings. The maximum of $\delta\sigma_{s,f}$ is about 20% and the mean of $\delta\sigma_{s,f}$ is 0.57%.

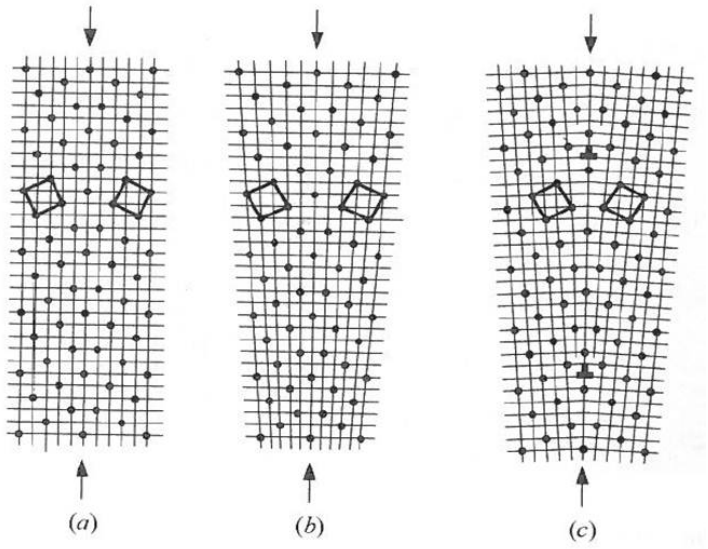

Figure 3.12: *(a) A common tilt grain boundary with a* 53.1 *degree tilt angle. (b) The configuration after applying a little additional tilt angle on the grain boundary in (a), without any rearrangement, which will have far field stress. (c) The configuration with some dislocations introduced along the interface to eliminate far field stress. (Figures reproduced from [BAC05] with permission from John Wiley and Sons.)*

3.5.6.2 Tilt grain boundary comprising disclination dipoles and dislocations

In some circumstances, dislocations and disclination dipoles both exist along a boundary interface, as shown in Figure 3.12 from [BAC05]. Figure 3.12(a) shows a large-angle, symmetric tilt grain boundary with a 53.1° misorientation. A slightly increased tilt angle is established by a bending load while maintaining the grain boundary structure intact, as shown in Figure 3.12(b). In Figure 3.12(c), dislocations are introduced to eliminate the long-range stresses generated in Figure 3.12(b), i.e. the configuration with the additional tilt can be supported with no bending loads in the presence of the added dislocations; such a configuration is actually observed in reality [BAC05].

We now calculate the fields of a tilt grain boundary without dislocations as in Figure 3.12(b) and the tilt grain boundary with dislocations as in Figure 3.12(c), aiming to prove that the tilt grain boundary with dislocations in this case is a preferred state with lower energy. The crystal rotation field with respect to the interface of both sides far away from

the interface in Figure 3.12(b) is the same as the one in Figure 3.12(c). To model the configuration in Figure 3.12(b), the grain boundary is modeled as a series of disclination dipoles as shown in Figure 3.13(a), where the red points represent positive disclinations and the blue points represent the negative disclinations. A Dirichlet boundary condition is applied, equivalent to a bending deformation due to an increased angle of 5°. Namely, the dislocation-free case in Figure 3.12(b) can be treated as a superposition of a grain boundary problem and an elastic bending problem. The grain boundary interface in Figure 3.12(c) is modeled as an array of disclination dipoles with dislocations being inserted between every three dipoles, as shown in Figure 3.13(b). The magnitude of the Burgers vector of the inserted dislocations is obtained from the Frank-Bilby formula $|\boldsymbol{b}| = \theta/d$ where θ is the additional tilt angle (5° in this problem) and d is the dislocation spacing. Thus, the additional title angle is generated by the extra half planes introduced by the inserted dislocations, instead of additional elastic bending. In Figure 3.13(b), the red points represent positive disclinations, the blue points represent negative disclinations, and the green diamonds represent dislocations. The stress fields σ_{11} of the with-dislocation configuration in Figure 3.12(c) from the small and finite deformation settings are shown in Figure 3.14(a) and 3.14(b) respectively. Figure 3.14(c) shows $\delta\sigma_{s,f}$ between the two deformation settings. The maximum of $\delta\sigma_{s,f}$ is 53% and the mean of $\delta\sigma_{s,f}$ is 1.62%. The stress field σ_{11} of the dislocation-free case in Figure 3.12(b) is shown in Figure 3.14(d) and the total energy of the dislocation-free problem is 10^3 times larger than the one in the with-dislocation case. Thus, this calculation indicates that with-dislocation case is the preferred state because of its lower total energy.

3.5.7 Disconnection on a grain boundary

A disconnection is the region that connects two parallel grain boundary segments, referred to as terraces, that do not belong to a common plane. Extensive work on grain boundary

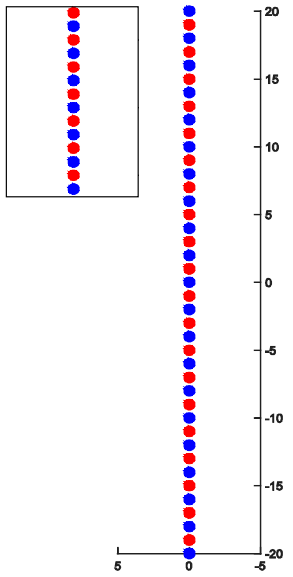

(a) Defect prescription for tilt grain boundary without dislocations.

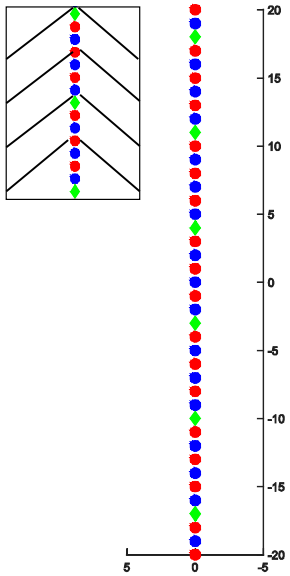

(b) Defect prescription for tilt grain boundary with dislocations.

Figure 3.13: *Defect illustrations for tilt grain boundary. In both with-dislocation case and without-dislocation case, the red dots represent positive disclinations; the blue dots represent negative disclinations and the green diamonds represent dislocations.*

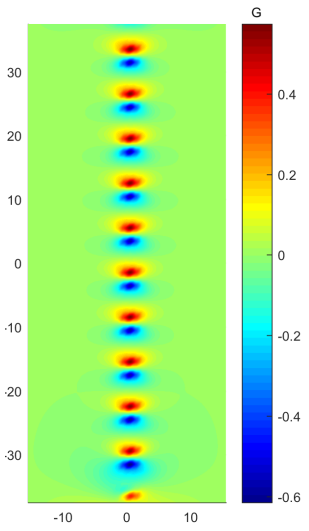

(a) Stress σ_{11} for a tilt grain boundary from with-dislocation model in small deformation setting.

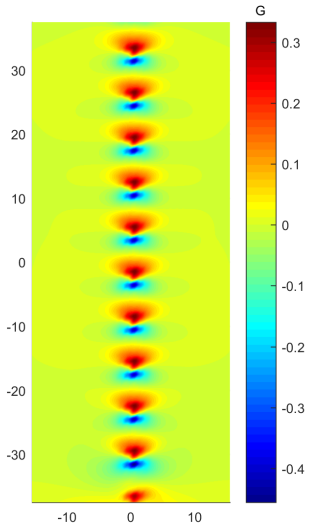

(b) Stress σ_{11} for a tilt grain boundary from with-dislocation model in finite deformation setting.

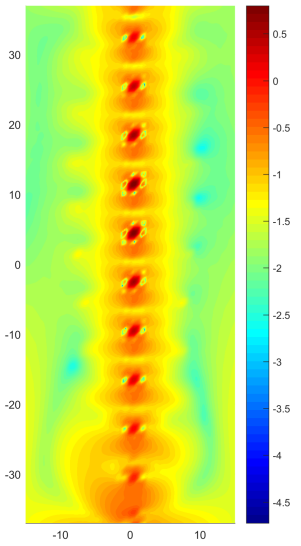

(c) $\delta\sigma_{s,f}$ between small and finite deformation settings. The colormap is plotted in logarithmic scale.

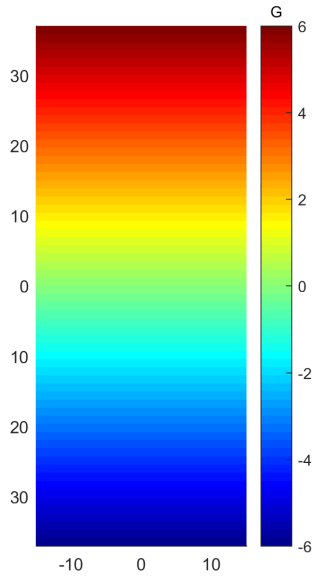

(d) Stress field σ_{11} for dislocation-free case.

Figure 3.14: *Stress fields σ_{11} of the tilt grain boundary with and without introduced dislocations, from both small and finite deformation settings. The maximum of $\delta\sigma_{s,f}$ is about* 53% *and the mean of $\delta\sigma_{s,f}$ is* 1.62%.

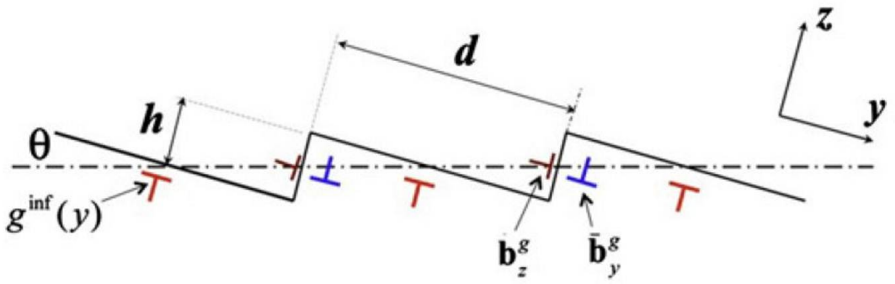

Figure 3.15: *The disconnection is modeled as a dislocation whose Burgers vector can be decomposed into the y and z directions. The brown dislocation represents the component in the z direction, while the blue one represents the component in the y direction. The red dislocations along the interface are the interface dislocations. (Figures reproduced from [HPH+13] with permission from Elsevier.)*

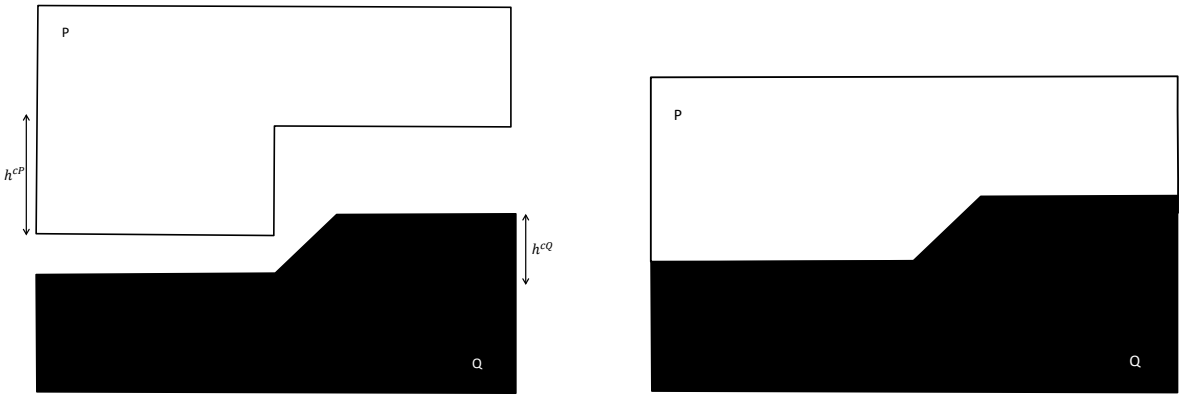

(a) The schematic illustration of two crystals before bonding.

(b) The configuration after bonding, with a disconnection formed.

Figure 3.16: *Schematic of a grain boundary with terraces and a disconnection. Since the lattice vectors of the two crystals do not match, a step is formed after bonding. (Figures reprinted from [HPH+13] with permission from Elsevier.)*

disconnections have been done by Hirth, Pond and co-workers [HPH$^+$13, HPL06]. They described the entire grain boundary as a series of terraces joined by disconnections. Figure 3.15 from [HPH$^+$13] shows the terrace model and Figure 3.16 shows a schematic for understanding the reason for the occurrence of a disconnection. The terraces are assumed to contain misfit dislocations, and the disconnections are interpreted as additional dislocations located at the steps joining the terraces.

In this work, a disclination dipole model is introduced and computed to describe the grain boundary disconnection discussed in [HPH$^+$13] shown in Figure 3.16. Figure 3.17 shows the thought experiment for representing the disconnection by a disclination dipole and a dislocation. According to g.disclination theory, we start from the current configuration of a disconnection that is represented by a disclination dipole and a dislocation, as shown in Figure 3.17(a). The red part is one grain and the blue part is another grain. The black dot at A represents a negative disclination and the yellow dot at B represents a positive disclination. Both disclinations have the same Frank vector magnitude Ω with opposite signs. The disclination density for each disclination is assumed to be derived from the difference of two (inverse) rotation matrices. The dislocation is located at B. The green lines represents the interface of the grain boundary. To get the reference configuration (the stress-free configuration shown in Figure 3.16(a), we need to relax the body by the following steps:

- Cut the interface from the right end to B and relax the negative disclination at B. Thus, the red part rotates clockwise by Ω, generating an overlap wedge. The configuration after this step is shown in Figure 3.17(b).
- Cut the interface from the B to A and relax the positive disclination at A. The red crystal rotates anticlockwise by Ω. Therefore, the point B on the red crystal moves to C and there is now a gap wedge CAB. Furthermore, the overlap wedge generated by relaxing the negative disclination is counteracted by the opposite rotation in this

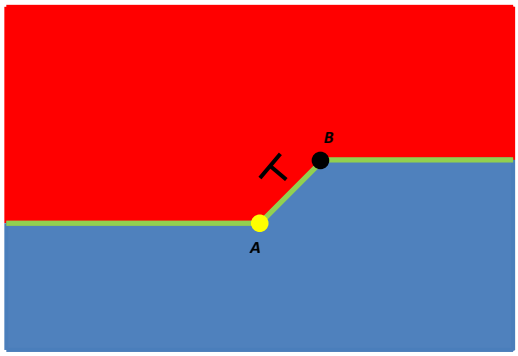

(a) The current configuration of a disconnection on the grain boundary, represented by a disclination dipole and a dislocation.

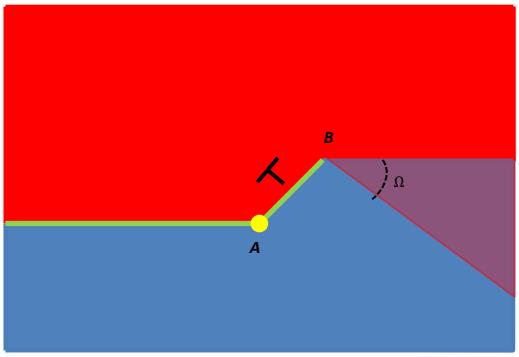

(b) Cut the interface from the right end to B and relax the negative disclination. An overlap wedge appears with angle Ω.

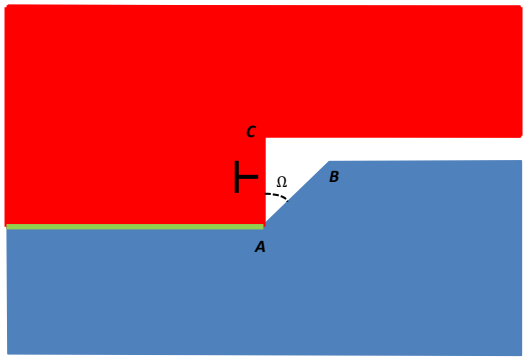

(c) Cut the interface from B to A and relax the positive disclination.The overlap wedge is eliminated while a gap wedge existing.

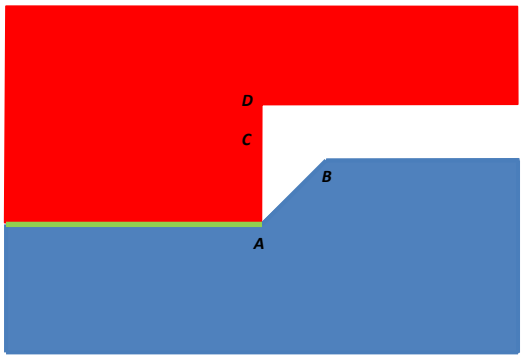

(d) Relax the dislocation at C. The red part moves upwards.

Figure 3.17: *The mechanism to represent a disconnection by a disclination dipole and a dislocation, starting from the current configuration to the reference configuration.*

step, as shown in Figure 3.17(c).

- We now assume that the (true, F-S) Burgers vector of the dislocation at B in Fig. 3.17(a) measured on the relaxed configuration is given by the vector joining C to D in Fig. 3.17(d). We now relax this dislocation.

Figure 3.18 shows the composite Burgers vector obtained from the above relaxation as a superposition of the Burgers vectors of the disclination dipole and the dislocation. It turns out that the Burgers vector from our model matches with the Burgers vector

from [HPH$^+$13]. Figure 3.18(a) is the Burgers vector diagram based on g.disclination theory - disclination densities are based on the inverse rotation matrices. Considering finite deformations, $\boldsymbol{t}$ is rotated to $\boldsymbol{s}$ by relaxing the disclinations and $\boldsymbol{b}^f_{dipole}$ is denoted as the Burgers vector of the disclination dipole. Denote the i-elastic 1-distortion difference of the positive disclination as $\boldsymbol{\Delta}$. The dipole separation vector in Figure 3.18(a) is $\boldsymbol{t}$. Based on a result in Chapter 2, the Burgers vector of the g.disclination dipole $\boldsymbol{b}^f_{dipole}$ is given as

$$\boldsymbol{b}^f_{dipole} = \boldsymbol{\Delta t}.$$

Assuming a completely in-plane problem, denote the rotation tensor acting on $\boldsymbol{t}$ to produce $\boldsymbol{s}$ in Figure 3.18(a) as $\boldsymbol{R}$. The vector $\boldsymbol{t}$ on the blue crystal is assumed to remain unchanged under the whole relaxation. Thus the i-elastic, 1-distortion difference is given by

$$\boldsymbol{\Delta} = \boldsymbol{R} - \boldsymbol{I},$$

with the matrix of $\boldsymbol{R}$ (in any orthonormal basis) given by

$$\begin{bmatrix} cos\Omega & -sin\Omega \\ sin\Omega & cos\Omega \end{bmatrix}.$$

With reference to Fig. 3.18(a), $\boldsymbol{b}^f_{dipole}$ can be written as

$$\boldsymbol{b}^f_{dipole} = (\boldsymbol{R} - \boldsymbol{I})\boldsymbol{t} = \boldsymbol{Rt} - \boldsymbol{t} = \boldsymbol{s} - \boldsymbol{t} = \boldsymbol{u}$$

From the description shown in Figure 3.17, the Burgers vector of the dislocation, $\boldsymbol{b}^f_{dislocation}$, can be written as $\boldsymbol{b}^f_{dislocation} = \boldsymbol{v} - \boldsymbol{s} = \boldsymbol{p}$. Therefore, the total Burgers vector of

the disconnection is given by

$$\boldsymbol{b}^f_{total} = \boldsymbol{b}^f_{dipole} + \boldsymbol{b}^f_{dislocation} = \boldsymbol{u} + \boldsymbol{p} = \boldsymbol{q},$$

matching the result from [HPH$^+$13]. Figure 3.18(b) is the Burgers vector diagram for the small deformation case. In this approximation, the dipole Burgers vector, $\boldsymbol{b}^s_{dipole}$, is given by Chapter 2

$$\boldsymbol{b}^s_{dipole} = \boldsymbol{\Omega} \times \boldsymbol{t},$$

where $\boldsymbol{\Omega}$ is the Frank vector of the positive disclination and is given by $tan\Omega\boldsymbol{e}_3$ by (3.20). Then, $\boldsymbol{b}^s_{dipole}$ can be written as

$$\boldsymbol{b}^s_{dipole} = \boldsymbol{u}',$$

where $\boldsymbol{u}'$ is a vector perpendicular to $\boldsymbol{t}$ with length $tan\Omega|t|$. The 'rotated' image of $\boldsymbol{t}$ is $\boldsymbol{s}' = \boldsymbol{t} + \boldsymbol{u}'$. The Burgers vector of the dislocation $\boldsymbol{b}^s_{dislocation}$ is ,

$$\boldsymbol{b}^s_{dislocation} = \boldsymbol{v} - \boldsymbol{s}' = \boldsymbol{p}'$$

Thus, the total Burgers vector $\boldsymbol{b}^s_{total}$ is given as

$$\boldsymbol{b}^s_{total} = \boldsymbol{b}^s_{dipole} + \boldsymbol{b}^s_{dislocation} = \boldsymbol{u}' + \boldsymbol{p}'.$$

Note that if we use the $\boldsymbol{b}^f_{dislocation}$ as the Burgers vector of the dislocation in the small deformation case, since $\boldsymbol{p} \neq \boldsymbol{p}'$, $\boldsymbol{b}^s_{total} = \boldsymbol{u}' + \boldsymbol{p} \neq \boldsymbol{q}$. Writing $\boldsymbol{t} = t_1\boldsymbol{e}_1 + t_2\boldsymbol{e}_2$ w.r.t any orthonormal basis, we have

$$\boldsymbol{u} = \boldsymbol{R}\boldsymbol{t} - \boldsymbol{t} = (\cos\Omega t_1 - \sin\Omega t_2 - t_1)\boldsymbol{e}_1 + (\sin\Omega t_1 + \cos\Omega t_2 - t_2)\boldsymbol{e}_2.$$

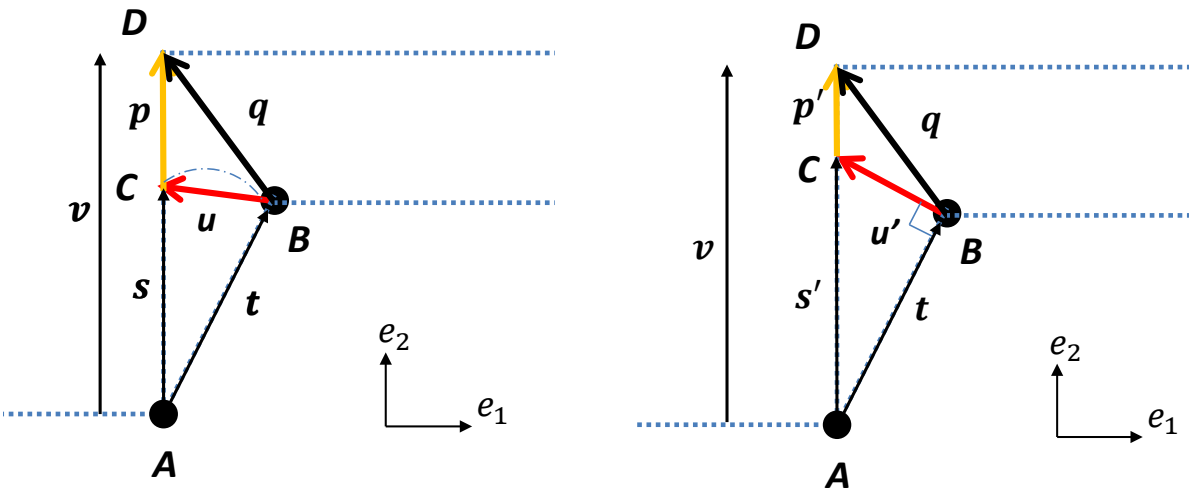

(a) The composite Burgers vector diagram of a disconnection from a disclination dipole and a dislocation.

(b) The composite Burgers vector diagram for the small deformation case.

Figure 3.18: *The composite Burgers vector diagram of a disconnection. The composite Burgers vector from the disclination dipole and dislocation give the same vector as the one in [HPH+13].*

For $|\Omega| \ll 1$, $\cos\Omega \approx 1$ and $\sin\Omega \approx \tan\Omega$, we have

$$\boldsymbol{u} \approx -\tan\Omega t_2 \boldsymbol{e}_1 + \tan\Omega t_1 \boldsymbol{e}_2 = \boldsymbol{u}'.$$

In addition, we can have the following approximations

$$\boldsymbol{s}' = \boldsymbol{u}' + \boldsymbol{t} \approx \boldsymbol{u} + \boldsymbol{t} = \boldsymbol{s}$$

$$\boldsymbol{p}' = \boldsymbol{v} - \boldsymbol{s}' \approx \boldsymbol{v} - \boldsymbol{s} = \boldsymbol{p}$$

$$\boldsymbol{u}' + \boldsymbol{p}' \approx \boldsymbol{u}' + \boldsymbol{p} \approx \boldsymbol{u} + \boldsymbol{p} = \boldsymbol{q}.$$

and the total Burgers vector of the disconnection in the small deformation setting closely approximates the finite deformation result for small disclination strengths Ω.

3.5.7.1 'Topological equaivalence $\neq$ energetic equivalence'

Figure 3.19 shows the stress field and total energy comparisons between the disconnection represented by an effective dislocation with Burgers vector $\boldsymbol{q}$ (Fig. 3.18), and three different disclination dipole-dislocation representations of the disconnection where the dislocation is prescribed at different locations along the disconnection step. The total Burgers vector is identical for all cases involved.

In Figure 3.19, the green points are negative disclinations, the red points are positive disclinations, the yellow stars are the disconnection dislocations and the blue star is the dislocation of strength equal to the overall disconnection Burgers vector. In the cases with the disclination dipole (the second, third, and fourth rows in Figure 3.19), the misorientations of all disclinations are 45° and the magnitude of Burgers vector of the dislocation is 2 lattice constants. In the case without the disclination dipole, namely the first row of Figure 3.19, the magnitude of the Burgers vector is 5 lattice constants, based on the explanation in Figure 3.18. The first column of Figure 3.19 shows different defect configurations; the second column of Figure 3.19 is the stress field σ_{11} and the total energy from the small deformation setting; and the last column is the stress field σ_{11} and the total energy from the finite deformation setting. These results show that although the Burgers vectors, for every circuit encircling the disconnection step, for all four cases are the same, the stress fields and the total energy are quite different. Furthermore, the total energy of the configuration with the dislocation being coincident with the negative disclination is the lowest.

In general, we find that the (outside core) topologically equivalent, dislocation-only configuration is the highest energy configuration, this being similar to the finding of Kamien et al [AMK17] in the context of smectics.

Defect Configuration	*Small deformation*		*Finite deformation*	
	Stress field	*Total Energy*	*Stress field*	*Total Energy*
	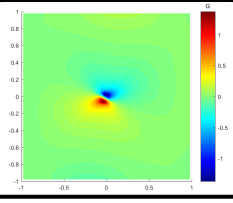	1	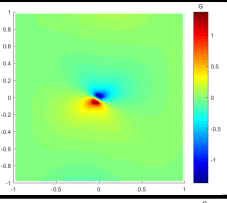	0.67
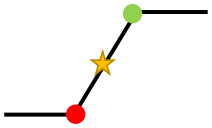	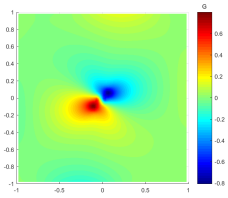	0.83	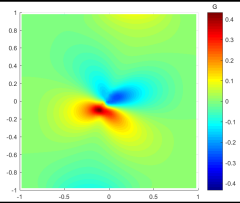	0.44
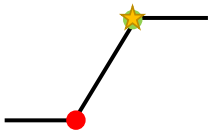	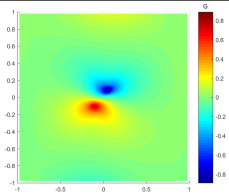	0.46	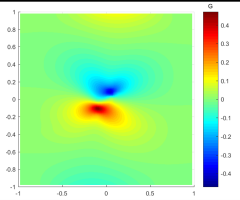	0.23
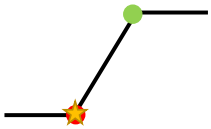	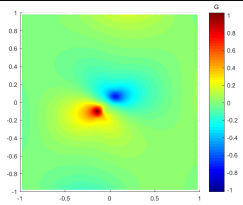	0.73	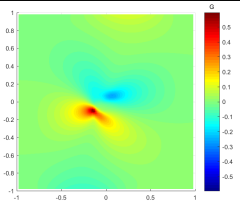	0.43

Figure 3.19: *A comparison of the stress fields σ_{11} and the total energies from both the small and finite deformation settings for different defect configurations. The red dots are positive disclinations, the green dots are negative disclinations and the yellow star are dislocations. The blue star is the dislocation with the same overall Burgers vector as other cases. Although the overall Burgers vectors are same in all cases, the stress fields and the total energies are quite different.*

3.5.8 A disconnected grain boundary with misfit dislocations on terraces

We utilize the arguments of Section 3.5.7 to model a grain boundary with a series of disconnections. The disconnections are represented as a series of disclination dipoles with the dislocations. The misorientation angle for every disclination is set to be 45°. The Burgers vector of the dislocation in each disconnection is assumed to be $\boldsymbol{b} = -0.5\boldsymbol{e}_1 - 0.5\boldsymbol{e}_2$ (that in reality is to be determined by the crystal structure of the constituent crystals forming the interface). In addition, we consider the terraces as containing misfit dislocations. Figure 3.21 is the defect configuration of the incoherent grain boundary with the disconnections, where the incoherency is represented by the misfit dislocations whose Burgers vectors are determined by the crystal structure of the interface. In this calculation, we assume the two grain materials are Cu and Ag, with the ratio of the lattice parameter being $a_{Cu}/a_{Ag} = 36/41$ based on [WBH12]. Figure 3.20(a) shows two grains before bonding together, where the top is Cu and the bottom is Ag. Based on the lattice parameter ratio, it can be shown that the far field incoherency strain can be eliminated by introducing an extra half Cu plane every seven lattice constants, as shown in Figure 3.20(b). Therefore, the Burgers vector of the misfit dislocation is one lattice constant and the interval distance between the misfit dislocations is seven lattice constants. In Figure 3.21, the black lines represent the terraces; the red points are positive disclinations; the green points are negative disclinations; the blue stars are the disconnection dislocations; and the blue triangles are the misfit dislocations. Figure 3.22 displays the stress field σ_{11} for this configuration in both the small and finite deformation settings. The maximum of $\delta\sigma_{s,f}$ is about 170% and the mean of $\delta\sigma_{s,f}$ is 0.67%.

Since defect dynamics depends upon the local stress field, such difference may be expected to have significant impacts for kinetics.

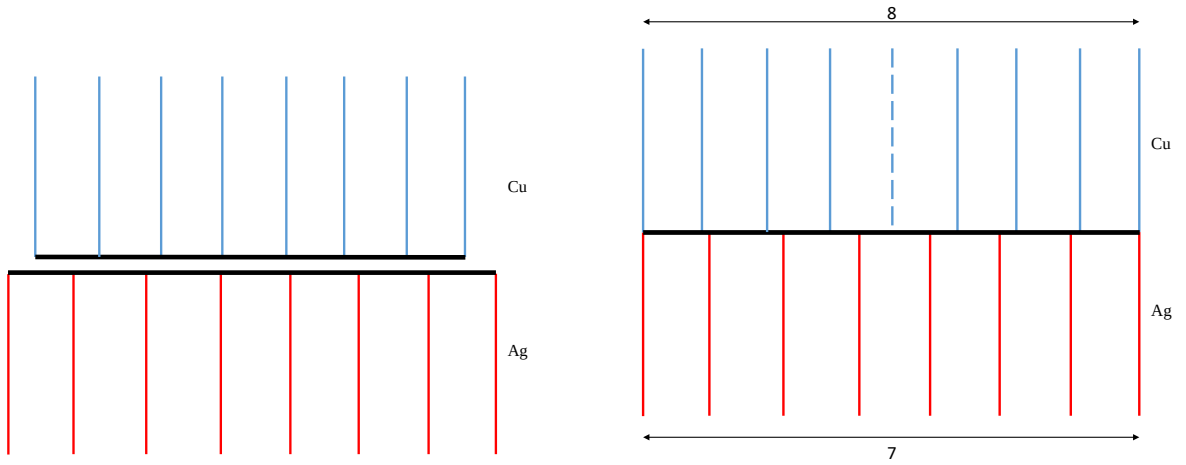

(a) The misfit configuration of two grains with different lattice parameters.

(b) The configuration after introducing an extra half plane (a dislocation).

Figure 3.20: *Defining a misfit dislocation. By introducing a dislocation, the far field incoherency strain of two misfit grains is eliminated.*

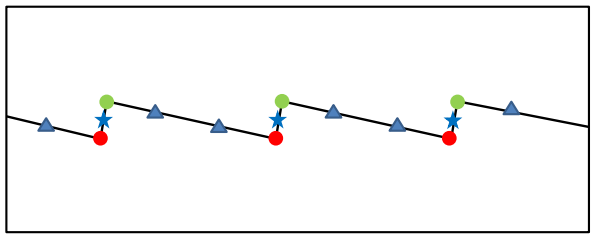

Figure 3.21: *Defect configuration of the incoherent grain boundary disconnection. The black lines within the body are grain boundary interfaces; the red dots are positive disclinations; the green dots are negative disclinations; the blue stars are disconnection dislocations; and the blue triangles are misfit dislocations.*

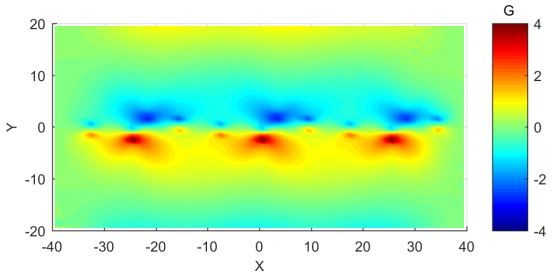

(a) Stress σ_{11} for the incoherent grain boundary disconnection in small deformation setting.

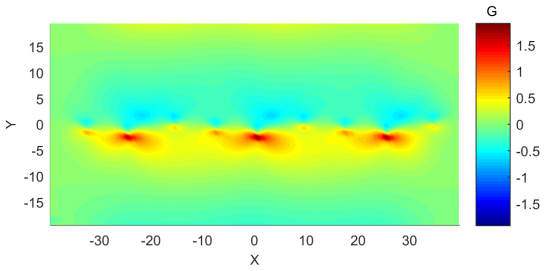

(b) Stress σ_{11} for the incoherent grain boundary disconnection in finite deformation setting.

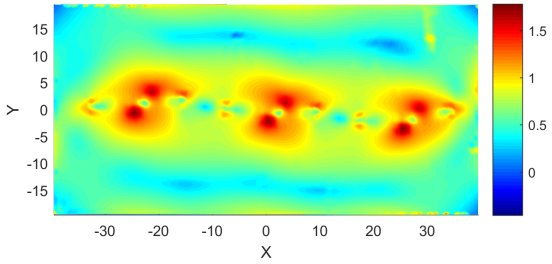

(c) $\delta\sigma_{s,f}$ between the small and finite deformation settings.

Figure 3.22: *Stress field σ_{11} for the incoherent grain boundary disconnection and the stress field difference $\delta\sigma_{s,f}$. The maximum of $\delta\sigma_{s,f}$ is about* 170% *and the mean of $\delta\sigma_{s,f}$ is* 0.67%.

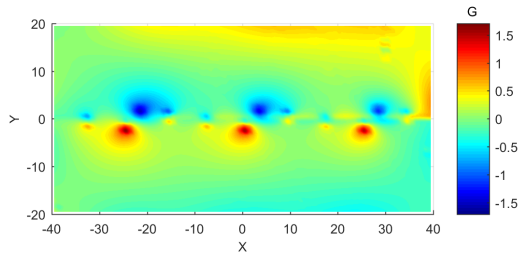

(a) Stress σ_{11} for a grain boundary with dislocations and disconnections separating crystals with anisotropic bulk elastic properties in the finite deformation setting.

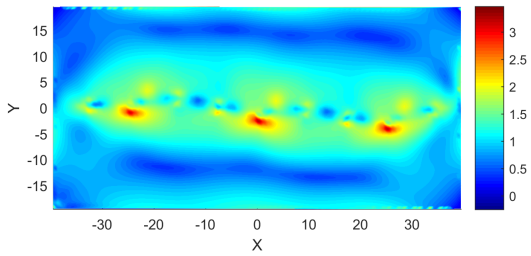

(b) The difference between the isotropic case and the anisotropic case, $\delta\sigma_{iso,aniso}$.

Figure 3.23: *Stress field σ_{11} for an incoherent grain boundary with dislocations and disconnections in finite deformation setting, and a comparison between the isotropic case and anisotropic case. The maximum of $\delta\sigma_{iso,aniso}$ is 320%, and the mean of $\delta\sigma_{iso,aniso}$ is 320% is 12.3%.*

3.5.8.1 Anisotropic disconnected grain boundary with misfit dislocations on terrace

Anisotropic elasticity is the physically natural elastic response of single crystals across a grain boundary. Here, we study a grain boundary with anisotropic elastic bulk response and compare the results with the isotropic case. Consider a grain boundary where the misdistortion across the $Cu - Ag$ interface is the same as the one in Sec. 3.5.8. The specification of the anisotropic stiffness tensors for the top and bottom crystals is described in Appendix G. Figure 3.23(a) shows the stress field σ_{11} with anisotropy from the finite deformation settings and Figure 3.23(b) shows the difference between the isotropic finite deformation stress and the anisotropic finite deformation stress, $\delta\sigma_{iso,aniso}$, following the definition (3.1). The maximum of $\delta\sigma_{iso,aniso}$ is 320%, and the mean of $\delta\sigma_{iso,aniso}$ is 12.3%.

3.5.9 Flat, through, and terminating twin and grain boundaries

In this section we explain the implications of our model with regard to the modeling of elastic fields of flat interfaces. We consider both the case of a twin and a grain boundary.

Before considering grain and phase boundaries separately, we note a feature of our

model pertaining to both of them. With regard to stress, the governing equations common to both situations are given by

$$\begin{aligned} &\text{curl } \hat{\boldsymbol{W}} = \boldsymbol{S}^{\perp} : \boldsymbol{X} - \boldsymbol{\alpha} \\ &\boldsymbol{T} = \boldsymbol{T}(\hat{\boldsymbol{W}}) \\ &\text{div } \boldsymbol{T}(\hat{\boldsymbol{W}}) = \boldsymbol{0} \\ &\boldsymbol{T}\boldsymbol{n} = \boldsymbol{t} \qquad \text{on the boundary,} \end{aligned} \tag{3.32}$$

as implied by (3.7) and (3.9), where $\boldsymbol{T}$ is the stress. With statically admissible traction boundary conditions (and assuming for the sake of argument the traction b.c.s to vanish), this implies that the stress field on the body is solely determined by the fields $\boldsymbol{\alpha}$ and $\boldsymbol{S}^{\perp} : \boldsymbol{X}$ - in the linear case, such uniqueness is proven in Appendix H. An important implication of this fact is that two different $\boldsymbol{S}$ fields lead to the same stress field as long as their g. disclination fields $\boldsymbol{\Pi} = \text{curl}\, \boldsymbol{S}$ are identical, since $\boldsymbol{S}^{\perp}$ is uniquely determined from $\boldsymbol{\Pi}$. We return to this issue in Section 3.6.

3.5.9.1 The through twin

In order to model a twin boundary it is imperative to predict an elastic distortion field that is a gradient of a vector field (i.e. compatible) representing a shear of one crystal with respect to the other, which nevertheless results in a stress-free state. In our model, a flat twin boundary can be represented by an eigenwall field $\boldsymbol{S}$ with support in a layer along the interface and of the form $\boldsymbol{a} \otimes \boldsymbol{n} \otimes \boldsymbol{n}$ where $\boldsymbol{a}$ is a vector parallel to the interface plane with magnitude determined by the amount of shearing involved, and $\boldsymbol{n}$ is the unit normal vector of the interface. This is motivated from the fact that the inverse deformation for a twin is continuous at the interface.

Recall from (3.4) that when $\boldsymbol{\alpha} = \mathbf{0}$, the i-elastic 1-distortion $\boldsymbol{W}$ satisfies

$$\operatorname{curl} \boldsymbol{W} = \boldsymbol{S} : \boldsymbol{X}.$$

Given the configuration shown in Figure 3.24(a), if $\boldsymbol{S}$ is prescribed in the form $\boldsymbol{a} \otimes \boldsymbol{n} \otimes \boldsymbol{n}$ in the layer and vanishing outside it, then $\boldsymbol{S} : \boldsymbol{X} = \mathbf{0}$ due to the symmetry of $\boldsymbol{S}$ in its last two indices. Thus $\operatorname{curl} \boldsymbol{W} = \mathbf{0}$.

Since the through boundary has a constant distribution of $\boldsymbol{S}$ along it,

$$\begin{aligned} &\operatorname{curl} \boldsymbol{S} = curl \boldsymbol{S}^{\perp} = \boldsymbol{\Pi} = \mathbf{0} \\ &\operatorname{div} \boldsymbol{S}^{\perp} = \mathbf{0} \\ &\boldsymbol{S}^{\perp} \boldsymbol{n} = \mathbf{0}, \end{aligned}$$

indicating $\boldsymbol{S}^{\perp} = \mathbf{0}$. With this observation, and the discussion surrounding (3.32), we have $\hat{\boldsymbol{W}} = \boldsymbol{I}$ (with appropriate boundary conditions imposed on $\boldsymbol{f}$ to eliminate rigid deformation from the current configuration) and the stress vanishes. Also, since $\operatorname{curl} \boldsymbol{W} = \mathbf{0}$ in this case, $(3.9)_2$ implies $\operatorname{curl} \boldsymbol{H}^s = \mathbf{0}$ and (3.8) implies that the i-elastic distortion $\boldsymbol{W} = \boldsymbol{I} + \boldsymbol{H}^s = -\boldsymbol{Z}^s$ is indeed a non-trivial gradient.

Our computations recover this exact result; Figure 3.24(b) shows the l^2-norm of the stress field $|\boldsymbol{\sigma}|$ and it turns out the full stress tensor field vanishes for this prescribed $\boldsymbol{S}$ field. The compatible deformation due to the i-elastic distortion $\boldsymbol{W}$ is shown in Figure 3.24(d) and 3.24(c). Figure 3.24(d) is the current configuration with a twin boundary. Figure 3.24(c) is the reference configuration containing the image of the twin mapped by $\boldsymbol{W}^{-1}$ (the mirror planes for this twin boundary are marked as blue dash lines and the red lines in Fig. 3.24(d)). In Figure 3.24(c), the inverse deformation at the left bottom corner and the vertical inverse deformation at the right bottom corner are fixed. With this particular Dirichlet boundary condition, $\hat{\boldsymbol{W}} = \boldsymbol{I}$.

It should be noted that if the stress response function was simply a function of $\boldsymbol{W}$ instead of $\hat{\boldsymbol{W}}$, it would not have been possible to predict the non-trivial twinning deformation corresponding to the stress-free state.

3.5.9.2 The terminating twin

Consider now a terminating twin boundary. The specification of the $\boldsymbol{S}$ field is the same as before in the layer, but the layer does not go through the body, as shown in Figure 3.25(a). The terminating twin calculated in this part is equivalent to a negative g.disclination problem. The field $\boldsymbol{S} : \boldsymbol{X} = \boldsymbol{0}$ on the body as before; however, $\operatorname{curl} \boldsymbol{S} = \boldsymbol{\Pi} \neq \boldsymbol{0}$ and (3.32) implies there is a non-vanishing stress field now.

As for the i-elastic distortion, we note first that, for $\boldsymbol{\alpha} = \boldsymbol{0}$, (3.4) implies that $\operatorname{curl} \boldsymbol{W} = \boldsymbol{0}$ so that the i-elastic distortion is compatible. This can alternatively be understood from the fact that $\boldsymbol{S} = \boldsymbol{S}^{\perp} - \mathit{grad}\, \boldsymbol{H}^s$ so that $\boldsymbol{S} : \boldsymbol{X} = \boldsymbol{0}$ and $(3.32)_1$ imply that $\operatorname{curl} \boldsymbol{H}^s = -\boldsymbol{S}^{\perp} : \boldsymbol{X} = -\operatorname{curl} \hat{\boldsymbol{W}}$ and $(3.9)_2$ then implies that $\boldsymbol{W}$ is compatible.

Figure 3.25(b) shows the stress field σ_{11} of the defect configuration in Figure 3.25(a) with the stress function given as $\boldsymbol{T}(\hat{\boldsymbol{W}})$.

We note that had the stress response been taken as simply a function of $\boldsymbol{W}$, then we would have $\operatorname{curl} \boldsymbol{W} = \boldsymbol{0}$ from (3.4) and this associated with $\operatorname{div} \boldsymbol{T}(\boldsymbol{W}) = \boldsymbol{0}$ would yield the erroneous result that the stress field vanishes.

3.5.9.3 The through grain boundary

For the through grain boundary, the $\boldsymbol{S}$ distribution is specified much like in the case of the through twin, except now $\boldsymbol{S} : \boldsymbol{X} \neq \boldsymbol{0}$, but for the same reasons as for the through twin, $\boldsymbol{S}^{\perp} = \boldsymbol{0}$. Since the misdistortion at a grain boundary involves a difference in rotations, it cannot be represented in the form of a rank-one tensor. Thus, the interface is incompatible and, in the absence of g.disclinations, a dislocation density field must be located along the interface. In general, the dislocation density should be measured and prescribed from

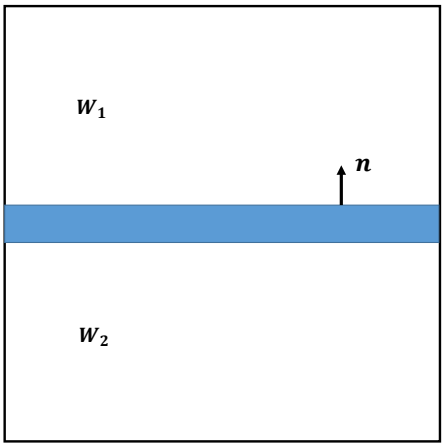

(a) The eigenwall field is prescribed within the layer that does not terminate in the body.

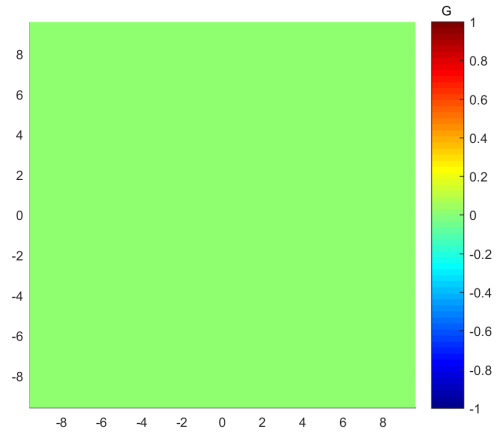

(b) The magnitude of the stress field $\boldsymbol{\sigma}$. The stress field is zero for the eigenwall field in (a).

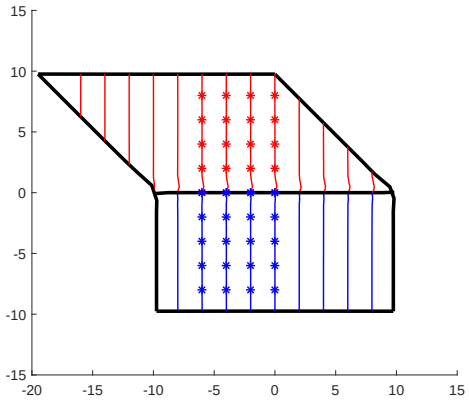

(c) The reference configuration for the through twin boundary.

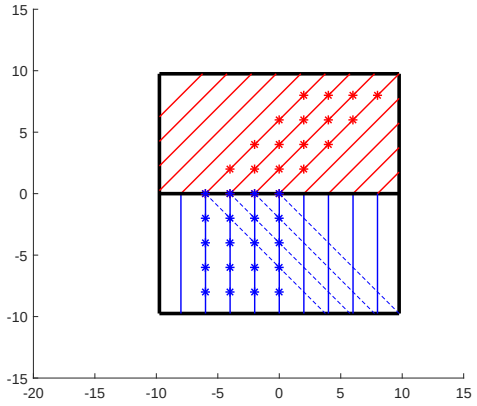

(d) The current configuration for the through twin boundary.

Figure 3.24: *The eigenwall field prescription of a through twin boundary and its corresponding stress as well as the inverse deformation fields. Red lines and blue lines represent different lattice orientations, and the deformation fields indicate a shear difference cross the boundary interface. The stars on blue dashed lines and the red lines in (d) are the mirrored images of lattice sites across this twin boundary.*

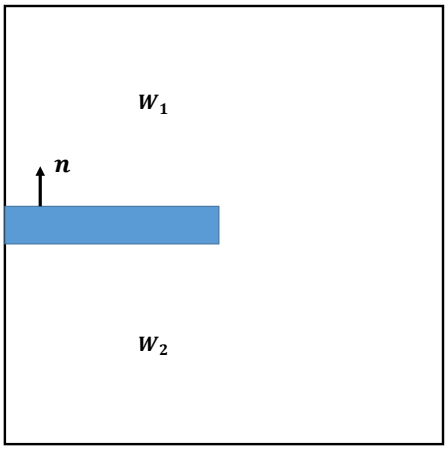

(a) The eigenwall field is prescribed within the layer and terminates inside the body. The body size is 20×20.

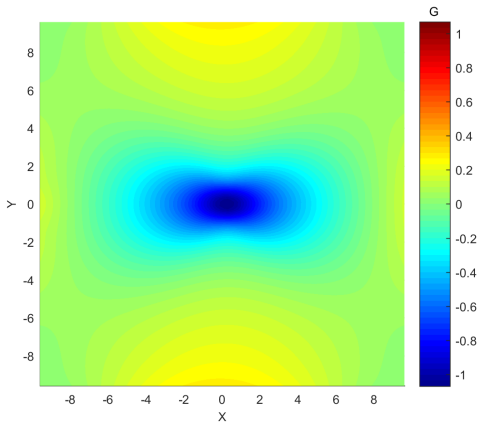

(b) The stress field σ_{11} is non-zero for the corresponding eigenwall field in (a).

Figure 3.25: *The eigenwall field prescription for the terminating twin boundary and its corresponding stress field* σ_{11}.

experiments. Here we we approximate the interfacial dislocation density as

$$\boldsymbol{\alpha} = \left(\frac{\boldsymbol{W}_1 - \boldsymbol{W}_2}{t} \otimes \boldsymbol{n} \right) : \boldsymbol{X}, \tag{3.33}$$

with t being the layer width and $\boldsymbol{n}$ the interface unit normal.

As shown in Figure 3.24(a), an eigenwall field $\boldsymbol{S}$ is prescribed along the interface through the body and the dislocation density field (3.33) is also prescribed in the layer; $\boldsymbol{W}_1 - \boldsymbol{W}_2$ in the expression represents a misorientation of 10°. Figure 3.26 shows the l^2-norm of the stress field $\boldsymbol{\sigma}$ of the prescribed grain boundary in the small deformation setting. Since $\boldsymbol{\alpha}$ is calculated from a skew matrix, the stress field is zero in the small deformation case.

In the finite deformation setting, the interfacial dislocation density specification (3.33) results in a non-vanishing stress field. However, an alternate prescription of the $\boldsymbol{\alpha}$ field in the layer can be generated from an interpolation of the two (constant) finite rotations $\boldsymbol{W}_1$ and $\boldsymbol{W}_2$ by a pure rotation field across the layer and subsequently taking a *curl* of this field. In such a case, the $\hat{\boldsymbol{W}}$ solution to (3.32) would be an inhomogeneous rotation field,

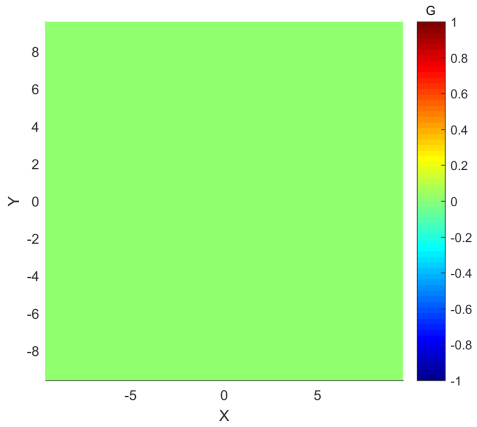

Figure 3.26: *The magnitude of the stress field $\boldsymbol{\sigma}$ for a through grain boundary in the small deformation setting. The stress field vanishes.*

resulting in vanishing stress everywhere.

3.5.9.4 When is stress induced by flat grain/phase boundaries?

By the considerations presented in this Section 3.5.9, we have obtained the interesting result that for flat twins and grain boundaries that do not induce a g.disclination density along them due to gradients of misorientation/misdistortion, there is no stress in the body. In addition, the elastic distortion for such twins are compatible whereas for grain boundaries they are not, agreeing with classical notions that twin boundaries result in compatible deformations [Bha03] and that a strain-free elastic distortion field is necessarily consistent only with a spatially uniform rotation field [Shi73], a property not satisfied by a body containing a through grain boundary. Moreover, we see the vanishing-stress result of through boundaries as a justification for many works on grain boundary microstructure evolution [DeW72, BZB$^+$12, HLL$^+$12] that do not involve the notion of stress at all in the first instance.

Another interesting (and somewhat curious) feature of our model with respect to the modeling of twin boundaries is the fact that regardless of the distribution of flat twin boundaries (possibly terminating) in a body, all individually modeled by an in-layer dis-

tribution of the type $\boldsymbol{a} \otimes \boldsymbol{n} \otimes \boldsymbol{n}$, (3.4) implies that the i-elastic distortion $\boldsymbol{W}$ is curl-free. However, as the case of the terminating twin and the considerations of the next section (3.5.10) show, there can still be induced stresses due to terminating twin boundaries, picked up by a different condition related to the incompatibility of the $\hat{\boldsymbol{W}}$ field, sourced by $\boldsymbol{S}^{\perp}$ that is in turn sourced by the g.disclination density field $\boldsymbol{\Pi}$. This is reminiscent of the additional condition for compatibility beyond the twinning equation that needs to be satisfied for the occurrence of stress-free crossing twins [Bha03, p. 83-84, Sec. 5.10] - in our case an additional condition is the vanishing of $\boldsymbol{\Pi}$, beyond the $\boldsymbol{S}$ field being, pointwise, representable as $\sum_i \boldsymbol{a}_i \otimes \boldsymbol{n}_i \otimes \boldsymbol{n}_i$ (with range of i possibly varying from point to point).

As an example, we demonstrate the stress field of a hypothetical configuration of five compatible phase boundaries converging at a point, modeled after a penta-twin configuration [DeW72]. We refer to this idealized configuration as a 'penta-a-twin' configuration and the boundaries as a-twin boundaries, the 'a' standing for almost. Each a-twin interface involves a 72° misorientation, resulting in prefect compatibility at their junction. Fig. 3.27 shows the configuration of five intersecting a-twin boundaries and two reference tiles (see Appendix E) sharing a common edge (the black vector). The i-elastic distortion difference between two parts X and Y, denoted as $\delta\boldsymbol{W}^{X,Y}$, is defined as $\delta\boldsymbol{W}^{X,Y} := \boldsymbol{W}^{X} - \boldsymbol{W}^{Y}$. For a compatible a-twin boundary, $\delta\boldsymbol{W}^{X,Y}$ can be written in the form $\delta\boldsymbol{W}^{X,Y} = s\boldsymbol{a} \otimes \boldsymbol{n}^{i}$, where i is the a-twin boundary index, s represents the shear strain of one part relative to its adjoining part across the boundary in question, $\boldsymbol{n}^{i}$ is the unit normal vector field for each a-twin boundary in the current configuration, and $\boldsymbol{a}$ is a unit vector parallel to the interface in the reference configuration. Following the interpretation in Appendix E, we assume the reference tile at any point $\boldsymbol{x}$ to be the same rectangle up to a rigid rotation, as shown in Fig. 3.27. With the assumed reference tile, any unit vector parallel to the a-twin boundary interface in the current configuration is mapped to the black vector ($\boldsymbol{e}_2$) in the reference configuration, indicating $\boldsymbol{a}$ to be the black vector in the reference tile. Therefore, the contribution to the eigenwall field $\boldsymbol{S}$ from each a-twin boundary i (in its

region of support is) is

$$\boldsymbol{S}^i = \frac{s}{t}\boldsymbol{e}_2 \otimes \boldsymbol{n}^i \otimes \boldsymbol{n}^i. \tag{3.34}$$

where t is the layer thickness for each a-twin boundary. The unit normal vector for each a-twin boundary is specified as $\boldsymbol{n}^i = \cos(\alpha^i)\boldsymbol{e}_1 + \sin(\alpha^i)\boldsymbol{e}_2$, with α^i given as follows

i	1	2	3	4	5
α^i	0.2π	0.6π	π	1.4π	1.8π

.

The numbers $1, 2, .., 5$ correspond to the indices in Figure 3.27. The total eigenwall field $\boldsymbol{S}$ is the superimposition of contributions from all five a-twin boundaries, $\boldsymbol{S} = \sum_i \chi^i \boldsymbol{S}^i$, where χ^i represents the characteristic function of the i^{th} a-twin boundary. In the region of overlap of the boundaries, based on (3.15), $\boldsymbol{\Pi}$ can be written as

$$\boldsymbol{\Pi} = \sum_i \frac{\boldsymbol{S}^i \boldsymbol{n}^i}{c} \otimes \boldsymbol{e}_3 = \frac{s}{ct}\boldsymbol{e}_2 \otimes (\sum_i \boldsymbol{n}^i), \tag{3.35}$$

where c is the width of the overlap region. Since $\sum_i \boldsymbol{n}^i = \boldsymbol{0}$ for the prescribed five a-twin boundaries, $\boldsymbol{W}$ corresponding to this $\boldsymbol{S}$ field is is compatible and $\hat{\boldsymbol{W}}$ should be as well since $\boldsymbol{\Pi} = \boldsymbol{0}$. Indeed, in our modeling we find that both fields $\boldsymbol{W}$ and $\hat{\boldsymbol{W}}$ are curl-free for this problem and we demonstrate the stress-free body in Fig. 3.28(a). Fig. 3.28(b) shows the reference tiles across each a-twin boundary in the compatible reference configuration. Given the rectangular reference tile shown in Fig. 3.27, we rotate the reference tile such that the contiguous edge of two reference tiles matches the a-twin boundary interface direction, as shown in Fig. 3.28(b). Fig. 3.28(c) is a rendition of the deformed image of these reference tiles in the current configuration under the elastic distortion $\boldsymbol{W}^{-1}$. The red dashed lines represent the a-twin boundary interfaces. The blue dashed lines show the connecting shapes in the reference and current configurations; the black dashed lines are the contiguous edges for each pair of shapes across an a-twin boundary. Since $\boldsymbol{W}$ is compatible, the connectivity of each pair remains intact.

Given different reference tiles (to be decided by crystallography), the corresponding

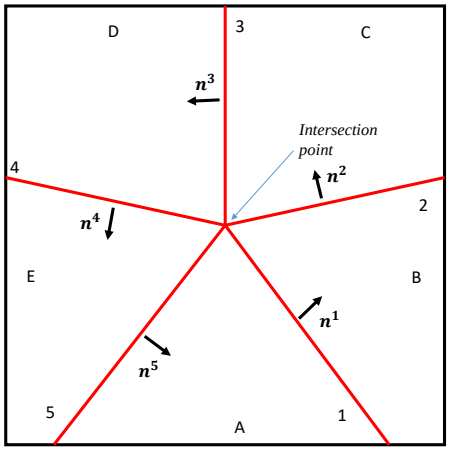

Figure 3.27: *An illustration of the configuration of five intersecting a-twin boundaries. The red lines show five a-twin boundaries with index* 1 *to* 5*. The right part shows two reference tiles sharing a common edge (the black vector). Each reference tile is a rectangle.*

prescribed eigenwall fields $\boldsymbol{S}$ are different, leading to different i-elastic distortions $\boldsymbol{W}$. Fig. 3.29(a) is the body in the current configuration. Fig. 3.29(b) shows the rendition of the body in the reference configuration mapped by $\boldsymbol{W}$ with $\boldsymbol{a}$ being $\boldsymbol{e}_2$; Fig. 3.29(c) is the body in the reference configuration mapped by $\boldsymbol{W}$ with $\boldsymbol{a}$ being $\cos(0.7\pi)\boldsymbol{e}_1 + \sin(0.7\pi)\boldsymbol{e}_2$.

3.5.10 A stress-inducing almost penta-twin

A special stress-inducing almost penta-twin (with short form i-a penta twin standing for incompatible almost penta-twin) is studied in the context of the g.disclination model, serving as an analog of star disclination [DeW72, GSJ+05]. A star disclination is an observed configuration consisting of five flat twin boundary interfaces converging at the same point, as shown in Figure 3.30 [DeW72, GSJ+05]. The five twin boundary interfaces appear as straight lines in observations [QYC+15], as shown in Figure 3.31. The misorientation angle for each twin boundary is $70°32'$. The resulting 'stress-free multicrystal' therefore has a gap wedge of $7°20'$.

Motivated by the star disclination, we set up an analogous problem by putting five

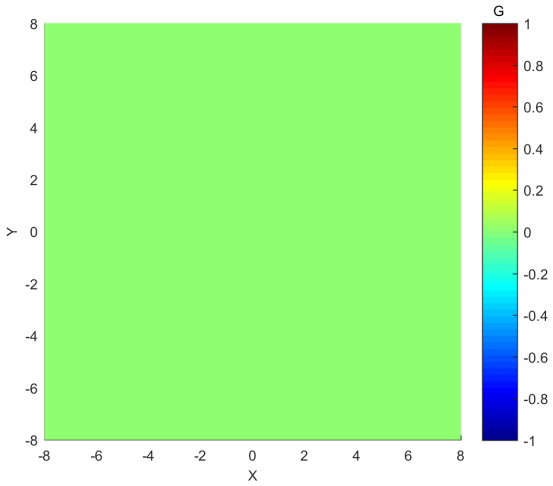

(a) The magnitude of the stress field for the penta-a-twin configuration.

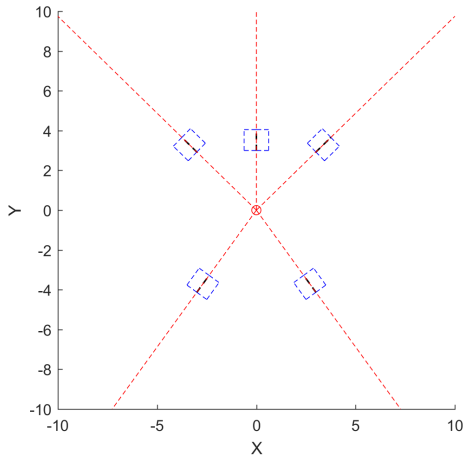

(b) The reference tiles across a-twin boundaries with contiguous edges in the reference configuration.

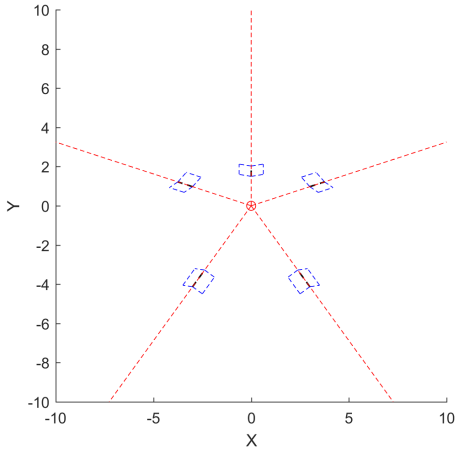

(c) The rendition of the reference tiles in the current configuration mapped by $\boldsymbol{W}^{-1}$.

Figure 3.28: *The zero stress field and the rendition of reference tiles for the penta-a-twin configuration. The misorientation angle for each a-twin boundary is* $72°$*. The connectivity for each pair of reference tiles across the a-twin boundary remains intact.*

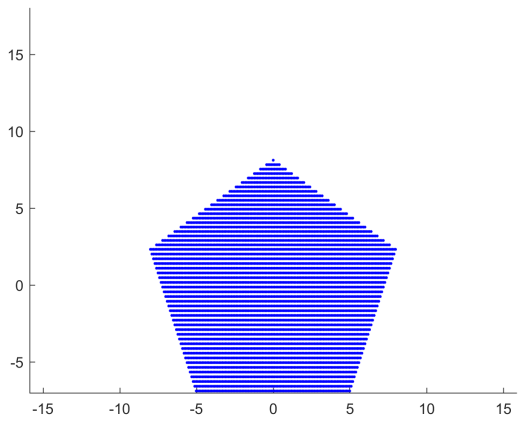

(a) The body in the current configuration.

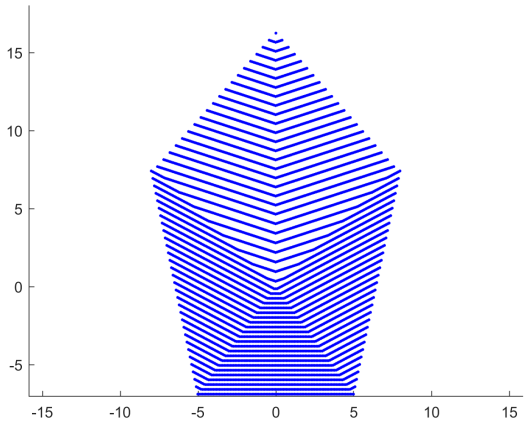

(b) The body in the reference configuration mapped by $\boldsymbol{W}$ with $\boldsymbol{a} = \boldsymbol{e}_2$.

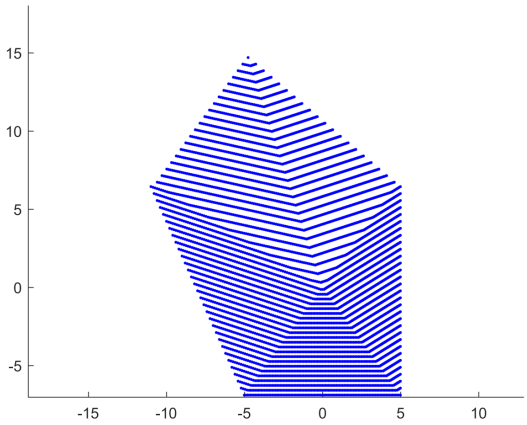

(c) The body in the reference configuration mapped by $\boldsymbol{W}$ with $\boldsymbol{a} = cos(0.7\pi)\boldsymbol{e}_1 + sin(0.7\pi)\boldsymbol{e}_2$.

Figure 3.29: *The renditions of the body in the reference configuration mapped by* $\boldsymbol{W}$ *with different prescribed* $\boldsymbol{a}$.

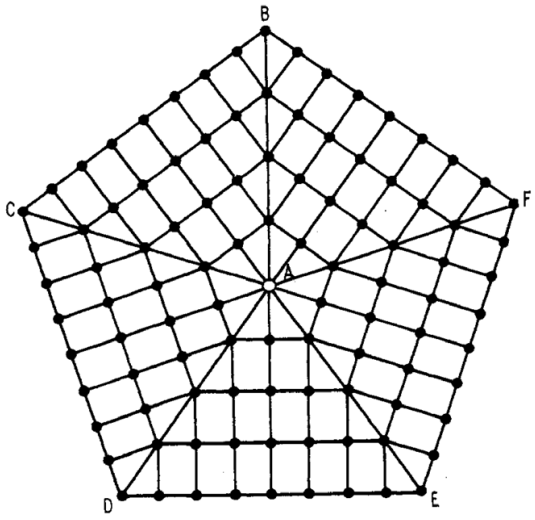

Figure 3.30: *The star disclination configuration with five twin boundaries intersecting at point A. Each twin boundary has misorientation angle* $70°32'$*. (Figure reproduced from [DeW72] with permission from IOP Publishing.)*

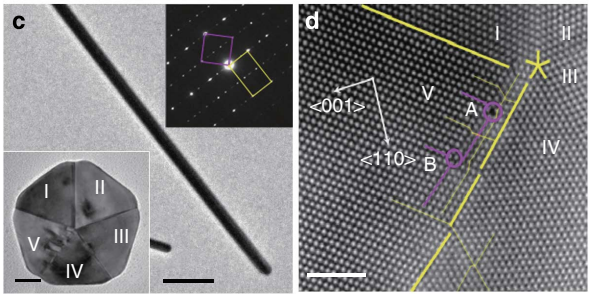

Figure 3.31: *Experimental observation of the star disclination, indicating the five twin interfaces are straight. (Figure reproduced from [QYC+15] with permission from Nature Publishing Group of article under an open-access Creative Commons license.)*

a-twin boundaries as follows.

- Put an a-twin boundary indexed as 1 in Fig. 3.32.
- Rotate 70°32′ anti-clockwise from a-twin boundary 1 and put another a-twin boundary 2.
- Rotate 70°32′ anti-clockwise from a-twin boundary 2 and put another a-twin boundary 3.
- Rotate 70°32′ anti-clockwise from a-twin boundary 3 and put another a-twin boundary 4.
- Rotate 70°32′ anti-clockwise from a-twin boundary 4 and put another a-twin boundary 5.

The misorientation angle for all prescribed a-twin boundaries is 70°32′. The eigenwall field $\boldsymbol{S}^i$ for each a-twin boundary has support within the interface layers as shown in Fig. 3.32, and is specified through (3.34), with vectors $\boldsymbol{a} = \boldsymbol{e}_2$ and α^i as follows:

i	1	2	3	4	5
α^i	0.212π	0.606π	π	1.394π	1.788π

.

The numbers $1, 2, .., 5$ correspond to the indices in Figure 3.32. Recall (3.35)

$$\boldsymbol{\Pi} = \frac{s}{ct}\boldsymbol{e}_2 \otimes (\sum_i \boldsymbol{n}^i),$$

it can be verified that $\sum_i \boldsymbol{n}^i$ is no longer $\boldsymbol{0}$ for the prescribed i-a penta-twin. Thus, $\boldsymbol{\Pi}$ is non-zero. Although $\boldsymbol{W}$ is still compatible for the same reason discussed in the penta-a-twin case, $\hat{\boldsymbol{W}}$ will not be zero and this produces stress. Figure 3.33 shows the stress fields σ_{11} from the small and finite deformation settings, respectively.

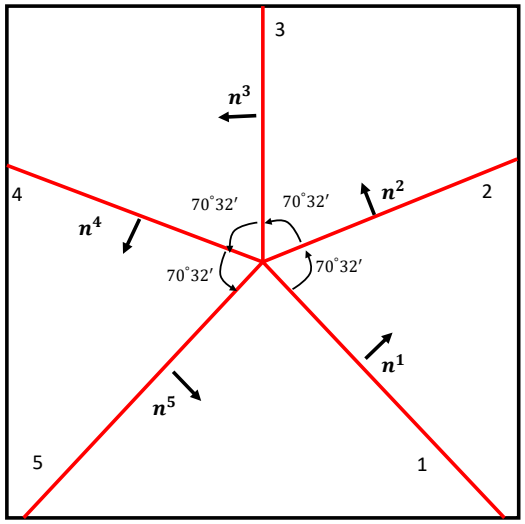

Figure 3.32: *An illustration of the configuration of i-a penta-twin with misorientation angle* $70°32'$. *The red lines show five a-twin boundary interfaces where* $\boldsymbol{S}$ *has support.*

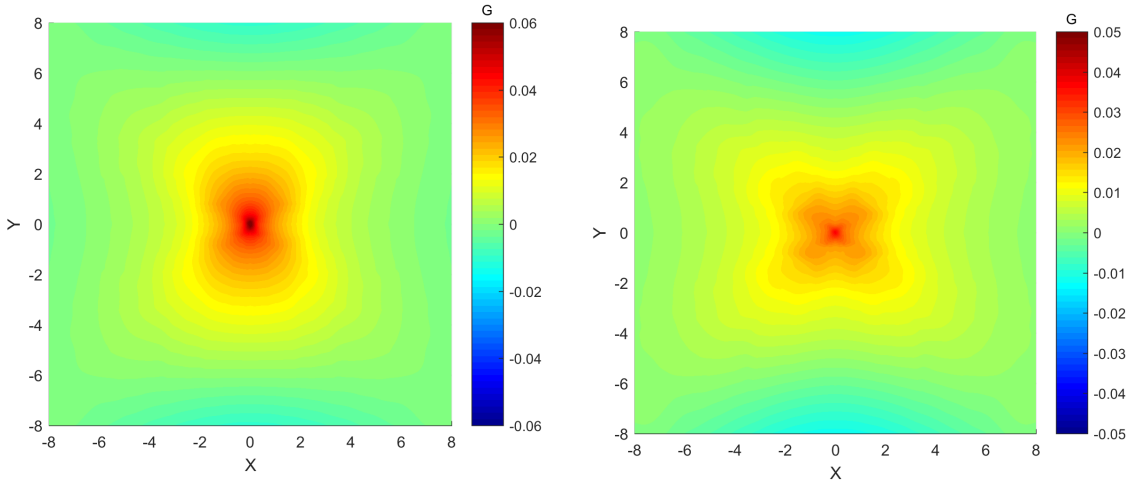

(a) Stress σ_{11} from small deformation setting. (b) Stress σ_{11} from finite deformation setting.

Figure 3.33: *Stress field* σ_{11} *of i-a penta-twin from both small deformation and finite deformation settings.*

3.5.11 Incompatible almost penta-twin with dislocations: stress shielding

Here we allow for dislocations to be present to maximally shield the stress field produced by the i-a penta-twin configuration in Sec. 3.5.10 and explore the resulting stress field and lattice orientation. The main idea is to introduce a dislocation density field to exactly be the excess content in $\boldsymbol{S}^{\perp} : \boldsymbol{X}$ beyond its projection on *curl*s of rotation fields, where $\boldsymbol{S}^{\perp}$ is the incompatible part of the eigenwall field $\boldsymbol{S}$ obtained by solving the dislocation-free problem of Sec. 3.5.10. The obtained rotation field is denoted as $\tilde{\boldsymbol{W}}$. Given the incompatible $\boldsymbol{S}^{\perp}$, $\tilde{\boldsymbol{W}}$ is obtained by

$$\tilde{\boldsymbol{\varphi}} := arg \min_{\boldsymbol{\varphi}} \int_B \frac{1}{2} \left(\operatorname{curl}((\boldsymbol{e}^{\boldsymbol{\varphi}})^{-1}) - \boldsymbol{S}^{\perp} : \boldsymbol{X} \right)^2 dv \tag{3.36}$$
$$\tilde{\boldsymbol{W}}^{-1} = \boldsymbol{e}^{\tilde{\boldsymbol{\varphi}}},$$

where $\boldsymbol{\varphi}$ is the rotation vector and $\boldsymbol{e}^{\boldsymbol{\varphi}}$ is the exponential map of the same, producing the corresponding orthogonal tensor (an alternative is to require $\tilde{\boldsymbol{W}}$ as an exponential map). By requiring $\tilde{\boldsymbol{W}}^{-1} = \boldsymbol{e}^{\tilde{\boldsymbol{\varphi}}}$, the i-elastic distortion field is required to be a rotation matrix. It can be shown that $\tilde{\boldsymbol{W}}$ obtained from (3.36) is one solution to the g.disclination theory as follows.

The introduced dislocation density is defined as

$$\boldsymbol{\alpha} := \boldsymbol{S}^{\perp} : \boldsymbol{X} - \operatorname{curl} \tilde{\boldsymbol{W}}. \tag{3.37}$$

Recalling (3.4),

$$\boldsymbol{\alpha} = \boldsymbol{S} : \boldsymbol{X} - \operatorname{curl} \boldsymbol{W} = \boldsymbol{S}^{\perp} : \boldsymbol{X} - \operatorname{curl} \hat{\boldsymbol{W}}. \tag{3.38}$$

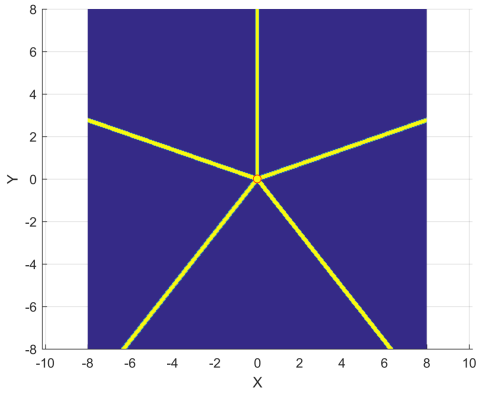

Figure 3.34: *Dislocation distribution in stress shielding case of the i-a penta-twin. The dislocation densities are localized along the five a-twin boundary interfaces with the identical magnitude.*

We now substitute (3.37) into (3.38),

$$\boldsymbol{S}^{\perp} : \boldsymbol{X} = (\boldsymbol{S}^{\perp} : \boldsymbol{X} - \operatorname{curl} \tilde{\boldsymbol{W}}) + \operatorname{curl} \hat{\boldsymbol{W}} \tag{3.39}$$

to obtain

$$\operatorname{curl} \hat{\boldsymbol{W}} = \operatorname{curl} \tilde{\boldsymbol{W}},$$

which implies $\tilde{\boldsymbol{W}}$ is a solution for $\hat{\boldsymbol{W}}$ in generalized disclination theory for this problem.

In the with-dislocation case, we find that the dislocation density field defined by (3.37) is localized along the five a-twin boundary interfaces (Figure 3.34). Furthermore, the norm of the dislocation density along all five a-twin boundary interfaces is the same.

Fig. 3.35(a) shows the lattice vectors of the dislocation-free case mapped by $\hat{\boldsymbol{W}}^{-1}$ from a uniformly oriented reference. Fig. 3.35(b) shows the lattice shapes of the with-dislocation case mapped by $\tilde{\boldsymbol{W}}$. The dislocation densities eliminate the stress as well as far-field distortion caused by the disclination at the center of the domain. In Figure 3.35(b), the lattice shapes in the current configuration are chosen to be the same ones in Fig. 3.28(b). Since $\tilde{\boldsymbol{W}}$ is a spatially inhomogeneous rotation field, it cannot be compatible and the connectivity for each pair across the a-twin boundaries does not persist, as shown in Fig. 3.35(b). In Fig. 3.35(b), the black contiguous edges in the current configuration

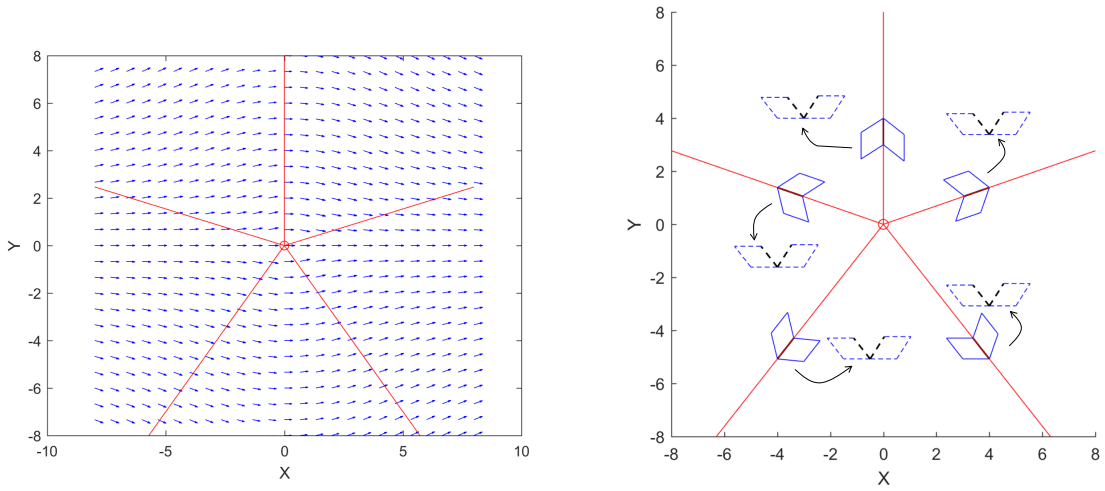

(a) i-elastic distortion field in dislocation-free case mapped by $\hat{\boldsymbol{W}}$.

(b) The rendition of unit cell shapes in the with-dislocation case mapped by $\tilde{\boldsymbol{W}}$.

Figure 3.35: *The i-distortion fields of the dislocation-free case represented by a vector field, and the rendition of unit cell shapes for the with-dislocation i-a penta-twin case. In the dislocation-free case, the distortion field involves elastic strain. In the with-dislocation case, the distortion field is a stress-free rotation field, which is incompatible. The connectivity at the black contiguous edges do not persist.*

do not remain connected in the reference.

This example emphasizes the need for dynamics as it is physically reasonable to expect that the production of the maximal supply of dislocations to shield the stress field of the i-a penta-twin should be subject to kinetic constraints.

3.5.12 3-D fields: disclination loop and lenticular, plate, and lath microstructures

Problems that have to be posed in three-dimensional domains are now solved. We apply g.disclination theory to study a disclination loop, and lenticular, plate, and lath microstructures. All the results presented in this section are solved within with the finite deformation setting. The body is assumed to be a brick with dimensions of $10 \times 10 \times 10$ and eight-node, hexahedral, bilinear finite elements are used with size $0.1 \times 0.1 \times 0.1$ (recall that lengths are in terms of the layer width for the eigenwall distributions involved).

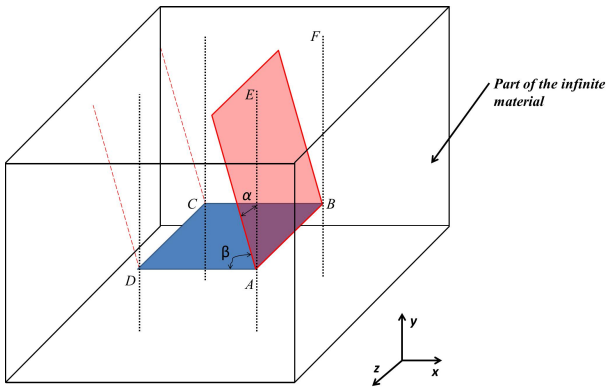

Figure 3.36: *Disclination loop configuration in 3d case. The misorientation angle is α. AB and CD are wedge disclinations while AD and BC are twist disclinations.*

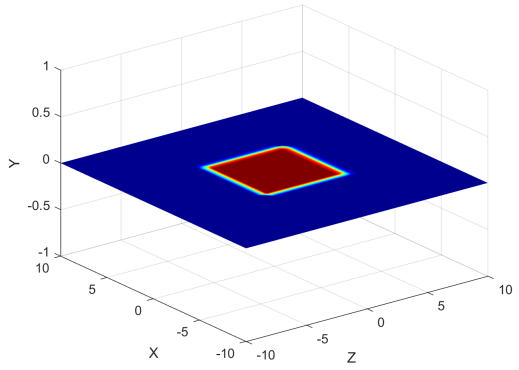

Figure 3.37: *The eigenwall field $\boldsymbol{S}$ is constant with support in the layer.*

3.5.12.1 Disclination loop in 3d brick body

Consider a disclination loop in a 3d domain that is discussed in Chapter 2. The configuration of the disclination loop is shown in Figure 3.36, where AB and CD are wedge disclinations while AD and BC are twist disclinations. In this problem, we assume that the $\boldsymbol{S}$ comprises a rotation discontinuity with a 45° misorientation angle along the z axis, constant in the layer, as shown in Figure 3.37.

After assuming the matrix as the reference configuration, the prescribed eigenwall field is defined as

$$\boldsymbol{S} = \begin{cases} \Delta G_{ij} \boldsymbol{e}_i \otimes \boldsymbol{e}_j \otimes \boldsymbol{e}_3 & |y| \leq 1, |x| \leq 3 \text{ and } |z| \leq 3 \\ \boldsymbol{0} & \text{otherwise,} \end{cases}$$

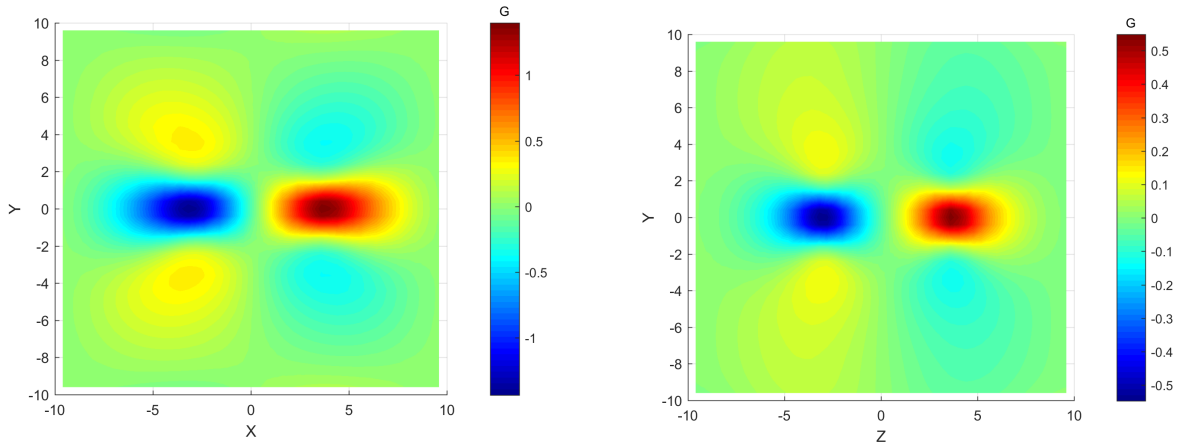

(a) Stress σ_{11} for disclination loop viewed on $z = 0$ plane in finite deformation setting.

(b) Stress σ_{13} for disclination loop viewed on $x = 0$ plane in finite deformation setting.

Figure 3.38: *Stress fields σ_{11} on $z = 0$ plane and σ_{13} on $x = 0$ plane in the finite deformation setting.*

where $i, j = 1, 2, 3$ and ΔG is given as

$$\begin{bmatrix} cos45° - 1 & sin45° & 0 \\ -sin45° & cos45° - 1 & 0 \\ 0 & 0 & 0 \end{bmatrix}.$$

Figure 3.38(a) and Figure 3.38(b) are the stress fields σ_{11} on the $z = 0$ plane and σ_{13} on $x = 0$ plane. The stress fields physically match with the description of the disclination loop in Chapter 2 that the disclination lines AB and CD parallel to z axis are wedge disclinations (σ_{11} is concentrated along AB and CD) and the disclination lines AD and BC parallel to x axis are twist disclinations (σ_{13} is concentrated along AD and BC).

3.5.12.2 Stress-inducing inclusion microstructures

In this Section we consider four different scenarios by which phase inclusions may induce stresses.

Figures 3.39(a) and 3.39(b) show the configurations of a lenticular inclusion and a

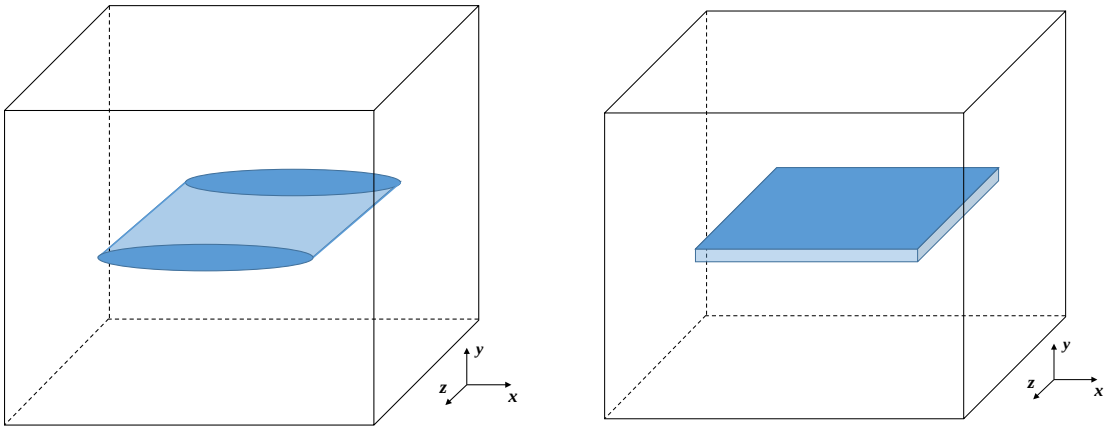

(a) Configuration of a lenticular inclusion in a matrix.

(b) Configuration of a plate inclusion in a matrix.

Figure 3.39: *Illustrations of the lenticular and plate inclusions in a 3d matrix. In both cases, the inclusions are surrounded, on all sides, by the matrix.*

plate inclusion. In all cases, the eigenwall fields $\boldsymbol{S}$ are prescribed along the top and bottom planes of the inclusions; a dislocation density field $\boldsymbol{\alpha}$ is also prescribed when the interface is incompatible.

In the calculations for the plate inclusion, we consider martensite variant transformation problems where the distortions comprising the discontinuity represented by $\boldsymbol{S}$ are based on [LIO98]. The i-elastic distortion $\boldsymbol{W}_1$ of the martensite inclusion and $\boldsymbol{W}_2$ of the matrix are given as

$$\boldsymbol{W}_1 = \begin{bmatrix} 1 & -0.195 & 0 \\ 0 & 0.975 & 0 \\ 0 & 0 & 1 \end{bmatrix} \qquad \boldsymbol{W}_2 = \begin{bmatrix} 1 & 0 & 0 \\ 0 & 1 & 0 \\ 0 & 0 & 1 \end{bmatrix}. \tag{3.40}$$

The thickness of the top and bottom layers comprising the boundaries of the inclusion is 1. Figure 3.40 shows the stress components σ_{11} on the $z = 0$ plane and σ_{13} on the $x = 0$ plane for the plate inclusion. For the plate inclusion, the top and bottom interfaces are flat so the g.disclination density field $\boldsymbol{\Pi}$ as well as the stress field is localized at the terminating cores. Another commonly observed microstructural unit is a lath that can be easily modeled within our setting as a very thin and tall plate inclusion.

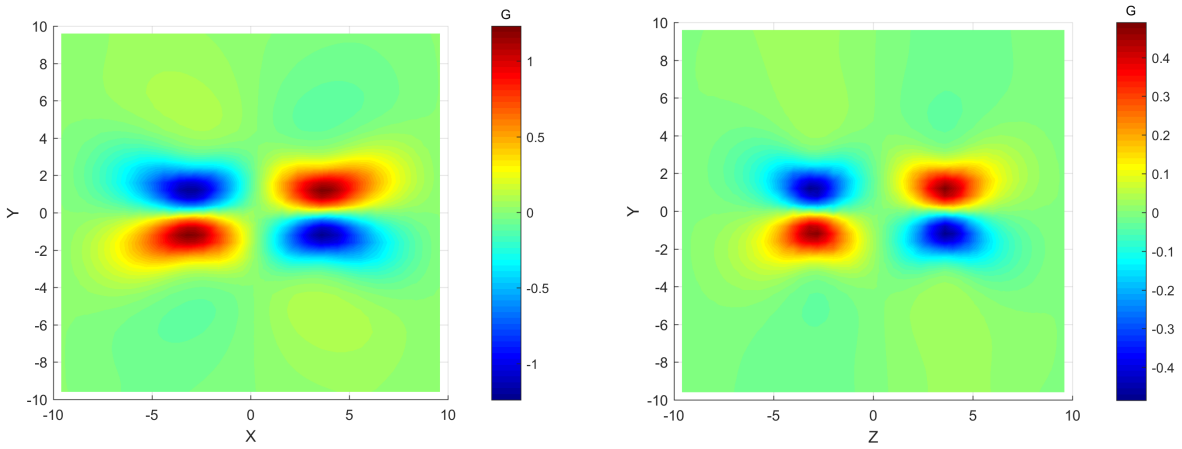

(a) Stress σ_{11} for the plate inclusion viewed on $z = 0$ plane in finite deformation setting.

(b) Stress σ_{13} for the plate inclusion viewed on $x = 0$ plane in finite deformation setting.

Figure 3.40: *Stress fields σ_{11} on $z = 0$ plane and σ_{13} on $x = 0$ plane for the plate inclusion problem.*

A second case we consider is a lenticular martensite inclusion with the transformation distortion of NiTi martensite-austenite adopted from [Bha03, Sec. 4.1] as follows

$$\boldsymbol{e}_i^m = \boldsymbol{F}\boldsymbol{e}_i^a,$$

where $\boldsymbol{e}_i^m$ is the image, in the martensite, of $\boldsymbol{e}_i^a$ a lattice vector in the austenite, and $\boldsymbol{F}^e$ is the austenite-martensite transformation distortion. $\boldsymbol{F}^e$ is given as

$$\boldsymbol{F}^e = \begin{bmatrix} 0.985 & -0.825 & -0.825 \\ 0 & 9.284 & 0.5 \\ 0 & 0.5 & 9.284 \end{bmatrix}.$$

In this situation, there does not exist a normal direction to a single interface such that $\boldsymbol{I} - \boldsymbol{F}^{e-1}$ can be represented in rank-one form. Consequently, there have to be dislocations along the interface. Assuming the austenite matrix as the reference configuration and

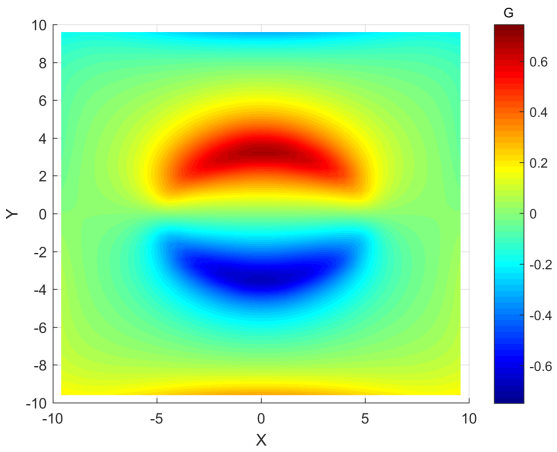

(a) Stress σ_{11} for the martensite lenticular inclusion in the austenite matrix viewed on $z = 0$ plane in finite deformation setting.

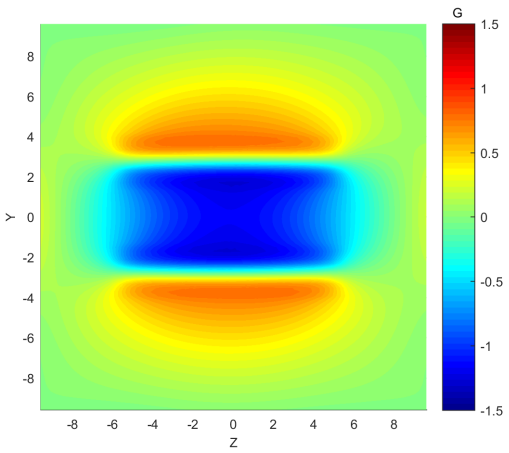

(b) Stress σ_{13} for the martensite lenticular inclusion in the austenite matrix viewed on $x = 0$ plane in finite deformation setting.

Figure 3.41: *Stress fields σ_{11} on $z = 0$ plane and σ_{13} on $x = 0$ plane for the martensite lenticular inclusion in an austenite matrix.*

following (3.13), we have

$$\boldsymbol{S} = \frac{\boldsymbol{I} - \boldsymbol{F}^{e-1}}{t} \otimes \boldsymbol{n},$$

where $t = 1$ is the layer thickness, and $\boldsymbol{n}$ is the layer normal pointing outwards from the inclusion. Since the misdistortion (and the eigenwall field) is constant along the interface, the g.disclination density $\boldsymbol{\Pi}$ is only non-zero at the terminating cores as discussed in Sec. 3.3.1. In addition, the interface for this martensite-austenite transformation is incompatible and a dislocation density field needs to be prescribed along the interface. In this calculation, we approximate the dislocation density $\boldsymbol{\alpha}$ following (3.33),

$$\boldsymbol{\alpha} = \left(\frac{\boldsymbol{I} - \boldsymbol{F}^{e-1}}{t} \otimes \boldsymbol{n} \right) : \boldsymbol{X}.$$

Figure 3.41 shows the stress component σ_{11} on $z = 0$ plane and σ_{13} on $x = 0$ plane for the lenticular martensite-austenite transformation. Due to the dislocation density $\boldsymbol{\alpha}$ along the interface, the stress is not zero along the interface.

Another case of theoretical interest is a lenticular martensite variant transformation,

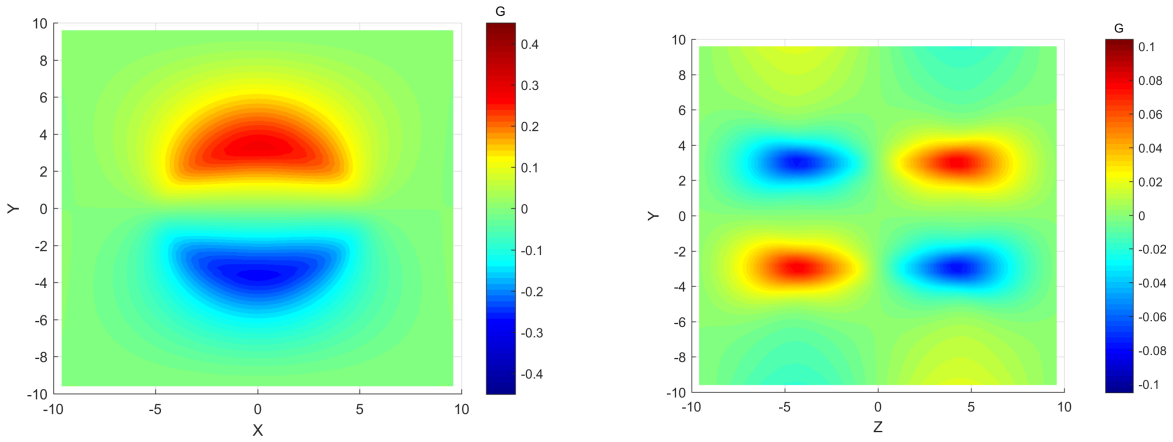

(a) Stress σ_{11} for the lenticular martensite transformation viewed on $z = 0$ plane in finite deformation setting.

(b) Stress σ_{13} for the lenticular martensite transformation viewed on $x = 0$ plane in finite deformation setting.

Figure 3.42: *Stress fields σ_{11} on $z = 0$ plane and σ_{13} on $x = 0$ plane for the lenticular martensite transformation.*

where the interface is compatible. In this calculation, we adopt the Ni-Mn-Ga material from [KNT+11], whose orientation angle between two (stress-free) variants is 11.6°. We assume the misdistortion between the inclusion and the matrix along the curved interface to be $\tan(11.6°)\boldsymbol{t} \otimes \boldsymbol{n}$, with $\boldsymbol{t}$ being a unit vector parallel to the curved interface and $\boldsymbol{n}$ being the interface normal vector. Thus, the eigenwall field $\boldsymbol{S}$ is non-zero within the curved layers (top and bottom boundaries of the inclusion) and can be written as

$$\boldsymbol{S} = \begin{cases} \tan(11.6°)\boldsymbol{t} \otimes \boldsymbol{n} \otimes \boldsymbol{n} & \text{in the layer} \\ \boldsymbol{0} & \text{otherwise.} \end{cases}$$

Figure 3.42 shows the stress components σ_{11} on $z = 0$ plane and σ_{13} on $x = 0$ plane for the lenticular martensite transformation. Although we do not prescribe the dislocation density $\boldsymbol{\alpha}$ due to the compatible interface, the $\boldsymbol{\Pi}$ is no longer localized at the terminating cores based on the reasoning in (F.8) in Appendix F. Thus, the stress field along the interfaces is non-zero, as shown in Figure 3.42(a).

We now calculate the fields of a needle shaped inclusions of one martensite variant in

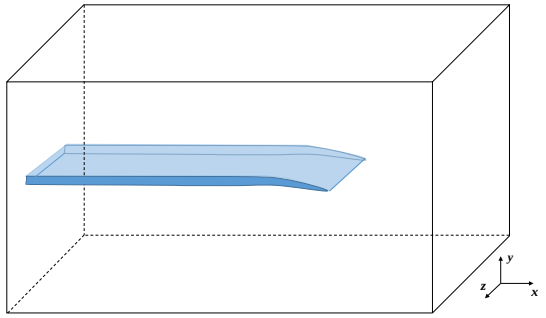

(a) Illustration of the needle inclusion of one martensite variant in another.

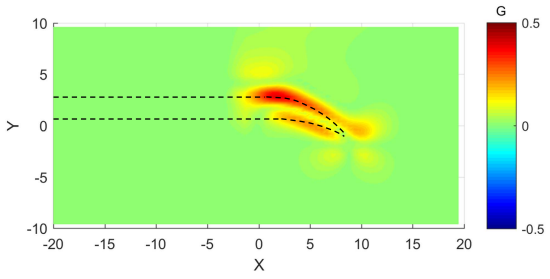

(b) Magnitude of the stress $\boldsymbol{\sigma}$ for the needle inclusion viewed on $z = 0$ plane in finite deformation setting.

Figure 3.43: *The needle martensite inclusion configuration and magnitude of the stress $\boldsymbol{\sigma}$ on $z = 0$ plane. The stress field is localized along the curved interface.*

another, motivated by the observations in [SGL11]. As opposed to the previous case of a curved interface carrying a rank-one misdistortion at all points, but inducing stresses due to the development of a g.disclination distribution along it, in this example the flat parts of the interface carry no defects, but a stress is developed because the normal to the curved parts of the interface do not agree with the normal direction required by the misdistortion to be compatible (note that this is different from the austenite-martensite transformation described earlier where no flat compatible interface exists). Thus, a dislocation density field needs to be specified along the interface and we specify it in the form

$$\boldsymbol{\alpha} = \left(\frac{\boldsymbol{W}_2 - \boldsymbol{W}_1}{t} \otimes \boldsymbol{n} \right) : \boldsymbol{X},$$

where $\boldsymbol{n}$ is the interface normal pointing outwards from the inclusion, t is the layer thickness, and $\boldsymbol{W}_1$ and $\boldsymbol{W}_2$ are i-elastic distortions specified in (3.40).

Figure 3.43(a) shows the needle inclusion configuration of our calculation and the Figure 3.43(b) shows the l^2-norm of $\boldsymbol{\sigma}$ for the needle inclusion viewed on $z = 0$ plane with finite deformation setting. The stress is localized along the curved interface due to the dislocation density generated from the incompatibility.

3.6 Contact with the classical elastic disclination theory.

We show here the circumstances in which g.disclination theory reduces exactly to DeWit's [DeW73a] defect model, including uniqueness assertions for the stress in both models. Due to the classical theory being established for small deformations, our considerations here are restricted to the small deformation case.

Recall the governing relation $\operatorname{curl} \boldsymbol{S} = \boldsymbol{\Pi}$. A single isolated g.disclination can be specified by specifying $\boldsymbol{S}$ as an eigenwall field with support in a terminating layer, with appropriate decay properties in a core cylinder at its termination that results in a non-vanishing $\boldsymbol{\Pi}$ field being defined there. As in (3.5), $\boldsymbol{S} = \boldsymbol{S}^{\perp} + \operatorname{grad} \boldsymbol{Z}^{s}$. We can decompose $\boldsymbol{S}^{\perp}$ into two part, $\boldsymbol{S}^{\perp} = \boldsymbol{S}^{\perp skw} + \boldsymbol{S}^{\perp sym}$, where $\boldsymbol{S}^{\perp skw}$ is a third-order tensor tensor skew in the first two indices and $\boldsymbol{S}^{\perp sym}$ is symmetric in the first two indices:

$$\boldsymbol{S}^{\perp skw}_{ijk} = \frac{1}{2}(\boldsymbol{S}^{\perp}_{ijk} - \boldsymbol{S}^{\perp}_{jik}); \qquad \boldsymbol{S}^{\perp sym}_{ijk} = \frac{1}{2}(\boldsymbol{S}^{\perp}_{ijk} + \boldsymbol{S}^{\perp}_{jik}).$$

Then we have

$$\boldsymbol{\Pi} = \operatorname{curl} \boldsymbol{S}^{\perp} = \operatorname{curl}(\boldsymbol{S}^{\perp skw} + \boldsymbol{S}^{\perp sym}) = \operatorname{curl} \boldsymbol{S}^{\perp skw} + \operatorname{curl} \boldsymbol{S}^{\perp sym},$$

and we define

$$\boldsymbol{\Pi}^{skw} := \operatorname{curl} \boldsymbol{S}^{\perp skw}; \quad \boldsymbol{\Pi}^{sym} := \operatorname{curl} \boldsymbol{S}^{\perp sym}$$

so that

$$\boldsymbol{\Pi} = \boldsymbol{\Pi}^{skw} + \boldsymbol{\Pi}^{sym}.$$

It can be checked from the definitions (3.5) and (3.6) that if $\boldsymbol{S}$ is skew in its first two-indices, then $\boldsymbol{S}^{\perp}_{sym} = \boldsymbol{0}$. The same conclusion holds if $\boldsymbol{\Pi}$ is skew in its first two indices.

Recall the dislocation density $\boldsymbol{\alpha}$ defined in (3.4)

$$\begin{aligned}
&\boldsymbol{\alpha} = \boldsymbol{S} : \boldsymbol{X} + \operatorname{grad} \boldsymbol{W} : \boldsymbol{X} \Rightarrow \boldsymbol{\alpha} = \boldsymbol{S}^{\perp} : \boldsymbol{X} + \operatorname{grad} \hat{\boldsymbol{W}} : \boldsymbol{X} \\
&\alpha_{il} = -\epsilon_{lkj} \hat{W}_{ij,k} + \epsilon_{jkl} S^{\perp}_{ijk} \\
&\Rightarrow \epsilon_{rqi} \alpha_{il,q} = -\epsilon_{rqi} \epsilon_{lkj} \hat{W}_{ij,kq} + \epsilon_{rqi} \epsilon_{jkl} S^{\perp}_{ijk,q} \Rightarrow \epsilon_{rqi} \alpha^{T}_{li,q} = -\epsilon_{rqi} \epsilon_{lkj} \hat{W}_{ij,kq} + \epsilon_{ljk} \epsilon_{rqi} S^{\perp}_{ijk,q}.
\end{aligned} \tag{3.41}$$

Substituting $\boldsymbol{S}^{\perp} = \boldsymbol{S}^{\perp skw} + \boldsymbol{S}^{\perp sym}$ into the second term of (3.41), we have

$$\epsilon_{ljk} \epsilon_{rqi} S^{\perp}_{ijk,q} = \epsilon_{ljk} \epsilon_{rqi} (S^{\perp skw}_{ijk,q} + S^{\perp sym}_{ijk,q}). \tag{3.42}$$

Since $\boldsymbol{S}^{\perp skw}$ is skew in the first two indices, there exists a second order tensor $\boldsymbol{\omega}$ such that

$$S^{\perp skw}_{ijk} = \epsilon_{ijs} \omega_{sk} \tag{3.43}$$

so that

$$\Pi^{skw}_{ijk} = \epsilon_{knm} S^{\perp skw}_{ijm,n} \;\Rightarrow\; \Pi^{skw}_{ijk} = \epsilon_{knm} \epsilon_{ijs} \omega_{sm,n} \;\Rightarrow\; \epsilon_{ijq} \Pi^{skw}_{ijk} = \epsilon_{knm} \omega_{qm,n}. \tag{3.44}$$

Equations (3.42), (3.43), and (3.44) yield

$$\epsilon_{ljk} \epsilon_{rqi} S^{\perp}_{ijk,q} = \epsilon_{ljk} \epsilon_{rqi} \epsilon_{ijs} \omega_{sk,q} + \epsilon_{ljk} \epsilon_{rqi} S^{\perp sym}_{ijk,q}. \tag{3.45}$$

Using (3.45) and (3.44) to note that

$$\epsilon_{rqi} \epsilon_{ljk} \epsilon_{ijs} \omega_{sk,q} = \epsilon_{rqi} [\delta_{li} \delta_{ks} - \delta_{ls} \delta_{ki}] \omega_{sk,q} = \epsilon_{lrq} \omega_{kk,q} + \epsilon_{ijl} \Pi^{skw}_{ijr}, \tag{3.46}$$

we have

$$\epsilon_{ljk} \epsilon_{rqi} S^{\perp}_{ijk,q} = \epsilon_{lrq} \omega_{kk,q} + \epsilon_{ijl} \Pi^{skw}_{ijr} + \epsilon_{ljk} \epsilon_{rqi} S^{\perp sym}_{ijk,q}. \tag{3.47}$$

For small deformations, $\hat{\boldsymbol{W}} = \boldsymbol{I} - \hat{\boldsymbol{U}}^e$ and we decompose $\hat{\boldsymbol{U}}^e$ into symmetric and skew parts, $\hat{\boldsymbol{U}}^e = \hat{\boldsymbol{\epsilon}}^e + \hat{\boldsymbol{\Omega}}^e$. Then we have

$$\frac{1}{2}\left(\epsilon_{rqi}\epsilon_{lkj}\hat{W}_{ij,kq} + \epsilon_{lqi}\epsilon_{rkj}\hat{W}_{ij,kq}\right) = -\epsilon_{rqi}\epsilon_{lkj}\hat{\epsilon}^e_{ij,kq}. \tag{3.48}$$

Therefore, substituting (3.47) and (3.48) into (3.41) and taking the symmetric part, we have

$$\left[\text{curl}\left(\boldsymbol{\alpha}^T\right)\right]_{sym} - (\boldsymbol{\Pi} : \boldsymbol{X})_{sym} - \left(\text{curl}\left[\left(\boldsymbol{S}^{\perp sym} : \boldsymbol{X}\right)^T\right]\right)_{sym} = \text{inc}(\hat{\boldsymbol{\epsilon}}^e), \tag{3.49}$$

where *inc* is the St. Venant compatibility operator. When $\boldsymbol{S}^{\perp sym} = \boldsymbol{0}$, $\boldsymbol{\Pi} = \boldsymbol{\Pi}^{skw}$ and (3.49) becomes

$$\left[\text{curl}(\boldsymbol{\alpha}^T)\right]_{sym} - (\boldsymbol{\Pi} : \boldsymbol{X})_{sym} = \text{inc}(\hat{\boldsymbol{\epsilon}}^e), \tag{3.50}$$

which indicates that $\text{inc}(\hat{\boldsymbol{\epsilon}}^e)$ is sourced by the defect density fields $\boldsymbol{\alpha}$ and $\boldsymbol{\Pi}$. The linear elastic stress field $\boldsymbol{T} = \boldsymbol{C}\hat{\boldsymbol{\epsilon}}^e$, with $\boldsymbol{C}$ having the minor symmetries, satisfies equilibrium

$$\text{div}(\boldsymbol{C} : \hat{\boldsymbol{\epsilon}}^e) = \boldsymbol{0}. \tag{3.51}$$

When $\boldsymbol{S}^{\perp sym} = \boldsymbol{0}$, DeWit's disclination density $\boldsymbol{\theta}$ can be defined as $\boldsymbol{\Pi} : \boldsymbol{X}$ and equations (3.50) and (3.51) become exactly DeWit's model [DeW73a].

Thus, we have shown that the stress and $\hat{\boldsymbol{U}}^e_{sym}$ of any solution of small deformation g.disclination theory (3.10) satisfies the equations of DeWit's theory when $\boldsymbol{S}^{\perp sym} = \boldsymbol{0}$.

It is shown in Appendix H that (3.50) and (3.51) suffice to uniquely determine the stress field in finite bodies when $\boldsymbol{C}$ is positive-definite (possibly spatially inhomogeneous and with arbitrary anisotropy), when the left-hand-side of (3.50) and statically admissible applied boundary tractions are prescribed data. Hence, for this data, solutions for stress and $\boldsymbol{U}^e_{sym}$ exactly match solutions for the same quantities from DeWit's model.

In Appendix H we also prove uniqueness of solutions to linear g.disclination theory and show that for identical prescribed data corresponding to pure disclinations, dislocations and applied tractions, g.disclination theory produces more information than classical disclination theory.

3.7 Conclusion

G.disclination theory [AF15] is reviewed and computationally implemented in the limited context where the dislocation density field $\boldsymbol{\alpha}$ and either the eigenwall field $\boldsymbol{S}$ or g.disclination density field $\boldsymbol{\Pi}$ are given as input data. The theory deals with discontinuities in elastic distortion involving defects beyond translational dislocations and rotational disclinations.

A numerical scheme based on the Least Squares and Galerkin Finite element methods for solving the g.disclination theory is developed. Both the small deformation (linear) and finite deformation (nonlinear) settings are considered. Various grain and phase boundary problems, including dislocations and disconnections, are solved. By comparing results from our model with the results of classical linear defect theory due to DeWit [DeW73a] for both the single disclination and the single dislocation, we have demonstrated that our model is capable of recovering the essential beyond-core features of Volterra defects. Contact has also been made with the Eshelby cut-weld interpretation of a single disclination, at finite deformations. The necessity of accounting for finite deformation theory in many problems related to defects with high misorientations has been demonstrated.

Future work will involve the development of computational tools for the analysis of the full dynamical theory of defect evolution presented in [AF15]. Interestingly, the results of this paper seem to suggest that it may very well be within the reach of the dynamical model to deal with non-convex surface energies typical of physically measured grain boundary energies, and to deal with phase transformation problems at large deformations without

the use of non-convex elastic stress-strain relationships.

Chapter 4

A non-traditional view on the modeling of nematic disclination dynamics

4.1 Introduction

Liquid crystals (LC) are matter in a state whose properties are between liquids and solids. Research on liquid crystals is currently advancing quite rapidly motivated by applications and discoveries in material science as well as in biological systems. There are many types of liquid crystal states, depending on the amount of order in the material. A nematic phase consists of rod like molecules that retain some long-range orientational order. In this work, we are primarily interested in modeling disclinations in a uniaxial nematic liquid crystalline medium, treated by an augmentation of the classical model (cf. [Ste04]) where the director order parameter is represented by a unit vector field.

The classical theories of liquid crystal mechanics like the Oseen-Frank and Ericksen-Leslie models predict unbounded energy in finite bodies with discrete disclinations. Recently, a kinematic augmentation of classical Leslie-Ericksen theory [AD13, PAD15] has been devised that allows alleviating the singularity, with results being demonstrated for the case where the defect field is not allowed to evolve. These works aim to achieve an understanding of the connections between the classical theory of defects, such as solid dislocations and disclinations introduced by Weingarten and Volterra, and the theory of defected liquid crystals, a line of enquiry that began from the work of Kleman [Klé73]. In [AD13], the model introduces an augmented Oseen-Frank kinematics and involves a director field and an incompatible director distortion field that is not *curl-free*. In [PAD15], a finite element based numerical scheme was used to solve for the director fields of prescribed static disclinations and a critical examination presented of the similarities and differences that arise between the modeling of LC disclinations and solid dislocations using the eigendeformation approach [PAD15]. In this paper, we study this augmented model with natural constitutive modifications to enable the study of equilibria and evolution of LC disclinations, including those of half integer strength. First, a gradient flow dynamics of the augmented energy is utilized and used to calculate equilibrium solutions. However, we find that the gradient

flow dynamics for this energy is not suitable for modeling the defect evolution problem, and explain why this must be so. Motivated by the crystal dislocation case, a 2D model based on the augmented energy, thermodynamics, and the kinematics of conservation of defect topological charge is constructed to analyze nematic disclination dynamics. We validate this model through computations for disclination equilibria, annihilation, repulsion, and dissociation.

Non-singular equilibria and dynamics of liquid crystal point and line defects have been studied in the literature, particularly within the Landau de-Gennes (L-dG) framework [dGP95, SV12, MN14, SS87, BPP12, RŽ09, DFRSZ14, KŽA91, MMRN12, INSZ14, INSZ15, INSZ13, NZ10, CK72, BBCH92, BV97, Can13, FS09, GM14, HM12, KVŽ99, MGJ00]. A more limited number of studies have been carried out in the Oseen-Frank and Leslie-Ericksen models as well as Ericksen's model for nematics with variable degree of orientation [Fra58, CK72, BBCH92, Vir95, BS03, BS05, SV97, GSV02, HKL88, BCG05, LL95, LL00, Wal11b]. The general consensus from the literature is that finite energy line-defects, including those of half-integer strength, can only be predicted by the full L-dG theory among all the models mentioned above.

As a point of departure, Ball and Bedford [BB15] suggest the use of discontinuous order parameter fields, in particular a discontinuous vector order parameter field to represent uniaxial nematics. The exploration there is essentially kinematical and focuses primarily on the appropriate mathematical function spaces to be used, stopping short of demonstrating specific examples of solutions (or approximations thereof) of defect equilibria resulting from the use of energy functions and dynamical models based on their discontinuous kinematics. Our work, in essence, achieves precisely this goal, thus being complementary to [BB15]. While our computational work does not employ discontinuous fields, it is demonstrated and explained why our approach yields, in a sense, the natural practical approximation of such discontinuous limiting director fields.

The work of Gartland [GJ15] demonstrates how the classical Oseen-Frank energy may

be viewed as a constrained form of the Landau-deGennes energy at temperatures below the 'supercooling temperature.' Since in this temperature range the bulk Landau-deGennes energy is minimized by Q-tensors representing the uniaxial nematic phase, the constrained L-dG energy of nematic configurations that contain line defects is infinite. Our work develops a modification of the Oseen-Frank energy that enables the prediction of finite-energy defect fields, utilizing a core energy regularization that involves a material length scale which may be associated with the 'nematic correlation length' ξ as defined in [GJ15].

4.2 Notation

This chapter follows the same terminology as the one in Section 1.3. The following list describes some of the mathematical symbols we use in this work:

$\boldsymbol{n}$: director

k: disclination strength

θ: angle of director field

$\boldsymbol{\lambda}$: layer field

l: layer thickness

ξ: core width

4.3 Augmented Oseen-Frank energy and corresponding gradient flow computations

It is generally believed that a theory of nematic line defects cannot be established with a representation of the nematic director by a unit vector field. Indeed, consider a nematic occupying a two-dimensional domain with the director field $\boldsymbol{n}$ taking values in $\mathbb{S}^1$. Assuming the validity of the universally accepted Oseen-Frank energy density function [Fra58, Ose33]

given by

$$\mathcal{F}_{OF} = K_1(\operatorname{div} \boldsymbol{n})^2 + K_2(\boldsymbol{n} \cdot \operatorname{curl} \boldsymbol{n})^2 + K_3|\boldsymbol{n} \times \operatorname{curl} \boldsymbol{n}|^2$$
$$+K_{24}(\operatorname{div} \boldsymbol{n})^2 - \operatorname{tr}(\operatorname{grad} \boldsymbol{n})^2)$$

where K_1, K_2, K_3, K_{24} are material dependent Frank elastic constants, it can be seen that the planar configuration of a straight, half-integer strength wedge disclination necessarily results in at least one curve $\mathcal{C}$ in the plane connecting the core of the defect to the external boundary such that the vector field $\boldsymbol{n}$ has to be discontinuous along $\mathcal{C}$. If the discontinuity were to be approximated by a thin region along $\mathcal{C}$ characterized by high gradients of the director, the Oseen-Frank energy of the resulting configuration would yield a physically unobserved region of very high energy density. One of our goals in this paper is to propose a model that adequately resolves this problem by augmenting the director model by an additional field. The resulting model is different from the Landau De-Gennes Q-tensor model [MN14], and makes close connections to models of line defects in other fields, such as crystal plasticity and phase transitions in solids.

The Oseen-Frank energy function is a quadratic function in the director field[1] and its gradients. With the half-integer defect as a motivation, it would seem that if director discontinuity associated with the winding of the director by π radians were to be assigned a vanishing energy cost, then progress may be made on modeling line defects. Mathematically, suppose that the director $\boldsymbol{n}$ winds by π radians over the distance l in the direction of a unit vector $\boldsymbol{p}$, where l is a parameter with physical dimensions of length. Associating a zero energy cost to the jump of the director by π radians across the line perpendicular

[1]From here onwards, we will use the imprecise short-form of 'director field' to refer to the 'director vector field.'

to $\boldsymbol{p}$ can be stated as a condition

$$0 = \mathcal{F}(\boldsymbol{n}, \boldsymbol{0}) = \mathcal{F}\left(\boldsymbol{n}, \frac{2\boldsymbol{n}}{l} \otimes \boldsymbol{p}\right) = \mathcal{F}(-\boldsymbol{n}, -\frac{2\boldsymbol{n}}{l} \otimes \boldsymbol{p}) \ \ \forall\, \boldsymbol{p} \tag{4.1}$$

as $l \to 0_+$. This is equivalent to demanding a zero energy cost for a flip of π radians over a layer of width l in the limit of vanishing layer width. The second equlity in (4.1) stems from the condition

$$\mathcal{F}_{OF}(\boldsymbol{n}, \operatorname{grad} \boldsymbol{n}) = \mathcal{F}_{OF}(-\boldsymbol{n}, -\operatorname{grad} \boldsymbol{n})$$

arising from the head-tail symmetry of the nematic molecules[2]. As illustration, these requirements mean there is no energy in the case shown in Figure 4.1(a) which is physically equivalent to Figure 4.1(b) and Figure 4.1(c). For fixed $\boldsymbol{n}$, this implies a multiple-well structure of the energy density in the director gradient slot of $\mathcal{F}$.

Figure 4.2 shows another justification for demanding nonconvexity of the energy-density. It shows two spatial points in the nematic liquid crystal located close to each other, represented as the red dots (point ① and point ②). The director at point ① is assumed be in the horizontal direction pointing to the right, shown as the black line. At point ②, the director is considered as a vector originating from this point ② and rotates clockwise. The angle between the director at point ① and the director at point ② is denoted as θ. First, θ will increase from 0° to 90°, represented as the blue angle in Figure 4.2, and the angle α used to identify the angular separation and gradient for calculation of the the energy density equals θ, which causes the energy density to increase. When the director rotation passes 90°, although the angle θ between the two directors keeps increasing, the angle α used to calculate the energy density is $\pi - \theta$ (the orange angle in Figure 4.2) since physically the director has no direction. Thus, when θ increases from 90° to 180° the energy

[2]Of course, the choice of a flip by π radians in (4.1) is also intimately connected to head-tail symmetry of the nematic molecules.

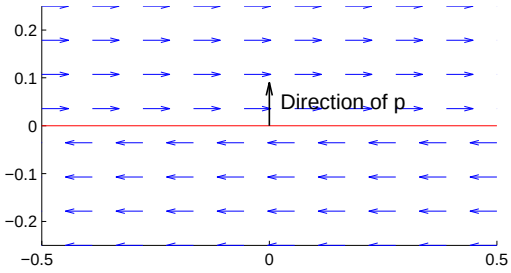

(a) Director field, represented as a vector field, changes direction through a layer in the center of the body, but there is no disclination and the energy is zero.

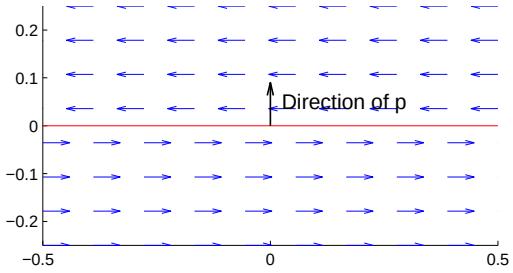

(b) The equivalent case with a different vector field.

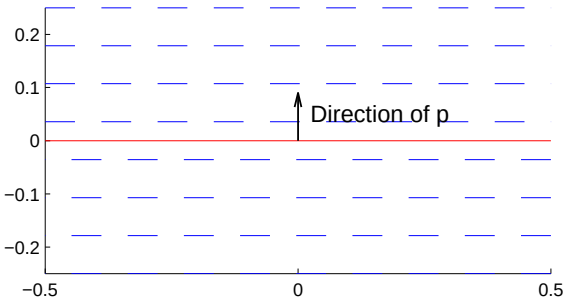

(c) The director field without artificial arrows.

Figure 4.1: *Illustration of issues with representation of the director field by a vector field.*

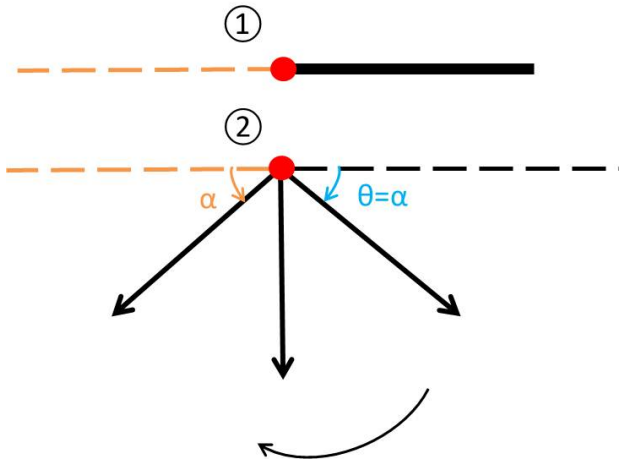

Figure 4.2: *Illustration of the reason for non-convexity of the energy density. The angle between the director and its neighbor displays periodicity with change in direction.*

density decreases. In addition, the energy density will reach its maximum when the angle θ reaches 90°.

High director gradients, uniform along layers, and with little energy cost from such layers may be expected in models with the above nonconvexity in the energy density. However, a state with a single disclination is the limit, as the layer width goes to zero, of a continuous, global director configuration that has a high, uniform director gradient in a section of a thin layer, transitioning to gradients of negligible magnitude in the rest of the layer (the parts of the layer $-l/2 < y < l/2$ to the right and to the left of $x = 0$, respectively, in Figure 4.3(e). Here $0 < l \ll 1$.). The transition region in the layer is the core of the disclination. Since the director configuration varies continuously, from its value on the top of the section of the layer with non-negligible gradient to its value at the bottom (of the same section of the layer) along any path going around the core, it is easy to see that such a global configuration has to contain substantial total energy on the whole (see Figure 4.3(e)). Since it is physically reasonable to expect such director configurations to exist without imposed loadings, it is clear that the attainment of such states cannot be a question of global energy minimization, and almost definitely not in a model whose energy density is quadratic in the director gradients (as for example in the

1-constant Oseen-Frank energy density approximation in Leslie-Ericksen theory). It is also believed that disclination cores move under their mutual interaction, even in the absence of applied loads, with speeds unrelated to causes of orientational or positional inertia of the material. Indeed, the Ericksen-Leslie equations governing the director field are most often used without any orientational inertia. Moreover, it seems reasonable to develop models where motion of defects are allowed even in the absence of flow; as justification we quote the following excerpt from Ericksen [Eri95], discussing parallel, straight disclinations:

"Saupe is very familiar with observations of disclinations of this kind, his own and those made by others. Typically, they are observed in specimens contained between a cover plate and a glass slide, in a polarizing microscope. Generally, they do move, but not alway[s] rapidly. There are empirical rules, of a topological nature, for determining the kinds that attract (or repel) each other, such as were discussed by Friedel [12], for example. *As they move, they cause little or no flow; experimentalists tell me that it is hard to detect any so caused, although, they don't doubt that, in principle, there is some.*[3] Dynamical theory does involve viscous contributions, modifying the constitutive equations, etc., associated with the time rate of change of the director as well as the velocity field. From what I know of the theory and observations, I don't believe that one can use equilibrium theory to analyze these phenomena...."

Based on the above observations, it appears to us that accommodating general disclination dynamics, including that of half-integer strength disclinations, within the structure of Leslie-Ericksen theory or Ericksen [Eri91] is probably an unattainable goal. Thus, we augment the kinematics (and dynamical structure) of Leslie-Ericksen theory with an additional field that allows for equilibria and motion of non-singular disclinations, as described below.

We follow the primarily kinematical ideas presented in [PAD15] and restrict attention to the planar case. We assume that the director $\boldsymbol{n}$ is a unit vector which therefore can be

[3]The italicization here is ours.

parametrized with an angle field, i.e., $\boldsymbol{n} = \cos\theta \boldsymbol{e}_1 + \sin\theta \boldsymbol{e}_2$. As in [PAD15] we introduce a *layer field* $\boldsymbol{\lambda}$. Furthermore, we assume that the energy E, depending on the fields $grad\,\theta$ and $\boldsymbol{\lambda}$, takes the form

$$E = \int_V \left[\frac{K}{2} |\operatorname{grad}\theta - \boldsymbol{\lambda}|^2 + \frac{\epsilon}{2} |\operatorname{curl}\boldsymbol{\lambda}|^2 + \gamma f(\boldsymbol{\lambda}) \right] dv. \tag{4.2}$$

Here $K > 0$ is a constant parameter representing 1-constant Oseen-Frank elasticity. The parameter $\epsilon := KCa\xi^2$ depends on the disclination core width $\xi > 0$, a fundamental length scale of the model, a non-dimensional parameter C to control the magnitude of the core energy, and the width of the layer $l = a\xi$, where $a \geq 0$ is a non-dimensional scaling factor. To allow for conventional expectations, we will accommodate the limit $a \to 0$ and still allow for finite energy disclination solutions (recall that $\xi > 0$). The parameter γ is defined as $\gamma := \frac{2PK\hat{k}}{a\xi^2}$, with P being a non-dimensional penalty parameter, and $\hat{k} := \frac{1}{2}$. f is a multi-well function with minima of wells at integer multiples of $\frac{2\pi\hat{k}}{a\xi}$. A typical candidate for the function f that we use in this work is

$$f(\boldsymbol{\lambda}) = 1 - \cos\left(2\pi \frac{|\boldsymbol{\lambda}|}{\left(\frac{2\pi\hat{k}}{a\xi}\right)} \right) = 1 - \cos\left(\xi |\boldsymbol{\lambda}| \left(\frac{\hat{k}}{a}\right)^{-1} \right). \tag{4.3}$$

Thus $|\boldsymbol{\lambda}| = \frac{2\pi k}{a\xi}$ for a strength-k disclination, where k is any integer-multiple of $\hat{k} = \frac{1}{2}$, minimizes this symmetry related, non-convex energy density term.

The intuition behind why the energy (4.2) can serve to represent disclinations is as follows. For a fixed specification of the field $\boldsymbol{\lambda}$ very similar to as specified in (4.6), it is shown in detail in [PAD15] that the director and energy density fields of disclination defects are well captured by a model whose static governing equation is the Euler-Lagrange equation of the energy (4.2) for variations only in the field θ. All that then remains to be convinced of is that the configuration of $\boldsymbol{\lambda}$ specified in (4.6) is close to one that extremizes the energy (4.2), with the associated θ field being the solution of the Euler-Lagrange equation of (4.2)

for θ-variations (i.e. the right-hand-side of $(4.5)_1$). This is easy to see as the magnitude of the $\boldsymbol{\lambda}$ field in (4.6) does lie in the wells of the function f. The term penalizing curl $\boldsymbol{\lambda}$ in (4.2) smooths out the transition of $\boldsymbol{\lambda}$ within the layer, as does the elastic energy term (the first term of the integrand in (4.2)[4]). This transition layer in curl $\boldsymbol{\lambda}$ within the layer signifies the core region of a disclination, and the parameter ϵ characterizes the core energy of the defect, with $\sqrt{\epsilon}$ roughly setting the core-width in the equilibrium solution. It is to be noted that the core energy (i.e the second term in the integrand in (4.2)) does not penalize the vertical gradients of the $\boldsymbol{\lambda}$ field in (4.6) across the horizontal boundaries of the layer.

The various parameters of the model have the following physical dimensions: $[E] = Force \times Length$, $[K] = Force$, $[\boldsymbol{\lambda}] = Length^{-1}$, $[\epsilon] = Force \times Length^2$, $[\xi] = Length$, $[\gamma] = Force \times Length^{-2}$.

To obtain the gradient flow equations, the first variation of the energy E is,

$$\delta E = \int_V \left\{ K(\theta_{,i} - \lambda_i)\delta\theta_{,i} - K(\theta_{,i} - \lambda_i)\delta\lambda_i + \epsilon e_{ijk}e_{irs}\lambda_{s,r}\delta\lambda_{k,j} + \gamma\frac{\partial f}{\partial \lambda_i}\delta\lambda_i \right\} dv.$$

Integrate by parts and assume boundary terms to vanish. Then we obtain

$$\delta E = \int_V \left\{ K(-\theta_{,ii} + \lambda_{i,i})\delta\theta_i + \left(\gamma\frac{\partial f}{\partial \lambda_k} - K(\theta_{,k} - \lambda_k) - \epsilon e_{ijk}e_{irs}\lambda_{s,rj} \right) \delta\lambda_k \right\} dv.$$

Extracting terms for θ and λ respectively, we obtain the evolution equations

$$\begin{aligned} \frac{\partial \theta}{\partial t} &= M_1 K(\theta_{,ii} - \lambda_{i,i}) \\ \frac{\partial \lambda_k}{\partial t} &= M_2 \left(-\gamma\frac{\partial f}{\partial \lambda_k} + K(\theta_{,k} - \lambda_k) + \epsilon e_{ijk}e_{irs}\lambda_{s,rj} \right) \end{aligned} \tag{4.4}$$

Here M_1 and M_2 represent mobility coefficients. Their physical dimensions are $[M_1] = Velocity \times Length \times Force^{-1}$ and $[M_2] = Velocity \times Force^{-1} \times Length^{-1}$.

To non-dimensionalize the above equations, we introduce the following dimensionless

[4]In this special case where $\boldsymbol{\lambda}$ is expected to have only one non-vanishing component.

variables,

$$\tilde{x_i} = \frac{1}{\xi} x_i; \quad \tilde{s} = KM_2 t; \quad \tilde{\gamma} = \frac{\xi^2}{K}\gamma = \frac{2P\hat{k}}{a}; \quad \tilde{\boldsymbol{\lambda}} = \xi\boldsymbol{\lambda}; \quad \tilde{\epsilon} = \frac{1}{K\xi^2}\epsilon = Ca$$

Also, we assume $M_1 = M_2\xi^2$; this is justified by the fact that we view the gradient flow equation for θ as simply a device to achieve equilibrium in θ with $\boldsymbol{\lambda}$ fixed. Indeed, in all gradient-flow results presented in the following, we have checked our results to ensure that they are invariant to solving directly for the equilibrium of θ for fixed $\boldsymbol{\lambda}$. Then the non-dimensionalized version of (4.4) reads as:

$$\begin{aligned} \frac{\partial\theta}{\partial\tilde{s}} &= (\theta_{,ii} - \tilde{\lambda}_{i,i}) \\ \frac{\partial\tilde{\lambda}_k}{\partial\tilde{s}} &= -\tilde{\gamma}\frac{\partial f}{\partial\tilde{\boldsymbol{\lambda}}_k} + (\theta_{,k} - \tilde{\lambda}_k) + \tilde{\epsilon}e_{ijk}e_{irs}\tilde{\lambda}_{s,rj} \\ \text{where} \quad f &= 1 - \cos\left(|\tilde{\boldsymbol{\lambda}}|\left(\frac{\hat{k}}{a}\right)^{-1}\right). \end{aligned}$$

After substituting the expressions for $\tilde{\gamma}$ and $\tilde{\epsilon}$, the nondimensional evolution equations are

$$\left.\begin{aligned} \frac{\partial\theta}{\partial s} &= (\theta_{,ii} - \lambda_{i,i}) \\ \frac{\partial\lambda_k}{\partial s} &= -2P\sin\left(|\boldsymbol{\lambda}|\left(\frac{\hat{k}}{a}\right)^{-1}\right)\hat{\lambda}_k + (\theta_{,k} - \lambda_k) + Cae_{ijk}e_{irs}\lambda_{s,rj} \end{aligned}\right\} \text{in the body } B \quad (4.5)$$

where $\hat{\boldsymbol{\lambda}}$ is the unit vector in the direction of $\boldsymbol{\lambda}$, and *we have removed all tildes for convenience*. For the purposes of Section 4.4, all symbols henceforth represent non-dimensional quantities.

In all that follows, we think of our computational solutions employing $a > 0$ as approximations of the limiting case $a = 0$ which assigns no physical significance to the layer. In Section 4.4.5 we show that our equilibrium disclination solutions show a trend to finite total energy even in that limit. *Thus, the nondimensionalized model effectively has two*

non-dimensional constants, C, P.

4.4 Static results from gradient flow

We evaluate the gradient flow model by presenting results for straight wedge disclinations. All calculations are done on a square domain of non-dimensional extent $L \times L$ with $L = 50$. Unless otherwise specified, we assume $a = 1$, $C = 1$ and $P = 20$.

We compute results for four cases in this section, namely strength half disclinations ($k = \pm 0.5$) and strength one disclinations ($k = \pm 1$). The initial condition for the layer field for calculations in this section is defined as

$$\boldsymbol{\lambda} = \begin{cases} \frac{-2k\pi}{a}\boldsymbol{e}_2, & \text{if } |x_2| < \frac{a}{2} \text{ and } x_1 > 0 \\ 0, & \textit{otherwise.} \end{cases} \tag{4.6}$$

The initial condition on the θ field is based on Frank's solution [Fra58],

$$\theta = k \ \tan^{-1}\left(\frac{x_1}{x_2}\right) + Q \tag{4.7}$$

where Q is a constant. Here, Q is set to be $-\frac{\pi}{4}$ and the range of the arctan function is assumed to be $[-\frac{3\pi}{2}, \frac{\pi}{2}]$.

A zero-moment boundary condition is imposed to solve for the θ field, for each given $\boldsymbol{\lambda}$. In the following calculations, θ at the boundary point $(x_1 = 25, x_2 = -\frac{a}{2})$ is fixed to be 0.

4.4.1 Strength $+\frac{1}{2}$ disclination

For a positive half disclination, $k = 0.5$, the director rotates π radians clockwise while traversing a loop clockwise from the bottom of the layer to the top, starting from an ori-

entation of $\theta = \pi$ with respect to the positive x-axis at the bottom of the layer. The initial prescription of the $\boldsymbol{\lambda}$ field is shown in Figure 4.3(a). λ_2 is the only non-zero component inside the layer and thus the director distortion field is not *curl*-free at the disclination core where the layer terminates. Figure 4.3(b), 4.3(d) and 4.3(e) are computational equilibria obtained from the gradient flow evolution from the initial conditions described in (4.7). Equilibrium is considered achieved if the magnitudes of the 'rates' of evolution become less than 10^{-4} for both θ and $\boldsymbol{\lambda}$ on the entire domain. The director field over the whole body is represented with dashed line field in Figure 4.3(d). A magnified view of the core area is shown in Figure 4.3(e).*In this paper, the spacing of the dashed curves do not represent spacing of the computational mesh.* Figure 4.3(b) shows the energy density distribution for this case. The energy is concentrated in the core and the location of the layer is energetically 'invisible'.

Figure 4.4(a) shows the director field within the layer at $l/L = 0.005$. As shown in Figure 4.4(a), the director field actually rotates within the layer *but with no energy cost.* In the limit $a \to 0$ this 'rotation' of the director field in the layer becomes 'invisible', portraying a discontinuity without energy cost, except at the core which is physically realistic.

4.4.2 Strength $-\frac{1}{2}$ disclination

For the negative half disclination $k = -0.5$, the director rotates π radians anticlockwise while traversing a loop clockwise from the bottom of the layer to the top, starting from a $\theta = \pi$ orientation with respect to the positive x-axis at the bottom of the layer. Figure 4.5(a) shows the initial condition on the $\boldsymbol{\lambda}$ field for this case. The prescribed value of $\boldsymbol{\lambda}$ inside the layer has the same magnitude as for the positive half disclination, but with opposite sign. Figure 4.5(d) shows the equilibrated director field over the whole body. A magnified view of the core is shown in Figure 4.5(e). Figure 4.5(b) shows the energy

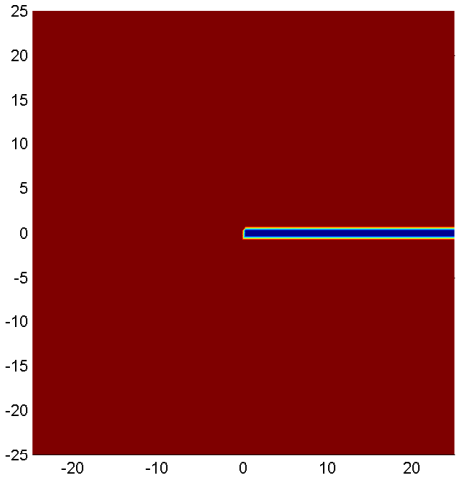

(a) Plot of λ_2 of initialization. $\boldsymbol{\lambda}$ is non-zero only inside the layer, with λ_2 as only non-zero component.

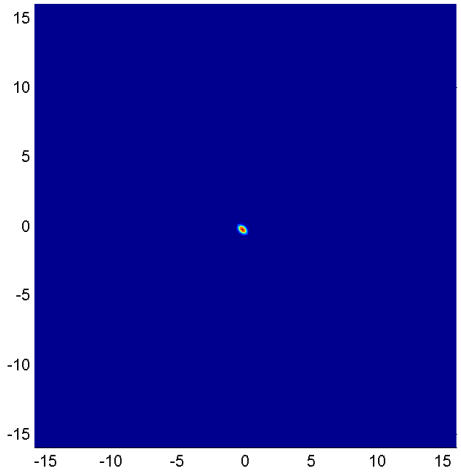

(b) The energy density plot for this positive half disclination.

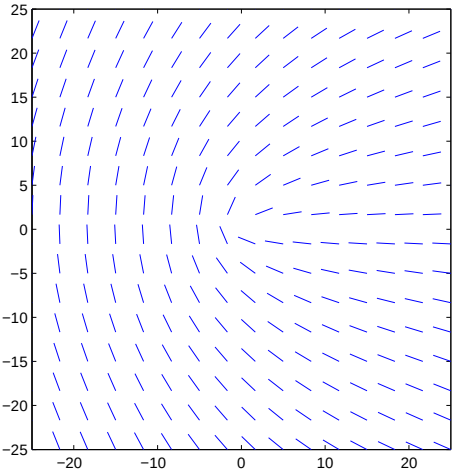

(c) Director field θ on the whole body at $l/L = 0.02$.

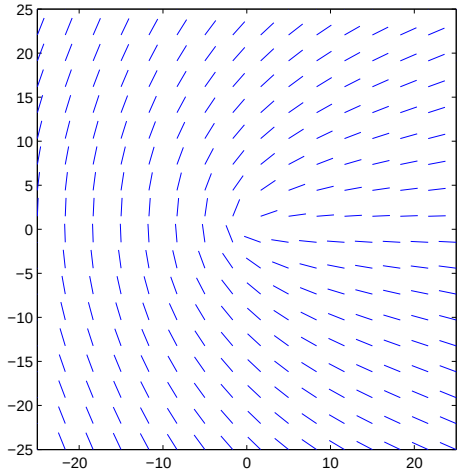

(d) Director field θ on the whole body at $l/L = 0.005$.

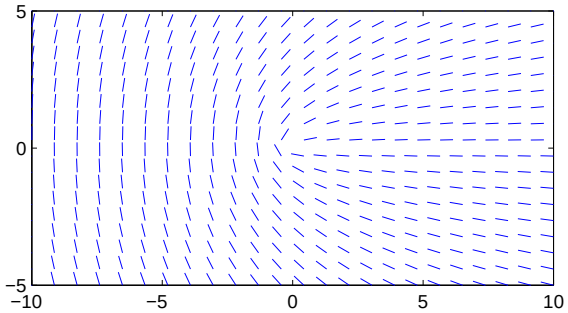

(e) Magnified view of the director field at $l/L = 0.005$ near the core.

Figure 4.3: *Results for strength $+\frac{1}{2}$ disclination.*

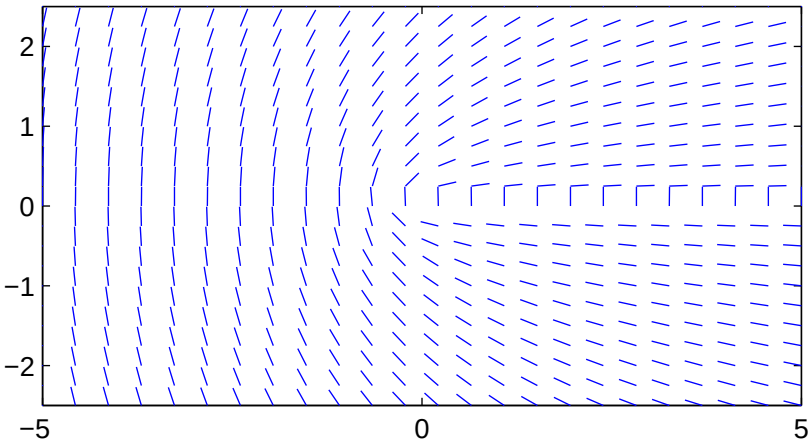

(a) Magnified view of the equilibrated director field near the layer for $+\frac{1}{2}$ disclination. The director turns in the layer but the corresponding energy is as it should be.

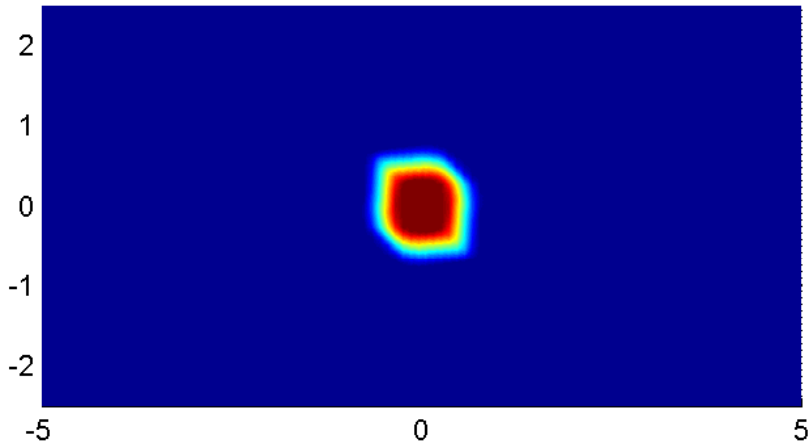

(b) Magnified view of the energy density on the same scale as 4.4(a).

Figure 4.4: *Magnified view of director field and energy density field near the layer for a* $+\frac{1}{2}$ *disclination at* $l/L = 0.005$.

density distribution for the equilibrium of this case.

4.4.3 Strength ± 1 disclination

Now consider $k = \pm 1$, which implies a director rotation of 2π radians across the layer. Following the definition of $\boldsymbol{\lambda}$, we can prescribe $\boldsymbol{\lambda}$ fields for one disclination as well. Figure 4.6 presents the equilibrated director results of ± 1 disclinations. Since strength ± 1 disclinations contain higher energy than the sum of the total energies of two half disclinations, strength ± 1 disclinations are not stable and tend to dissociate into two strength $\pm \frac{1}{2}$ disclinations. The capability of our model in representing this physical process will be discussed in Section 4.6.4.

4.4.4 Comparisons with Frank's analytical solution

The angle of the director field with the x_1 axis in Frank's solution [Fra58] is

$$\theta = K \tan^{-1}\left(\frac{x_1}{x_2}\right) + q$$

where q is a constant. For the purpose of evaluating the energy for the domain involved, it suffices to consider $\operatorname{grad}\theta$ given as

$$\frac{K}{r^2}(-x_1\boldsymbol{e}_1 + x_2\boldsymbol{e}_2).$$

Thus the energy density variation along the x_1 axis of the domain for this solution is

$$\psi = \frac{1}{2}|\operatorname{grad}\theta|^2 = \frac{K^2}{2}\left(\frac{1}{x_1}\right)^2.$$

Figure 4.7 shows the various contributions for the energy density in our model, as well as a comparison of the energy density field with that of the Frank analytical solution.

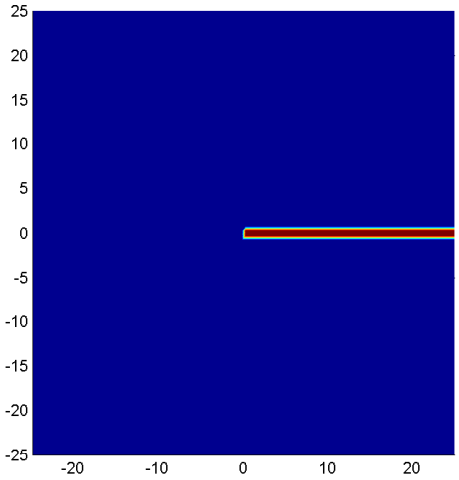

(a) Plot of λ_2 of initialization. $\boldsymbol{\lambda}$ is non-zero only inside the layer where λ_2 is the only non-zero component. Compared to the positive half disclination 4.3(a), $\boldsymbol{\lambda}$ in this case has the same magnitude but opposite sign.

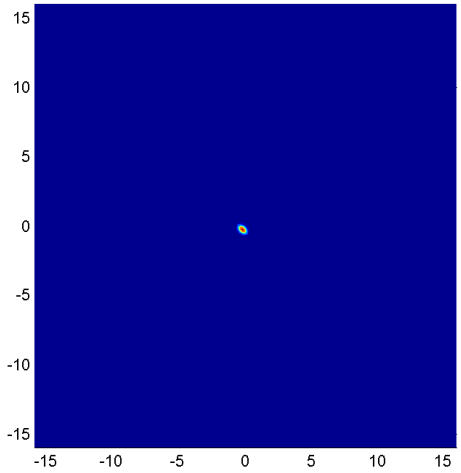

(b) The energy density plot for this strength $-\frac{1}{2}$ disclination.

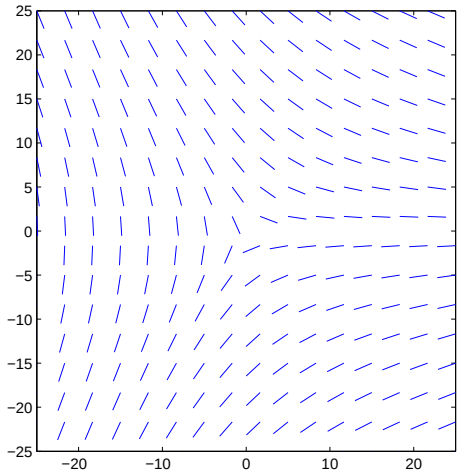

(c) Director field θ on the whole body at $l/L = 0.02$.

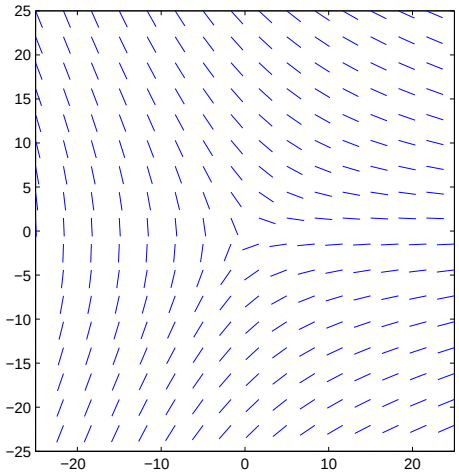

(d) Director field θ on the whole body at $l/L = 0.005$.

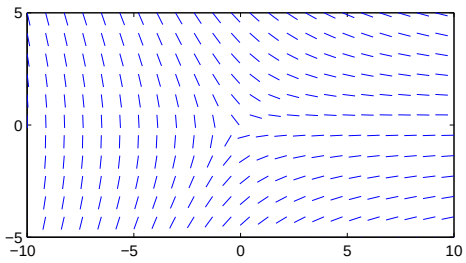

(e) Magnified view of the director field at $l/L = 0.005$ near the core.

Figure 4.5: *Results for strength* $-\frac{1}{2}$ *disclination.*

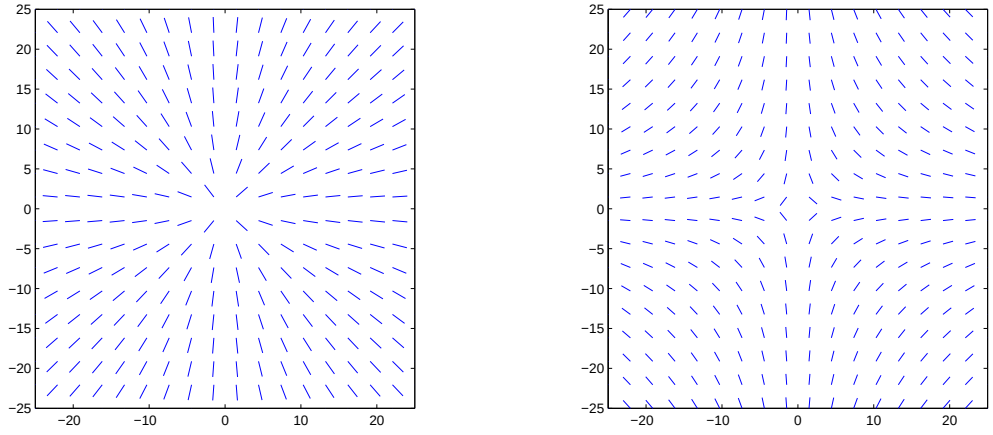

(a) Director field θ for a $+1$ disclination. (b) Director field θ for a -1 disclination.

Figure 4.6: *The equilibrated director results for* ± 1 *disclinations.*

The energy density should decay as $1/r^2$ when moving away from core where r is the distance from core. In Figure 4.7, the black line is the energy density along the horizontal axis from the Frank analytical solution, labeled as *Frank analytical solution*; the red line is the contribution of the energy density from the Oseen-Frank part $\frac{K}{2}(\text{grad}\,\theta - \boldsymbol{\lambda})^2$ in our model, labeled as *OF part*; and the blue line is the whole energy density from our model, labeled as *Whole energy density*. The overall comparisons as well as the comparisons near the core area for both $+1/2$ and $+1$ disclinations are presented in Figure 4.7. These comparisons show good agreement between the energy density and that of the Frank analytical result outside the core. Inside core, our results are nonsingular while the Frank analytical results blow up. Figure 4.8 shows the energy density comparisons for strength $+1/2$ disclination along the y axis. The energy densities are symmetrically distributed along both the x and y axes and they show good agreement with the Frank solution. The profiles for strength $-\frac{1}{2}$ and strength -1 disclinations also follow the correct trends.

Figure 4.9 shows a convergence study of our approximate solutions for the energy density along the x-axis for the $+1/2$ disclination. In Figure 4.9, the lines of different color

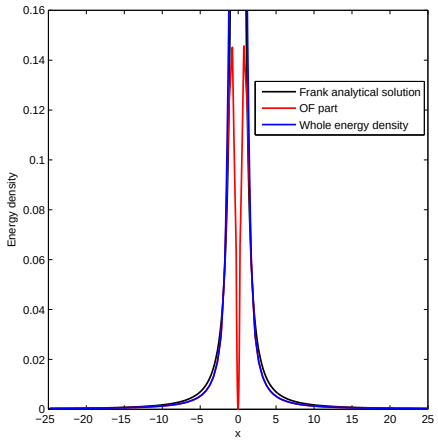

(a) Overall energy density comparison along x axis for strength $+\frac{1}{2}$ disclination.

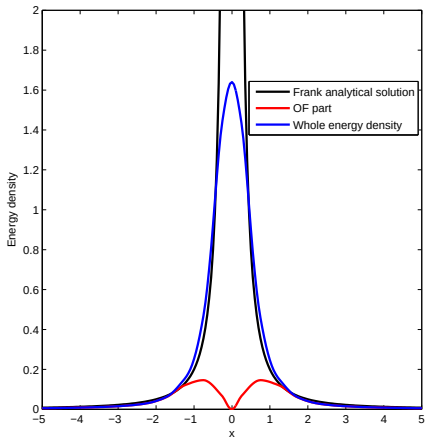

(b) Energy density comparison along x axis near strength $+\frac{1}{2}$ disclination core.

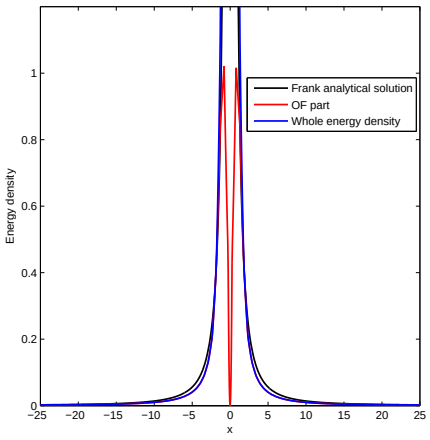

(c) Overall energy density comparison for strength $+1$ disclination.

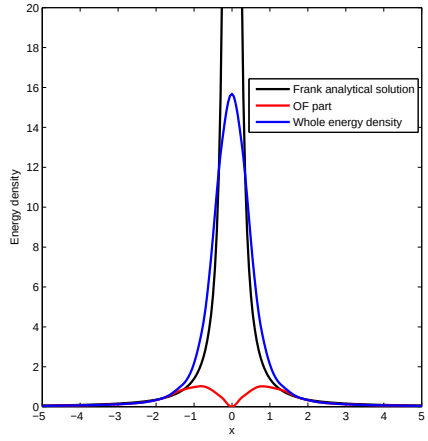

(d) Energy density comparison near strength $+1$ disclination core.

Figure 4.7: *Energy density comparisons between Frank analytical results and our results along x axis, in both overall domain and near-core area, indicating a good agreement.*

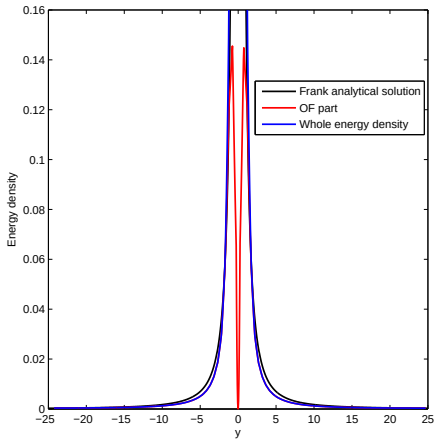

(a) Overall energy density comparison along y axis for strength $+\frac{1}{2}$ disclination.

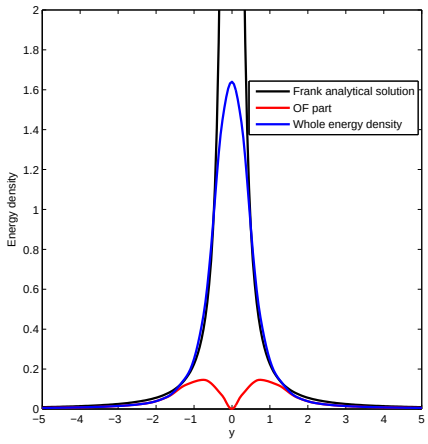

(b) Energy density comparison along y axis near strength $+\frac{1}{2}$ disclination core.

Figure 4.8: *Energy density comparisons between Frank analytical results and our results of* $+1/2$ *disclination along* y *axis, for both the overall domain and near-core area, indicating a good agreement.*

represent mesh sizes from 1 to 0.1. For a fixed problem defined in Section 4.4.1, the energy density results converge with mesh refinement.

4.4.5 Variation of total energy as a function of layer thickness

For nematic disclinations, a layer where the director vector 'unwinds' is to be considered as an approximation to the physical case of a sharp discontinuity in the director vector field. Thus it is necessary to demonstrate, at least approximately, that in the limit $a \to 0$ the total energy of the body with a disclination remains non-zero but finite.

Recall the nondimensionalized energy in this work takes the form

$$E = \int_V \left[\frac{1}{2} |\operatorname{grad} \theta - \boldsymbol{\lambda}|^2 + \frac{Ca}{2} |\operatorname{curl} \boldsymbol{\lambda}|^2 + \frac{2P\hat{k}}{a} f(\boldsymbol{\lambda}) \right] dv.$$

Figure 4.10 is a the plot of total non-dimensional value for a $+\frac{1}{2}$ disclination as a tends to zero. The red line, labeled as $Whole$, is the value of total non-dimensional energy E; the

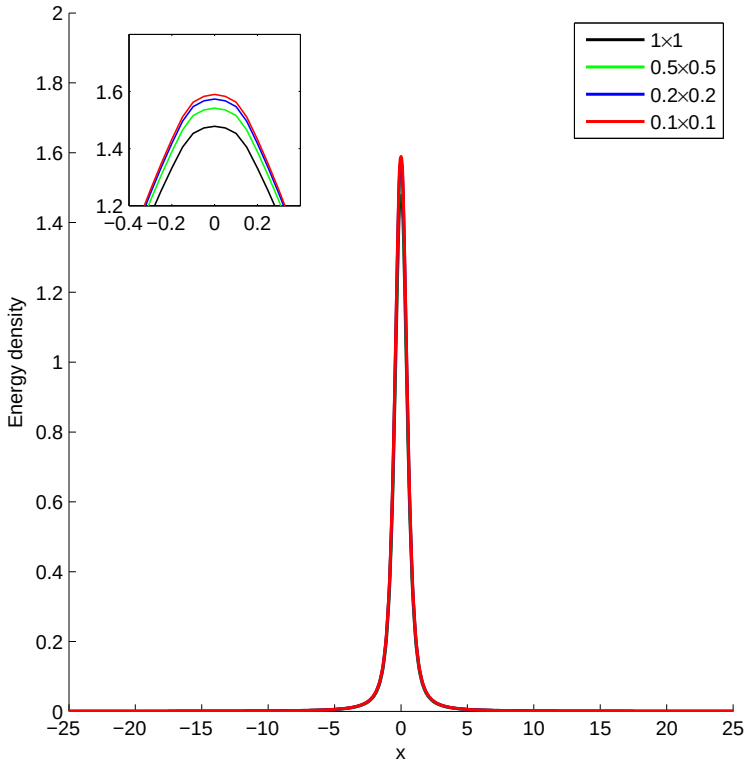

Figure 4.9: *Energy density plots along layer direction with different meshing. In the legend, the form $a \times b$ represents the element size, where a is the element size in the x direction and b is the element size in the y direction. The domain size is 50×50. The inset plot is a magnified view at the center of the core. The energy density results converge with mesh refinement.*

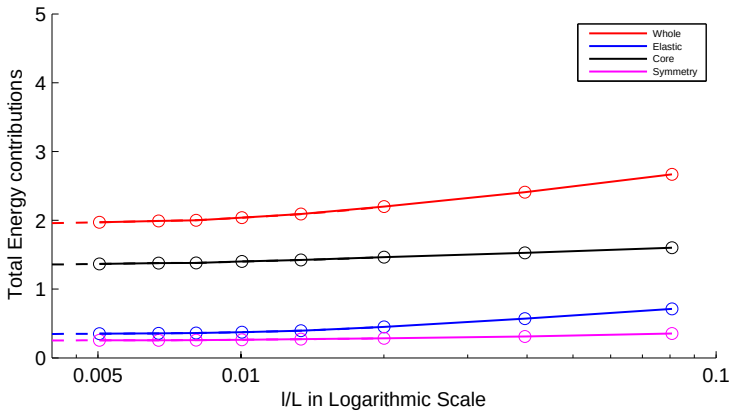

Figure 4.10: *Trends of different parts of the total energy as the layer width tends to zero. The total energy as well as the individual contributions converge as a tends to zero.*

blue line, labeled as *Elastic*, is the contribution from $\frac{1}{2}|\operatorname{grad}\theta - \boldsymbol{\lambda}|^2$; the black line, labeled as *Core*, is the contribution from $\frac{Ca}{2}|\operatorname{curl}\boldsymbol{\lambda}|^2$; and the green line, labeled as *Symmetry*, is the contribution from $\frac{2P\hat{k}}{a}f$. This plot shows that the total energy as well as the individual contributions converge as a tends to zero. The circles represent values obtained from the calculations at different l/L ratios. The total non-dimensional energy shows a trend of converging to a finite value of 1.915; the Frank elastic contribution part converges to 17.5% of the total energy; the contribution from the disclination core converges to 69.3% of the total energy; and the contribution from the symmetry-related component converges to 13.2% of the total energy.

4.4.6 Shortcoming of the gradient flow dynamics for this energy function

In spite of the fact that the gradient flow method for this energy works very well in the computation of defect equilibria as demonstrated in Sections 4.4.1 - 4.4.3, it is not able to predict the motion of disclinations. To illustrate this point, we consider disclination annihilation as an example. Figure 4.11(a) shows the corresponding initial $|\boldsymbol{\lambda}|$ field, i.e., a half disclination dipole is prescribed within the layer as initial condition. Figure 4.11(b) shows

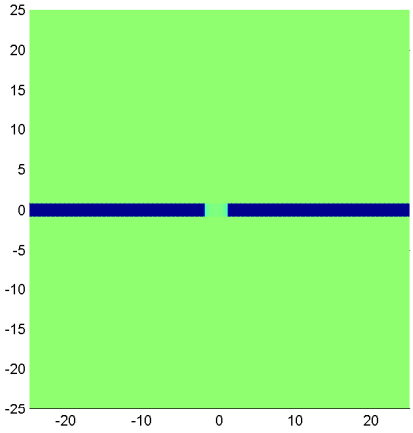

(a) Initial prescription for $|\boldsymbol{\lambda}|$ field.

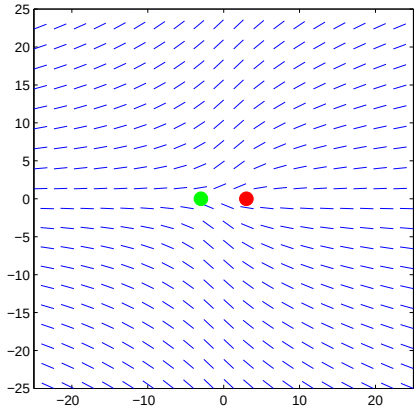

(b) Initial prescription for θ field.

the initialization of the θ field, where the red dot represents a strength $+1/2$ disclination and the green dot represents a strength $-1/2$ disclination core.

The physical expectation is that on evolution those two disclinations merge with each other and annihilate, leaving no energy in the end. Recall that for the equilibrium solutions, $P = 20$. With this relatively high penalty on the non-convex term, we find that while the two oppositely charged disclinations evolve to their equilibrium configurations, they simply do not evolve from their equilibrium positions and annihilate, contrary to physical expectation. This can be understood as follows: invoking a dynamical process for the evolution requires continuous evolution in time of the fields at any spatial point. For a disclination to move, the value of $|\boldsymbol{\lambda}|$ at a spatial point ahead of the core has to rise continuously from 0 to $2\pi k/a$ (for a prescribed value of k) over a finite time interval. However, for the intervening states in this path, states that are not minima of the wells of the function f have to be sampled, and this leads to a large energy barrier - for large P - that has to be overcome by the driving forces arising from director gradients (grad θ). What occurs in the calculations is that large restoring energetic forces arise from the multiwell term that forces the spatial point (just ahead of the core) to stay at the minima of the *0-well* of the function f. Hence the disclination cannot move.

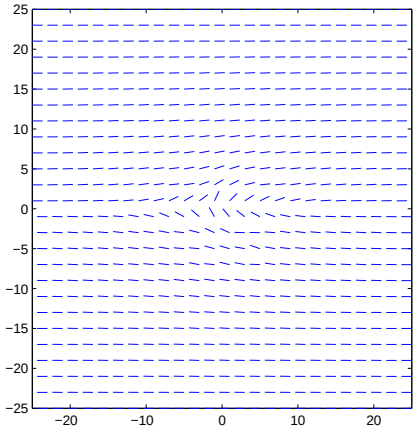

(c) Director field θ for the disclination annihilation problem using the gradient flow method.

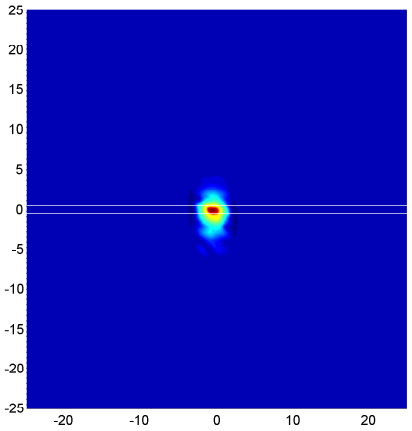

(d) Energy density in relaxed state achieved by the gradient flow calculation.

Figure 4.11: *Director field and energy density plot for disclination annihilation using the gradient flow method. The two white lines are artificially inserted to display the top and bottom layer boundaries. The results from the gradient flow calculation do not match physical expectation.*

A natural remedy then is to think of reducing the penalty on the non-convex term - giving it the flavor of a physical component of the total energy function rather than an artificial mathematical device to represent a constraint limiting $|\boldsymbol{\lambda}|$ values to discrete states. To this end, we set $P = 2$. This raises another problem. The results from the gradient flow clearly do not match our expectation; there is a clear energy pattern near the core area, as observed in Figure 4.11(d), where the two white lines are artificially inserted to display the top and bottom layer boundaries. Even worse, there is a large area outside the layer where the corresponding director profile is inhomogeneous, as shown in Figure 4.11(c). Clearly, the physical expectation is that the disclinations should annihilate moving in a straight line leaving behind a homogeneous director field with horizontal orientation everywhere except the layer, and zero energy everywhere (including the layer). This does not happen because with a lower penalty, $\boldsymbol{\lambda}$ can evolve from $\mathbf{0}$, not only along the layer but elsewhere as well wherever there is a driving force, and, indeed, since there are director gradients outside the layer where $|\boldsymbol{\lambda}| = 0$, there is no impediment to growth of $\boldsymbol{\lambda}$ at such points, since

a steady state of $(4.5)_1$ is given by $\theta_{,i} = \lambda_i$, up to constraints posed by Dirichlet boundary conditions as well as the incompatibility of the field $\boldsymbol{\lambda}$.

4.5 A dynamic model for nematic disclinations in 2D

We seek an alternative to the gradient flow dynamics of the energy (4.5) to model energetically driven disclination dynamics. We follow the ideas in [AD13] motivated from the field of dislocation dynamics in solids to derive an appropriate model for the dynamics of straight wedge disclinations (a 2d model,) based on the statements of balance of mass, linear and angular momentum, the second law of thermodynamics, and a conservation statement for topological charge of these lines. We first show the derivation of the general 2D theory, and then derive a simple layer model from the theory as a particular example. In this section, $\boldsymbol{\lambda}$ and θ have the same meanings as in Sections 4.3.

4.5.1 Derivation for general 2D case

As before, we assume that the energy E is given in the form of

$$E \;=\; \int_V [\psi(\operatorname{grad}\theta - \boldsymbol{\lambda}, \operatorname{curl}(\boldsymbol{\lambda})) + \gamma f(\boldsymbol{\lambda})]dv,$$

where $\gamma = \frac{2PK\hat{k}}{a\xi^2}$ with the same definition as in Section 4.3, f is a multi-well function with wells at $\frac{2\pi\hat{k}}{a\xi}$, with $a \to 0$. For the sake of numerical approximation, we shall choose a as a positive scalar that allows us to approximate director discontinuities of infinite magnitude. $k = n\hat{k}$ (n can be any integer) is the disclination strength. To be concise in the following derivations, we denote

$$\begin{aligned} \boldsymbol{e} &:= \operatorname{grad}\theta - \boldsymbol{\lambda} \\ \boldsymbol{b} &:= \operatorname{curl}(\boldsymbol{e}). \end{aligned}$$

$\boldsymbol{b} = \operatorname{curl}(\operatorname{grad}\theta - \boldsymbol{\lambda})$ represents the departure of the director distortion from being the director gradient. In the absence of defects, $\boldsymbol{e} = \operatorname{grad}\theta$ and hence $\boldsymbol{b} = \operatorname{curl}(\operatorname{grad}\theta) = \boldsymbol{0}$. Thus, $\boldsymbol{b}$ is considered as the defect field.

Balancing the content of topological charge carried by defect lines within arbitrary area patches, a conservation law for the defect field [AD13] emerges in the form

$$\begin{aligned} \frac{\partial \boldsymbol{b}}{\partial t} &= -\operatorname{curl}(\boldsymbol{b} \times \boldsymbol{v}) \\ -\operatorname{curl}\left(\frac{\partial \boldsymbol{\lambda}}{\partial t}\right) &= -\operatorname{curl}(\boldsymbol{b} \times \boldsymbol{v}) \\ \frac{\partial \boldsymbol{\lambda}}{\partial t} &= \boldsymbol{b} \times \boldsymbol{v}. \end{aligned}$$

The mechanical dissipation is the conversion of mechanical energy into heat, namely the difference between external power supplied to the body and the sum of the total rate of change of kinetic energy and the rate of change of free energy. In this case, the dissipation reads as (we ignore kinetic energy and flow here for simplicity)

$$D = \int_{\partial V} \dot{\theta}\, \boldsymbol{m}\, \boldsymbol{\nu} da - \int_V \dot{\psi} dv - \int_V \gamma \dot{f} dv \geq 0.$$

where $\boldsymbol{\nu}$ is the normal vector on the boundary ∂V and $\boldsymbol{m}$ is the moment given by $\boldsymbol{\Lambda}^{\intercal}\boldsymbol{e}_3$ with $\boldsymbol{\Lambda}$ is the couple stress tensor. In the following, superposed dots are meant to represent material time derivatives (in the language of continuum mechanics), but since we are ignoring flow, they are identical to spatial time derivatives. Apply the divergence theorem to the dissipation and require the second law of thermodynamics to be in effect to obtain

$$\begin{aligned} D &= \int \{(\dot{\theta} m_i)_{,i} - \dot{\psi} - \gamma \dot{f}\} dv \geq 0 \\ \Rightarrow \quad D &= \int \left(m_i - \frac{\partial \psi}{\partial e_i}\right) \dot{\theta}_{,i} - \left(-\frac{\partial \psi}{\partial e_i}\dot{\lambda}_i + \frac{\partial \psi}{\partial b_i}\dot{b}_i + \gamma \frac{\partial f}{\partial \lambda_i}\dot{\lambda}_i\right) dv \geq 0. \end{aligned}$$

Since nematic elasticity has to be recovered by the model, $(m_i - \frac{\partial \psi}{\partial e_i})\dot{\theta}_{,i} = 0$ is necessary for

every possible $\dot{\theta_{,i}}$ when dissipative mechanisms are inoperative (i.e. $\dot{\boldsymbol{\lambda}} = 0 \Rightarrow \dot{\boldsymbol{b}} = 0$). Thus, to satisfy this requirement, we choose $m_i = \frac{\partial \psi}{\partial e_i}$, and perform the following manipulations:

$$\int - \left[-\frac{\partial \psi}{\partial e_i} \dot{\lambda}_i + \frac{\partial \psi}{\partial b_i} \dot{b}_i + \gamma \frac{\partial f}{\partial \lambda_i} \dot{\lambda}_i \right] dv \geq 0$$

$$\int - \left[-\frac{\partial \psi}{\partial e_i} (\boldsymbol{b} \times \boldsymbol{v})_i + \frac{\partial \psi}{\partial b_i} (-e_{ijk} (\boldsymbol{b} \times \boldsymbol{v})_{k,j}) + \gamma \frac{\partial f}{\partial \lambda_i} (\boldsymbol{b} \times \boldsymbol{v})_i \right] dv \geq 0$$

$$\int - \left[-\frac{\partial \psi}{\partial e_i} (\boldsymbol{b} \times \boldsymbol{v})_i + \left(\frac{\partial \psi}{\partial b_i} \right)_{,j} (e_{ijk} (\boldsymbol{b} \times \boldsymbol{v})_k) + \gamma \frac{\partial f}{\partial \lambda_i} (\boldsymbol{b} \times \boldsymbol{v})_i \right] dv \geq 0$$

$$\int \left[\frac{\partial \psi}{\partial e_k} e_{krs} b_r v_s + \left(\operatorname{curl} \frac{\partial \psi}{\partial \boldsymbol{b}} \right)_k e_{krs} b_r v_s - \gamma \frac{\partial f}{\partial \lambda_k} e_{krs} b_r v_s \right] dv \geq 0$$

$$\int \left\{ e_{krs} \left[\frac{\partial \psi}{\partial e_k} + \left(\operatorname{curl} \frac{\partial \psi}{\partial \boldsymbol{b}} \right)_k - \gamma \frac{\partial f}{\partial \lambda_k} \right] b_r \right\} v_s dv \geq 0.$$

Based on the second law of thermodynamics, we need to ensure a non-negative dissipation as stated in the above inequality. To fulfill this requirement, the simplest and most natural choice is to require

$$\boldsymbol{v} \quad \text{parallel to} \quad \left[\boldsymbol{m} + \operatorname{curl} \frac{\partial \psi}{\partial \boldsymbol{b}} - \gamma \frac{\partial f}{\partial \boldsymbol{\lambda}} \right] \times \boldsymbol{b}.$$

It is characterized in the most simple of circumstances by choosing $\boldsymbol{v}$ of the form

$$\boldsymbol{v} = \frac{1}{B_m |\boldsymbol{b}|^m} \left[\left(\boldsymbol{m} + \operatorname{curl} \left(\frac{\partial \psi}{\partial \boldsymbol{b}} \right) - \gamma \frac{\partial f}{\partial \boldsymbol{\lambda}} \right) \times \boldsymbol{b} \right]$$

with $m = 0$ and B_m is a material constant required on dimensional grounds. The parameter m can probe different types of behaviors. With this choice of $\boldsymbol{v}$, we can verify that the dissipation is larger or equal to zero globally, which means the second law of thermodynamics is satisfied by our model.

Recall that

$$\begin{aligned} \frac{\partial \boldsymbol{b}}{\partial t} &= -\operatorname{curl}(\boldsymbol{b} \times \boldsymbol{v}) \\ \frac{\partial \boldsymbol{\lambda}}{\partial t} &= \boldsymbol{b} \times \boldsymbol{v}. \end{aligned} \tag{4.8}$$

After substituting $\boldsymbol{v}$ in (4.8), the evolution equations for $\boldsymbol{b}$ and $\boldsymbol{\lambda}$ can be written as

$$\begin{aligned} \frac{\partial \boldsymbol{b}}{\partial t} &= -\operatorname{curl}\left[\boldsymbol{b} \times \frac{1}{B_m |\boldsymbol{b}|^m}\left\{\left(\boldsymbol{m} + \operatorname{curl}\left(\frac{\partial \psi}{\partial \boldsymbol{b}}\right) - \gamma \frac{\partial f}{\partial \boldsymbol{\lambda}}\right) \times \boldsymbol{b}\right\}\right] \\ \frac{\partial \boldsymbol{\lambda}}{\partial t} &= \frac{1}{B_m |\operatorname{curl} \boldsymbol{\lambda}|^m} \operatorname{curl} \boldsymbol{\lambda} \times \left[\left(\boldsymbol{m} + \operatorname{curl}\left(\frac{\partial \psi}{\partial (\operatorname{curl} \boldsymbol{\lambda})}\right) - \gamma \frac{\partial f}{\partial \boldsymbol{\lambda}}\right) \times \operatorname{curl} \boldsymbol{\lambda}\right]. \end{aligned} \tag{4.9}$$

We have ignored flow, and assume that balance of linear momentum and mass are trivially satisfied. Balance of angular momentum, assuming no director momentum is given by

$$\operatorname{div}(\boldsymbol{m}) = 0.$$

This reduces to the governing equation

$$\operatorname{div}(\operatorname{grad} \theta - \boldsymbol{\lambda}) = 0. \tag{4.10}$$

The utility of (4.9) over the gradient flow dynamics (4.5) is the presence of a non-vanishing $\operatorname{curl} \boldsymbol{\lambda}$ in the evolution of the $\boldsymbol{\lambda}$ field in $(4.9)_2$. At spatial points where $\boldsymbol{\lambda}$ is zero and $\operatorname{curl} \boldsymbol{\lambda} = 0$, $\boldsymbol{\lambda}$ cannot evolve (regardless of the value of the penalty parameter P); however, at the boundaries of the core region where one might expect $\boldsymbol{\lambda} = \boldsymbol{0}$ but $\operatorname{curl} \boldsymbol{\lambda} \neq \boldsymbol{0}$, evolution is possible allowing motion of the core.

4.5.2 A 'layer' model

4.5.2.1 Model description

Based on the above formalism for the general 2-d case, we build a simple layer model to explore several physically fundamental behaviors of disclination defects. The model is directly adapted from [AZ15] that was developed for dislocation dynamics in solids, with a translation for symbols representing the different fields in the two models.

In the following, we will interchangeably refer to the coordinates x_1 as x and x_2 as y. A subscript x, y, or t, even when not following a subscript comma, will refer to partial differentiation with respect to those independent variables.

The fundamental assumption is that disclinations are allowed to move in a horizontal line, regularized here to a thin layer (with the correct scaling properties so that total energy remains finite even in the limit $a \to 0$). Consider a square geometry with a layer $\mathcal{L}$ of thickness $l = a\xi$, as shown in Figure 4.12,

$$\mathcal{V} = \{(x, y) : (x, y) \in [-L/2, +L/2] \times [-L/2, +L/2]\}$$
$$\mathcal{L} = \{(x, y) : (x, y) \in [-L/2, +L/2] \times [-l/2, +l/2]\}$$
$$0 \leq l < L, \quad L > 0.$$

The stored energy density function takes the same form as (4.2). Then the dissipation can be written as

$$D = \int_{\mathcal{L}} \left(K(\operatorname{grad}\theta - \boldsymbol{\lambda}) - \gamma \frac{\partial f}{\partial \boldsymbol{\lambda}} \right) : \dot{\boldsymbol{\lambda}} dv + \int_{\mathcal{L}} \frac{\partial \psi}{\partial \boldsymbol{b}} : \operatorname{curl}(\boldsymbol{b} \times \boldsymbol{v}) dv$$
$$D = \int_{\mathcal{L}} \left(K(\operatorname{grad}\theta - \boldsymbol{\lambda}) - \gamma \frac{\partial f}{\partial \boldsymbol{\lambda}} \right) : (\boldsymbol{b} \times \boldsymbol{v}) dv + \int_{\mathcal{L}} \operatorname{curl} \left(\frac{\partial \psi}{\partial \boldsymbol{b}} \right) : (\boldsymbol{b} \times \boldsymbol{v}) dv + \int_{\partial \mathcal{L}} \frac{\partial \psi}{\partial \boldsymbol{b}} : (\boldsymbol{b} \times \boldsymbol{v}) \times \boldsymbol{\nu} da$$

where $\dot{\boldsymbol{\lambda}} = \boldsymbol{b} \times \boldsymbol{v}$, $\dot{\boldsymbol{b}} = -\operatorname{curl}(\boldsymbol{b} \times \boldsymbol{v})$, $\boldsymbol{b} = -\operatorname{curl} \boldsymbol{\lambda}$, and $\boldsymbol{\nu}$ is the unit normal vector of the layer boundary.

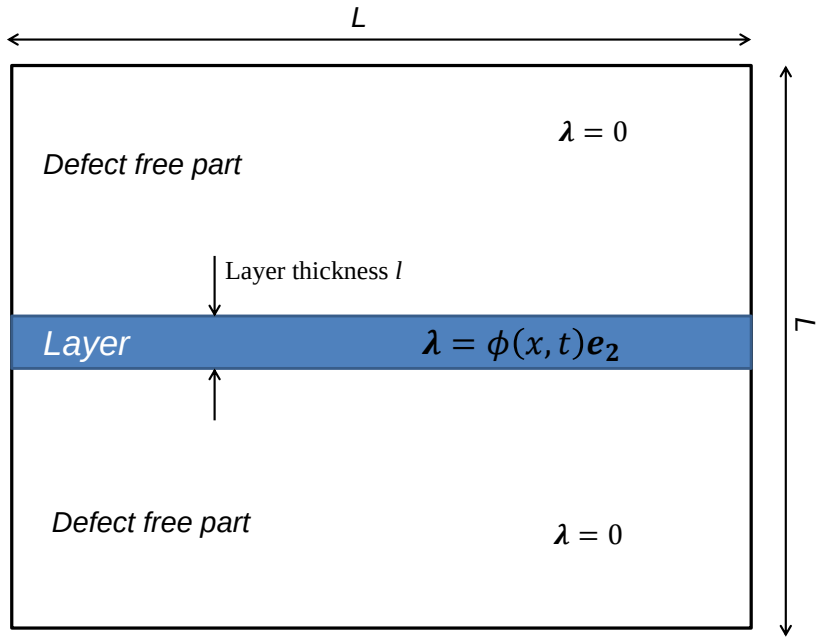

Figure 4.12: *Geometry for layer problem.* $\boldsymbol{\lambda}$ *has only non-zero component* λ_2 *inside the layer.*

In this model, we assume $\boldsymbol{\lambda}$ takes the form

$$\boldsymbol{\lambda}(x,y,t) = \begin{cases} \phi(x,t)\,\boldsymbol{e}_2, & \text{in the layer } (|x_2| < \frac{l}{2}) \\ 0, & \text{otherwise.} \end{cases}$$

Therefore $\boldsymbol{b}$ is also non-zero only in the layer, with component form

$$\boldsymbol{b} = -\operatorname{curl}\boldsymbol{\lambda} = -e_{ijk}\lambda_{k,j}\boldsymbol{e}_i = -e_{321}\lambda_{2,1}\boldsymbol{e}_3 = -\phi_x\boldsymbol{e}_3$$

$$\operatorname{curl}\boldsymbol{b} = e_{ijk}b_{k,j}\boldsymbol{e}_i = e_{213}b_{3,1}\boldsymbol{e}_2 = \phi_{11}\boldsymbol{e}_2.$$

We assume $\boldsymbol{v}$ to be of the form,

$$\boldsymbol{v} = v_1(x,y,t)\boldsymbol{e}_1 =: v(x,t)\boldsymbol{e}_1.$$

Substitute $\boldsymbol{\lambda}$ in f (4.3),

$$f = 1 - \cos\left(\xi|\phi|\left(\frac{\hat{k}}{a}\right)^{-1}\right).$$

We assume boundary condition $\phi_x(\pm\frac{L}{2}, t) = 0$. From $\dot{\boldsymbol{b}} = -\operatorname{curl}(\boldsymbol{b} \times \boldsymbol{v})$, we have

$$\phi_t(x,t) = -\phi_x(x,t)v(x,t).$$

Since $\boldsymbol{b} \times \boldsymbol{v}$ points in the direction of $\boldsymbol{e}_2$, the same direction of $\boldsymbol{\nu}$, then $(\boldsymbol{b} \times \boldsymbol{v}) \times \boldsymbol{\nu} = \mathbf{0}$. Thus, only the layer is relevant for the dissipation and this becomes

$$D = \int_{\mathcal{L}} v(x,t)\left[K(\theta_y - \phi) - \gamma\frac{\partial f}{\partial \phi} + \epsilon\phi_{xx}\right](-\phi_x)dv$$

We note that all terms in the above equation depend only on the x coordinate except for θ_y which also depends on the y coordinate. To build the simplest possible model consistent with thermodynamics, it is essential to average $(\theta_y - \phi)$ over the layer[AZ15]. For any feasible $v(x,t)$, the dissipation can be rewritten as

$$D = \int_{\mathcal{L}} v(x,t)\left[\tau(x,t) - \gamma\frac{\partial f(\phi(x,t))}{\partial \phi(x,t)} + \epsilon\phi_{xx}(x,t)\right](-\phi_x(x,t))dv + R$$

where

$$R = \int_{\mathcal{L}} v(x,t)[\theta_2(x,y,t) - \phi(x,t) - \tau(x,t)](-\phi_x(x,t))dv.$$

If we make the choice

$$\tau = \frac{K}{a\xi}\int_{-\frac{a\xi}{2}}^{\frac{a\xi}{2}} (\theta_y(x,y,t) - \phi(x,t))\, dy,$$

it is immediate that $R = 0$ due to the definition of τ. We make the constitutive assumption

for the velocity as

$$v(x,t) = \frac{-1}{B_m|\phi_x|^m}\{\phi_x[\tau - \tau^b + \epsilon\phi_{xx}]\}$$
$$\frac{\partial\phi}{\partial t} = \frac{|\phi_x|^{2-m}}{B_m}\left(\tau - \tau^b + \epsilon\phi_{xx}\right)$$
$$\text{where} \quad \tau = \frac{K}{a\xi}\int_{-\frac{a\xi}{2}}^{\frac{a\xi}{2}}(\theta_y - \phi)dy; \quad \tau^b = \gamma\frac{\partial f}{\partial\phi}; \quad f = 1 - \cos\left(\xi|\phi|\left(\frac{\hat{k}}{a}\right)^{-1}\right).$$

Here, B_m is a non-negative coefficient characterizing energy dissipation with physical dimensions depending on m. The parameter m can be chosen to probe different types of behavior. Especially, the model for $m = 2$ is the analog of the gradient flow case (4.5) with layer restriction. $m = 0$ has been shown to demonstrate possible pinning of defects in computational experiments [ZAWB15].

By choosing the following dimensionless variables

$$\tilde{x} = \frac{1}{\xi}x; \quad \tilde{y} = \frac{1}{\xi}y; \quad \tilde{\epsilon} = \frac{1}{K\xi^2}\epsilon = Ca; \quad \tilde{\tau} = \frac{\xi}{K}\tau; \quad \tilde{\tau}^b = \frac{\xi}{K}\tau^b;$$
$$\tilde{s} = \frac{K}{\xi^{4-2m}B_m}t; \quad \tilde{\phi} = \xi\phi$$

we arrive at the dimensionless governing equations as described below.

$$\begin{cases} \theta_{\tilde{x}\tilde{x}} + \theta_{\tilde{y}\tilde{y}} - \tilde{\phi}_{\tilde{y}} = 0 \quad \text{in } \mathcal{V} \\ \dfrac{\partial\tilde{\phi}}{\partial\tilde{s}} = |\tilde{\phi}_{\tilde{x}}|^{2-m}\left(\tilde{\tau} - \tilde{\tau}^b + \tilde{\epsilon}\tilde{\phi}_{\tilde{x}\tilde{x}}\right) \quad \text{in } \mathcal{L}. \end{cases}$$

After removing tildes for simplicity, the dimensionless system that governs the problem reads as

$$\begin{cases} \theta_{xx} + \theta_{yy} - \phi_y = 0 \quad \text{in } \mathcal{V} \\ \dfrac{\partial \phi}{\partial s} = |\phi_x|^{2-m} \left(\tau - \tau^b + Ca\phi_{xx} \right) \quad \text{in } \mathcal{L} \end{cases} \tag{4.11}$$

where

$$\tau = \frac{1}{a} \int_{-a/2}^{a/2} (\theta_y - \phi)\, dy, \quad \tau^b = 2P \sin \left(|\phi| \left(\frac{\hat{k}}{a} \right)^{-1} \right).$$

The corresponding numerical scheme for the above dimensionless system is developed in Appendix I.

4.6 Disclination annihilation, repulsion, and dissociation

We explore several disclination dynamic cases (in the absence of flow) within the 2D layer model. The domain is shown in Figure 4.12 with geometry 50×50. The parameter $a = 1$ is assumed the same as in the gradient flow simulations. The layer field $\boldsymbol{\lambda}$ is prescribed and restricted within a thin layer whose thickness is a, so that the disclination can only move along the x direction. The penalty parameter P is set to 1 (recall that in the gradient flow simulations $P = 20$, and $P = 2$ was unsuccessful in recovering physically expected equilibria). In the following, we will demonstrate and discuss results on disclination annihilation, repulsion, and dissociation.

In this section, all cases are calculated from ϕ evolution equations with $m = 0$, unless otherwise mentioned.

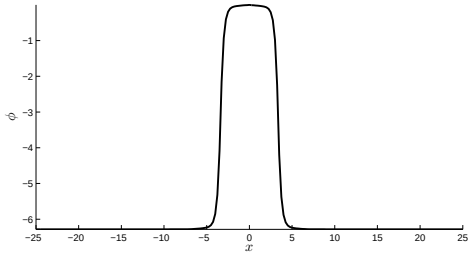

(a) Initialization of ϕ for disclination annihilation. A ϕ field corresponding to a strength $+\frac{1}{2}$ and a strength $-\frac{1}{2}$ disclination is prescribed.

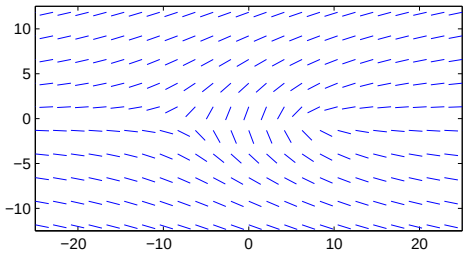

(b) Director field corresponding to the initialized ϕ.

Figure 4.13: *Initialization for the disclination annihilation problem.*

4.6.1 Disclination annihilation

We start with disclination annihilation, which the gradient flow approach failed to predict in Section 4.4.6. Even in this dynamic 'layer problem', if $P = 20$, and $m = 2$ (i.e. the analog of the gradient flow in the layer case), we find that, as expected, the oppositely charged disclinations do not annihilate. Within the layer ansatz and now setting $P = 1$, initially, a disclination dipole, i.e., two disclinations with opposite signs of $+\frac{1}{2}$ and $-\frac{1}{2}$, is prescribed as shown in Figure 4.13(a). The horizontal axis in Figure 4.13 represents the x axis along the layer and the vertical axis shows the magnitude of ϕ. Figure 4.13(b) shows the director field corresponding to the initialized ϕ prescription obtained by solving $(4.11)_1$. Figure 4.14 shows the snapshots of defect movement during the simulation. The vertical axis shows the gradient of ϕ along the layer (ϕ_x), representing the location of the core. Different colors represent the results at different times and at each time two opposite bumps are interpreted as a disclination dipole because $\operatorname{curl} \boldsymbol{\lambda} = -\boldsymbol{b} = \phi_x \boldsymbol{e}_3$. As time evolves, these two cores move toward each other, and finally merge. In the final result, the disclination dipole annihilates and no disclination exists in the body.

Figure 4.15 shows the snapshots of the director field at different times and their corresponding energy density fields at that time. Both the director snapshots and energy density plots show that the disclination dipole annihilates in the end, which leads to zero

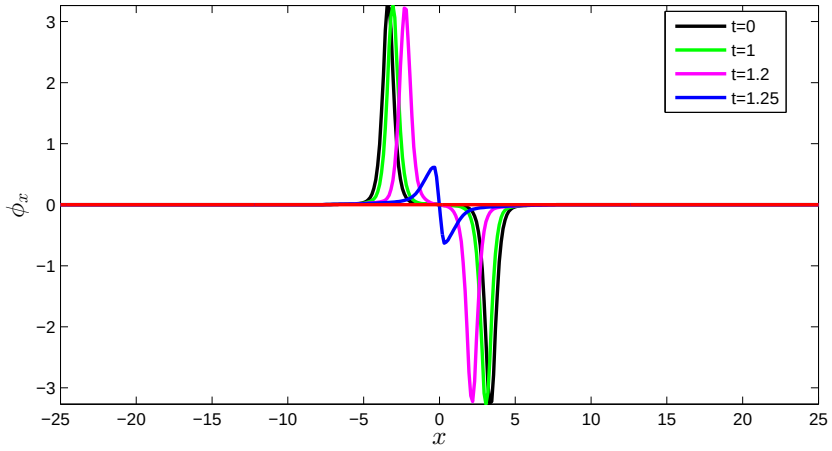

Figure 4.14: *ϕ_x snapshots at different time steps. The bumps represent disclination cores. The disclination dipoles eventually annihilates.*

energy.

4.6.2 Disclination repulsion

The difference between the disclination repulsion and annihilation is that now two disclinations with the same sign are used in the initial condition, as shown in Figure 4.16(a). Figure 4.16(b) shows the director field corresponding to the initial ϕ prescription. Figure 4.17 represents the motions of the disclination cores during the dynamic simulation. We observe that the two disclinations move apart due to the repulsive force of elastic origin between them.

Figure 4.18 shows the director snapshots and energy density plots for disclination repulsion at different time steps.

4.6.3 Velocity profiles with separation distance in different m cases

Figure 4.19 compares the the velocity versus dipole separation relationship of a single disclination in a dipole field, with the expected result from the linear theory of defects [Esh80]. In each case, the two disclinations are initialized with a separation distance of 50

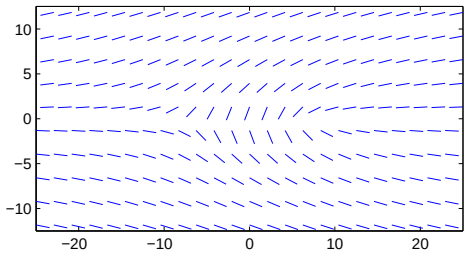

(a) Director snapshot at t=0.

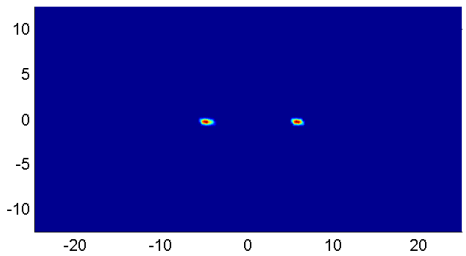

(b) Energy density plot at t=0.

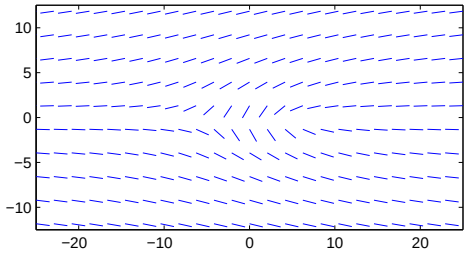

(c) Director snapshot at t=1.

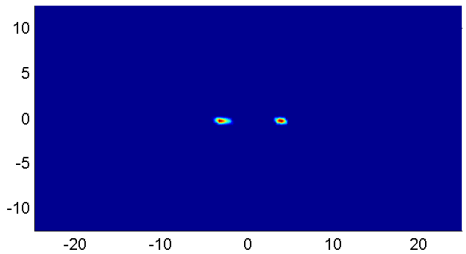

(d) Energy density plot at t=1.

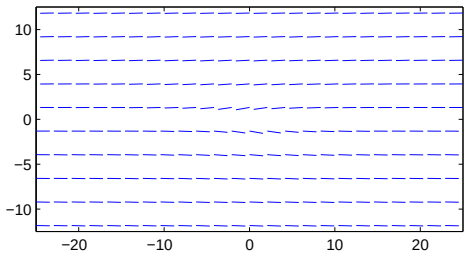

(e) Director snapshot at t=1.2.

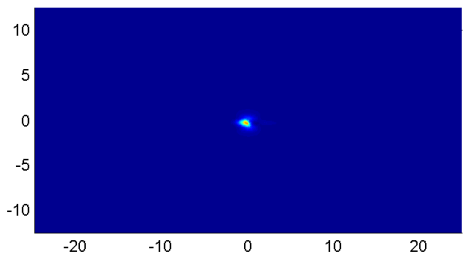

(f) Energy density plot at t=1.2.

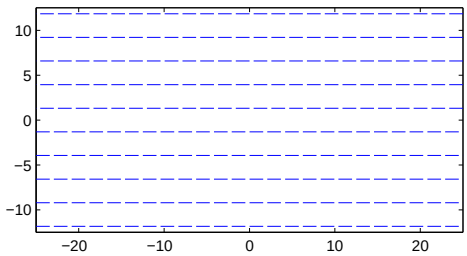

(g) Director snapshot at t=1.25.

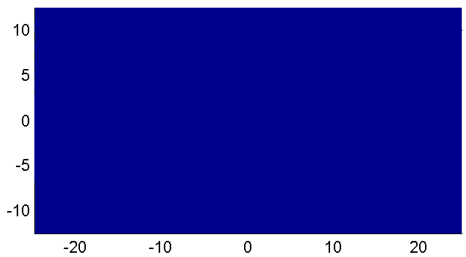

(h) Energy density plot at t=1.25.

Figure 4.15: *Snapshots for the director field and energy density at different time steps. The disclination dipole merges and annihilates.*

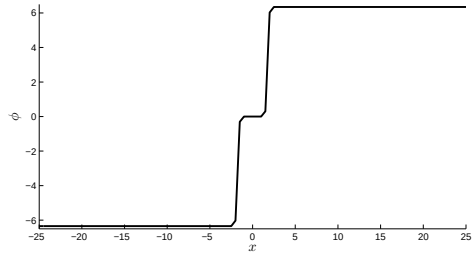

(a) Initialization of ϕ for disclination repulsion. A ϕ fields corresponding to a pair of strength $-\frac{1}{2}$ disclinations is prescribed.

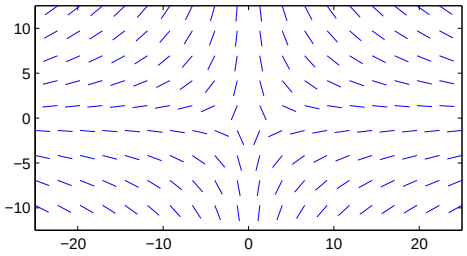

(b) The director field corresponding to the initialized ϕ.

Figure 4.16: *Initialization for disclination repulsion.*

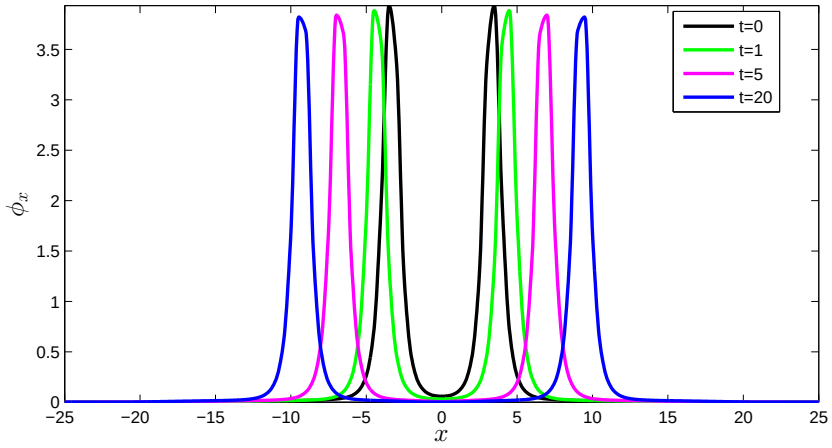

Figure 4.17: *ϕ_x snapshots at different time steps. The disclination dipole moves apart.*

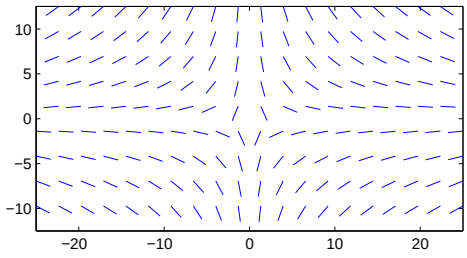

(a) Director snapshot at t=0.

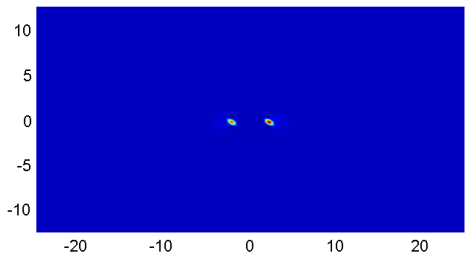

(b) Energy density plot at t=0.

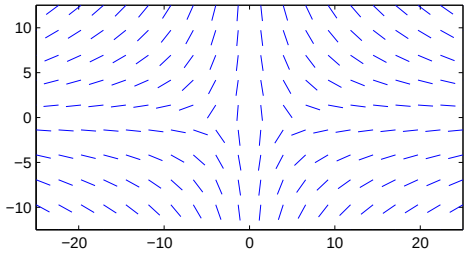

(c) Director snapshot at t=1.

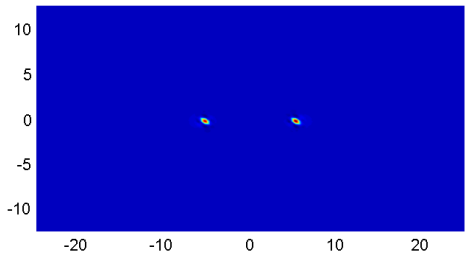

(d) Energy density plot at t=1.

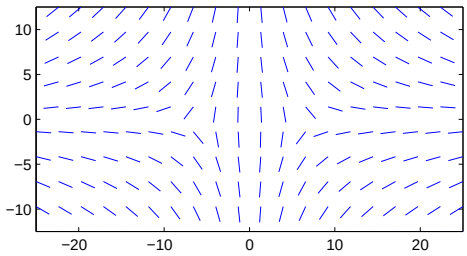

(e) Director snapshot at t=5.

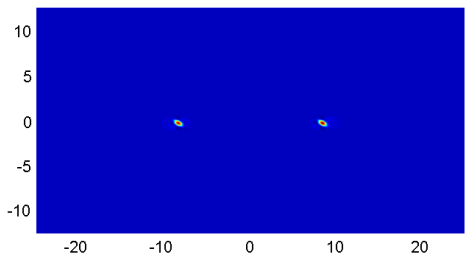

(f) Energy density plot at t=5.

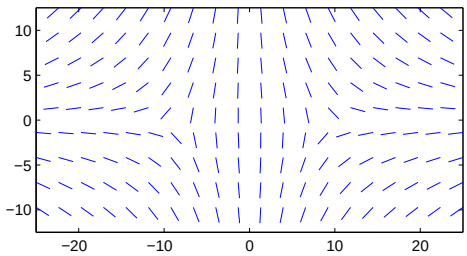

(g) Director snapshot at t=20.

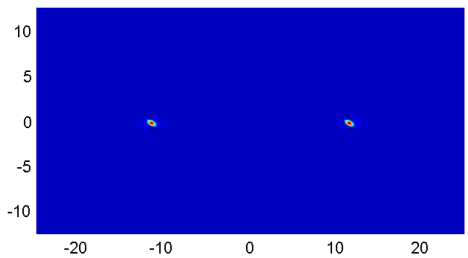

(h) Energy density plot at t=20.

Figure 4.18: *Snapshots for the director field and energy density at different time steps. The two disclinations move apart and repel each other.*

in a body of 100×100. a is set to be 0.5 in these cases. The core locations are marked at every 200 time steps and the physical discrete time at these instants is recorded. This allows the determination of the (absolute) velocity of (any) one disclination in the dipole pair as a function of the separation distance, as shown in Figure 4.19. In (4.11), τ serves as the driving force for the disclination motion. The driving force on one disclination of the dipole core is generated from the elastic interaction with the other disclination, which scales like the reciprocal of the separation distance according to the linear theory of defects. Hence, the motion of the disclinations slows down as the separation distances increases. In Figure 4.19, the red line presents a trend of $1/r$ while the blue line represents the velocity of one disclination. Figure 4.19(a) shows the relationship between velocity and separation distance in the $m = 1$ case. Thus, the velocity matches with $1/r$ trend very well in this case. Figure 4.19(b) shows the relationship between velocity and separation distance in $m = 2$ case. In this case, the velocity is the largest of all the three cases and matches $1/r$ trend in the large separation distance range. Within the separation distance from 5 to 15, the disclinations begin to annihilate. For $m = 0$ case, the disclinations are found not to move until the separation distance is less than 35. Figure 4.20 shows the velocity profile of the $m = 0$ case. It shows that the velocity does not match the $1/r$ very well when the separation distance is small but has a better agreement with $1/r$ trend as far away separation distance.

We note here that there is no reason, *a-priori*, for the velocity in our nonlinear, *dynamic* model to match the expected result from the notion of 'non-Newtonian forces' of static defect theory [Esh80, Eri95] but our results demonstrate that to a large extent there is consonance between our results and that of traditional defect theory. However, the differences are noteworthy as well - in particular the emergence of apparent 'intrinsic pinning' in a translationally-invariant pde model (cf.[ZAWB15] where the details of this phenomena are investigated in greater detail) for the case $m = 0$, the most natural kinetic model in our setting.

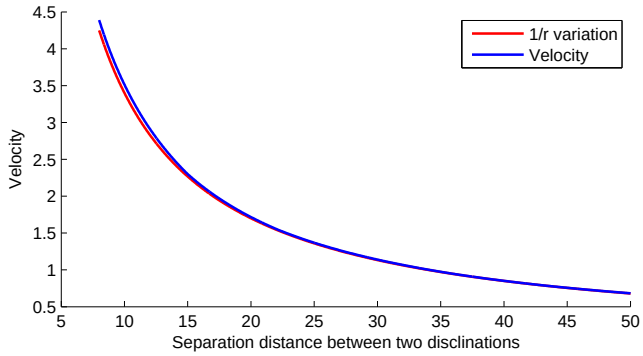

(a) Velocity variation of one disclination in a dipole as a function of separation distance. $m = 1$.

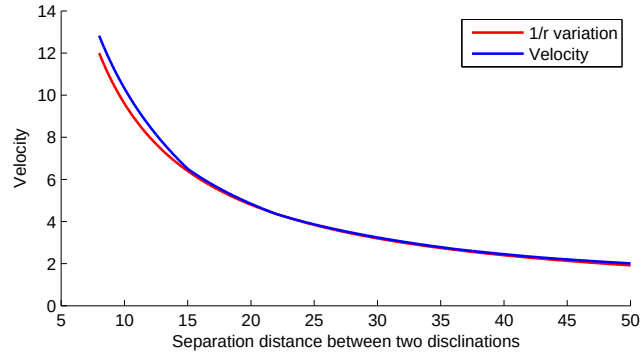

(b) Velocity variation of one disclination in a dipole as a function of separation distance. $m = 2$.

Figure 4.19: *Relation between velocity and the separation distance for* $m = 1$ *and* $m = 2$.

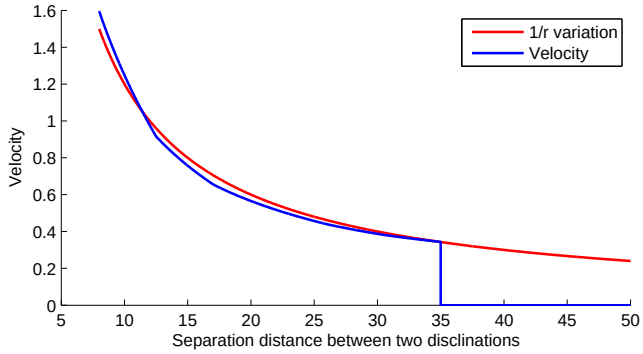

Figure 4.20: *Velocity variation of one disclination in a dipole as a function of separation distance.* $m = 0$.

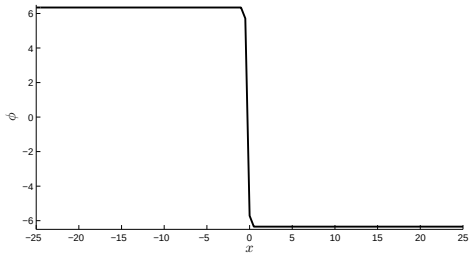

(a) Initialization of ϕ for strength +1 disclination splitting. A ϕ field corresponding to strength +1 disclination is prescribed.

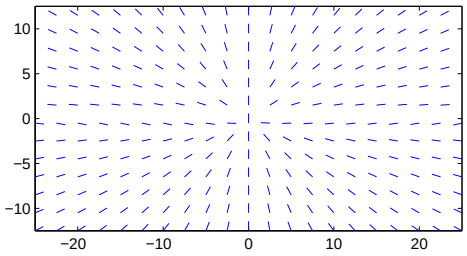

(b) Director field corresponding to initialized ϕ.

Figure 4.21: *Initialization for strength +1 disclination dissociation.*

4.6.4 Disclination dissociation

We model the process of a strength-one disclination dissociating into two strength-half disclinations. Dissociations of a positive and a negative strength-one disclination are simulated.

We prescribe a strength +1 disclination at the center of the body as shown in Figure 4.21(a). Figure 4.21(b) shows the director field corresponding to the initial $\boldsymbol{\lambda}$. The initial condition on the θ field is generated by solving for moment equilibrium using the Neumann boundary condition on the director field corresponding to the moment distribution on the boundary generated from the exact solution for a strength +1 disclination in an infinite medium. During evolution, a 0-moment Neumann boundary condition is imposed. Figure 4.22 shows how the strength +1 disclination splits into two +1/2 disclinations. We observe that the strength +1 disclination first splits into two strength +1/2 disclinations and then these two strength +1/2 disclinations move apart and repel each other.

Similarly, the director field behaviors are shown in Figure 4.23. Initially, the director field represents a strength +1 disclination. And then it splits into two strength +1/2 disclinations from the core and these two disclinations are both subject to repulsion. From the energy density plots, we can also see that the energy core splits into two cores and these two energy cores repel each other.

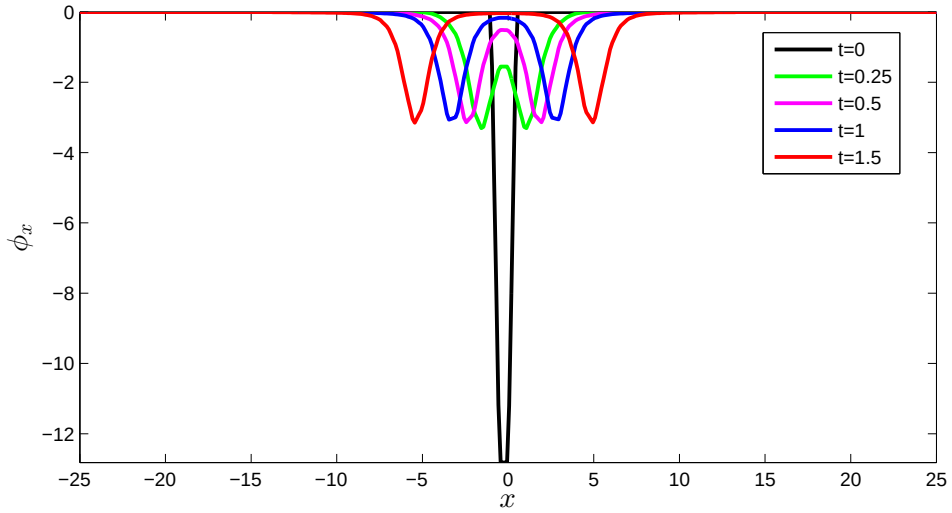

Figure 4.22: *ϕ_x snapshots at different time steps. It shows one $+1$ disclination splits into two $+1/2$ disclinations and these two disclinations repel each other.*

The splitting of a strength -1 disclination is similar. We prescribed a strength -1 disclination at the center of the body as shown in Figure 4.24(a) and the boundary conditions were set up following exactly the procedure for the previous case, accounting for the change in strength of the disclination. Figure 4.25 shows the process of the strength -1 disclination splitting into two strength $-1/2$ ones.

Figure 4.26 shows the process of the strength -1 disclination dissociating into two strength $-1/2$ disclinations in terms of the director field. From both the director field snapshots and energy density plots, we can see that the dissociation process is qualitatively similar to the strength $+1$ disclination dissociation.

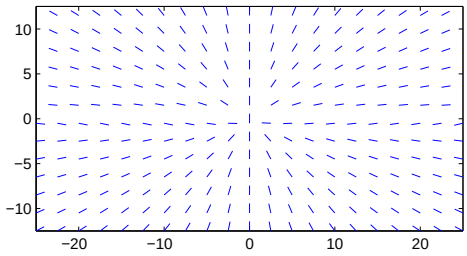

(a) Director snapshot at t=0.

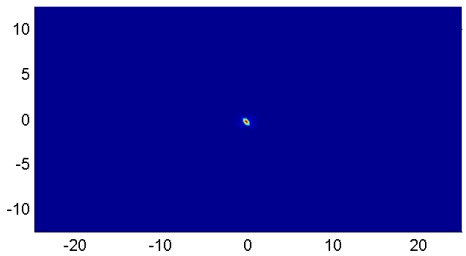

(b) Energy density plot at t=0.

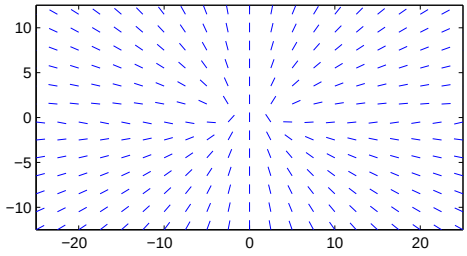

(c) Director snapshot at t=0.25.

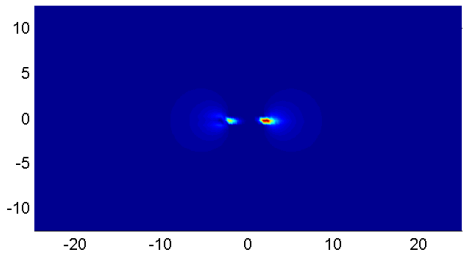

(d) Energy density plot at t=0.25.

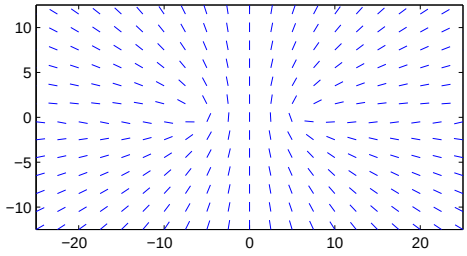

(e) Director snapshot at t=1.

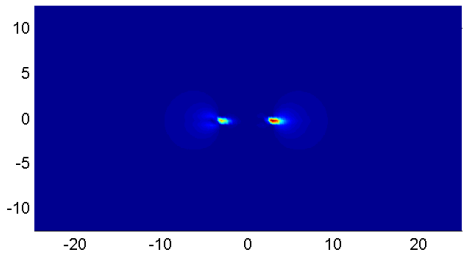

(f) Energy density plot at t=1.

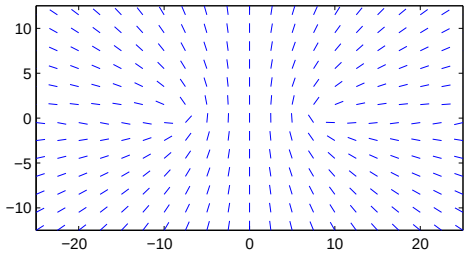

(g) Director snapshot at t=1.5.

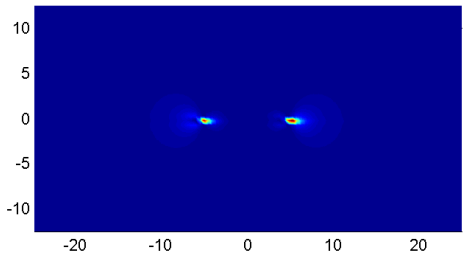

(h) Energy density plot at t=1.5.

Figure 4.23: *Snapshots for director field and energy density at different time steps. One disclination splits into two half disclinations and these two disclinations repel each other.*

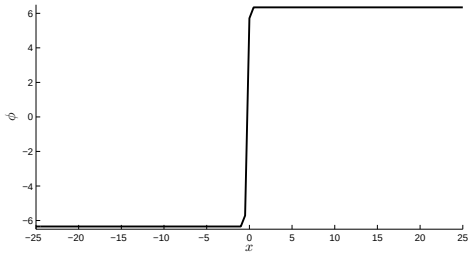

(a) Initialization of ϕ for -1 disclination dissociation. ϕ fields corresponding to strength -1 disclination is prescribed.

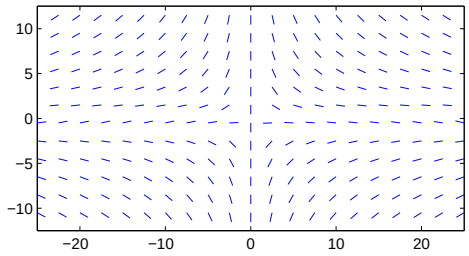

(b) Director field corresponding to initialized ϕ.

Figure 4.24: *Initialization for strength* -1 *disclination dissociation.*

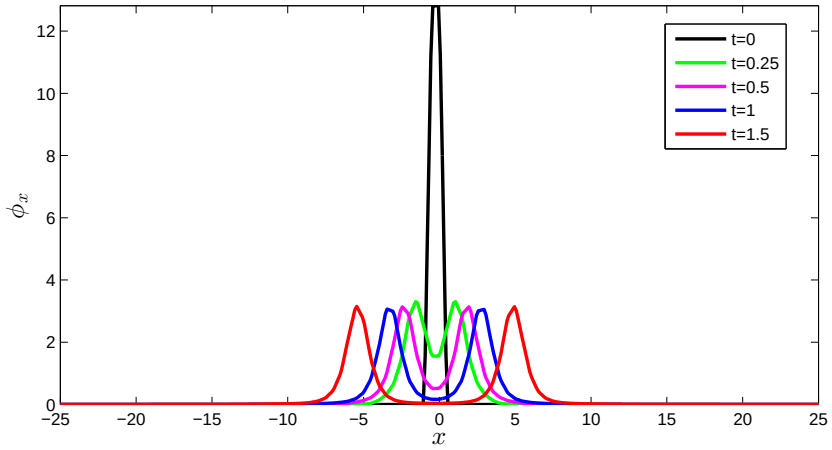

Figure 4.25: ϕ_x *snapshots at different time steps. It shows* -1 *disclination splits into two* $-1/2$ *disclinations and these two disclinations repel each other.*

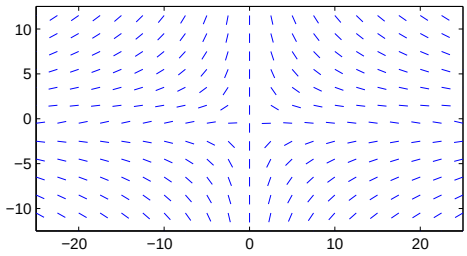

(a) Director snapshot at t=0.

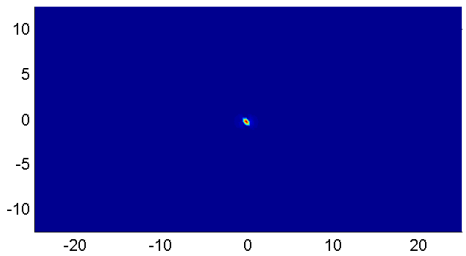

(b) Energy density plot at t=0.

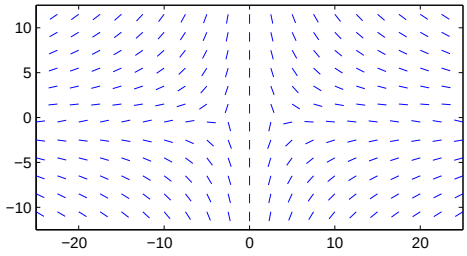

(c) Director snapshot at t=0.25.

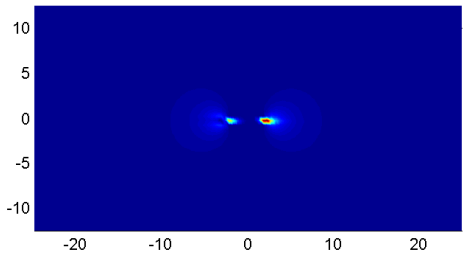

(d) Energy density plot at t=0.25.

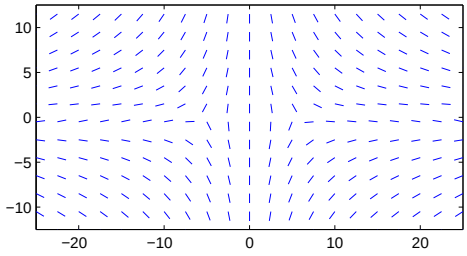

(e) Director snapshot at t=1.

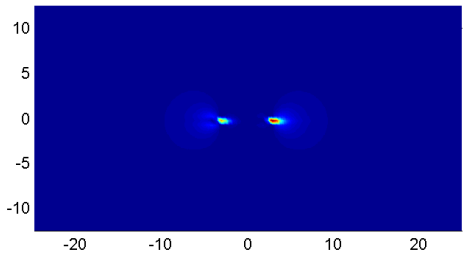

(f) Energy density plot at t=1.

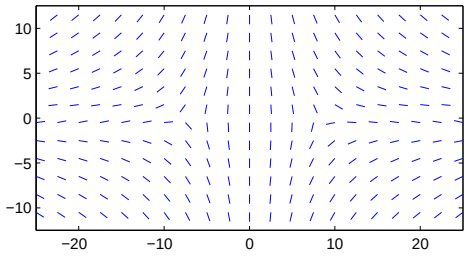

(g) Director snapshot at t=1.5.

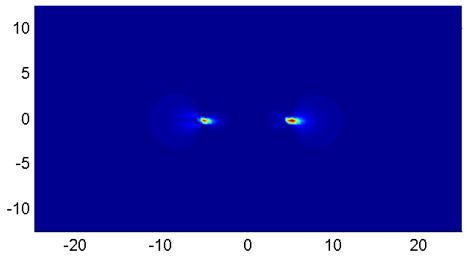

(h) Energy density plot at t=1.5.

Figure 4.26: *Snapshots for director field and energy plot at different times. One disclination splits into two half disclinations and these two disclinations repel each other.*

4.6.5 Invariance of disclination dissociation with different $\boldsymbol{\lambda}$ initializations

In Section 4.6.4, the initialization of $\boldsymbol{\lambda}$ for the k-strength disclination dissociation is given as

$$\boldsymbol{\lambda} = \begin{cases} \frac{-k\pi}{a}\boldsymbol{e}_2, & \text{if } |y| < \frac{a}{2} \text{ and } x \geq 0 \\ \frac{k\pi}{a}\boldsymbol{e}_2, & \text{if } |y| < \frac{a}{2} \text{ and } x < 0 \\ 0, & \text{otherwise.} \end{cases}$$

In this Section, we will consider a different $\boldsymbol{\lambda}$ initialization as follows

$$\boldsymbol{\lambda} = \begin{cases} \frac{-2k\pi}{a}\boldsymbol{e}_2, & \text{if } |y| < \frac{a}{2} \text{ and } x \geq 0 \\ 0, & \text{otherwise,} \end{cases}$$

in order to probe the extent of the dependence of the dissociation phenomena, i.e. defect core dynamics affected by the evolution of the couple stress field in the body, on the fine details of the layer field ($\boldsymbol{\lambda}$) evolution.

This new initialization can be achieved by applying a $\frac{k\pi}{a}$ shift on the original $\boldsymbol{\lambda}$ field within the layer, while keeping the 'jump' of $\boldsymbol{\lambda}$ within the layer same equal to $\frac{2k\pi}{a}$. Figure 4.27(a) shows the new ϕ initialization for +1 disclination dissociation, and Figure 4.27(b) is the director field corresponding to the ϕ initialization. Figure 4.27(c) and Figure 4.27(d) show the results of dissociations of strength +1 disclination. With the new initialization, the single strength +1 disclination still dissociates into two $+\frac{1}{2}$ disclinations. Figure 4.28 shows the $|\boldsymbol{\lambda}|$ evolutions with two different ϕ initializations, and the comparison of ϕ and ϕ_x at different time steps during the +1 disclination dissociation. In Figure 4.28, the solid lines represent the results from the "old" initialization applied in Section 4.6.4, while the broken lines represent the results from the new initialization. Although $|\boldsymbol{\lambda}|$ and ϕ are different at every time step, ϕ_x maintains the same profile during the whole dissociation process,

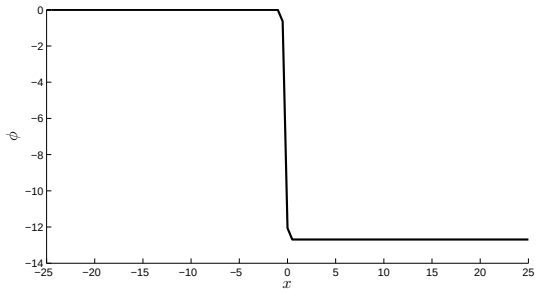

(a) Initialization of ϕ for $+1$ disclination dissociation. Difference with the initialization shown in Figure 4.21(a) is to be noted.

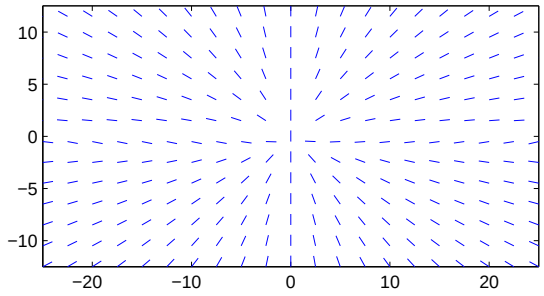

(b) Director field corresponding to the initialized ϕ. The result is identical to that shown in Figure 4.21(b).

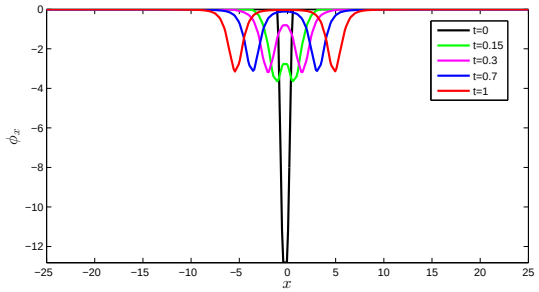

(c) ϕ_x snapshots at different time steps, showing the splitting of the $+1$ disclination.

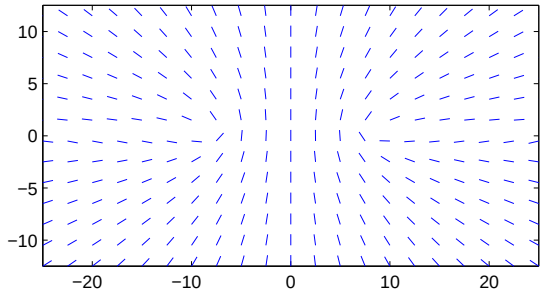

(d) A director snapshot after a $+1$ disclination has dissociated into two $+1/2$ disclinations.

Figure 4.27: *Initialization and results for* $+1$ *disclination dissociation with the new* $\boldsymbol{\lambda}$ *initialization. The dissociation process is the same as the one in Section 4.6.4.*

which shows that the dissociations are the same with these two different $\boldsymbol{\lambda}$ initializations. The -1 disclination dissociation shows the same results. The $+1$ disclination splits into two $+1/2$ disclinations and the -1 disclination splits into two $-1/2$ disclinations. Thus, although the initializations are different, the dissociation processes of ± 1 disclinations are same as before.

This example shows that to the extent that two $\boldsymbol{\lambda}$ evolutions maintain identical disclination fields, the dynamics and energetics of the defect field, at least at an overall 'macroscopic' observational level, appears to be unaltered. This fact has important modeling implications, as will be discussed in the last Section 4.8.

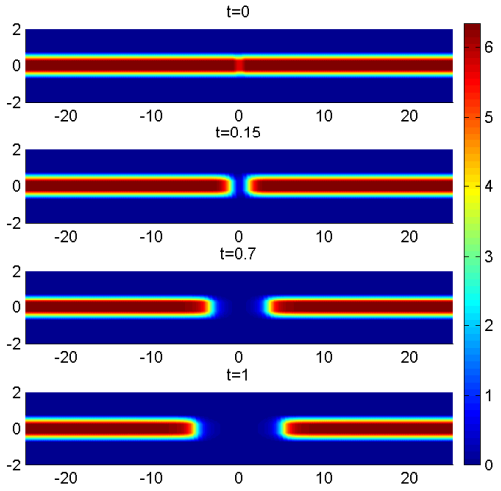

(a) $|\boldsymbol{\lambda}|$ evolution during disclination dissociation with ϕ initialization defined in Section 4.6.4.

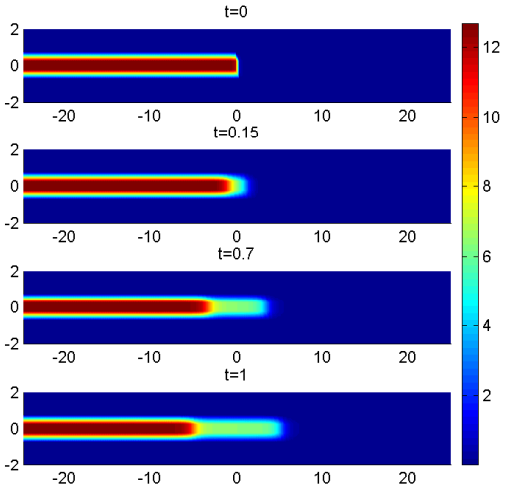

(b) $|\boldsymbol{\lambda}|$ evolution during dissociation of a +1 disclination from the new ϕ initialization.

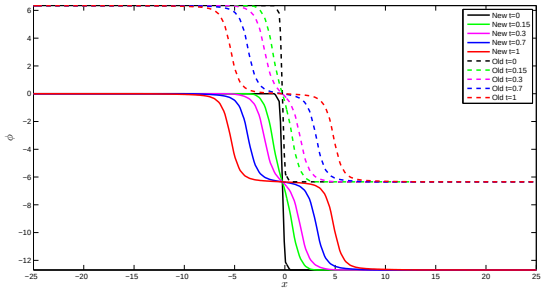

(c) ϕ comparison for +1 disclination dissociation.

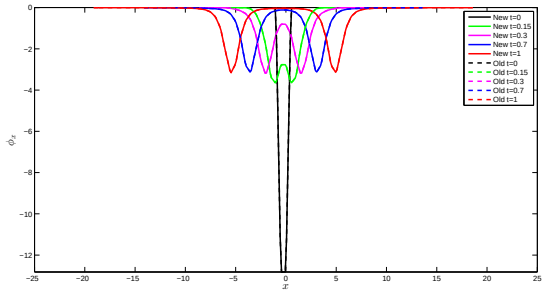

(d) ϕ_x comparison for +1 disclination dissociation.

Figure 4.28: *The comparisons of $|\boldsymbol{\lambda}|$, ϕ and ϕ_x for a strength +1 disclination dissociation. The dashed lines are the results from the "old" initialization defined in Section 4.6.4 and Figures 4.21(a),4.21(b) and 4.22. Although the $|\boldsymbol{\lambda}|$ evolutions and ϕ are different, the ϕ_x prfiles are identical during the whole process.*

4.7 Modification of the gradient flow dynamics to deal with disclination motion

In Section 4.4.6, we have shown that the gradient flow dynamics cannot deal with disclination motion. In this section, motivated by the insights gained from the disclination dynamics model in Sections 4.5 and 4.6, we suggest a modification to the gradient flow dynamics to enable it to solve physically realistic disclination dynamics problems. Recall the evolution equation (4.9) in the general disclination dynamic theory:

$$\begin{aligned}\frac{\partial \boldsymbol{\lambda}}{\partial t} &= \frac{1}{B_m |\operatorname{curl} \boldsymbol{\lambda}|^m} \operatorname{curl} \boldsymbol{\lambda} \times \left[\left(\operatorname{grad} \theta - \boldsymbol{\lambda} + \operatorname{curl} \left(\frac{\partial \psi}{\partial \operatorname{curl} \boldsymbol{\lambda}} \right) - \gamma \frac{\partial f}{\partial \boldsymbol{\lambda}} \right) \times \operatorname{curl} \boldsymbol{\lambda} \right] \\ &= \frac{|\operatorname{curl} \boldsymbol{\lambda}|^{2-m}}{B_m} \frac{\operatorname{curl} \boldsymbol{\lambda}}{|\operatorname{curl} \boldsymbol{\lambda}|} \times \left[\left(\operatorname{grad} \theta - \boldsymbol{\lambda} + \operatorname{curl} \left(\frac{\partial \psi}{\partial \operatorname{curl} \boldsymbol{\lambda}} \right) - \gamma \frac{\partial f}{\partial \boldsymbol{\lambda}} \right) \times \frac{\operatorname{curl} \boldsymbol{\lambda}}{|\operatorname{curl} \boldsymbol{\lambda}|} \right].\end{aligned}$$

We notice that the term $\operatorname{grad} \theta - \boldsymbol{\lambda} + \operatorname{curl} \left(\frac{\partial \psi}{\partial \operatorname{curl} \boldsymbol{\lambda}} \right) - \gamma \frac{\partial f}{\partial \boldsymbol{\lambda}}$ in this evolution equation is the same as the right-hand-side of the gradient flow dynamics (4.5). As mentioned earlier, a salient feature of the $\operatorname{curl} \boldsymbol{\lambda}$ multiplier allows evolution only at points where $\operatorname{curl} \boldsymbol{\lambda}$ is non-zero, i.e. in the core and immediate vicinity of the core. Thus, instead of using the regular gradient flow evolution of Section 4.4.6, we modify the $\boldsymbol{\lambda}$ evolution equation as follow:

$$\frac{\partial \boldsymbol{\lambda}}{\partial s} = H(|\operatorname{curl} \boldsymbol{\lambda}| - T) \left[\operatorname{grad} \theta - \boldsymbol{\lambda} + \operatorname{curl} \left(\frac{\partial \psi}{\partial \operatorname{curl} \boldsymbol{\lambda}} \right) - \gamma \frac{\partial f}{\partial \boldsymbol{\lambda}} \right].$$

where T is a prescribed threshold and the Heaviside step function is set to be

$$H(x) = \begin{cases} 0 & x < 0 \\ 1 & x \geq 0. \end{cases}$$

In other words, the layer field is evolved according to

$$\frac{d\lambda_k}{ds} = \begin{cases} -\frac{\delta W}{\delta \lambda_k} = -\gamma \frac{\partial f}{\partial |\lambda|} \frac{1}{|\lambda|} \lambda_k + \theta_{,k} - \lambda_k + \epsilon e_{ijk} e_{irs} \lambda_{s,rj} & \text{if } |\operatorname{curl} \boldsymbol{\lambda}| \geq T \\ 0 & \text{otherwise.} \end{cases}$$

Based on the above modified evolution equation, we recalculate the disclination annihilation case. The results are shown in Figure 4.29(c) and (d). Compared to the energy density and director results from Section 4.4.6, the energy density as well as the director results obtained from the modified evolution equations, shown in Figure 4.29(c) and (d), are much more reasonable, matching physical expectation.

4.8 Some observations

We conclude with three further observations.

Figure 4.30 shows a comparison of the norm of two different $\boldsymbol{\lambda}$ fields for the $+1/2$ disclination. Figure 4.30(a) is the norm field of the new $\boldsymbol{\lambda}$ prescription and Figure 4.30(b) shows the norm of the $\boldsymbol{\lambda}$ field given in Figure 4.3. The $\operatorname{curl} \boldsymbol{\lambda}$ fields are identical in these two $\boldsymbol{\lambda}$ settings. Figure 4.31 shows the director pattern and energy density results based on the two $\boldsymbol{\lambda}$ prescriptions given in Figure 4.30. As theoretically explained in [PAD15], the comparison shows that as far as static director and energy distributions are concerned, an identical 'one-point' specification of the director on the domain renders two distinct $\boldsymbol{\lambda}$ fields with identical $curl\boldsymbol{\lambda}$ fields, indistinguishable. Furthermore, the results of Section 4.6.5 show that this invariance is carried over to the disclination dynamics as well. Of course, this invariance is not to be mistaken with 'gauge-invariance' in the sense that, for a fixed $\boldsymbol{b}$ field, the theory requires the use of at least one, non-divergence-free $\boldsymbol{\lambda}$ field of the 'layer-type' consistent with $\boldsymbol{b} = -\operatorname{curl} \boldsymbol{\lambda}$ for the correct prediction of the director distribution, i.e. not employing a $\boldsymbol{\lambda}$ field and insisting on just the use of the $\boldsymbol{b}$ field is not feasible (even

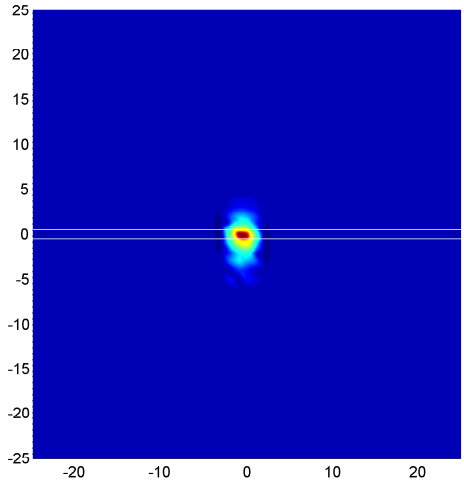

(a) Energy density plot from the regular gradient flow method.

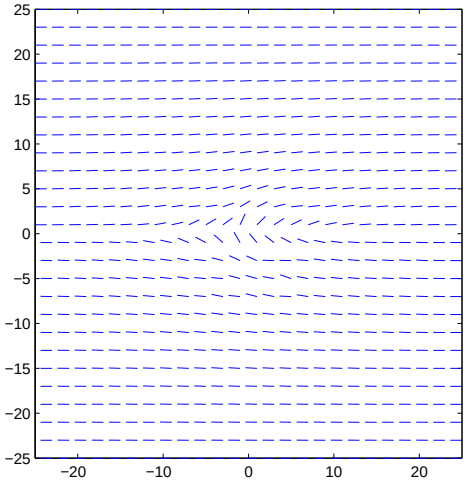

(b) Director field result from regular gradient flow method.

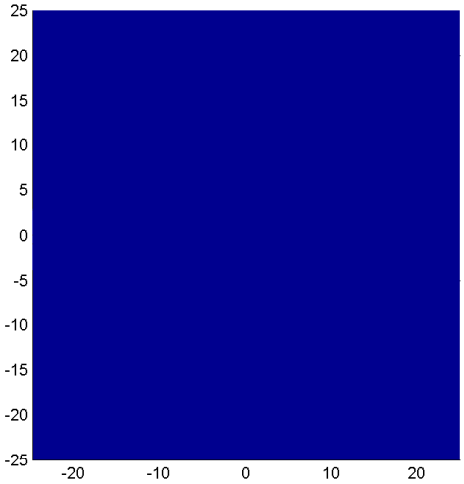

(c) Energy density plot from the modified gradient flow method.

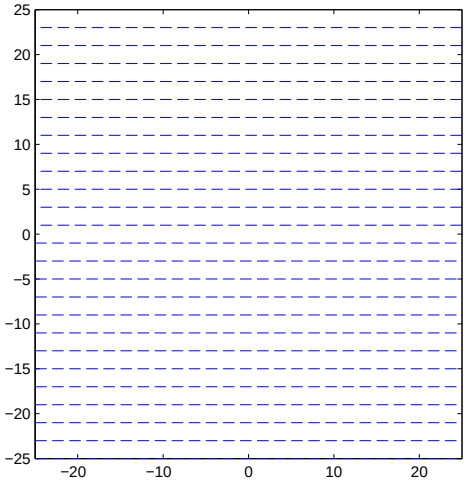

(d) Director field result from the modified gradient flow method.

Figure 4.29: *Top: the energy density and director field results from regular gradient flow method. Bottom: the energy density and director field results from the modified gradient flow method, which match physical expectation.*

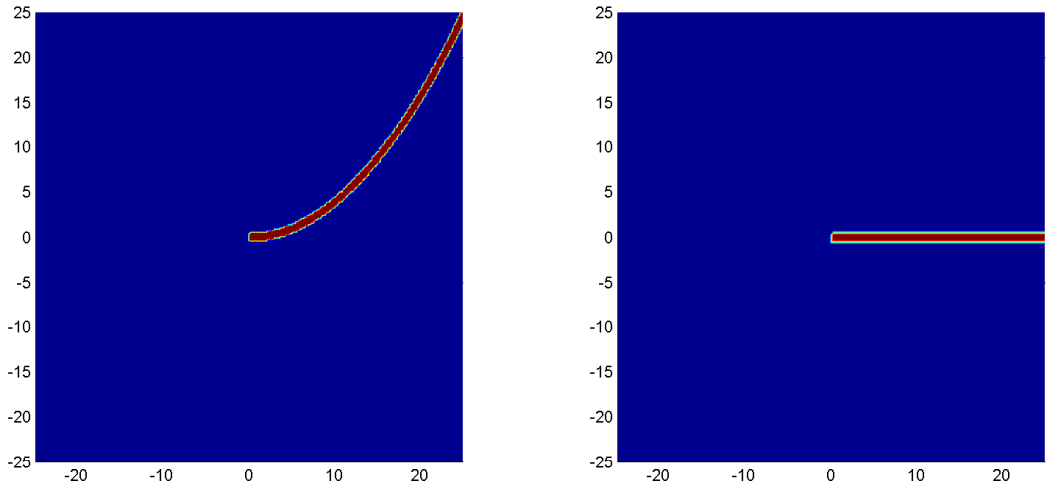

(a) The norm of a distinct $\boldsymbol{\lambda}$ field from that in Fig. 4.3, but with identical curl $\boldsymbol{\lambda}$ field, for a $+1/2$ disclination.

(b) The norm of the $\boldsymbol{\lambda}$ field given in Figure 4.3.

Figure 4.30: *The comparison of two* $|\boldsymbol{\lambda}|$ *fields with identical* curl $\boldsymbol{\lambda}$ *fields for a* $+1/2$ *disclination. The direction of* $\boldsymbol{\lambda}$ *is perpendicular to the layer at each point along the layer.*

though, in some instances, not introducing a layer-type $\boldsymbol{\lambda}$ field can suffice for the correct prediction of *only* the energy density field). This partial invariance of the results of our model with respect to the precise details of the $\boldsymbol{\lambda}$ field suggests a useful freedom in numerical simulations. Essentially, in principle, the $\boldsymbol{\lambda}$ field can be reinitialized at every instant of time, consistent with the evolving $\boldsymbol{b}$ field. Thus, a strategy may be to evolve the $\boldsymbol{b}$ field instead of $\boldsymbol{\lambda}$ and use the $\boldsymbol{\lambda}$ construct to simply facilitate the calculation of the energetics and the director distribution at each instant of time. Moreover, our demonstration that a 'layer' of finite thickness is merely a geometric approximation, without energetic consequences, of a surface of director-vector discontinuity suggests natural ways of associating a 'non-turning' director distribution within the layer for calculations of Leslie-Ericksen viscous stresses. We shall demonstrate such features in future work.

Second, Appendix J shows the energetic, dynamic, and topological interoperability between our model of disclination dynamics in nematic liquid crystals with orientational

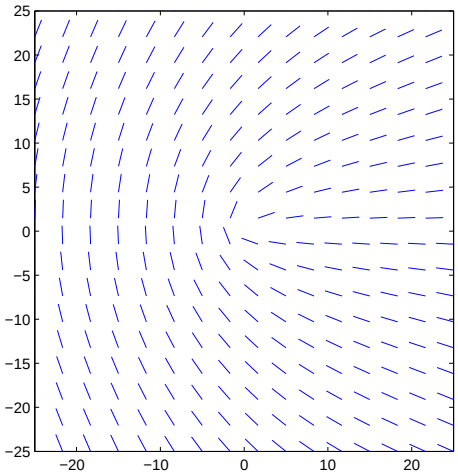

(a) Director field at $l/L = 0.005$ with the $\boldsymbol{\lambda}$ initialization given in Figure 4.3.

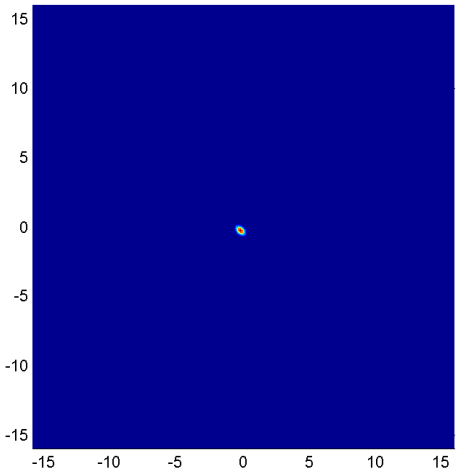

(b) The energy density plot for the $+1/2$ disclination with the $\boldsymbol{\lambda}$ initialization given in Figure 4.3.

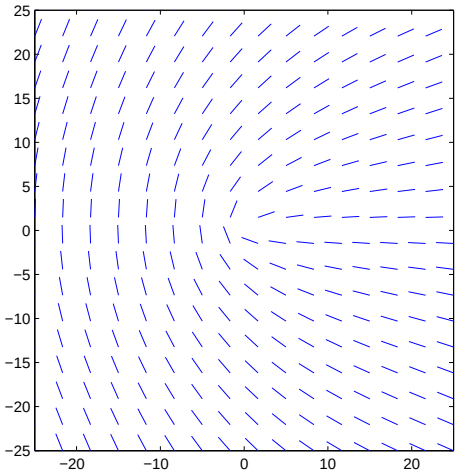

(c) Director field at $l/L = 0.005$ with the $\boldsymbol{\lambda}$ initialization given in Figure 4.30(a).

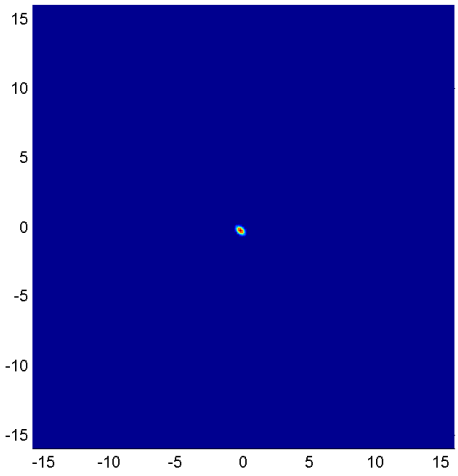

(d) The energy density plot for the $+1/2$ disclination with the $\boldsymbol{\lambda}$ initialization given in Figure 4.30(a).

Figure 4.31: *Director and energy density for the $+\frac{1}{2}$ disclination with two different $\boldsymbol{\lambda}$ initializations. The results show that two distinct $\boldsymbol{\lambda}$ fields with identical* curl $\boldsymbol{\lambda}$ *fields give identical director and energy distributions.*

order and that of screw dislocation dynamics in elastic solids with positional order. We consider this as a positive development that can only benefit the understanding of defect dynamics in liquid crystals and elastic solids, leading to their plasticity.

Third, there are very interesting similarities and contrasts between the models and results of energy driven pattern formation discussed in the papers [Koh06, JS98, ADLGP14, EV09, New12] and our model. A comparative study is an undertaking in its own right that will form the subject of future study.

Chapter 5

Computational modeling of tactoid dynamics in lyotropic chromonic liquid crystals

5.1 Introduction

Liquid crystals (LC) are a state of matter with long-range orientational order and complete (nematic) or partial (smectics, columnar phases) absence of long-range positional order of 'building units' (molecules, viruses, aggregates, etc.). Liquid crystals can flow like viscous liquids, and also possess features that are characteristic of solid crystals, such as elasticity and birefringence. In the simplest liquid crystalline phase, called the nematic, the molecules have no positional order but tend to point in the same direction. In this work, we focus on a nematic lyotropic liquid crystal (LCLC) that possesses a broad biphasic region of coexisting nematic and isotropic phases [KSL13].

LCLCs are formed by water-based dispersions of organic molecules, see the recent reviews [Lyd11, CGH$^+$15, PL12]. The molecules are of a rigid disc-like or plank-like shape with polar groups at the periphery. Once in water, they form elongated aggregates by stacking on top of each other. The aggregates elongate as the concentration is increased and the temperature is reduced, which allows one to trigger phase transitions in the system by changing either the temperature or concentration [NLS$^+$04, PKT$^+$11]. In particular, the temperature changes can trigger a first order isotropic-nematic (I-N) phase transition of the LCLC. As the temperature increases, the nematic liquid crystal loses orientational order and transits to the isotropic phase, with molecular aggregates being short and oriented randomly. On the contrary, if the temperature decreases, the isotropic phase transits to the nematic phase. Both phase transitions occur through nucleation of the so-called tactoids, representing inclusions of one phase in the other [KSL13, TPK$^+$10a, NLS$^+$05, TL11]. Tactoids of the nematic phase nucleating upon cooling are called positive tactoids [NLS$^+$05] and are the subject of the present work. Tactoids of the isotropic phase nucleating in the nematic background upon heating are called negative tactoids [NLS$^+$05]. If the temperature is fixed in the range in which the two phases coexist, these tactoids expand and merge. The uniaxial nematic phase allows three types of topologically stable defects:

linear disclinations, point defects-hedgehogs and point defect-boojums; the latter can exist only at the surface of the nematic [KL07, CD$^+$91, BCSS94, Vac91]. In confined volumes, such as droplets and tactoids, some of the topological defects correspond to the equilibrium state of the system, thanks to the anisotropic surface tension that sets a well-defined angle between the director and the normal to the interface [VL83].

The principal objectives of this work are to:

- derive a practical equation of evolution for the degree of orientation based on kinematics and thermodynamics;
- introduce a dynamic model for the nematic-isotropic phase transition of LCLC with an augmented Oseen-Frank energy and non-convex interfacial energy;
- demonstrate the capability of the proposed dynamical model by analyzing the results of static equilibrium and the dynamic behaviors.

The main experimental observations and applications of LCLC and their computation are reviewed in [KSL13, PL12, Lyd11, CGH$^+$15]. Currently, there is an extensive database on the principal material parameters of the LCLCs and defects in them. All three bulk elastic constants (for splay K_{11}, twist K_{22} and bend K_{33}) have been measured for two main representatives of LCLCs [ZNO$^+$12, ZNN$^+$14, ZCL14]. It was found that the elastic constants of bend and splay can be tuned in a broad range, from a few pN to 70 pN, by changing temperature or the chemical composition of the system (e.g., by adding salts [ZCL14]). The director of LCLCs can align either parallel to the interface with an adjacent medium [SAF$^+$05] or in a perpendicular fashion, with possible transitions between these two states [NBP$^+$10]. At the interface with its own isotropic melt, the director of a nematic LCLC aligns parallel to it [TPK$^+$10b]. The interfacial surface tension at the isotropic-nematic interface was estimated to be on the order of 10^{-4} J/m^2 [KSL13]. The defect cores of disclinations in LCLCs extend over long distances (microns and even tens of microns), much larger than the cores of disclinations in thermotropic liquid crystals [ZSPL17].

In this work, we are primary interested in the observations reported in [KSL13] to develop a model for understanding the behavior of tactoids during the isotropic-nematic transformation. The isotropic-nematic interface in LCLC favors the director to be tangential to the tactoid interface. Fig. 5.1 shows the experimental observations of the isotropic-nematic phase transition from [KSL13]. Fig. 5.1(a) shows a single tactoid, where the black color represents the isotropic phase while the orange color represents the nematic phase. The black arrows inside the tactoid represent the director field. Nontrivial morphologies of tactoids with surface cusps and director fields are observed. Due to the surface anisotropy, cusps are associated with surface defects called boojums, as shown in Fig. 5.1(a). Fig. 5.1(b) to 5.1(e) represent the phase transition process from the isotropic to the nematic phase, where the nematic tactoids expand and merge. Merging tactoids often produce disclinations via the Kibble mechanism [CD$^+$91, BCSS94, Kib76], as shown in Fig. 5.1(e), where a strength $-\frac{1}{2}$ disclination is formed at the point where tactoids merge. In addition, integer strength disclinations are stable only when their cores constitute a large isotropic inclusion; otherwise, as demonstrated experimentally and analytically by Y.-K. Kim et al [KSL13] and numerically in Chapter 4, the integer strength disclinations split into pairs of half-integer ones. The motion of an interface between a nematic liquid crystal phase and the isotropic phase is investigated with a Ginzburg-Landau equation in [PNS96]. The confinement of the director field for a spherical particle that explains the observation of a Saturn ring is studied in [GAdP03].

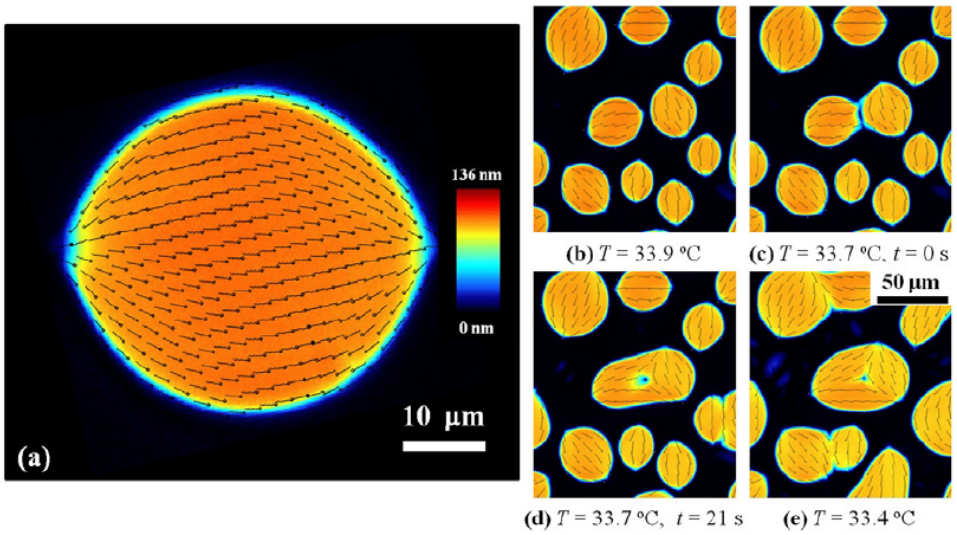

Figure 5.1: *Experiment observations of isotropic-nematic phase transition from [KSL13].*

In studies of nematic liquid crystals, a classical convention is to represent the local orientational order by a unit-length director field [Vir95, Eri91]. Oseen and Frank developed an energy density of nematic liquid crystals, with constants representing different director deformations [Fra58, Ose33]. The existence and partial regularity theory of some boundary-value problems based on Oseen-Frank energy density are discussed in [HKL86]. The Oseen-Frank energy can be augmented by adding an additional surface energy density to represent the interaction between the LC and an adjacent medium; a common form of such a surface energy density is the Rapini-Papoular surface energy.

In this paper we develop a computational model for the isotropic-nematic phase transition accounting for interfacial energy as an enhancement of Ericksen's variable degree of order $(s, \boldsymbol{n})$ model [Eri91]. We introduce the pair $(s, \boldsymbol{d})$ with $(\boldsymbol{d} = s\boldsymbol{n})$. The state variable s has the meaning of the degree of order parameter in Ericksen's model [Eri91] and $\boldsymbol{d}$ serves for the director whose magnitude is constrained to be equal to $|s|$. Thus, the director is of unit length in the nematic phase, it vanishes in the isotropic phase, and it is of variable length at interfaces between the two phases. This practical device of replacing $\boldsymbol{n}$ by $\boldsymbol{d}$ is essential in terms of having a setting that is well-posed for computations of a

time-dependent nonlinear theory, since leaving the value of the director field undefined in parts of the domain, that furthermore evolve in time, does not lead to unique evolution and simply cannot be practically implemented.

The rest of this paper is organized as follows: In Section 5.2, we outline our notation and terminology. In Section 5.3, a dynamic model for the phase transition process based on kinematics as well as thermodynamics is derived.Also, the results of equilibrium and dynamic behaviors are shown and discussed. The significance of the dynamic model is demonstrated and explained. In Section 5.4, we report on a preliminary parametric study of material constants in the model. We end with some concluding remarks in Section 5.5.

5.2 Notation and terminology

The symbol div represents the divergence and grad represents the gradient. In this paper all tensor or vector indices are written with respect to the basis $\boldsymbol{e}_i$, $\boldsymbol{i}$=1 to 3, of a rectangular Cartesian coordinate system. The following component-form notation holds:

$$(\boldsymbol{a} \times \boldsymbol{b})_i = e_{ijk} a_j b_k$$

$$(\operatorname{curl} \boldsymbol{a})_i = e_{ijk} a_{k,j}$$

where e_{mjk} is a component of the alternating tensor $\boldsymbol{X}$.

The following list describes some of the mathematical symbols we use in this work:

$\boldsymbol{n}$: the unit vector field representing the director

s: the degree of orientation, $s = 0$ represents the isotropic phase while $s = 1$ represents the nematic phase

$\boldsymbol{d}$: the alternative vector field representing the director with $\boldsymbol{d} = s\boldsymbol{n}$

ψ: the free energy density

5.3 Derivation of dynamic model

5.3.1 s evolution equation in Ericksen-Leslie model

In [Eri91], Ericksen introduced a variable degree of orientation s to represent different phase states of a liquid crystal. In his model, $s = 0$ represents the isotropic phase and $s = 1$, the nematic phase. Also, a unit length vector field is introduced to represent the director field, denoted as $\boldsymbol{n}$. In Ericksen's model, the balance law to derive the s evolution equation is given as

$$\dot{P} = \operatorname{div}(\boldsymbol{T}) + G^I + G^E,$$

where ψ is free energy density, P is a generalized momentum with $P = \partial\psi/\partial s$, $\boldsymbol{T}$ is a generalized stress, G^I represents a kind of internal body force with $G^I = -\partial\psi/\partial s + \hat{G}$, and G^E is an external effect. Assuming the free energy density ψ depends on $(s, \operatorname{grad} s, \boldsymbol{n}, \operatorname{grad} \boldsymbol{n})$, and following the argument in [Eri91], we have

$$\begin{gathered}\dot{\overline{\frac{\partial\psi}{\partial s}}} = \operatorname{div}(\tfrac{\partial\psi}{\partial\nabla s}) - \tfrac{\partial\psi}{\partial s} + \hat{G} + G^E \\ \Rightarrow \tfrac{\partial^2\psi}{\partial s^2}\dot{s} + \tfrac{\partial^2\psi}{\partial s\partial \operatorname{grad} s} \cdot \dot{\overline{\operatorname{grad} s}} + \tfrac{\partial^2\psi}{\partial s\partial \boldsymbol{n}} \cdot \dot{\boldsymbol{n}} + \tfrac{\partial^2\psi}{\partial s\partial \operatorname{grad} \boldsymbol{n}} : \dot{\overline{\operatorname{grad} \boldsymbol{n}}} = \operatorname{div}(\tfrac{\partial\psi}{\partial \operatorname{grad} s}) - \tfrac{\partial\psi}{\partial s} + \hat{G} + G^E.\end{gathered}$$

After rearranging the terms, s evolution equation in Ericksen's model can be written as

$$\begin{gathered}(\tfrac{\partial^2\psi}{\partial s^2})\dot{s} + \tfrac{\partial^2\psi}{\partial s\partial \operatorname{grad} s} \cdot \dot{\overline{\operatorname{grad} s}} = \\ \operatorname{div}(\tfrac{\partial\psi}{\partial \operatorname{grad} s}) - \tfrac{\partial\psi}{\partial s} + \hat{G} + G^E - \tfrac{\partial^2\psi}{\partial s\partial \boldsymbol{n}} \cdot \dot{\boldsymbol{n}} - \tfrac{\partial^2\psi}{\partial s\partial \operatorname{grad} \boldsymbol{n}} : \dot{\overline{\operatorname{grad} \boldsymbol{n}}}.\end{gathered}$$

In this work, we would like to adopt a simpler evolution statement since the fundamental basis for Ericksen's balance law $\dot{P} = \operatorname{div}(\boldsymbol{T}) + G^I + G^E$ is not clear to us. In particular, the coefficient $\frac{\partial^2\psi}{\partial s^2}$ may change signs as the dependence on s of the energy is nonconvex.

5.3.2 Motivation and derivation of s evolution

We derive a practical model for tactoid and isotropic-nematic phase transition dynamics based on continuum kinematics and thermodynamics. To get the evolution equation for s, suppose there is a level set of s with normal velocity field $\boldsymbol{V}^{(s)}$ along it, traveling from $\boldsymbol{x}_2$ to $\boldsymbol{x}_1$ during a time interval Δt, as shown in Fig. 5.2. The time derivative of s at $\boldsymbol{x}_1$ and t is

$$\frac{\partial s}{\partial t} = \lim_{\Delta t \to 0} \frac{s(\boldsymbol{x}_1, t + \Delta t) - s(\boldsymbol{x}_1, t)}{\Delta t}. \tag{5.1}$$

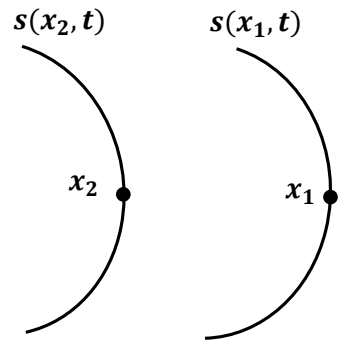

Figure 5.2: *A levelset of s moving from $\boldsymbol{x}_2$ to $\boldsymbol{x}_1$ during Δt.*

Since the level set of s travels from $\boldsymbol{x}_2$ to $\boldsymbol{x}_1$ during the time interval Δt, $s(\boldsymbol{x}_1, t+\Delta t) = s(\boldsymbol{x}_2(\Delta t), t)$. Thus, $\frac{\partial s}{\partial t}$ may also be expressed as

$$\frac{\partial s}{\partial t} = \lim_{\Delta t \to 0} \frac{s(\boldsymbol{x}_2(\Delta t), t) - s(\boldsymbol{x}_1, t)}{\Delta t}. \tag{5.2}$$

Assuming s is differentiable in its arguments and writing the derivative in the first argument as $\operatorname{grad} s$, we have

$$\begin{aligned} s(\boldsymbol{x}_2(\Delta t), t) - s(\boldsymbol{x}_1, t) &= \operatorname{grad} s(\boldsymbol{x}_1, t)[\boldsymbol{x}_2(\Delta t) - \boldsymbol{x}_1] + o(\boldsymbol{x}_2(\Delta t) - \boldsymbol{x}_1) \\ \Rightarrow \frac{s(\boldsymbol{x}_2(\Delta t), t) - s(\boldsymbol{x}_1, t)}{\Delta t} &= \operatorname{grad} s(\boldsymbol{x}_1, t)\frac{1}{\Delta t}[\boldsymbol{x}_2(\Delta t) - \boldsymbol{x}_1] + \frac{1}{\Delta t} o(\boldsymbol{x}_2(\Delta t) - \boldsymbol{x}_1). \end{aligned} \tag{5.3}$$

Substitute (5.3) in (5.2), we have

$$\frac{\partial s}{\partial t} = \operatorname{grad} s(\boldsymbol{x}_1, t) \lim_{\Delta t \to 0} \frac{\boldsymbol{x}_2(\Delta t) - \boldsymbol{x}_1}{\Delta t} + \lim_{\Delta t \to 0} \frac{o(\boldsymbol{x}_2(\Delta t) - \boldsymbol{x}_1)}{\Delta t}. \tag{5.4}$$

Denote $\boldsymbol{V}^{(s)}$ as the velocity of movement of a level set of s, $\boldsymbol{V}^{(s)} = \lim_{\Delta t \to 0} \frac{\boldsymbol{x}_1 - \boldsymbol{x}_2(\Delta t)}{\Delta t}$. Since

$$\lim_{\Delta t \to 0} \left| \frac{o(\boldsymbol{x}_2(\Delta t) - \boldsymbol{x}_1)}{\Delta t} \right| = \lim_{\Delta t \to 0} \frac{|o(\boldsymbol{x}_2(\Delta t) - \boldsymbol{x}_1)|}{|\boldsymbol{x}_2(\Delta t) - \boldsymbol{x}_1|} \frac{|\boldsymbol{x}_2(\Delta t) - \boldsymbol{x}_1|}{\Delta t} = -0 \cdot |\boldsymbol{V}^{(s)}| = 0.$$

(5.4) becomes

$$\frac{\partial s}{\partial t} = -\operatorname{grad} s \cdot \boldsymbol{V}^{(s)}.$$

If the material velocity is $\boldsymbol{v}$ and the change in the value of s at $\boldsymbol{x}_1$ arises from factors more than the pure advection of the value of s from $\boldsymbol{x}_2$ to $\boldsymbol{x}_1$ due to material motion, then we assign the rest of this change as occurring due to the progress of the phase transition front. In general, we can decompose $\boldsymbol{V}^{(s)} = \boldsymbol{v} + \boldsymbol{V}$, where $\boldsymbol{V}$ is the phase front velocity relative to the material and $\boldsymbol{v}$ is the material velocity. Recall that the material time derivative of s is defined as

$$\dot{s} := \frac{ds}{dt} = \frac{\partial s}{\partial t} + \operatorname{grad} s \cdot \boldsymbol{v};$$

therefore, the s evolution is given as

$$\dot{s} = -\operatorname{grad} s \cdot \boldsymbol{V}. \tag{5.5}$$

In particular, there are two special cases:

- Suppose this velocity was purely due to s being transported by the material velocity $\boldsymbol{v}$. Then we have that $\dot{s} = \frac{\partial s}{\partial t} + \frac{\partial s}{\partial \boldsymbol{x}} \cdot \boldsymbol{v} = 0$.
- If there is no material velocity but transport is only due to motion of the phase front,

then $\boldsymbol{V}^{(s)}$ is just the speed of the phase front transition $\boldsymbol{V}$.

To get an explicit form of the phase front velocity $\boldsymbol{V}$, assume the free energy density per unit mass takes the form $\psi(\boldsymbol{n}, \operatorname{grad}\boldsymbol{n}, s, \operatorname{grad} s)$. Following [Les92, AD13], take the external power as

$$P(t) = \int_{\partial V} (\boldsymbol{\Lambda\nu}) \cdot \boldsymbol{\omega} da + \int_V \rho \boldsymbol{K} \cdot \boldsymbol{\omega} dv,$$

where $\boldsymbol{\Lambda}$ is the couple stress tensor, $\boldsymbol{K}$ is the external body moment per unit mass, $\boldsymbol{\nu}$ is the unit normal vector on the boundary of the body, and $\boldsymbol{\omega}$ is the director angular velocity (we have ignored material motion for simplicity). Applying the divergence theorem,we have

$$\int_{\partial V} (\boldsymbol{\Lambda\nu}) \cdot \boldsymbol{\omega} da = \int_{\partial V} \Lambda_{ij}\omega_i\nu_j da = \int_V (\Lambda_{ij,j}\omega_i + \Lambda_{ij}\omega_{i,j}) dv.$$

Thus, the external power P can be written as

$$P(t) = \int_V [\operatorname{div}\boldsymbol{\Lambda} + \rho\boldsymbol{K}] \cdot \boldsymbol{\omega} dv + \int_V \boldsymbol{\Lambda} : \boldsymbol{M} dv,$$

where $\boldsymbol{M}$ is defined as director angular velocity gradient $\boldsymbol{M} = \operatorname{grad}\boldsymbol{\omega}$. Recall that the balance law of angular momentum reads as

$$\operatorname{div}\boldsymbol{\Lambda} + \rho\boldsymbol{K} = \boldsymbol{0},$$

leading to

$$P(t) = \int_V \boldsymbol{\Lambda} : \boldsymbol{M} dv.$$

In addition, the second law of thermodynamics requires the dissipation to be equal or

larger than zero, which is given as

$$\int_V [\boldsymbol{\Lambda} : \boldsymbol{M}] - \rho\dot{\psi}]dv \geq 0 \tag{5.6}$$
$$\Rightarrow \int_V \left[\Lambda_{ij}\omega_{i,j} - \rho\frac{\partial\psi}{\partial n_i}\dot{n}_i - \rho\frac{\partial\psi}{\partial(n_{i,j})}\dot{\overline{n_{i,j}}} - \rho\frac{\partial\psi}{\partial s}\dot{s} - \rho\frac{\partial\psi}{\partial(s_{,j})}\dot{\overline{s_{,j}}}\right] dv \geq 0.$$

As flow is ignored for the moment, the inequality takes the form

$$\int_V \left[\Lambda_{ij}\omega_{i,j} - \rho\frac{\partial\psi}{\partial n_i}\dot{n}_i - \rho\frac{\partial\psi}{\partial(n_{i,j})}\dot{n}_{i,j} - \rho\frac{\partial\psi}{\partial s}\dot{s} - \rho\frac{\partial\psi}{\partial(s_{,j})}\dot{s}_{,j}\right] dv \geq 0$$
$$\Rightarrow \int_V \left[\Lambda_{ij}\omega_{i,j} - \rho\frac{\partial\psi}{\partial n_i}(\omega\times n)_i - \rho\frac{\partial\psi}{\partial(n_{i,j})}(\omega\times n)_{i,j} - \rho\frac{\partial\psi}{\partial s}\dot{s} + \rho(\frac{\partial\psi}{\partial(s_{,j})})_{,j}\dot{s}\right] dv$$
$$- \int_{\partial V} \rho\frac{\partial\psi}{\partial(s_{,j})}\dot{s}\nu_j da \geq 0.$$

Defining the couple stress $\boldsymbol{\Lambda}$ as

$$\Lambda_{ij} := \rho e_{inm} n_n \frac{\partial\psi}{\partial n_{m,j}},$$

and applying the Ericksen identity [Eri61] as

$$\left(\frac{\partial\psi}{\partial\boldsymbol{n}}\otimes\boldsymbol{n} + \frac{\partial\psi}{\partial\operatorname{grad}\boldsymbol{n}}(\operatorname{grad}\boldsymbol{n})^{\intercal} + \left(\frac{\partial\psi}{\partial\operatorname{grad}\boldsymbol{n}}\right)^{\intercal}\operatorname{grad}\boldsymbol{n}\right)_{skew} = \boldsymbol{0},$$

we obtain

$$\Lambda_{ij}\omega_{i,j} - \rho\frac{\partial\psi}{\partial n_i}(\omega\times n)_i - \rho\frac{\partial\psi}{\partial(n_{i,j})}(\omega\times n)_{i,j} = 0.$$

Then the dissipation inequality becomes

$$\int_V \left[-\rho\frac{\partial\psi}{\partial s}\dot{s} + \rho\left(\frac{\partial\psi}{\partial(s_{,j})}\right)_{,j}\dot{s}\right] dv - \int_{\partial V}\rho\frac{\partial\psi}{\partial(s_{,j})}\dot{s}\nu_j da \geq 0.$$

To fulfill this inequality, recalling (5.5) that $\dot{s} = -\operatorname{grad} s \cdot \boldsymbol{V}$, one requires

$$\begin{aligned} -\left[\rho\frac{\partial\psi}{\partial s} - \rho\left(\frac{\partial\psi}{\partial(s_{,j})}\right)_{,j}\right] s_{,i}V_i &\geq 0 \quad \text{at interior points} \\ -\rho\frac{\partial\psi}{\partial(s_{,j})}\nu_j s_{,i}V_i &\geq 0 \quad \text{at points on boundary.} \end{aligned}$$

Therefore, the choice of $\boldsymbol{V}^B$ on the boundary pointing in the direction of

$$-\rho\left(\frac{\partial\psi}{\partial(\operatorname{grad} s)} \cdot \boldsymbol{\nu}\right) grads,$$

and $\boldsymbol{V}^I$ in the interior pointing in the direction of

$$-\left[\rho\frac{\partial\psi}{\partial s} - \rho\operatorname{div}\left(\frac{\partial\psi}{\partial(\operatorname{grad} s)}\right)\right]\operatorname{grad} s$$

satisfy the non-negative dissipative requirement. In particular, $\boldsymbol{V}^I$ in the interior may be further assumed as

$$\boldsymbol{V}^I = -\frac{\operatorname{grad} s}{B_m|\operatorname{grad} s|^m}\left[-\rho\operatorname{div}\left(\frac{\partial\psi}{\partial(\operatorname{grad} s)}\right) + \rho\frac{\partial\psi}{\partial s}\right].$$

where B_m is a material constant required on dimensional grounds related to 'drag', and m is a parameter representing different scenarios, which can be 0, 1 and 2. With $\dot{s} = -\operatorname{grad} s \cdot \boldsymbol{V}$, the evolution equation of s can be written as

$$\dot{s} = \frac{1}{B_m}|\operatorname{grad} s|^{2-m}\rho\left[-\frac{\partial\psi}{\partial s} + \operatorname{div}\left(\frac{\partial\psi}{\partial(\operatorname{grad} s)}\right)\right]. \tag{5.7}$$

$m = 0$ is the *simplest* natural choice representing a linear kinetic assumption. $m = 2$ corresponds to the evolution equation derived from the gradient flow method. To this is appended the balance laws of linear momentum and angular momentum, utilizing the constitutive equations for couple stress and stress, the latter arising from the thermodynamic

procedure above when flow is included [Ste04].

Another way to obtain the s evolution equation is the gradient flow method. The gradient flow dynamics (for a non-conserved quantity) assumes that all information on evolution is directly available (up to a material parameter) once the energy function is known. Consider the total energy

$$E = \int_V \rho\psi(\boldsymbol{n}, \operatorname{grad}\boldsymbol{n}, s, \operatorname{grad} s)dv.$$

The first variation of the energy E is

$$\delta E = \int_V \left(\frac{\partial\psi}{\partial \boldsymbol{n}} \cdot \delta\boldsymbol{n} + \frac{\partial\psi}{\partial \operatorname{grad}\boldsymbol{n}} : \delta(\operatorname{grad}\boldsymbol{n}) + \frac{\partial\psi}{\partial s}\delta s + \frac{\partial\psi}{\partial \operatorname{grad} s} \cdot \delta(\operatorname{grad} s) \right) dv.$$

Integrate by parts the term involving $\delta(\operatorname{grad} s)$ to obtain the s evolution equation based on an L^2 gradient flow as

$$\dot{s} = \gamma \left[\operatorname{div} \frac{\partial\psi}{\partial \operatorname{grad} s} - \frac{\partial\psi}{\partial s} \right], \tag{5.8}$$

where γ is a dimensional constant. The result from the energy gradient flow method is equivalent to the evolution equation given in (5.7) for $m = 2$.

5.3.3 Phase transition model formulation

In Ericksen's model [Eri91], the director field is represented by a unit length vector field $\boldsymbol{n}$. To practically implement the computation of a time-dependent nonlinear theory, we use an alternative vector field $\boldsymbol{d}$ to represent the director field subject to the constraint $|\boldsymbol{d}|^2 = s^2$.

Assuming the generalized Parodi relation, the governing equations are an extension of

the work in [Wal11a], and take the form

$$\begin{aligned}\rho\dot{v} + \operatorname{grad} p - \operatorname{div}\left(\frac{\partial R}{\partial \operatorname{grad} \boldsymbol{v}} - (\operatorname{grad} \boldsymbol{d})^T \frac{\partial W}{\partial \operatorname{grad} \boldsymbol{d}} - (\operatorname{grad} s) \otimes \frac{\partial W}{\partial \operatorname{grad} s}\right) &= \rho \boldsymbol{f} \\ \frac{\partial R}{\partial \dot{\boldsymbol{d}}} + \frac{\partial W}{\partial \boldsymbol{d}} - \operatorname{div}\left(\frac{\partial W}{\partial \operatorname{grad} \boldsymbol{d}}\right) + \lambda \boldsymbol{d} &= \rho \boldsymbol{m} \\ \frac{\partial R}{\partial \dot{s}} + \frac{\partial W}{\partial s} - \operatorname{div}\left(\frac{\partial W}{\partial \operatorname{grad} s}\right) - \lambda s &= \rho f_s\end{aligned} \tag{5.9}$$

where ρ is the material density, p and λ are Lagrange multipliers dual to the constraints

$$\operatorname{div}(v) = 0 \quad \text{and} \quad |\boldsymbol{d}|^2 - s^2 = 0,$$

W is a modified Oseen-Frank energy, and R is an appropriately designed dissipation function.

We introduce the modified Oseen-Frank energy as

$$\begin{aligned}W(\boldsymbol{d}, \operatorname{grad} \boldsymbol{d}, s, \operatorname{grad} s) = \frac{k_1}{2} \operatorname{div}(\boldsymbol{d})^2 + \frac{k_2}{2}(\boldsymbol{d} \cdot \operatorname{curl}(\boldsymbol{d}))^2 \\ + \frac{k_2 - k_4}{2}(|\operatorname{grad} \boldsymbol{d}|^2 - \operatorname{div}(\boldsymbol{d})^2 - |\operatorname{curl}(\boldsymbol{d})|^2) + \frac{k_3}{2}|\boldsymbol{d} \times \operatorname{curl}(\boldsymbol{d})|^2 \\ + \frac{L_1}{2}|\operatorname{grad} s|^2 + f(s) + g(\operatorname{grad} s, \boldsymbol{d}),\end{aligned} \tag{5.10}$$

where k_1, k_2, k_3 and k_4 correspond to the Frank constants, L_1 is the Leslie parameter and $f(s)$ is a non-convex function of s indicating the preferred phase state. The $(s, \boldsymbol{d})$ modified Oseen-Frank energy function has been further augmented by the function $g(\operatorname{grad} s, \boldsymbol{d})$ which is a non-convex function representing interfacial energy. A natural candidate for $g(\operatorname{grad} s, \boldsymbol{d})$ is given as

$$g(\operatorname{grad} s, \boldsymbol{d}) = |\operatorname{grad} s| \left[\sigma_0 \left(1 + w \frac{(\operatorname{grad} s \cdot \boldsymbol{d})^2}{|\operatorname{grad} s|^2 |\boldsymbol{d}|^2}\right)\right], \tag{5.11}$$

where σ_0 is an isotropic interfacial energy and w is the anchor coefficient [KSL13]. This is

an adaption of the Rapini-Papoular function [RP69]. The analog of the Parodi condition has Raleighian

$$R = (\gamma_0/2)(\boldsymbol{d}\cdot\boldsymbol{D}\boldsymbol{d})^2 + (\hat{\gamma}_2/2)|\boldsymbol{d}\otimes\boldsymbol{D}\boldsymbol{d}|^2$$
$$+(\gamma_1/2)|\mathring{\boldsymbol{d}}|^2 + \gamma_2\mathring{\boldsymbol{d}}\cdot\boldsymbol{D}\boldsymbol{d} + \beta_1\dot{s}\boldsymbol{d}\cdot\boldsymbol{D}\boldsymbol{d} + (\beta_2/2)\dot{s}^2.$$

where $\mathring{\boldsymbol{d}} := \boldsymbol{R}^*\frac{d}{dt}(\boldsymbol{R}^{*T}\boldsymbol{d}) = \dot{\boldsymbol{d}} - \boldsymbol{\Omega}\boldsymbol{d}$ is the convected derivate of $\boldsymbol{d}$ with respect to $\boldsymbol{R}^*$ (also called the Jaumann derivative), and $\boldsymbol{R}^*$ satisfies $\dot{\boldsymbol{R}}^*\boldsymbol{R}^{*T} = \boldsymbol{\Omega}$. $\boldsymbol{D}$ and $\boldsymbol{\Omega}$ are the symmetric and skew parts of the velocity gradient. The coefficients may depend upon $(s, \boldsymbol{d}, \operatorname{grad} s, \operatorname{grad}\boldsymbol{d})$ and temperature. Equivalence between (5.7) and the s evolution embedded in (5.9) is obtained by setting $\beta_1 = 0$ and $\beta_2 = B_m/|\operatorname{grad} s|^{2-m}$, in which R depends upon *grads*.

However, since the non-convexity of interfacial energy involves *grads*, it is possible that the evolution equation for s is numerically unstable in the cases where w is large. Recall the s evolution equation in (5.7) is

$$\dot{s} = \frac{1}{B_m}|\operatorname{grad} s|^{2-m}\rho\left[-\frac{\partial\psi}{\partial s} + \operatorname{div}\left(\frac{\partial\psi}{\partial(\operatorname{grad} s)}\right)\right],$$

where ψ is taken as $W(\boldsymbol{d}, \operatorname{grad}\boldsymbol{d}, s, \operatorname{grad} s)$. Then with the energy density given in (5.10), $\frac{\partial\psi}{\partial\operatorname{grad} s}$ is calculated as

$$\left(\frac{\partial\psi}{\partial\operatorname{grad} s}\right)_i = L_1(\operatorname{grad} s)_i + \frac{\sigma_0}{|\operatorname{grad} s|}(\operatorname{grad} s)_i + \frac{2\sigma_0 w}{|\operatorname{grad} s||\boldsymbol{d}|^2}(d_i d_j s_{,j}) - \frac{\sigma_0 w\cos^2\theta}{|\operatorname{grad} s|}(\operatorname{grad} s)_i$$
$$+\text{other terms},$$

with θ being the angle between the interface normal direction and the tactoid interface,

i.e. the angle between the directions grad s and $\boldsymbol{d}$. Thus, after substituting $\frac{\partial \psi}{\partial \operatorname{grad} s}$, we have

$$\dot{s} = C\left\{\operatorname{div}\left[\left(\left(L_1 + \frac{\sigma_0}{|\operatorname{grad} s|}\right)\boldsymbol{I} - w\left(\frac{\sigma_0 \cos^2\theta}{|\operatorname{grad} s|}\boldsymbol{I} - \frac{2\sigma_0}{|\operatorname{grad} s||\boldsymbol{d}|^2}\boldsymbol{d}\otimes\boldsymbol{d}\right)\right)\operatorname{grad} s\right]\right\}$$
$$+\text{other terms},$$

where $C = \frac{|\operatorname{grad} s|^{2-m}\rho}{B_m}$. Denote the diffusion tensor $\boldsymbol{A}$ as

$$\boldsymbol{A} = \left(L_1 + \frac{\sigma_0}{|\operatorname{grad} s|}\right)\boldsymbol{I} - w\left(\frac{\sigma_0 \cos^2\theta}{|\operatorname{grad} s|}\boldsymbol{I} - \frac{2\sigma_0}{|\operatorname{grad} s||\boldsymbol{d}|^2}\boldsymbol{d}\otimes\boldsymbol{d}\right).$$

Then the s evolution equation can be written as

$$\dot{s} = C\operatorname{div}(\boldsymbol{A}\operatorname{grad} s) + \text{other terms}. \tag{5.12}$$

Since $\boldsymbol{d}\cdot grads$ is about 0 near the tactoid interface where $grads$ is nonzero (note that(5.11) implies that $\boldsymbol{d}$ prefers to be perpendicular to $grads$ to minimize interfacial energy), the diffusion tensor$\boldsymbol{A}$ in $\operatorname{div}(\boldsymbol{A}\operatorname{grad} s)$ may be negative-definite depending on the relative magnitude of w, a potential cause for numerical instability.

In order to deal with this problem, we introduce a new field $\boldsymbol{p}$ representing the interfacial normal whose reciprocal magnitude roughly represents the width of the interface. The modified energy density with this new state descriptor is written as follows:

$$W(\boldsymbol{d}, \nabla\boldsymbol{d}, s, \nabla s, \boldsymbol{p}) = \frac{k_1}{2}\operatorname{div}(d)^2 + \frac{k_2}{2}(\boldsymbol{d}\cdot\operatorname{curl}(\boldsymbol{d}))^2$$
$$+\frac{k_2 - k_4}{2}(|\nabla\boldsymbol{d}|^2 - \operatorname{div}(\boldsymbol{d})^2 - |\operatorname{curl}(d)|^2) + \frac{k_3}{2}|\boldsymbol{d}\times\operatorname{curl}(\boldsymbol{d})|^2$$
$$+\frac{L_1}{2}|\nabla s - \boldsymbol{p}|^2 + f(s) + g(\boldsymbol{p}, \boldsymbol{d}),$$

where $f(s)$ is still the non-convex function of s in (5.10) and $g(\boldsymbol{p}, \boldsymbol{d})$ is a modified non-

convex function representing interfacial energy given as

$$g(\boldsymbol{p}, \boldsymbol{d}) = |\boldsymbol{p}| \left[\sigma_0 \left(1 + w \frac{(\boldsymbol{p} \cdot \boldsymbol{d})^2}{|\boldsymbol{p}|^2 |\boldsymbol{d}|^2} \right) \right]. \tag{5.13}$$

By placing the non-convexity of the interfacial energy to be a function of $\boldsymbol{p}$ and $\boldsymbol{d}$, and elastically penalizing the difference between $\boldsymbol{p}$ and $grads$, we get a stable system for the phase transition model. With the modified energy density with the new state descriptor, the dissipation in (5.6) (we ignore material motion for simplicity) can be written as

$$\begin{gathered} \int_V [\boldsymbol{\Lambda} : \boldsymbol{M}] - \rho \dot{\psi}] dv \geq 0 \\ \Rightarrow \int_V \left[\Lambda_{ij} \omega_{i,j} - \rho \tfrac{\partial W}{\partial d_i} \dot{d}_i - \rho \tfrac{\partial W}{\partial (d_{i,j})} \dot{\overline{d_{i,j}}} - \rho \tfrac{\partial W}{\partial s} \dot{s} - \rho \tfrac{\partial W}{\partial (s_{,j})} \dot{\overline{s_{,j}}} - \rho \tfrac{\partial W}{\partial p_i} \dot{p}_i \right] dv \geq 0. \end{gathered}$$

Following the same procedure as in Sec. 5.3.2, we can verify that the dissipation is non-negative when $\dot{\boldsymbol{p}}$ is in the direction of $-\frac{\partial W}{\partial \boldsymbol{p}}$. Thus, the dynamic evolution equation of the $\boldsymbol{p}$ field is given as

$$\dot{\boldsymbol{p}} = -Q \frac{\partial W}{\partial \boldsymbol{p}} = -Q \left[L_1 (\boldsymbol{p} - \operatorname{grad} s) + \frac{\partial g}{\partial \boldsymbol{p}} \right], \tag{5.14}$$

where Q is a material dependent constant. An example of the advantage of the modified $\boldsymbol{p}$ model is discussed in Section 5.3.4.

The variables $\boldsymbol{d}$, s, and the anchoring coefficient w are dimensionless. The variable $\boldsymbol{p}$ has dimension $[\boldsymbol{p}] = Length^{-1}$. The physical dimensions of the parameters in the modified Oseen-Frank energy are $[k_1] = Force$, $[k_2] = Force$, $[k_3] = Force$, $[k_4] = Force$, $[L_1] = Force$, and $[\sigma_0] = Force \times Length^{-1}$. The physical dimensions of the coefficients C in (5.12) and Q in (5.14) are $[C] = Length^2 \times Time^{-1} \times Force^{-1}$, and $[Q] = Time^{-1} \times Force^{-1}$.

To non-dimensionalize the above parameters, we introduce the following dimensionless

variables,

$$\tilde{\boldsymbol{p}} = R\boldsymbol{p}; \quad \tilde{k}_i = \frac{k_i}{k_1}; \quad \tilde{L}_1 = \frac{L_1}{k_1}; \quad \tilde{\sigma}_0 = R\frac{\sigma_0}{k_1}; \quad \tilde{l} = \frac{l}{R},$$

where l is the dimensional length, $\tilde{l}$ is the dimensionless length, and R is half of a typical tactoid size. In this work, we assume $k_1 = k_2 = k_3 = k$ (except in Sec. 5.4.1), $k_4 = 0$, and $L_1 = k$. Therefore, $\tilde{k}_1 = \tilde{k}_2 = \tilde{k}_3 = 1$, $\tilde{k}_4 = 0$, and $\tilde{L}_1 = 1$. The dimensionless $\tilde{\sigma}_0$ physically represents the ratio of the total surface energy and the total elastic energy, which would be $\frac{\sigma_0 R^2}{kR}$ for a three-dimensional nematic tactoid [Lav98]. In this work, we assume R to be 10 μm, based on the estimate of the long-axis length of a 'two-cusp tactoid' of 20 μm given in [KSL13]. The physical parameters of LCLCs are adopted from [KSL13] as follows: $k = 2 \times 10^{-12} N$, $\sigma_0 = 10^{-4} J/m^2$, which implies $\tilde{\sigma}_0 = 500$. Since we do not focus on the evolution rates of s and $\boldsymbol{p}$, we assume that the time scales in s and $\boldsymbol{p}$ evolutions are similar by setting $Q = \frac{C}{R^2}$.

5.3.4 Tactoid static equilibrium

We discuss the results of tactoid equilibrium calculations with different anchor coefficients w. Based on the Wulff construction of equilibrium shapes of perfect crystals with the interfacial energy given in (5.13), we can construct the equilibrium shapes of tactoids under the condition of constant surface area and a frozen director field [KSL13, BCF51, LL64, OP05, Whe06, KKJ$^+$03, Noz92]. In the static problem, we assume the non-convex function $f(s)$ in the energy density has identical values at $s = 0$ and $s = 1$ characterizing its minimum. Fig. 5.3 shows the initializations and the corresponding equilibrium results for various tactoids. The tactoid is initialized in the nematic $s = 1$ state and the matirx in the isotropic $s = 0$ phase. For fixed w, no large scale evolution is seen to occur in tactoid shapes, but director re-orientation occurs as the system seeks out a local minima.

The left column in Fig. 5.3 shows the initializations of the director field and tactoid

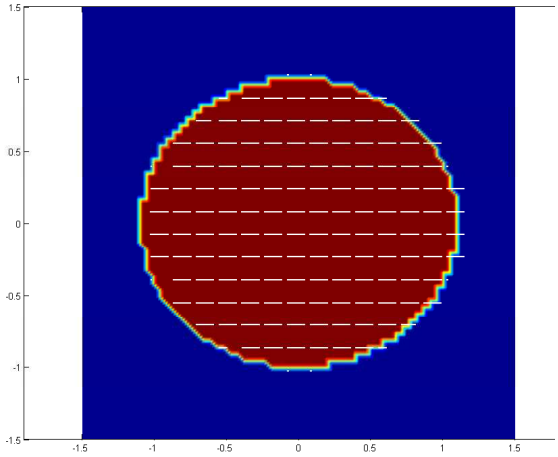

(a) The initialized tactoid shape and director field with $w = 0.1$.

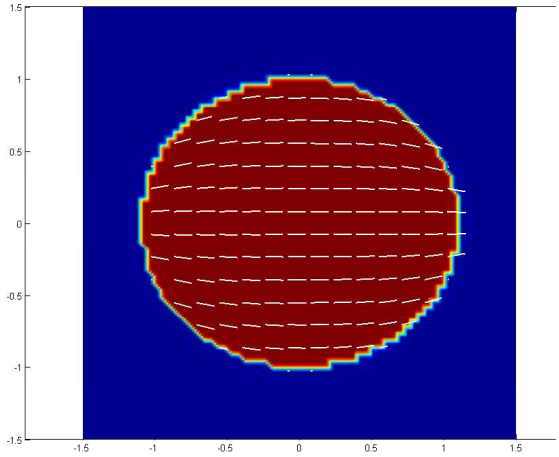

(b) The equilibrium of the tactoid shape and director field with $w = 0.1$.

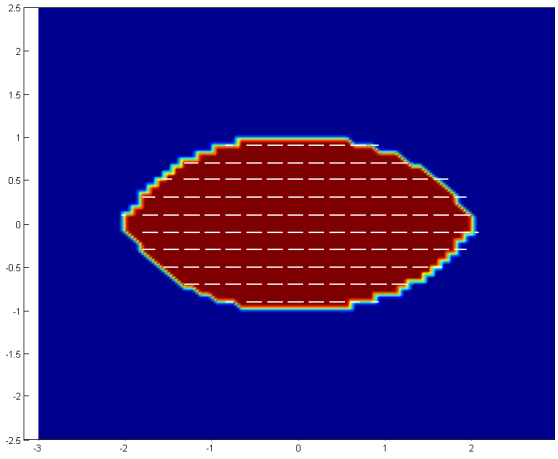

(c) The initialized tactoid shape and director field with $w = 1$.

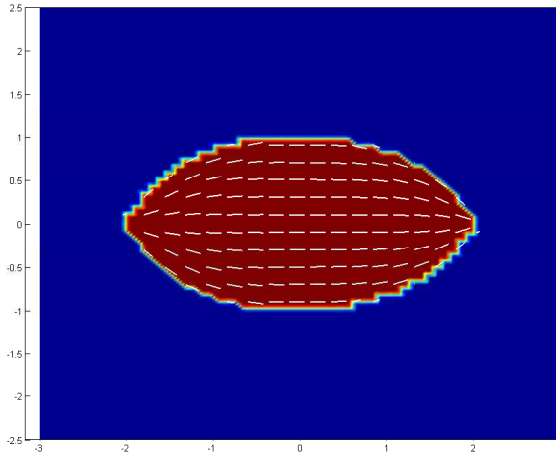

(d) The equilibrium of the tactoid shape director field with $w = 1$.

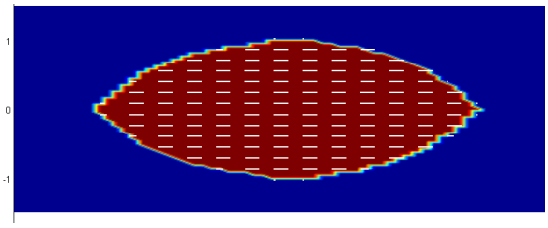

(e) The initialized tactoid shape and director field with $w = 2$.

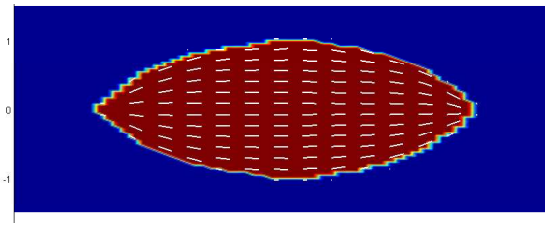

(f) The equilibrium of the tactoid shape and director field with $w = 2$.

Figure 5.3: *Initializations and equilibria of tactoid static problems with different anchor coefficients. The red color represents $s = 1$, the blue color represents $s = 0$ and the white dash lines represent the director field. The tactoid initializations are calculated from the Wulff construction.*

shapes for different anchor coefficients w. The initialized tactoid shapes are calculated from the Wulff construction and the director fields start from a uniform unit vector field where $s = 1$. The right column in Fig. 5.3 are the equilibrium configurations corresponding to the initializations. It shows that with increasing w, the single tactoid shape started from the Wulff construction transforms from sphere-like to ellipse-like shape. In all cases, given the interfacial energy in (5.13), the director field tends to be perpendicular to the interface normal *grads*.

Recall that we introduced a new field $\boldsymbol{p}$ and discussed the theoretical motivation behind it in Section 5.3.3. In Fig. 5.3(f), the anchor coefficient w is set to be large, $w = 2$. In this case, without introducing the $\boldsymbol{p}$ field, the computation is unstable and an equilibrium could not be found. With the introduced field $\boldsymbol{p}$, this case can be solved with result shown in Fig. 5.3(f). The results of various tactoid shapes show that cusps are recovered in our model, matching with experimental observations [KSL13].

The initialized tactoid shapes in Fig. 5.3 are based on the Wulff construction. The determined shape from the Wulff procedure depends on the value of w. In addition, the calculation shown in Fig. 5.4 explores the capability of the proposed model with a specified w and an arbitrary initialized shape. In Fig. 5.4, w is assumed to be 2.5 but the initialized tactoid shape is a sphere which clearly does not match with the Wulff construction. Fig. 5.4(a) is the initialization of the tactoid shape and the director field and Fig. 5.4(b) is the corresponding computed equilibrium state. It shows that the initialized spherical tactoid shape transforms to an elliptic shape due to the high value of w.

Fig. 5.5 shows another example with a non-Wulff constructed initialized shape in which $w = 1.5$ and the director field is prescribed with a singularity corresponding to a negative disclination of strength -1. Fig. 5.5(a) is the initialized spherical tactoid shape and the director field with the discontinuity at the center of the tactoid. Fig. 5.5(b) shows the final equilibrium state indicating that the tactoid transforms to a rounded square, and a negative disclination (with its core in the isotropic phase $s = 0$) exists at the center of the

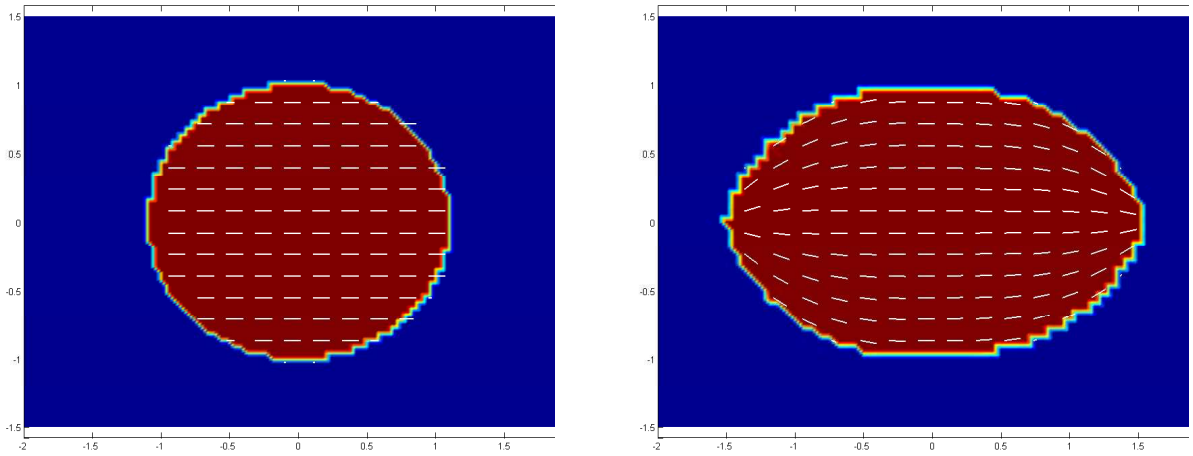

(a) The spherical initialized tactoid shape with $w = 2.5$.

(b) The equilibrium of the tactoid shape and director field with $w = 2.5$.

Figure 5.4: *The initialized tactoid shape is a sphere with* $w = 2.5$. *At the equilibrium, the spherical tactoid transforms to an ellipse-like tactoid and the director field evolves.*

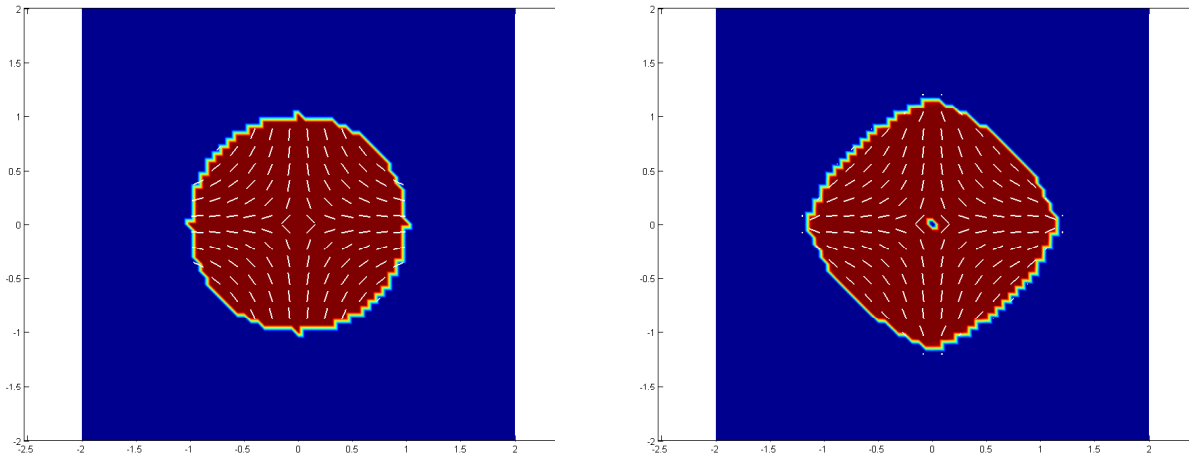

(a) The spherical initialized tactoid shape with $w = 1.5$ and the initialized director field corresponds to a negative disclination of strength -1.

(b) The tactoid shape and director field at equilibrium.

Figure 5.5: *A spherical tactoid transforms to a rounded-square tractoid with* $w = 1.5$ *and a negative disclination of strength* -1.

tactoid.

5.3.5 Dynamics of tactoids interaction

The interaction between two tactoids located close to each other is computed. Two spherical tactoids are initialized with different director orientations, as shown in Fig. 5.6(a). Since these two tactoids are located very close to each other, they are expected to interact with each other. As the calculation progresses, the tactoids begin to merge and the director field evolves to minimize the total energy, as shown in Fig. 5.6.

In this calculation, $m = 0$ and the barrier of the non-convex function $f(s)$ in the energy density between $s = 0$ and $s = 1$ is low. The shape of the non-convex function $f(s)$ is shown in Fig. 5.7. In the tactoid evolution, the effect of m is critical.

- For the static equilibrium problem of a single tactoid, with higher barrier of $f(s)$, a single tactoid will evolve to its equilibrium state with no problem.

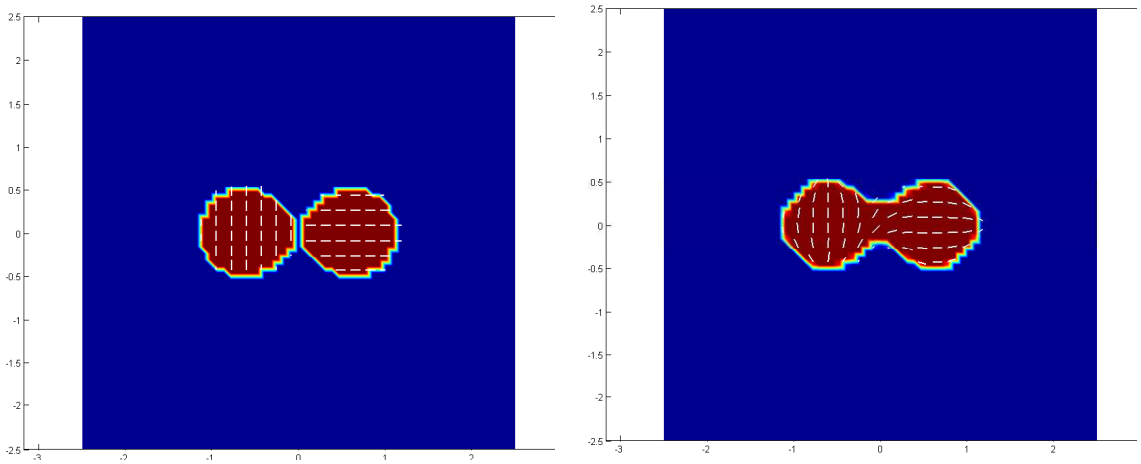

(a) The initialized tactoid shape and director field for two tactoids interaction.

(b) Two tactoids begin to merge and the director evolves.

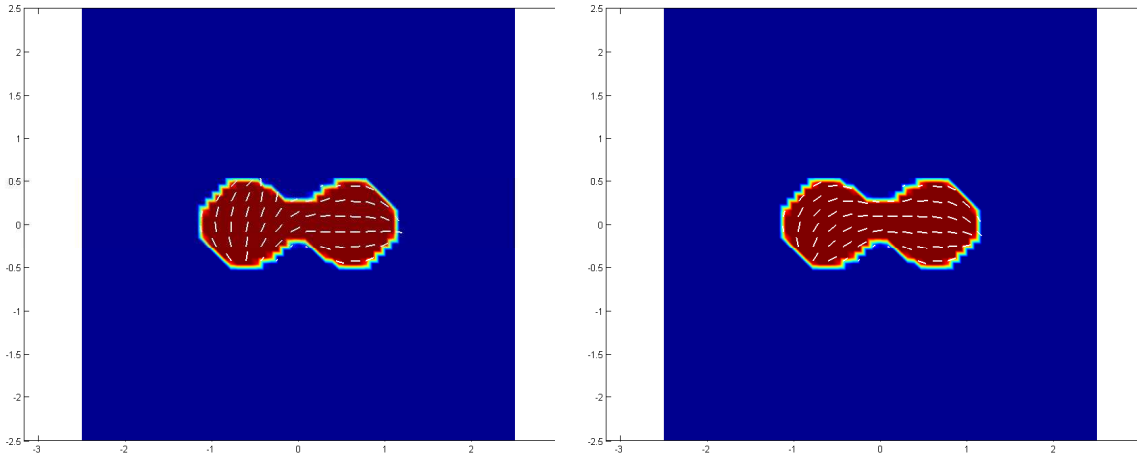

(c) The director keeps evolving.

(d) The equilibrium of two tactoid interaction.

Figure 5.6: *Interaction between two tactoids. These two tactoids tend to merge and the director field evolves.*

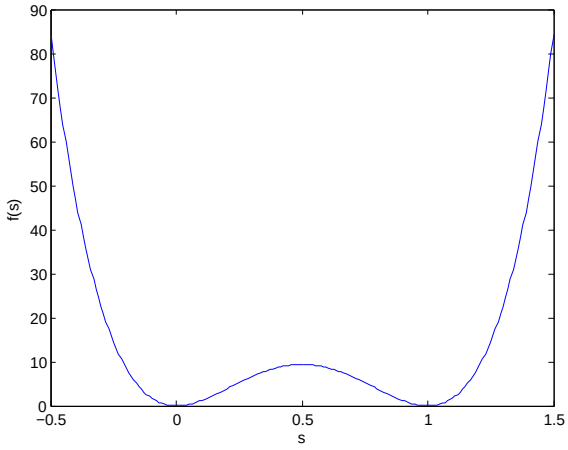

Figure 5.7: *The shape of $f(s)$ used in the two tactoid interaction calculation. The barrier between two wells at $s = 0$ and $s = 1$ is low.*

- For the static equilibrium problem, with a low barrier of $f(s)$, and $m = 2$, the single tactoid will diffuse into the isotropic matrix and the interface cannot maintain its shape. On the other hand, with a low barrier of $f(s)$, and $m = 0$, the single tactoid will evolve to its equilibrium state.
- For dynamic problems, such as the tactoid interaction discussed in this section, the tactoids are not able to merge with a high barrier in $f(s)$.
- With a low barrier of $f(s)$ as applied in this calculation and $m = 0$, the tactoids are able to move, expand, or merge.

To understand the reason for the effect of the energy barrier and m value, recall that the s evolution equation is given as

$$\dot{s} = \frac{1}{B_m} |\operatorname{grad} s|^{2-m} \rho[-\frac{\partial \psi}{\partial s} + div(\frac{\partial \psi}{\partial(\operatorname{grad} s)})].$$

In the case of high barrier of $f(s)$, regardless of m, s can barely evolve from their well values because of the high value of the 'resisting force' from $\frac{\partial \psi}{\partial s}$. In the case of low barrier

of $f(s)$, with $m = 2$, there is no impediment for s to evolve out of the isotropic well. In the case of low barier and with $m = 0$, although the barrier of $f(s)$ is low, s cannot evolve where *grads* is 0.

This is analogous to a problem in Chapter 4, where the dissipative dynamic behavior of disclinations in nematic liquid crystals is studied. By observing the effect of m on low barrier cases, we show that the dynamic model based on *kinematics* and thermodynamics is important for modeling dissipative dynamics.

5.3.6 Phase transition

We now discuss a problem of evolving phase transition across the whole domain. Three tactoids with different director orientations are initialized as shown in Fig. 5.8(a). The non-convex part $f(s)$ in the energy density is assumed to prefer the nematic phase, indicating the well at $s = 1$ is lower than the well at $s = 0$. The preference of the nematic phase of $f(s)$ indicates that the liquid crystal should transit from the isotropic to the nematic phase. Fig. 5.8(b) to 5.8(d) show snapshots at different times during the phase transition. As time increases, the tactoids expand and merge. In Fig. 5.8(d), a strength -1 disclination is formed inside the bulk which matches with experimental observations [KSL13].

5.4 Effect of material parameters on tactoid equilibria

Since the energy proposed in this model is non-convex and the equilibrium of the tactoid and the director field depend on the interfacial energy and the Frank constants, it is of interest to explore tactoid equilibria as a function of material parameters.

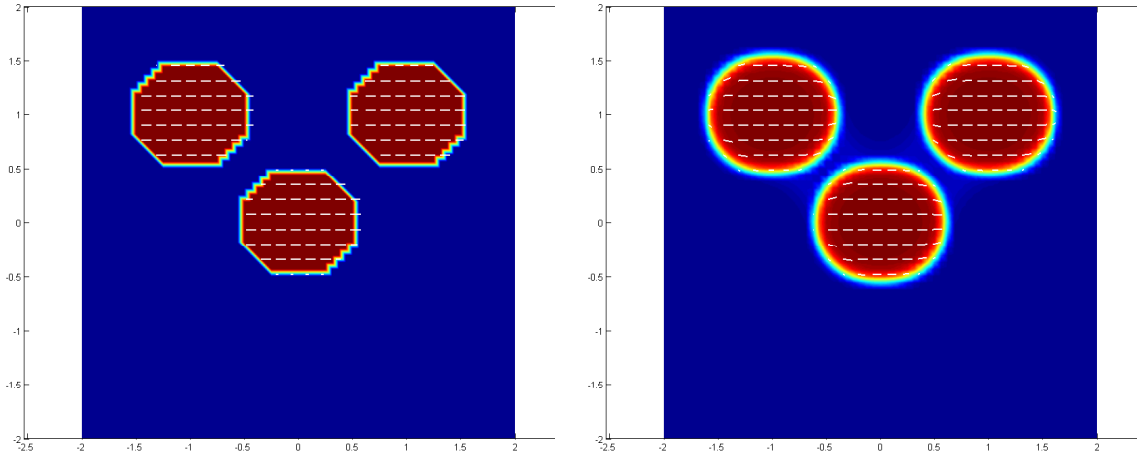

(a) The initialized tactoid shape and director field. Three spherical tactoids with same director fields are initialized.

(b) The tactoid shapes and director field at $t = 0.1$. Three tactoids expand.

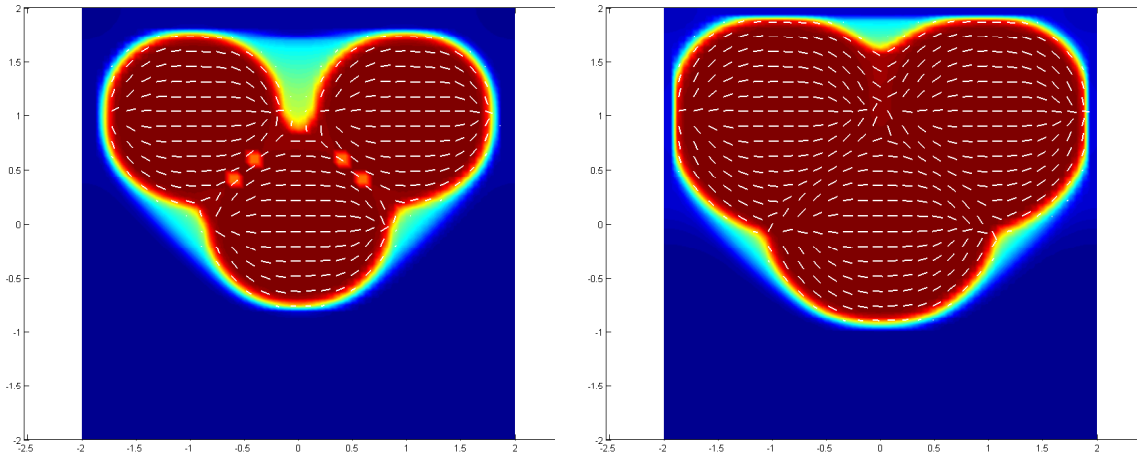

(c) The tactoid shapes and director field at $t = 0.2$. The tactoids begin to merge.

(d) The tactoid shapes and director field at $t = 0.5$. a strength -1 disclination is formed inside the bulk.

Figure 5.8: *Snapshots of isotropic-nematic phase transition at different times. As the calculation progresses, the tactoids expand, merge and a strength -1 disclination is formed inside the bulk.*

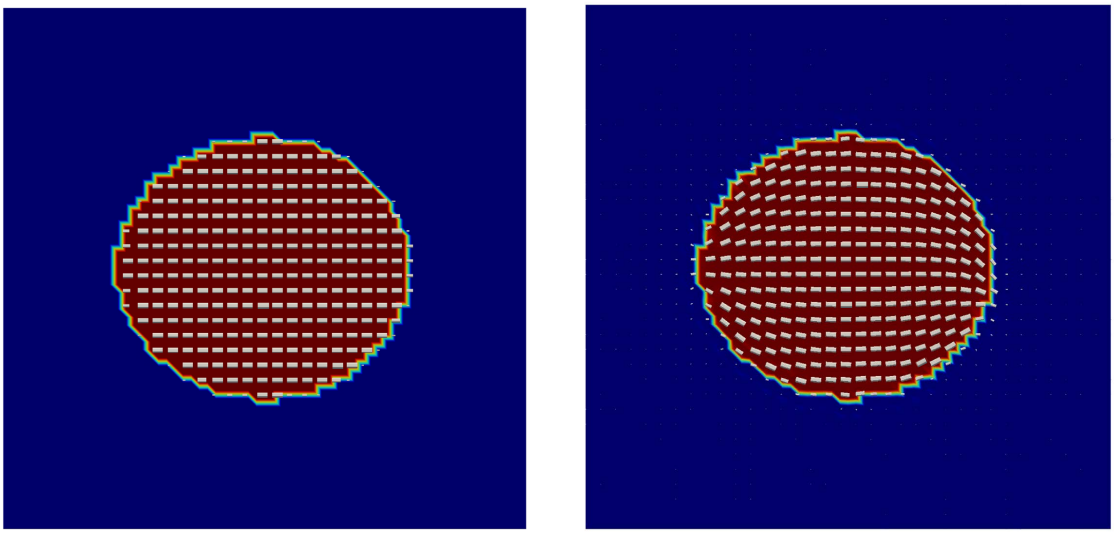

(a) The initialized tactoid shape and director field.

(b) The tactoid shape and director field at the equilibrium.

Figure 5.9: *The initialization and equilibrium configuration of the tactoid and director field in the case where $k_{11} > k_{33}$. Since splay is more expensive than bend, the director field tends to be perpendicular to the interface normal.*

5.4.1 Frank constants k_{11} and k_{33}

We consider two cases, $k_{11} > k_{33}$ (splay more expensive than bend) or $k_{11} < k_{33}$ (bend more expensive than splay). In one case, we assume k_{11} is five time larger than k_{33}; in the other, we assume k_{33} is five times larger than k_{11}. The tactoid shape is initialized as a sphere in both cases.

Figs. 5.9 and 5.10 show the initial configuration and the equilibrium state for both cases. In Fig. 5.9, k_{11} is larger than k_{33} and the director in the equilibrium tends to be perpendicular to the tactoid interface normal direction and bend is preferred over splay. On the other hand, in Fig. 5.10, the director tends to be parallel to the interface normal direction with splay preferred over bend. The difference between these two results indicates that the relationship between k_{11} and k_{33} is crucial to the interaction between the director and the tactoid interface, which is also discussed in the experiments reported in [ZCL14].

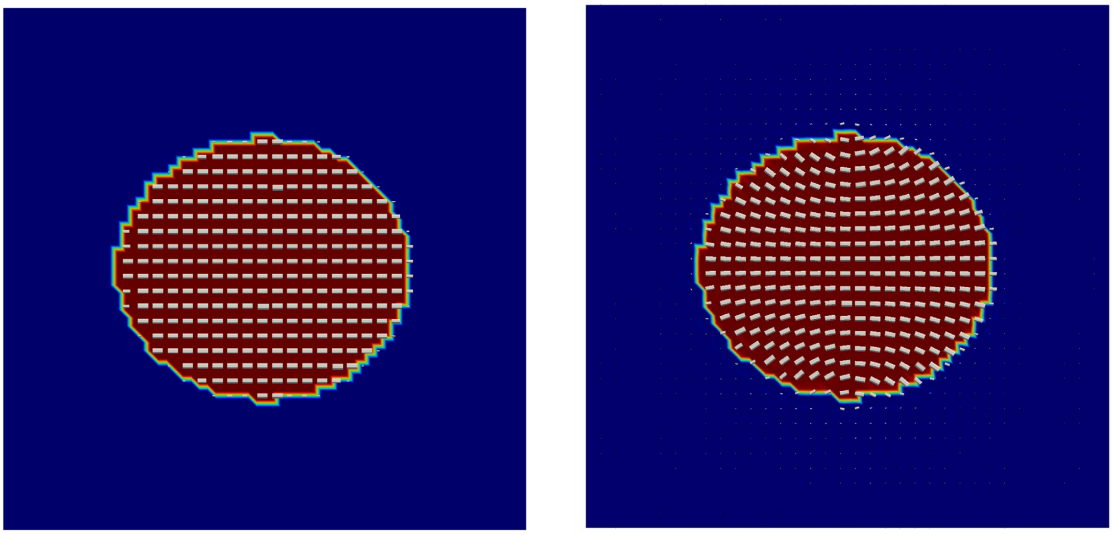

(a) The initialized tactoid shape and director field.

(b) The tactoid shape and director field at the equilibrium.

Figure 5.10: *The initialization and equilibrium configuration of the tactoid and director field in the case where $k_{11} < k_{33}$. Since bend is more expensive than splay, the director field tends to be parallel to the interface normal.*

5.4.2 Effect of interfacial energy barrier on tactoid shape

Recall that in (5.13), the interfacial energy is given in terms of the cosine of the angle θ between $\boldsymbol{p}$ representing the normal of the interface and the director field $\boldsymbol{d}$, which has a minimum at $\theta = \frac{\pi}{2}$. However, this approximation of the interfacial energy is only valid when the angle θ is close to $\frac{\pi}{2}$. We now assume an interfacial energy characterized by a fourth-order polynomial with two local minima and a local maximum as shown in Fig. 5.11. Such a form of the surface anchoring potential was first introduced by Sluckin and Poniewierski [SP86] and applied for the description of interfacial effects in LCLCs by Nazarenko et al [NBP$^+$10]. $\theta_0 = 0$ is where one local minimum occurs, θ_1 is the location of the local maximum, and $\theta_2 = \frac{\pi}{2}$ is the location of the other local minimum. σ_0, σ_1 and σ_2 are the interfacial energy values at θ_0, θ_1 and θ_2, respectively.

It is clear that the energy barrier between the two wells θ_0 and θ_2, as well as the values of σ_0 and σ_1, will influence the equilibrium state of the director field and the tactoid shape.

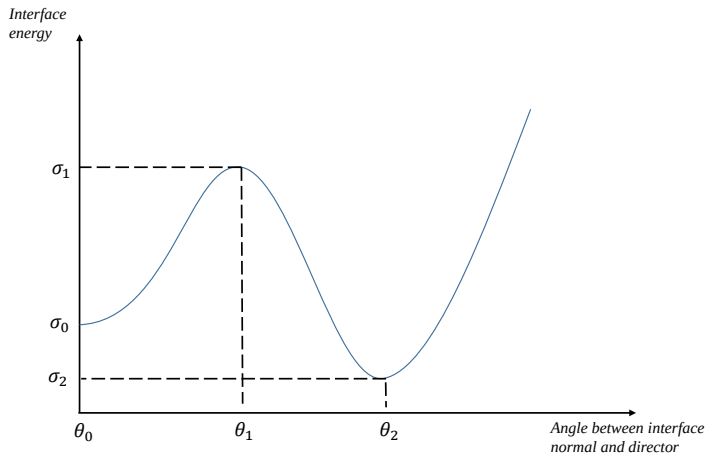

Figure 5.11: *The shape of the interfacial energy with two local minimal and a local maximal.*

Here we explore the relationship between the energy values of local maximum, as well as local minima, and the equilibrium of the director field. We assume $\theta_1 = \frac{\pi}{4}$ and change σ_0, σ_1 and σ_2.

Fig. 5.12 and Fig. 5.13 show the initializations and equilibria of tactoid shapes and their director fields given different interfacial energy parameters. In the first row of Fig. 5.12, σ_0, σ_1 and σ_2 are set to be 0 so the interfacial energy will be zero at any angle between the director and the interface normal. Thus, the director field in the equilibrium is the same as the initialization. The second row shows the initialized configuration and static equilibrium corresponding to a higher σ_1 values. Since the energy barrier between θ_0 and θ_2 is high, the director field tends to move to its local minimum, namely some points being parallel to the interface normal and some points being perpendicular to the interface normal. The last two rows in Fig. 5.12 show different equilibria with the increasing energy barrier σ_1 in the case where $\sigma_0 < \sigma_2$. With low barrier $\sigma_1 = 1$, the director field can evolve to the lower well at θ_0, thus the director field in the equilibrium is parallel to the interface normal. With high barrier $\sigma_1 = 5$, the director field cannot pass the local maximum between θ_0 and θ_2 and evolve to its local minimum in the equilibrium. In addition, Fig. 5.12 shows the total energy for each case, which are normalized by the total energy of the

case where $\sigma_0 = \sigma_1 = \sigma_2 = 0$.

Similarly, Fig. 5.13 shows the results with increasing energy barrier σ_1 in the case where $\sigma_0 > \sigma_2$. With low barrier $\sigma_1 = 1$, the director field can evolve to the lower well at θ_2, and the director field in the equilibrium are perpendicular to the interface normal. With high barrier $\sigma_1 = 5$, the director field can only evolve to its local minimum in the equilibrium. Fig. 5.13 also shows the total energy for each case, and the values of the total energy are normalized by the one of the case where $\sigma_0 = \sigma_1 = \sigma_2 = 0$.

5.5 Conclusion

A model based in continuum kinematics and thermodynamics is derived for LCLC isotropic-nematic phase transition dynamics. By adopting the order parameter s in [Eri91] to represent different phase states, an evolution equation of s is proposed and discussed. The main difference between our model and Ericksen's model in [Eri91] is that the model in this work starts from a kinematic 'tautology' with transparent physical/geometric motivation. The evolution of the director field described by the formulation in [Wal11a]. A new field $\boldsymbol{p}$ is introduced in the energy density to resolve the instabilities in the s evolution resulting from the non-convex interfacial energy when phrased only in terms of $grads$ and $\boldsymbol{d}$.

Both static equilibrium and dynamic tactoid behaviors are studied, including tactoid static microstructures from different initialized shapes, tactoid interactions, and isotropic-nematic phase transitions. The significance of the introduced evolution equation for s is discussed in the context of describing tactoid dynamic behaviors. A parametric study is performed to explore the effect of nematic elastic constants (splay and bend) and the interfacial energy parameters on the interaction between the tactoid interface normal and the director field.

σ_0	σ_1	σ_2	*Initialized Configuration*	*Energy*	*Equilibrium Configuration*	*Energy*
0	0	0	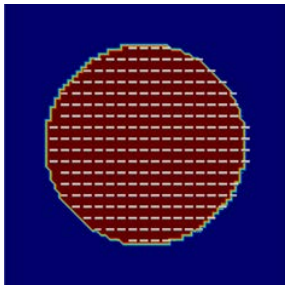	1	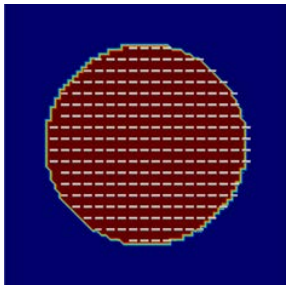	0.86
0	2	0	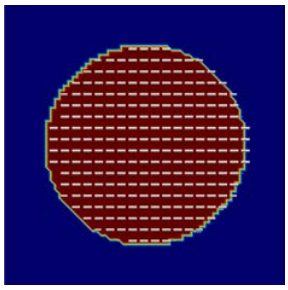	1.63	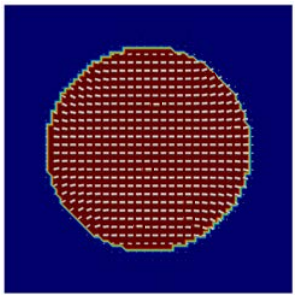	1.27
0	1	0.5	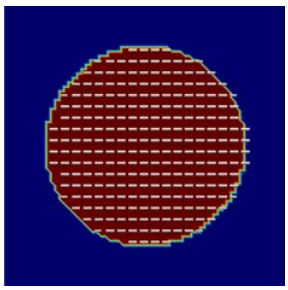	1.59	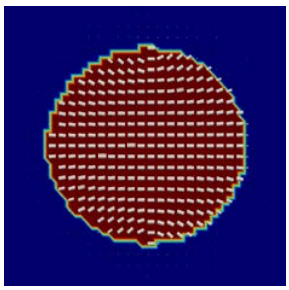	1.08
0	5	0.5	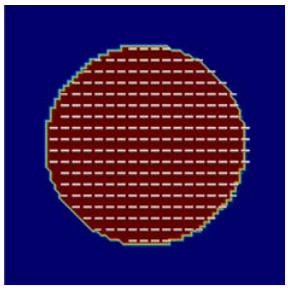	2.86	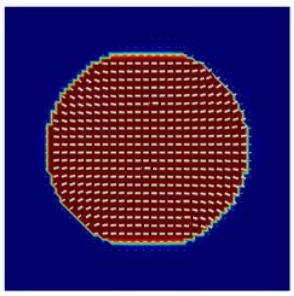	1.93

Figure 5.12: *The initializations and static equilibriums of the tactoid shape and director field given different interfacial energy parameters in the cases where $\sigma_0 = \sigma_2$ and $\sigma_0 < \sigma_2$. The total energy for each case are normalized by the energy value for the initialization of the case where $\sigma_0 = \sigma_1 = \sigma_2 = 0$.*

σ_0	σ_1	σ_2	*Initialized Configuration*	*Energy*	*Equilibrium Configuration*	*Energy*
0.5	1	0	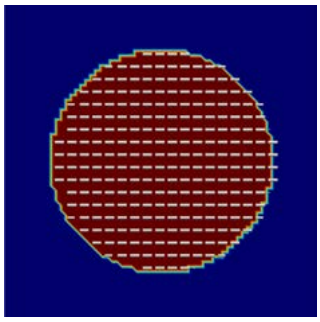	14.31	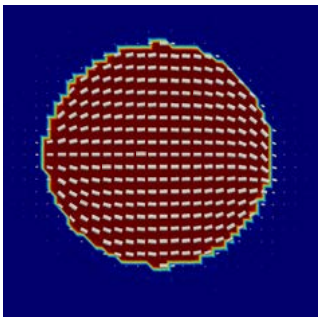	9.17
0.5	2	0	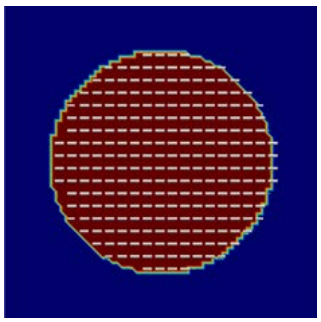	14.64	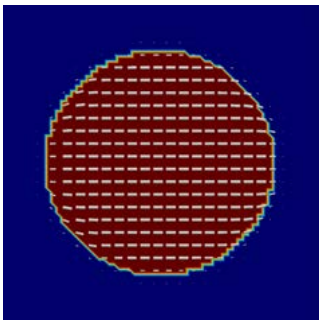	13.87
0.5	5	0	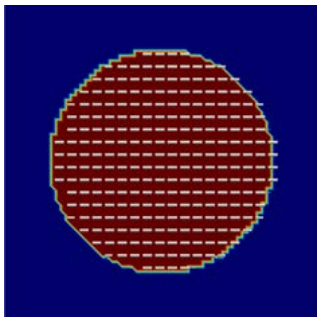	15.52	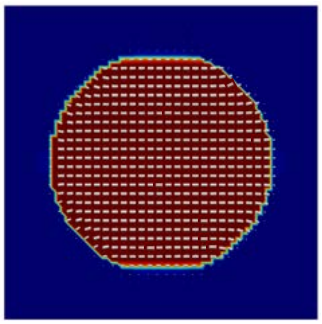	12.85

Figure 5.13: *The initializations and static equilibriums of the tactoid shape and director field given different interfacial energy parameters in the case where $\sigma_0 > \sigma_2$. The total energy for each case are normalized by the energy value for the initialization of the case where $\sigma_0 = \sigma_1 = \sigma_2 = 0$.*

Chapter 6

Discussion

In Chapters 2 and 3, theoretical implications and applications of g.disclinations in solids are studied in the context of thermodynamics and kinematics. The eigenwall field $\boldsymbol{S}$ is utilized, conceptually representing the point-wise out-of-plane distortion 'gradient' across a, generally curved, phase or grain boundary. The eigenwall field in detail is actually not necessarily a global gradient of any second order-tensor field. In addition, a 3-tensor g.disclination density field $\boldsymbol{\Pi} := \operatorname{curl} \boldsymbol{S}$ is introduced to represent the in-plane gradient of the eigenwall field. In Chapter 4, we introduce a layer field $\boldsymbol{\lambda}$ to deal with the director field discontinuity in the case of disclinations in nematic liquid crystals. The connection between the two models of g.disclinations and disclinations in NLC is that we interpret the interface, across which either the distortion or the director field has a discontinuity, as a layer. $\boldsymbol{S}$ or $\boldsymbol{\lambda}$ has support inside the layer, which converts the discontinuity to at least integrable fields - that are not global gradients. By solving various static as well as dynamic problems of g.disclinations and disclinations in NLC, we have shown that the introduced layer concept eliminates the singularity issue in the classical theories and render a finite total energy for a finite body with line defects. Even more importantly, they provide well-behaved, non-singular driving forces based on stresses and couple-stresses for dynamical interactions of defects with themselves and applied loads.

In Chapters 4 and 5, we discuss the shortcomings of the gradient flow method for continuous-in-time dynamics of non-convex energies in vectorial (or tensorial) variables for line defects and scalar variables for phase transitions. The reasons for the corresponding shortcomings are explained and a conceptually different route for posing problems of defect dynamics is introduced, capitalizing on the conservation of topological charge of the introduced defect fields. We show the sufficiency of simple thermodynamic arguments in conjunction with such kinematics for solving difficult problems, often long-standing, of disclination dynamics and isotropic-nematic phase transitions. Our conceptual findings and computational results have general import for slow dynamics of systems involving non-convex energies. Future work can involve exploration of both the mathematical and

numerical aspects of such observations in general dynamic problems.

In summary, the work presented in this dissertation proposes a method to understand line defects in both solids and liquid crystals. From the material science perspective, the models and examples demonstrated in this dissertation may help explore material properties better and synthesize new materials faster. Some potential future work could be building numerical scheme for g.disclination dynamics, implementing calculations involving g.disclinations, dislocations, and phase boundaries, and exploring the detailed formation and motion of line defects during phase transition.

Appendices

Appendix A

Analytical solution for $\boldsymbol{S}^*$ in the generalized disclination model

We recall the governing equations of $\boldsymbol{S}^*$ in g.disclination theory given as

$$\operatorname{curl} \boldsymbol{S}^* = \boldsymbol{\Pi}$$

$$\operatorname{div} \boldsymbol{S}^* = \boldsymbol{0}.$$

To solve $\boldsymbol{S}^*$ from these two equations, the Riemann-Graves integral operator [Ede85, EL88, Ach01] is applied. Suppose $\boldsymbol{\Pi}$ satisfies $\Pi_{ijk,k} = 0$, and define

$$\hat{\Pi}_{injk} = e_{jkm}\Pi_{inm}.$$

In the 2-D case, the only non-zero components of $\boldsymbol{\Pi}$ are Π_{ij3} with $i, j = 1, 2$. Thus $\hat{\boldsymbol{\Pi}}$ has no non-zero component with index 3. Then the relation between $\boldsymbol{\Pi}$ and $\hat{\boldsymbol{\Pi}}$ is

$$\hat{\Pi}_{1112} = \Pi_{113} \qquad \hat{\Pi}_{2212} = \Pi_{223} \qquad \hat{\Pi}_{1212} = \Pi_{123} \qquad \hat{\Pi}_{2112} = \Pi_{213}$$

$$\hat{\Pi}_{1121} = -\Pi_{113} \qquad \hat{\Pi}_{2221} = -\Pi_{223} \qquad \hat{\Pi}_{1221} = -\Pi_{123} \qquad \hat{\Pi}_{2121} = -\Pi_{213}$$

The integral is now introduced as

$$H_{ink} = (x_j - x_j^0) \int_0^1 \hat{\Pi}_{injk}(x^0 + \lambda(x - x^0))\lambda d\lambda,$$

where $\boldsymbol{x}^0$ is any fixed point in the body (and we assume a star-shaped domain).

Suppose Π_{ij3} takes the form

$$\Pi_{ij3} = \psi_{ij}(\sqrt{x_1^2 + x_2^2}),$$

and also assume $\boldsymbol{x}^0$ be the origin of the coordinates. Then for a positive disclination, the $\boldsymbol{H}$ at $\boldsymbol{x}$ is given as

$$H_{ij1} = \begin{cases} \frac{\Delta F_{ij}}{2\pi}(-\frac{x_2}{r^2}) & r > r_0 \\ \frac{-x_2}{r^2}\int_0^r \psi_{ij}(s)sds & r \leq r_0 \end{cases}$$

$$H_{ij2} = \begin{cases} \frac{\Delta F_{ij}}{2\pi}(\frac{x_1}{r^2}) & r > r_0 \\ \frac{x_1}{r^1}\int_0^r \psi_{ij}(s)sds & r \leq r_0 \end{cases}$$

Then it can be shown that $\boldsymbol{H}$ is the solution of $\boldsymbol{S}^*$ which satisfies $\operatorname{curl} \boldsymbol{S}^* = \boldsymbol{\Pi}$ and $\operatorname{div} \boldsymbol{S}^* = \boldsymbol{0}$.

In this work, we assume ψ takes the form

$$\psi_{ij}(r) = \begin{cases} \frac{\Delta F_{ij}}{\pi r_0}(\frac{1}{r} - \frac{1}{r_0}) & r < r_0 \\ 0 \quad r \geq r_0. \end{cases}$$

Thus,

$$H_{ij1} = \begin{cases} \frac{\Delta F_{ij}}{2\pi}\left(-\frac{x_2}{r^2}\right) & r > r_0 \\ \frac{-x_2 \Delta F_{ij}}{\pi r^2 r_0}\left(r - \frac{r^2}{2r_0}\right) & r \leq r_0 \end{cases}$$

$$H_{ij2} = \begin{cases} \frac{\Delta F_{ij}}{2\pi}\left(\frac{x_1}{r^2}\right) & r > r_0 \\ \frac{x_1 \Delta F_{ij}}{\pi r^2 r_0}\left(r - \frac{r^2}{2r_0}\right) & r \leq r_0. \end{cases}$$

Appendix B

Calculation of $\boldsymbol{A}^*$ for $\tilde{\boldsymbol{Y}}$

The governing equations for $\boldsymbol{A}^*$ are given as

$$\operatorname{curl} \boldsymbol{A}^* = \boldsymbol{S}^* : \boldsymbol{X}$$

$$\operatorname{div} \boldsymbol{A}^* = \boldsymbol{0}$$

Since in the 2-D case the last index of all non-zero components of $\boldsymbol{\Pi}$ is 3 and the first two are 1 or 2, $(div\,(\boldsymbol{S}^* : \boldsymbol{X}))_{ipp} = -\Pi_{ipp} = 0$, indicating solutions to $\boldsymbol{A}^*$ exist and we again utilize the Riemann-Graves integral.

Denote $\boldsymbol{B} = \boldsymbol{S}^* : \boldsymbol{X}$, then $B_{13} = S^*_{112} - S^*_{121}$ and $B_{23} = S^*_{212} - S^*_{221}$. After substituting the $\boldsymbol{S}^*$ from Appendix A,

$$B_{13} = \begin{cases} \frac{1}{2\pi r^2}(\Delta F_{12} x_2 + \Delta F_{11} x_1) & r \geq r_0 \\ \frac{1}{r^2}(x_2 \int_0^r \psi_{12} s ds + x_1 \int_0^r \psi_{11} s ds) & r < r_0 \end{cases}$$

$$B_{23} = \begin{cases} \frac{1}{2\pi r^2}(\Delta F_{22} x_2 + \Delta F_{21} x_1) & r \geq r_0 \\ \frac{1}{r^2}(x_2 \int_0^r \psi_{22} s ds + x_1 \int_0^r \psi_{21} s ds) & r < r_0 \end{cases}$$

In addition, we can assume ψ_{ij} also takes the form (as in Appendix A)

$$\psi_{ij}(r) = \begin{cases} \frac{\Delta F_{ij}}{\pi r_0}(\frac{1}{r} - \frac{1}{r_0}) & r < r_0 \\ 0 & r \geq r_0. \end{cases}$$

Thus,

$$B_{13} = \begin{cases} \frac{1}{2\pi r^2}(\Delta F_{12}x_2 + \Delta F_{11}x_1) & r \geq r_0 \\ \frac{1}{\pi r^2 r_0}(r - \frac{r^2}{2r_0})(\Delta F_{12}x_2 + \Delta F_{11}x_1) & r < r_0 \end{cases}$$

$$B_{23} = \begin{cases} \frac{1}{2\pi r^2}(\Delta F_{22}x_2 + \Delta F_{21}x_1) & r \geq r_0 \\ \frac{1}{\pi r^2 r_0}(r - \frac{r^2}{2r_0})(\Delta F_{22}x_2 + \Delta F_{21}x_1) & r < r_0 \end{cases}$$

The Riemann-Grave integral operator for the equation curl $\boldsymbol{A}^* = \boldsymbol{B}$ is

$$A^*_{ij} = (x_m - x^0_m)\int_0^1 \hat{B}_{imj}(x^0 + \lambda(x - x^0))\lambda d\lambda,$$

where $\hat{B}_{imj} = e_{mjr}B_{ir}$. Assuming $\boldsymbol{x}^0$ to be the origin, $\boldsymbol{A}^*$ can be written as

$$A^*_{11} = -x_2 \textstyle\int_0^1 B_{13}(\lambda \boldsymbol{x})\lambda d\lambda$$
$$A^*_{12} = x_1 \textstyle\int_0^1 B_{13}(\lambda \boldsymbol{x})\lambda d\lambda$$
$$A^*_{21} = -x_2 \textstyle\int_0^1 B_{23}(\lambda \boldsymbol{x})\lambda d\lambda$$
$$A^*_{22} = x_1 \textstyle\int_0^1 B_{23}(\lambda \boldsymbol{x})\lambda d\lambda.$$

Also, with the choice of $\boldsymbol{x}^0$ as the origin, and if $r < r_0$, then $\lambda r < r_0$, and we have

$$\textstyle\int_0^1 B_{13}(\lambda \boldsymbol{x})\lambda d\lambda = (1 - \frac{r}{3r_0})(\frac{\Delta F_{12}\sin\theta}{2\pi r_0} + \frac{\Delta F_{11}\cos\theta}{2\pi r_0})$$
$$\textstyle\int_0^1 B_{23}(\lambda \boldsymbol{x})\lambda d\lambda = (1 - \frac{r}{3r_0})(\frac{\Delta F_{22}\sin\theta}{2\pi r_0} + \frac{\Delta F_{21}\cos\theta}{2\pi r_0})$$

If $r \geq r_0$, then

$$\int_0^1 B_{13}(\lambda \boldsymbol{x})\lambda d\lambda = \int_0^{r_0/r} B_{13}(\lambda \boldsymbol{x})\lambda d\lambda + \int_{r_0/r}^1 B_{13}(\lambda \boldsymbol{x})\lambda d\lambda$$
$$\int_0^1 B_{23}(\lambda \boldsymbol{x})\lambda d\lambda = \int_0^{r_0/r} B_{23}(\lambda \boldsymbol{x})\lambda d\lambda + \int_{r_0/r}^1 B_{23}(\lambda \boldsymbol{x})\lambda d\lambda.$$

Since,

$$\int_{r_0/r}^r B_{13}(\lambda \boldsymbol{x})\lambda d\lambda = \tfrac{r-r_0}{2\pi r^2}(\Delta F_{12}\sin\theta + \Delta F_{11}\cos\theta)$$
$$\int_{r_0/r}^r B_{23}(\lambda \boldsymbol{x})\lambda d\lambda = \tfrac{r-r_0}{2\pi r^2}(\Delta F_{22}\sin\theta + \Delta F_{21}\cos\theta),$$

therefore

$$\int_0^1 B_{13}(\lambda \boldsymbol{x})\lambda d\lambda = (\tfrac{1}{3\pi r_0} + \tfrac{r-r_0}{2\pi r^2})(\Delta F_{12}\sin\theta + \Delta F_{11}\cos\theta)$$
$$\int_0^1 B_{23}(\lambda \boldsymbol{x})\lambda d\lambda = (\tfrac{1}{3\pi r_0} + \tfrac{r-r_0}{2\pi r^2})(\Delta F_{22}\sin\theta + \Delta F_{21}\cos\theta).$$

Converting from polar coordinates to Cartesian coordinates,

$$\int_0^1 B_{13}(\lambda \boldsymbol{x})\lambda d\lambda = (\tfrac{1}{3\pi r_0 r} + \tfrac{r-r_0}{2\pi r^3})(\Delta F_{12}x_2 + \Delta F_{11}x_1)$$
$$\int_0^1 B_{23}(\lambda \boldsymbol{x})\lambda d\lambda = (\tfrac{1}{3\pi r_0 r} + \tfrac{r-r_0}{2\pi r^3})(\Delta F_{22}x_2 + \Delta F_{21}x_1),$$

and the solution for $\boldsymbol{A}^*$ is

$$A_{11}^* = \begin{cases} (\frac{1}{2\pi r_0 r} - \frac{1}{6\pi r_0^2})(-\Delta F_{12} x_2^2 - \Delta F_{11} x_1 x_2) & r < r_0 \\ (\frac{1}{3\pi r_0 r} + \frac{r - r_0}{2\pi r^3})(-\Delta F_{12} x_2^2 - \Delta F_{11} x_1 x_2) & r \geq r_0 \end{cases}$$

$$A_{12}^* = \begin{cases} (\frac{1}{2\pi r_0 r} - \frac{1}{6\pi r_0^2})(\Delta F_{12} x_2 x_1 + \Delta F_{11} x_1^2) & r < r_0 \\ (\frac{1}{3\pi r_0 r} + \frac{r - r_0}{2\pi r^3})(\Delta F_{12} x_2 x_1 + \Delta F_{11} x_1^2) & r \geq r_0 \end{cases}$$

$$A_{21}^* = \begin{cases} (\frac{1}{2\pi r_0 r} - \frac{1}{6\pi r_0^2})(-\Delta F_{22} x_2^2 - \Delta F_{21} x_1 x_2) & r < r_0 \\ (\frac{1}{3\pi r_0 r} + \frac{r - r_0}{2\pi r^3})(-\Delta F_{22} x_2^2 - \Delta F_{21} x_1 x_2) & r \geq r_0 \end{cases}$$

$$A_{22}^* = \begin{cases} (\frac{1}{2\pi r_0 r} - \frac{1}{6\pi r_0^2})(\Delta F_{22} x_2 x_1 + \Delta F_{21} x_1^2) & r < r_0 \\ (\frac{1}{3\pi r_0 r} + \frac{r - r_0}{2\pi r^3})(\Delta F_{22} x_2 x_1 + \Delta F_{21} x_1^2) & r \geq r_0. \end{cases}$$

Appendix C

An auxiliary path-independence result in the dislocation-free case

Consider the configuration shown in Figure C.1 with the whole domain denoted as Ω, the core as Ω_c, the cut-surface as S, and the cut-induced simply-connected domain as $(\Omega\backslash\Omega_c)\backslash S$. Given any g.disclination density localized in the core Ω_c (the patch enclosed by the red line in Figure C.1) and the dislocation density $\boldsymbol{\alpha} = \boldsymbol{0}$, we can calculate $\boldsymbol{S}^*$ and $\boldsymbol{A}^*$ from the following

$$\left.\begin{aligned} \operatorname{curl} \boldsymbol{S}^* &= \boldsymbol{\Pi} \\ \operatorname{div} \boldsymbol{S}^* &= \boldsymbol{0} \end{aligned}\right\} \quad \text{in } \Omega$$

$$\left.\begin{aligned} \operatorname{curl} \boldsymbol{A}^* &= \boldsymbol{S}^* : \boldsymbol{X} \\ \operatorname{div} \boldsymbol{A}^* &= \boldsymbol{0} \end{aligned}\right\} \quad \text{in } \Omega$$

Given a fixed point $\boldsymbol{x}_r$, define $\tilde{\boldsymbol{T}}^p$ as

$$\tilde{\boldsymbol{T}}^p(\boldsymbol{x}; \boldsymbol{x}_r) := \int_{\substack{\boldsymbol{x}_r \\ p}}^{\boldsymbol{x}} \boldsymbol{S}^*(\boldsymbol{s}) d\boldsymbol{s} + \boldsymbol{A}^*(\boldsymbol{x}),$$

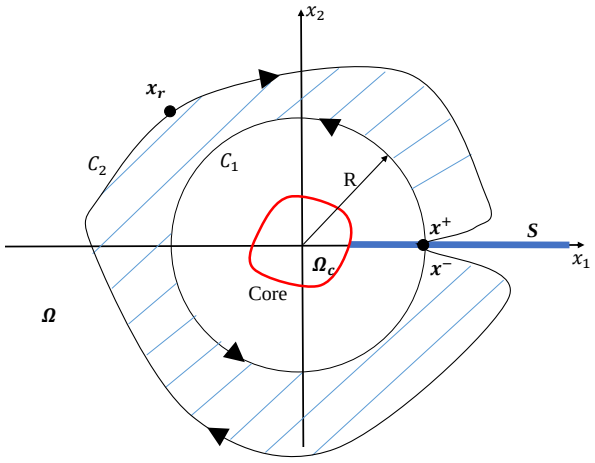

Figure C.1: *A single g.disclination with a circular and an arbitrary path connecting* $\boldsymbol{x}^-$ *and* $\boldsymbol{x}^+$ *in the simply-connected domain* $(\Omega\backslash\Omega_c)\backslash S$.

where p is a path from $\boldsymbol{x}_r$ to $\boldsymbol{x}$. Since $\operatorname{curl}\boldsymbol{S}^* = \boldsymbol{0}$ outside the core Ω_c, $\tilde{\boldsymbol{T}}^p$ is path-independent in the simply-connected domain $(\Omega\backslash\Omega_c)\backslash S$; hence, we denote $\tilde{\boldsymbol{T}}^p(\boldsymbol{x};\boldsymbol{x}_r)$ as $\tilde{\boldsymbol{T}}(\boldsymbol{x};\boldsymbol{x}_r)$. Also, since $\boldsymbol{A}^*$ is calculated from $\operatorname{curl}\boldsymbol{A}^* = \boldsymbol{S}^* : \boldsymbol{X}$, we have

$$
\begin{aligned}
\operatorname{curl}\tilde{\boldsymbol{T}}(\boldsymbol{x};\boldsymbol{x}_r) &= \operatorname{curl}\int_{\boldsymbol{x}_r}^{\boldsymbol{x}} \boldsymbol{S}^*(\boldsymbol{s})d\boldsymbol{s} + \operatorname{curl}\boldsymbol{A}^* \\
\Rightarrow \operatorname{curl}\tilde{\boldsymbol{T}}(\boldsymbol{x};\boldsymbol{x}_r) &= -\operatorname{grad}\left(\int_{\boldsymbol{x}_r}^{\boldsymbol{x}} \boldsymbol{S}^*(\boldsymbol{s})d\boldsymbol{s}\right) : \boldsymbol{X} + \operatorname{curl}\boldsymbol{A}^* \\
\Rightarrow \operatorname{curl}\tilde{\boldsymbol{T}}(\boldsymbol{x};\boldsymbol{x}_r) &= -\boldsymbol{S}^* : \boldsymbol{X} + \operatorname{curl}\boldsymbol{A}^* \\
\Rightarrow \operatorname{curl}\tilde{\boldsymbol{T}}(\boldsymbol{x};\boldsymbol{x}_r) &= \boldsymbol{0}.
\end{aligned}
$$

Let C_1 be the anti-clockwise circular path from $\boldsymbol{x}^+$ to $\boldsymbol{x}^-$ with radius R and C_2 be the clockwise outer path from $\boldsymbol{x}^-$ to $\boldsymbol{x}^+$ shown in the Figure C.1. Then $C = C_1 + C_2$ is the closed contour enclosing the blue shaded area. Take the integral of $\tilde{\boldsymbol{T}}$ along the closed contour C shown as in Figure C.1,

$$
\int_C \tilde{\boldsymbol{T}}(\boldsymbol{x};\boldsymbol{x}_r)d\boldsymbol{x} = \int_A \operatorname{curl}\tilde{\boldsymbol{T}}(\boldsymbol{x};\boldsymbol{x}_r)\boldsymbol{n}da,
$$

where A is the patch enclosed by the loop C and $\boldsymbol{n}$ is the normal unit vector of the patch

A. Therefore,

$$\begin{aligned} \int_C \tilde{\boldsymbol{T}}(\boldsymbol{x};\boldsymbol{x}_r)d\boldsymbol{x} &= \boldsymbol{0} \\ \Rightarrow \int_{C_1} \tilde{\boldsymbol{T}}(\boldsymbol{x};\boldsymbol{x}_r)d\boldsymbol{x} + \int_{C_2} \tilde{\boldsymbol{T}}(\boldsymbol{x};\boldsymbol{x}_r)d\boldsymbol{x} &= \boldsymbol{0} \\ \Rightarrow \int_{-C_1} \tilde{\boldsymbol{T}}(\boldsymbol{x};\boldsymbol{x}_r)d\boldsymbol{x} &= \int_{C_2} \tilde{\boldsymbol{T}}(\boldsymbol{x};\boldsymbol{x}_r)d\boldsymbol{x}. \end{aligned}$$

Namely, the integration of $\tilde{\boldsymbol{T}}(\boldsymbol{x};\boldsymbol{x}_r)$ from $\boldsymbol{x}^-$ to $\boldsymbol{x}^+$ along any path can be calculated as the integration of $\tilde{\boldsymbol{T}}(\boldsymbol{x};\boldsymbol{x}_r)$ along a circular path from $\boldsymbol{x}^-$ to $\boldsymbol{x}^+$.

Appendix D

Calculations for Burgers vector of a g.disclination dipole

Given the configuration in Chapter 2 Sec. 2.8, and for in-plane variations of fields, $\boldsymbol{\Pi}^{+}$ and $\boldsymbol{\Pi}^{-}$ only have non-zero component Π^{+}_{ij3} and Π^{-}_{ij3}, which are given as follows:

$$\Pi^{+}_{ij3} = \begin{cases} \frac{\Delta^{F}_{ij}}{\pi r_0}\left(\frac{1}{r_+} - \frac{1}{r_0}\right) & r_+ < r_0 \\ 0 \quad r_+ \geq r_0, \end{cases}$$

and

$$\Pi^{-}_{ij3} = \begin{cases} -\frac{\Delta^{F}_{ij}}{\pi r_0}\left(\frac{1}{r_-} - \frac{1}{r_0}\right) & r_- < r_0 \\ 0 \quad r_- \geq r_0, \end{cases}$$

where $r_+ = \sqrt{x_1^2 + x_2^2}$ and $r_- = \sqrt{(x_1 - d)^2 + x_2^2}$. As given in Appendix A, we obtain $\boldsymbol{S}^{*+}$ as

$$S_{ij1}^{*+} = \begin{cases} \frac{\Delta_{ij}^F}{2\pi}(-\frac{x_2}{r_+^2}) & r_+ > r_0 \\ \frac{-x_2\Delta_{ij}^F}{\pi r_+^2 r_0}(r_+ - \frac{r_+^2}{2r_0}) & r_+ \leq r_0 \end{cases}$$

$$S_{ij2}^{*+} = \begin{cases} \frac{\Delta_{ij}^F}{2\pi}(\frac{x_1}{r_+^2}) & r_+ > r_0 \\ \frac{x_1\Delta_{ij}^F}{\pi r_+^2 r_0}(r_+ - \frac{r_+^2}{2r_0}) & r_+ \leq r_0, \end{cases}$$

and $\boldsymbol{S}^{*-}$ as

$$S_{ij1}^{*-} = \begin{cases} \frac{\Delta_{ij}^F}{2\pi}(\frac{x_2}{r_-^2}) & r_- > r_0 \\ \frac{x_2\Delta_{ij}^F}{\pi r_-^2 r_0}(r_- - \frac{r_-^2}{2r_0}) & r_- \leq r_0 \end{cases}$$

$$S_{ij2}^{*-} = \begin{cases} \frac{\Delta_{ij}^F}{2\pi}(-\frac{x_1-d}{r_-^2}) & r_- > r_0 \\ \frac{-(x_1-d)\Delta_{ij}^F}{\pi r_-^2 r_0}(r_- - \frac{r_-^2}{2r_0}) & r_- \leq r_0. \end{cases}$$

Also, following the same arguments as in Appendix B, we obtain for $\boldsymbol{A}^{*+}$ and $\boldsymbol{A}^{*-}$:

$$A_{11}^{*+} = \begin{cases} C_1^+ \left(-\Delta_{12}^F x_2^2 - \Delta_{11}^F x_1 x_2\right) & r_+ < r_0 \\ C_2^+ \left(-\Delta_{12}^F x_2^2 - \Delta_{11}^F x_1 x_2\right) & r_+ \geq r_0 \end{cases}$$

$$A_{12}^{*+} = \begin{cases} C_1^+ \left(\Delta_{12}^F x_2 x_1 + \Delta_{11}^F x_1^2\right) & r_+ < r_0 \\ C_2^+ \left(\Delta_{12}^F x_2 x_1 + \Delta_{11}^F x_1^2\right) & r_+ \geq r_0 \end{cases}$$

$$A_{21}^{*+} = \begin{cases} C_1^+ \left(-\Delta_{22}^F x_2^2 - \Delta_{21}^F x_1 x_2\right) & r_+ < r_0 \\ C_2^+ \left(-\Delta_{22}^F x_2^2 - \Delta_{21}^F x_1 x_2\right) & r_+ \geq r_0 \end{cases}$$

$$A_{22}^{*+} = \begin{cases} C_1^+ \left(\Delta_{22}^F x_2 x_1 + \Delta_{21}^F x_1^2\right) & r_+ < r_0 \\ C_2^+ \left(\Delta_{22}^F x_2 x_1 + \Delta_{21}^F x_1^2\right) & r_+ \geq r_0 \end{cases}$$

$$A_{11}^{*-} = \begin{cases} C_1^- \left(\Delta_{12}^F x_2^2 + \Delta_{11}^F (x_1 - d) x_2\right) & r_- < r_0 \\ C_2^- \left(\Delta_{12}^F x_2^2 + \Delta_{11}^F (x_1 - d) x_2\right) & r_- \geq r_0 \end{cases}$$

$$A_{12}^{*-} = \begin{cases} C_1^- \left(-\Delta_{12}^F x_2 (x_1 - d) - \Delta_{11}^F (x_1 - d)^2\right) & r_- < r_0 \\ C_2^- \left(-\Delta_{12}^F x_2 (x_1 - d) - \Delta_{11}^F (x_1 - d)^2\right) & r_- \geq r_0 \end{cases}$$

$$A_{21}^{*-} = \begin{cases} C_1^- \left(\Delta_{22}^F x_2^2 + \Delta_{21}^F (x_1 - d) x_2\right) & r_- < r_0 \\ C_2^- \left(\Delta_{22}^F x_2^2 + \Delta_{21}^F (x_1 - d) x_2\right) & r_- \geq r_0 \end{cases}$$

$$A_{22}^{*-} = \begin{cases} C_1^- \left(-\Delta_{22}^F x_2 (x_1 - d) - \Delta_{21}^F (x_1 - d)^2\right) & r_- < r_0 \\ C_2^- \left(-\Delta_{22}^F x_2 (x_1 - d) - \Delta_{21}^F (x_1 - d)^2\right) & r_- \geq r_0 \end{cases}$$

where $C_1^+ = \frac{1}{2\pi r_0 r_+} - \frac{1}{6\pi r_0^2}$, $C_2^+ = \frac{1}{3\pi r_0 r_+} + \frac{r_+ - r_0}{2\pi r_+^3}$, $C_1^- = \frac{1}{2\pi r_0 r_-} - \frac{1}{6\pi r_0^2}$ and $C_2^- = \frac{1}{3\pi r_0 r_-} + \frac{r_- - r_0}{2\pi r_-^3}$. Given $\boldsymbol{x}_+$ as $(-x_0, 0)$, $\boldsymbol{x}_-$ as $(d - x_0, 0)$ and two paths p^+ and p^- as in Figure 2.24, following

the same notation as in Chapter 2 Sec. 2.8, we have

$$\oint_{p^+} \left\{ \int_{\boldsymbol{x}_-}^{\boldsymbol{x}} \boldsymbol{S}^{*+}(\boldsymbol{s}) d\boldsymbol{s} + \boldsymbol{A}^{*+}(\boldsymbol{x}) \right\} d\boldsymbol{x} =: \boldsymbol{I}^+$$
$$\oint_{p^-} \left\{ \int_{\boldsymbol{x}_-}^{\boldsymbol{x}} \boldsymbol{S}^{*-}(\boldsymbol{s}) d\boldsymbol{s} + \boldsymbol{A}^{*-}(\boldsymbol{x}) \right\} d\boldsymbol{x} =: \boldsymbol{I}^-.$$

After substituting $\boldsymbol{S}^{*+}$, $\boldsymbol{S}^{*-}$, $\boldsymbol{A}^{*+}$, and $\boldsymbol{A}^{*-}$, applying polar coordinates and some algebraic calculation, we obtain

$$I_1^+ = x_0 \Delta_{11}^F$$
$$I_2^+ = x_0 \Delta_{21}^F$$
$$I_1^- = -(x_0 - d) \Delta_{11}^F$$
$$I_2^- = -(x_0 - d) \Delta_{21}^F.$$

Appendix E

The fields $\hat{\boldsymbol{W}}$, $\boldsymbol{W}$, and kinematic constraints on $\hat{\boldsymbol{f}}$

In this Appendix we outline some physical thought-experiments for understanding the fields $\hat{\boldsymbol{W}}$ and $\boldsymbol{W}$, and guidelines for the kinematic constraints on the field $\hat{\boldsymbol{f}}$ for the unique solution of (3.28) when physically expected. The treatment is necessarily non-rigorous (given the scope of the undertaking), but we nevertheless provide it to lay out our intuition behind the various mathematical constructs used in the paper.

On the current configuration, $\hat{\boldsymbol{W}}$ is to be physically understood at any given point $\boldsymbol{x}$ by the relaxation of a small neighborhood of atoms around $\boldsymbol{x}$ (our interpretation of this procedure is explained in [AF15, Sec. 5.4.1], with $\boldsymbol{W}(\boldsymbol{x})$ there to be interpreted as $\hat{\boldsymbol{W}}(\boldsymbol{x})$ here). We assume that the relaxation always takes small neighborhoods to a state that is the 'closest' zero-energy state for the neighborhood from its state in the (generally) stressed current configuration. Let the arbitrarily chosen point where the condition $\boldsymbol{H}^s(\boldsymbol{x}_0) = \boldsymbol{0}$ is imposed be $\boldsymbol{x}_0$. Thus $\hat{\boldsymbol{W}}(\boldsymbol{x}_0) = \boldsymbol{W}(\boldsymbol{x}_0)$. This process of relaxation generates a relaxed shape of the local neighborhood around $\boldsymbol{x}_0$. We will refer to this shape as the reference *tile*. We physically interpret $\boldsymbol{W}(\boldsymbol{x})$ at any point $\boldsymbol{x}$ as follows:

- Select a small shape around $\boldsymbol{x}$ in the current configuration.

- 'Measure' the traction acting on the shape through its boundary in the current configuration.
- Calculate the traction that needs to be applied on the the reference tile to fit into the current shape.
- Compare two traction fields. If they match, then the shape under consideration is one admissible choice, and the deformation gradient from the current shape to the reference tile is one admissible value of $\boldsymbol{W}(\boldsymbol{x})$.
- Given a current configuration and $\hat{\boldsymbol{W}}(\boldsymbol{x}_0)$, in general there can be a set of admissible $\boldsymbol{W}(\boldsymbol{x})$ for each $\boldsymbol{x}$ in the current configuration. For example, consider a stress-free twin boundary in the current configuration with $\boldsymbol{x}_0$ being in one variant of martensite; then $\boldsymbol{W}(\boldsymbol{x})$ for $\boldsymbol{x}$ lying in an adjoining variant can be $\boldsymbol{I}$ or correspond to the twinning shear deformation between the two variants. The actual $\boldsymbol{W}(\boldsymbol{x})$ is decided by further physical considerations, e.g. the microstructure in the current configuration like the presence of boundaries or defects (of course, the mathematical theory is designed to predict a definite evolution for the $\boldsymbol{W}$ field).

The above procedure allows one to define the fields $\boldsymbol{S}$ and $\boldsymbol{\alpha}$, at least in principle. Our theory requires the specification of hard constraints on the field $\hat{\boldsymbol{f}}$ for a nominally unique solution to the system (3.28). Recall that $\hat{\boldsymbol{W}}(\boldsymbol{x}_0) = \hat{\boldsymbol{\chi}}(\boldsymbol{x}_0) + \text{grad}\, \hat{\boldsymbol{f}}(\boldsymbol{x}_0) - \boldsymbol{H}^s(\boldsymbol{x}_0)$. Given $\boldsymbol{S}$ and $\boldsymbol{\alpha}$, $\hat{\boldsymbol{\chi}}(\boldsymbol{x}_0)$ and $\boldsymbol{H}^s(\boldsymbol{x}_0)$ are known, and thus $grad\hat{\boldsymbol{f}}(\boldsymbol{x}_0)$ is known. The kinematic constraints on $\hat{\boldsymbol{f}}$ may be generated as follows: choose $\hat{\boldsymbol{f}}(\boldsymbol{x}_0)$ arbitrarily; then using grad $\hat{\boldsymbol{f}}(\boldsymbol{x}_0)$, determine $\hat{\boldsymbol{f}}(\boldsymbol{x}_0 + \delta\boldsymbol{x})$ around $\boldsymbol{x}_0$ for a small $\delta\boldsymbol{x}$. Then $\hat{\boldsymbol{f}}(\boldsymbol{x}_0)$ and $\hat{\boldsymbol{f}}(\boldsymbol{x}_0 + \boldsymbol{\delta})$, for appropriately chosen values of $\boldsymbol{\delta}$, can serve as the conditions on $\hat{\boldsymbol{f}}$ for eliminating 'rigid-body deformation' modes.

As illustrations of some of these ideas, consider the through twin boundary discussed in Section 3.5.9.1. Figure 3.24(d) is the current configuration. For the through twin boundary, $\hat{\boldsymbol{W}}$ is the identity field, and thus the closest-well, stress-free reference is compatible with,

and identical to, the current configuration. On the other hand, the elastic reference (Fig. 3.24(c)) obtained by mapping the current configuration by $\boldsymbol{W}$ is also compatible, but now represents a compatible shearing across the twin boundary.

For the case of the terminating twin discussed in Section 3.5.9.2, the current and elastic reference configurations are shown in Figure E.1. Figure E.1(a) is the (compatible) elastic reference configuration obtained by mapping the current configuration in Figure E.1(b) by the $\boldsymbol{W}$ field. Since the cwi-elastic field $\hat{\boldsymbol{W}}$ is incompatible on the current configuration, Figure E.2 shows the image of a series of vectors along a circle enclosing the core, mapped by $\hat{\boldsymbol{W}}$. The red arrows correspond to the closed circuit on the current configuration and the blue arrows represent the image of the circuit under $\hat{\boldsymbol{W}}$. Since the body is compressed as discussed in Figure 3.25(b), the blue circle is larger than the red circle. Furthermore, since $\hat{\boldsymbol{W}}$ is incompatible, there is a gap between the start and end of the mapped circuit as shown by the green arrow in Figure E.2. However, because of the fact that we are dealing with a (g.)disclination in this case and not a dislocation core, this gap would not be a constant for all loops surrounding the defect core, as can also be mathematically understood by the delocalized nature of the $\boldsymbol{S}^{\perp}$ field.

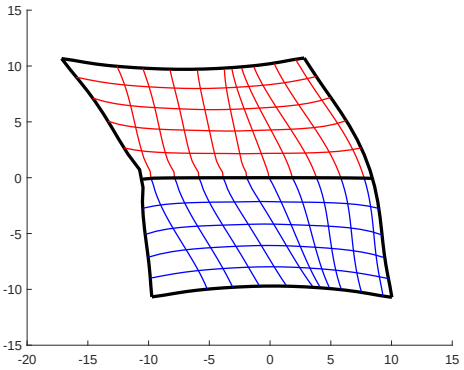

(a) The reference configuration mapped by $\boldsymbol{W}$ field for the compatible terminating twin.

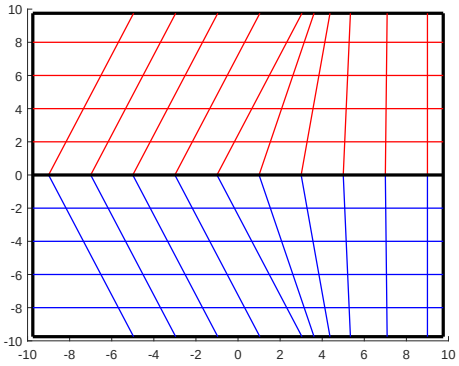

(b) The current configuration for the compatible terminating twin.

Figure E.1: *The reference configuration mapped by $\boldsymbol{W}$ and the current configuration of a compatible terminating twin. Since the current configuration has nonzero stress, the reference configuration of the terminating twin is different from the one of the through twin. The displacement at the left bottom and the vertical displacement at the right bottom are fixed to eliminate the rigid motion.*

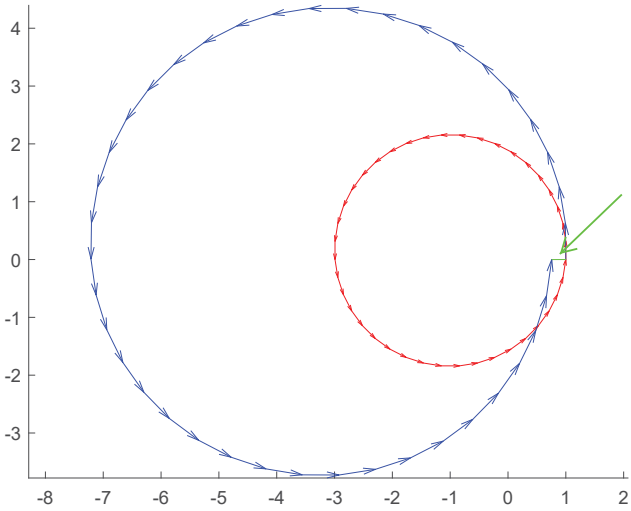

Figure E.2: *Vectors along a circle enclosing the core in the current configuration are mapped by $\hat{\boldsymbol{W}}$. Red arrows are the vectors in the current configuration and blue arrows are the vectors in the reference configuration mapped by $\hat{\boldsymbol{W}}$. The circle in the reference configuration mapped by $\hat{\boldsymbol{W}}$ is compressed, and the green arrow points to the gap representing the incompatibility of $\hat{\boldsymbol{W}}$.*

Appendix F

Construction of $\boldsymbol{S}$ and $\boldsymbol{\Pi}$

Recall Figure 3.2 and the definition of the g.disclination density $\boldsymbol{\Pi} = \operatorname{curl} \boldsymbol{S}$ from (3.15), whose components are given as

$$(\operatorname{curl} S)_{irm} = e_{mjk} S_{irk,j} = e_{mjk} a_{,j} \left(\frac{W_1 - W_2}{t} \right)_{ir} \nu_k + e_{mjk} a \left(\frac{W_1 - W_2}{t} \right)_{ir} \nu_{k,j}.$$

Namely,

$$\operatorname{curl} \boldsymbol{S} = \left(\frac{\boldsymbol{W}_1 - \boldsymbol{W}_2}{t} \right) \otimes (\operatorname{grad} a \times \boldsymbol{\nu}) + a \left(\frac{\boldsymbol{W}_1 - \boldsymbol{W}_2}{t} \right) \otimes \operatorname{curl} \boldsymbol{\nu}. \tag{F.1}$$

To calculate curl $\boldsymbol{\nu}$, we first consider grad $\boldsymbol{\nu}$ (on the 3-d layer) from (3.11) and (3.12) given by

$$\operatorname{grad} \boldsymbol{\nu} = \frac{\partial \boldsymbol{\nu}}{\partial \boldsymbol{s}} = \frac{\partial \boldsymbol{\nu}}{\partial \xi^1} \otimes \frac{\partial \xi^1}{\partial \boldsymbol{s}} + \frac{\partial \boldsymbol{\nu}}{\partial \xi^2} \otimes \frac{\partial \xi^2}{\partial \boldsymbol{s}} + \mathbf{0} \otimes \frac{\partial \xi^3}{\partial \boldsymbol{s}}, \tag{F.2}$$

where $\left(\frac{\partial \xi^i}{\partial \boldsymbol{s}} \right)$ is the dual basis corresponding to $\left(\frac{\partial \boldsymbol{s}}{\partial \xi^i} \right)$, and $\frac{\partial \boldsymbol{s}}{\partial \xi^i} \cdot \frac{\partial \xi^j}{\partial \boldsymbol{s}} = \delta_i^j$. In addition, based on the definition of $\boldsymbol{s}$ in (3.11), we have

$$\frac{\partial \boldsymbol{s}}{\partial \xi^i} = \frac{\partial \boldsymbol{x}}{\partial \xi^i} + \xi^3 \frac{\partial \boldsymbol{\nu}}{\partial \xi^i} \qquad i = 1, 2.$$

Furthermore, since $\boldsymbol{\nu} \cdot \boldsymbol{\nu} = 1$,

$$\frac{\partial \boldsymbol{\nu}}{\partial \xi^i} \cdot \boldsymbol{\nu} = 0 \qquad \text{for } i = 1, 2.$$

Thus, for $i = 1, 2$ and $j = 1, 2, 3$,

$$\begin{aligned} &\boldsymbol{\nu} \cdot \frac{\partial \boldsymbol{s}}{\partial \xi^i} = \boldsymbol{\nu} \cdot \frac{\partial \boldsymbol{x}}{\partial \xi^i} + \xi^3 \frac{\partial \boldsymbol{\nu}}{\partial \xi^i} \cdot \boldsymbol{\nu} = 0 \\ &\Rightarrow \frac{\partial}{\partial \xi^j} \left(\boldsymbol{\nu} \cdot \frac{\partial \boldsymbol{s}}{\partial \xi^i} \right) = 0 \\ &\Rightarrow \frac{\partial \boldsymbol{\nu}}{\partial \xi^j} \cdot \frac{\partial \boldsymbol{s}}{\partial \xi^i} + \frac{\partial \boldsymbol{s}}{\partial \xi^i \partial \xi^j} \cdot \boldsymbol{\nu} = 0 \\ &\Rightarrow \frac{\partial \boldsymbol{\nu}}{\partial \xi^j} \cdot \frac{\partial \boldsymbol{s}}{\partial \xi^i} = -\frac{\partial \boldsymbol{s}}{\partial \xi^i \partial \xi^j} \cdot \boldsymbol{\nu} \end{aligned} \tag{F.3}$$

Since $\frac{\partial \boldsymbol{s}}{\partial \xi^i \partial \xi^j}$ is symmetric with respect to i and j, for any $i = 1, 2, 3$ and any $j = 1, 2, 3$ we have

$$\frac{\partial \boldsymbol{\nu}}{\partial \xi^j} \cdot \frac{\partial \boldsymbol{s}}{\partial \xi^i} = \frac{\partial \boldsymbol{\nu}}{\partial \xi^i} \cdot \frac{\partial \boldsymbol{s}}{\partial \xi^j}, \tag{F.4}$$

(which can also be independently checked from $(\text{F.3})_4$ for $i = 3$). But this implies that grad $\boldsymbol{\nu}$ is a symmetric tensor since grad $\boldsymbol{\nu}$ may be expressed as

$$\text{grad } \boldsymbol{\nu} = \left\{ \frac{\partial \boldsymbol{s}}{\partial \xi^i} \cdot \left(\text{grad } \boldsymbol{\nu} \frac{\partial \boldsymbol{s}}{\partial \xi^j} \right) \right\} \frac{\partial \xi^i}{\partial \boldsymbol{s}} \otimes \frac{\partial \xi^j}{\partial \boldsymbol{s}} = \left(\frac{\partial \boldsymbol{\nu}}{\partial \xi^j} \cdot \frac{\partial \boldsymbol{s}}{\partial \xi^i} \right) \frac{\partial \xi^i}{\partial \boldsymbol{s}} \otimes \frac{\partial \xi^j}{\partial \boldsymbol{s}}.$$

Since $\text{curl}\, \boldsymbol{\nu} = -\,\text{grad } \boldsymbol{\nu} : \boldsymbol{X}$, we have $\text{curl}\, \boldsymbol{\nu} = \boldsymbol{0}$ (the computation can be done in an orthonormal basis if desired by noting that symmetry of the (covariant or contravariant) components of a tensor is a property that is invariant to choice of basis, whether orthonormal or not). Consequently, (F.1) implies

$$\boldsymbol{\Pi} = \text{curl}\, \boldsymbol{S} = \left(\frac{\boldsymbol{W}_1 - \boldsymbol{W}_2}{t} \right) \otimes (\text{grad } a \times \boldsymbol{\nu}).$$

It is important to note that the *curl* senses gradients only in the longitudinal directions

of the layer and is insensitive to the (large) gradient in $\boldsymbol{S}$ that exists across the external surfaces of the layer, transverse to the ξ^3 direction. To see this, we may assume an extension of the function $\boldsymbol{\nu}$ beyond the boundaries of the actual layer along the ξ^3 coordinate and assume a to be a smooth function of the form $a(\xi^1, \xi^3) = \hat{a}(\xi^1)b(\xi^3)$ with b such that it goes to 0 rapidly across the layer boundaries from a constant value of 1 in the layer. Then $\operatorname{curl} \boldsymbol{\nu} = \mathbf{0}$ in the transition layer for a for the same reasons as before, and grad $a \times \boldsymbol{\nu} = \frac{\partial a}{\partial \xi^1} \frac{\partial \xi^1}{\partial \boldsymbol{s}} \times \boldsymbol{\nu} + \frac{\partial a}{\partial \xi^3} \frac{\partial \xi^3}{\partial \boldsymbol{s}} \times \boldsymbol{\nu} = \frac{\partial a}{\partial \xi^1} \frac{\partial \xi^1}{\partial \boldsymbol{s}} \times \boldsymbol{\nu}$ since $\frac{\partial \xi^3}{\partial \boldsymbol{s}} = \boldsymbol{\nu}$, the large values of $\frac{\partial a}{\partial \xi^3}$ in the transition layer is not sensed by the expression.

Define D as the integral of $\boldsymbol{\Pi}$ over any area patch threaded by the core, such as the area patch A enclosed by the black dashed line in Figure 3.2:

$$\boldsymbol{D} := \int_A \boldsymbol{\Pi} d\boldsymbol{a}, \tag{F.5}$$

where $\hat{\boldsymbol{n}}$ is the unit normal vector of the core surface A. After substituting $\boldsymbol{\Pi}$ in (3.15), we have

$$\boldsymbol{D} = \int_A \left[\frac{\boldsymbol{W}_1 - \boldsymbol{W}_2}{t} \otimes (\text{grad } \boldsymbol{a} \times \boldsymbol{\nu}) \right] d\boldsymbol{a}$$
$$\boldsymbol{D} = \frac{\boldsymbol{W}_1 - \boldsymbol{W}_2}{t} \int_A (\text{grad } \boldsymbol{a} \times \boldsymbol{\nu}) \cdot d\boldsymbol{a}$$

With the parametrization in Figure 3.2, we have

$$\text{grad } a = \frac{\partial a}{\partial \xi^1} \frac{\partial \xi^1}{\partial \boldsymbol{s}},$$
$$d\boldsymbol{a} = \left(\frac{\partial \boldsymbol{s}}{\partial \xi^1} \times \boldsymbol{\nu} \right) d\xi^1 d\xi^3,$$

so that

$$\boldsymbol{D} = \frac{\boldsymbol{W}_1 - \boldsymbol{W}_2}{t} \int_{\xi^3=0}^{\xi^3=t} \int_{\xi_1=0}^{\xi^1=c} \frac{\partial a}{\partial \xi^1} \left[\frac{\partial \xi^1}{\partial \boldsymbol{s}} \times \boldsymbol{\nu} \right] \cdot \left[\frac{\partial \boldsymbol{s}}{\partial \xi^1} \times \boldsymbol{\nu} \right] d\xi^1 d\xi^3.$$

Note that

$$\left[\frac{\partial \xi^1}{\partial \boldsymbol{s}} \times \boldsymbol{\nu}\right] \cdot \left[\frac{\partial \boldsymbol{s}}{\partial \xi^1} \times \boldsymbol{\nu}\right] = \left[\left(\frac{\partial \xi^1}{\partial \boldsymbol{s}} \times \boldsymbol{\nu}\right) \times \frac{\partial \boldsymbol{s}}{\partial \xi^1}\right] \cdot \boldsymbol{\nu}$$
$$= \left[\boldsymbol{\nu}\left(\frac{\partial \xi^1}{\partial \boldsymbol{s}} \cdot \frac{\partial \boldsymbol{s}}{\partial \xi^1}\right) - \frac{\partial \xi^1}{\partial \boldsymbol{s}}\left(\boldsymbol{\nu} \cdot \frac{\partial \boldsymbol{s}}{\partial \xi^1}\right)\right] \cdot \boldsymbol{\nu}.$$

Since $\frac{\partial \xi^1}{\partial \boldsymbol{s}} \cdot \frac{\partial \boldsymbol{s}}{\partial \xi^1} = 1$ and $\boldsymbol{\nu} \cdot \frac{\partial \boldsymbol{s}}{\partial \xi^1} = 0$ as shown in $(\text{F.3})_1$, we have

$$\left[\frac{\partial \xi^1}{\partial \boldsymbol{s}} \times \boldsymbol{\nu}\right] \cdot \left[\frac{\partial \boldsymbol{s}}{\partial \xi^1} \times \boldsymbol{\nu}\right] = 1. \tag{F.6}$$

With $a(\xi^1)$ given in (3.14), and substituting (F.6), $\boldsymbol{D}$ can be written as

$$\boldsymbol{D} = \frac{\boldsymbol{W}_1 - \boldsymbol{W}_2}{t}\frac{tc}{c} = \boldsymbol{W}_1 - \boldsymbol{W}_2. \tag{F.7}$$

Thus, we obtain $\boldsymbol{D} = \boldsymbol{W}_1 - \boldsymbol{W}_2$ and therefore the equation

$$\operatorname{curl} \boldsymbol{Y} = \boldsymbol{\Pi}$$

implies that the integral of $\boldsymbol{Y}$ along any curve encircling the core is $\boldsymbol{W}_1 - \boldsymbol{W}_2$ (by noting that $\operatorname{div} \boldsymbol{\Pi} = \boldsymbol{0}$ and applying the divergence theorem on a 'cylinder' with the surface A as one end cap and any arbitrary surface as end-cap with the constraint that its boundary is a curve that encircles the core).

In the case of phase boundaries, the misdistortion $\boldsymbol{W}_1 - \boldsymbol{W}_2$ can be written as $\boldsymbol{c} \otimes \boldsymbol{\nu}$ representing a shear difference. Then the eigenwall field $\boldsymbol{S}$ takes the form $a(\boldsymbol{c} \otimes \boldsymbol{\nu} \otimes \boldsymbol{\nu})$ and therefore

$$(\operatorname{curl} \boldsymbol{S})_{irm} = e_{mjk} S_{irk,j} = e_{mjk} a_{,j} \left(\frac{c_i \nu_r}{t}\right) \nu_k + e_{mjk} a \left(\frac{c_i \nu_r}{t}\right) \nu_{k,j} + e_{mjk} a \left(\frac{c_i \nu_k}{t}\right) \nu_{r,j}. \tag{F.8}$$

Based on the same argument to go from (F.2) to (F.4), the second term is zero and the

first term is non-zero only in the core. If the layer where $\boldsymbol{S}$ has support is flat, then the last term vanishes and $\boldsymbol{\Pi}$ is localized in the core. However, the additional third term is non-vanishing along the layer when the layer is curved, serving as a non-zero source of $\boldsymbol{\Pi}$ distribution along the whole layer.

Appendix G

Specification of Anisotropic stiffness tensor

For the anisotropic stiffness tensor, the elastic constants for the cubic crystal of Cu and Ag are adopted from [SW$^+$71]. The stiffness tensor $\boldsymbol{C}$ can be written as

$$\boldsymbol{C} = \tilde{C}_{ijkl}\tilde{\boldsymbol{e}}_i \otimes \tilde{\boldsymbol{e}}_j \otimes \tilde{\boldsymbol{e}}_k \otimes \tilde{\boldsymbol{e}}_l,$$

where $\tilde{\boldsymbol{e}}_i$ is the ith principle direction of $\boldsymbol{C}$ and $\tilde{C}_{ijkl}$ is the elastic constant. Denote the transformation from any orthogonal basis $\{\boldsymbol{e}_i\}$ to $\{\tilde{\boldsymbol{e}}_i\}$ as $\boldsymbol{R}$. Namely, the component of $\boldsymbol{R}$, R_{ij}, can be define as $\tilde{\boldsymbol{e}}_i \cdot \boldsymbol{e}_j$. Then, we have

$$\begin{aligned} \boldsymbol{e}_m \cdot (((\boldsymbol{C}\boldsymbol{e}_t)\,\boldsymbol{e}_s)\,\boldsymbol{e}_n) &= \tilde{C}_{ijkl}(\tilde{\boldsymbol{e}}_i \cdot \boldsymbol{e}_m)(\tilde{\boldsymbol{e}}_j \cdot \boldsymbol{e}_n)(\tilde{\boldsymbol{e}}_k \cdot \boldsymbol{e}_s)(\tilde{\boldsymbol{e}}_l \cdot \boldsymbol{e}_t) \\ \Rightarrow C_{mnst} &= \tilde{C}_{ijkl}R_{im}R_{jn}R_{ks}R_{lt} \end{aligned}$$

In the incoherent grain boundary disconnection case discussed in Section 3.5.8.1, $\boldsymbol{R}$ is a rotation matrix with a rotation angle along $\boldsymbol{e}_3$ axis. The rotation angle of the top part is $22.5°$ and the rotation angle of the bottom part is $-22.5°$.

Appendix H

Uniqueness results in linear g.disclination and classical disclination theory

Recall the governing equations (3.10) of linear g.disclination theory:

$$\begin{aligned} &\operatorname{curl} \hat{\boldsymbol{U}}^e = -\boldsymbol{S}^{\perp} : \boldsymbol{X} + \boldsymbol{\alpha} \\ &\operatorname{div} (\boldsymbol{C} : \hat{\boldsymbol{U}}^e) = \boldsymbol{0} \\ &(\boldsymbol{C} : \hat{\boldsymbol{U}}^e)\boldsymbol{n} = \boldsymbol{t} \qquad \text{on the boundary.} \end{aligned} \tag{H.1}$$

We assume that the elasticity tensor $\boldsymbol{C}$ has minor symmetries and is positive definite, possibly anisotropic and spatially inhomogeneous with sufficient smoothness. We also assume the body to be simply-connected.

Now assume there is another solution $\hat{\boldsymbol{U}}^{e'}$ that also satisfies (H.1), and define $\delta\hat{\boldsymbol{U}}^{e} := \hat{\boldsymbol{U}}^{e} - \hat{\boldsymbol{U}}^{e'}$. Then, since (H.1) is linear, we have

$$\begin{aligned} &\operatorname{curl} \delta\hat{\boldsymbol{U}}^{e} = \boldsymbol{0} \\ &\operatorname{div}(\boldsymbol{C} : \delta\hat{\boldsymbol{U}}^{e}) = \boldsymbol{0} \\ &(\boldsymbol{C} : \delta\hat{\boldsymbol{U}}^{e})\boldsymbol{n} = \boldsymbol{0} \qquad \text{on the boundary,} \end{aligned} \tag{H.2}$$

which implies $\delta\hat{\boldsymbol{U}}^{e} = \boldsymbol{0}$ up to a spatially uniform skew tensor field, this being the standard Neumann proof of linear elasticity, since $\delta\hat{\boldsymbol{U}}^{e}$ is now a gradient. Thus, $\hat{\boldsymbol{U}}^{e} = \hat{\boldsymbol{U}}^{e'}$ up to a constant skew tensor and $\hat{\boldsymbol{U}}^{e}_{sym} = \hat{\boldsymbol{U}}^{e'}_{sym}$. Thus, $\hat{\boldsymbol{U}}^{e}$ and $\hat{\boldsymbol{U}}^{e'}$ lead to the same stress field, and their skew parts are also essentially uniquely determined up to a constant difference.

On the other hand, the elastic strain of the dislocation and disclination problem in DeWit's model [DeW73a] is obtained from

$$\begin{aligned} \left[\operatorname{curl}(\boldsymbol{\alpha}^{T})\right]_{sym} - \boldsymbol{\theta}_{sym} &= \operatorname{inc}(\boldsymbol{\epsilon}^{e}) \\ \operatorname{div}(\boldsymbol{C} : \boldsymbol{\epsilon}^{e}) &= \boldsymbol{0} \\ (\boldsymbol{C} : \boldsymbol{\epsilon}^{e})\boldsymbol{n} &= \boldsymbol{0} \qquad \text{on the boundary,} \end{aligned} \tag{H.3}$$

where $\boldsymbol{\epsilon}^{e}$ is the elastic strain, $\boldsymbol{\alpha}$ is the dislocation density and $\boldsymbol{\theta}$ is the disclination density. $\boldsymbol{C}$ is the stiffness tensor (with the same properties stipulated above). Consider another solution $\boldsymbol{\epsilon}^{e'}$ that also satisfies (H.3), and denote $\delta\boldsymbol{\epsilon}^{e} = \boldsymbol{\epsilon}^{e'} - \boldsymbol{\epsilon}^{e}$. Then we have

$$\begin{aligned} \operatorname{inc}(\delta\boldsymbol{\epsilon}^{e}) &= \boldsymbol{0} \\ \operatorname{div}(\boldsymbol{C} : \delta\boldsymbol{\epsilon}^{e}) &= \boldsymbol{0} \\ (\boldsymbol{C} : \delta\boldsymbol{\epsilon}^{e})\boldsymbol{n} &= \boldsymbol{0} \qquad \text{on the boundary.} \end{aligned}$$

The first equation in the above set and the simply-connected body implies that $\delta\boldsymbol{\epsilon}^{e}$ is a symmetrized gradient of a vector field, by St. Venant's compatibility theorem. Then again,

this becomes a standard Neumann uniqueness proof in linear elasticity theory and we have $\delta\boldsymbol{\epsilon}^e = \mathbf{0}$, and thus $\boldsymbol{\epsilon}^e_{sym} = \boldsymbol{\epsilon}^{e'}_{sym}$. Therefore the stress field from $\boldsymbol{\epsilon}^e$ and the stress from $\boldsymbol{\epsilon}^{e'}$ are identical, namely the stress field calculated from (H.3) is unique.

However, we note one important difference between the two models. For identically specified data, note that g.disclination theory determines the closest-well elastic rotation essentially uniquely, whereas classical disclination theory is completely silent about such determination. This is particularly relevant in the dislocation-only case where there can be no ambiguity in the definition of the elastic rotation in incompatible linear theory.

Appendix I

Numerical Schemes for ϕ evolution equations in 2D layer model

We adapt the computational scheme developed in [ZAWB15] for an exactly similar problem in the context of dislocation dynamics to solve our equations.

For the sake of completeness, we reproduce the details of the scheme from that paper with appropriate adjustments for field variable names and parameters. The numerical scheme we adopt to solve the problem is identical to that in [ZAWB15], again with just a translation of the names of the field variables. We include the details here for completeness. In general, the Finite Element Method (FE) is used to solve the equation for balance of linear momentum in a staggered scheme that utilizes ϕ as a given quantity obtained by evolving it in the remaining part of the scheme. The general computing flow is shown in Figure I.1.

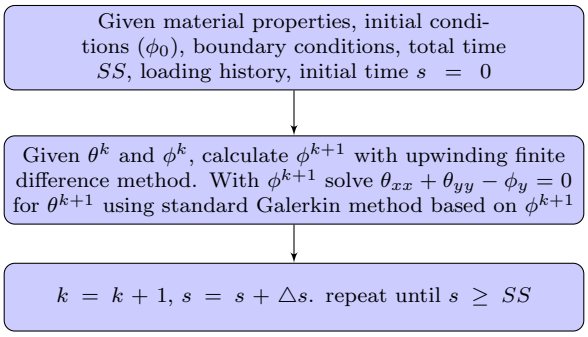

Figure I.1: *Flow charts for computing scheme: ϕ and θ are basic unkonwn fields.*

An FE mesh with an embedded 1-d finite difference grid is used. We use linear quadrilateral elements, with 5×5 Gauss quadrature points. All elements are of uniform size over the whole domain.

The 1-d, finite difference grid is embedded in the layer, coincident with the line $y = 0$. Suppose that the layer is meshed into M rows and N columns, where N is the total number of 1-d grid points and M is always an odd number so that the middle row of elements always have centers on $y = 0$. Each column of FE elements in the layer correspond to exactly one grid point. Let x_k be the x coordinate of the k^{th} 1-d grid point, which is at the center of the k_{th} element in the $(M + 1)/2$ row of layer elements. Recall that $\tau(x_k)$ is defined as $\frac{1}{a}\int_{-a/2}^{a/2}(\theta_y - \phi)\, dy$. Let $(\theta_y - \phi)(I, k)$ denotes the integrand evaluated at the I^{th} Gauss point whose x coordinate is x_k, and let N_k be the total number of such Gauss points. Then $\tau(x_k)$ is calculated as

$$\tau(x_k) = \frac{1}{N_k}\left(\sum_{I=1}^{N_k}(\theta_y - \phi)(I, k)\right).$$

The numerical scheme developed in [DAZM13] is adopted and improved to solve $(4.11)_2$, the ϕ evolution. The scheme is called upwinding as the basic idea is to infer the direction of wave propagation from the linearization of $(4.11)_2$ and use this direction in the actual nonlinear equation. Let us denote time step with $\triangle t$ and spatial grid size of the finite difference grid with $\triangle h$. Due to the necessity of very small element sizes to demonstrate convergence, an explicit treatment of the diffusion term in $(4.11)_2$ becomes prohibitive be-

cause of a $\triangle t = \mathcal{O}(\triangle h^2)$ scaling. This is circumvented by treating the ϕ_{xx} term implicitly, resulting in a linearly implicit scheme as follows. We first linearize $(4.11)_2$ and discretized:

$$\begin{aligned}\delta\phi_t^k(x_h) = &-(2-m)\left(-sgn\left(\phi_x^k(x_h)\right)\right)\left|\phi_x^k(x_h)\right|^{1-m}\left[\tau^k(x_h) + a\phi_{xx}^{k+1}(x_h) - \left(\tau^b(x_h)\right)^k\right]\delta\phi_x^k(x_h)\\ &+\left|\phi_x^k(x_h)\right|^{2-m}\left[\epsilon\delta\phi_{xx}^k(x_h)\right]\\ &+\left|\phi_x^k(x_h)\right|^{2-m}\left[\tau^{b'}(x_h)\,\delta\phi^k(x_h)\right],\end{aligned} \tag{I.1}$$

where a quantity such as $\phi_x^k(x_h)$ implies the value of $\phi_x(x)$ evaluated at h^{th} grid point at k^{th} time step. The first term in (I.1) provides an advection equation with wave speed

$$c^k(x_h) = (2-m)\left(-sgn\left(\phi_x^k(x_h)\right)\right)\left|\phi_x^k(x_h)\right|^{1-m}\left[\tau^k(x_h) + a\phi_{xx}^{k+1}(x_h) - \left(\tau^b(x_h)\right)^k\right].$$

$\phi_x^k(x_h)$ and $\phi_{xx}^k(x_h)$ are obtained from central finite differences:

$$\begin{aligned}\phi_x^k(x_h) &= \frac{\phi^k(x_{h+1}) - \phi^k(x_{h-1})}{2\triangle h}\\ \phi_{xx}^k(x_h) &= \frac{\phi^k(x_{h+1}) - 2\phi^k(x_h) + \phi^k(x_{h-1})}{\triangle h^2}.\end{aligned} \tag{I.2}$$

Based on the sign of c_k, ϕ_x^k is then computed by the following upwinding scheme:

$$\phi_x^k = \begin{cases}\frac{\phi^k(x_{h+1})-\phi^k(x_h)}{\triangle h} & \text{if } c^k(x_h) < 0\\ \frac{\phi^k(x_h)-\phi^k(x_{h-1})}{\triangle h} & \text{if } c^k(x_h) > 0\\ \frac{\phi^k(x_{h+1})-\phi^k(x_{h-1})}{2\triangle h} & \text{if } c^k(x_h) = 0.\end{cases} \tag{I.3}$$

The time step is governed by a combination of a CFL condition and a criterion for stability for an explicit scheme for a linear ordinary differential equation:

$$\triangle t^k = min\left(\frac{\triangle h}{c^k(x_h)}, \frac{1}{|\phi_x^k(x_h)|^{2-m}(-(\tau^{b'}(x_h))^k}\right). \tag{I.4}$$

Note that if ϕ_{xx} was evaluated at k, then the step size would also be bounded by $\frac{\triangle h^2}{a\left|\phi_x^k(x_h)\right|}$, leading to a quadratic decrease in $\triangle t^k$ with element size. Treating ϕ_{xx} implicitly eliminates this constraint resulting in significant savings in computation time. ϕ_h^{k+1} is updated according to

$$\begin{aligned}
&\frac{\phi^{k+1}(x_h) - \phi^k(x_h)}{\triangle t^k} = |\phi_x^k(x_h)|^{2-m}\left[\tau^k + a\phi_{xx}^{k+1} - (\tau^b(x_h))^k\right] \\
\Rightarrow &\phi^{k+1}(x_h) - a\triangle t^k|\phi_x^k(x_h)|^{2-m}\phi_{xx}^{k+1}(x_h) = \phi^k(x_h) + \triangle t^k|\phi_x^k(x_h)|^{2-m}\left[\tau^k - (\tau^b(x_h))^k\right].
\end{aligned} \tag{I.5}$$

The right hand side of the equation is known at current time k. But noting that $\phi_{xx}^{k+1}(x_h)$ is again computed from ϕ^{k+1} at x_{h+1}, x_h and x_{h-1}, a system of linear equations of size N has to be solved to get ϕ^{k+1}. The computational expense of the linear solve is small compared to the savings obtained by relaxing $\triangle t^k$ corresponding to the explicit treatment of diffusion.

Appendix J

Layer model for the screw dislocation case

Paralleling the development in Section 4.5.2, we define a layer model for straight screw dislocation dynamics in solids in this section. Consider the similar geometry as in Section 4.5.2 as shown in Figure 4.12:

$$\mathcal{V} = \{(x, y) : (x, y) \in [-W, +W] \times [-H, +H]\}$$
$$\mathcal{L} = \{(x, y) : (x, y) \in [-W, +W] \times [-l/2, +l/2]\}$$
$$0 \leq l < 2H, \quad W > 0.$$

The screw dislocation problem is one of anti-plane shear, i.e. there is only one non-vanishing displacement component of the solid, this being the out-of-plane one which is a function of the in-plane coordinates. In the present physical context, $\boldsymbol{u}$ is the displacement vector and $\boldsymbol{U}^P$ is the plastic distortion tensor, that plays an analogous role to $\boldsymbol{\lambda}$. The conservation law for the defect field for the screw dislocation [ZAWB15] is given in the form

$$\dot{\boldsymbol{\alpha}} = -\operatorname{curl}(\boldsymbol{\alpha} \times \boldsymbol{v}).$$

The displacement is assumed to be of the form

$$\boldsymbol{u} = w(x, y)\boldsymbol{e}_3$$

and $\boldsymbol{U}^P$ takes the form

$$\boldsymbol{U}^P = \begin{cases} \phi(x,t)\boldsymbol{e}_3 \otimes \boldsymbol{e}_2 & \text{in the layer} \\ 0 & \text{otherwise.} \end{cases}$$

We assume $\boldsymbol{v}$ to be of the form $\boldsymbol{v} = v(x,t)\boldsymbol{e}_1$.

Therefore, $\boldsymbol{\alpha}$ is also non-zero only in the layer, with component form

$$\boldsymbol{\alpha} = -\operatorname{curl} \boldsymbol{U}^P = -\phi_x \boldsymbol{e}_3 \otimes \boldsymbol{e}_3$$

$$\operatorname{curl} \boldsymbol{\alpha} = \phi_{xx} \boldsymbol{e}_3 \otimes \boldsymbol{e}_2.$$

The stored energy function for the screw dislocation model is assumed as

$$W = \int_{\mathcal{V}} \psi(\boldsymbol{\epsilon}^e, \boldsymbol{\alpha}) + \gamma f(|\boldsymbol{U}^p|) dv = \int_{\mathcal{V}} \left[\frac{K}{2} |\operatorname{grad} \boldsymbol{u} - \boldsymbol{U}^P|^2 + \frac{\epsilon}{2}(\phi_x)^2 + \gamma f(|\phi|) \right] dv.$$

Here, K is a shear modulus with dimension $Force \times Length^{-2}$; $\epsilon = KCa\xi^2$ is a parameter characterizing the energy density of the dislocation core; ξ is the Burgers vector magnitude of the dislocation, proportional to the lattice interatomic distance (with dimensions of $Length$), C is a non-dimensional parameter to control the magnitude of the core energy, and the product $a\xi$ is the separation between two atomic layers with $a \geq 0$ a non-dimensional scaling factor. Unlike the nematic disclination case, the layer has a physical significance in the case of the crystal dislocation as does the $\boldsymbol{\lambda}$ field in predicting, often 'stress-free,' permanent plastic deformation (with respect to a fixed reference) due to the motion of dislocations. The combination γf represents the 'generalized stacking fault energy' reflecting

lattice symmetries, and measurable from controlled computational atomistic experiments ([Vit68]) and we assume the simple forms $\gamma = \frac{PK}{a}$ and

$$f = 1 - \cos\left(2\pi|\phi|\left(\frac{\xi}{a\xi}\right)^{-1}\right)$$

where P is a dimensionless parameter.

From $\dot{\boldsymbol{\alpha}} = -\operatorname{curl}(\boldsymbol{\alpha} \times \boldsymbol{v})$, we have $\phi_t = -\phi_x v(x,t)$. Given the ansatz, only the layer is relevant for the dissipation and it can be written as

$$D = \int_{\mathcal{L}} v\{[T_{32} - \tau^b + \epsilon\phi_{xx}](-\phi_x)\}dv,$$

where

$$\tau^b := \gamma\frac{df}{d\phi} = 2\pi PK\sin(2\pi\phi\, a)$$

and

$$T_{32} = K(u_{3,2} - \phi) := K(\omega_y - \phi).$$

As in Section 4.5.2 , we take the average of $(w_y - \phi)$ over the layer and requiring the dissipation $D \geq 0$, the evolution equation for ϕ reads as

$$\frac{\partial\phi}{\partial t} = \frac{|\phi_x|^{2-m}}{B_m}\left(\tau - \tau^b + \epsilon\phi_{xx}\right)$$
$$\text{where} \quad \tau = \frac{K}{a\xi}\int_{-\frac{a\xi}{2}}^{\frac{a\xi}{2}}(w_y - \phi)dy.$$

Again, B_m is a non-negative coefficient characterizing energy dissipation with physical dimensions depending on m. The parameter m can be chosen to probe different types of

behavior. By introducing the following dimensionless variables,

$$\tilde{x} = \frac{1}{\xi}x; \quad \tilde{y} = \frac{1}{\xi}y; \quad \tilde{\epsilon} = \frac{1}{K\xi^2}\epsilon = Ca; \quad \tilde{\tau} = \frac{1}{K}\tau; \quad \tilde{\tau}^b = \frac{1}{K}\tau^b;$$
$$\tilde{s} = \frac{K}{\xi^{2-m}B_m}t; \quad \tilde{w} = \frac{1}{\xi}w,$$

we obtain the dimensionless evolution equation for the layer model as described below:

$$\frac{\partial\phi}{\partial\tilde{s}} = |\phi_{\tilde{x}}|^{2-m}\left(\tilde{\tau} - \tilde{\tau}^b + \tilde{\epsilon}\phi_{\tilde{x}\tilde{x}}\right).$$

After removing tildes for simplicity, the dimensionless governing equations for the screw dislocation problem become

$$\begin{cases} w_{xx} + w_{yy} - \phi_y = 0 \quad \text{in } \mathcal{V} \\ \dfrac{\partial\phi}{\partial s} = |\phi_x|^{2-m}\left(\tau - \tau^b + Ca\phi_{xx}\right) \quad \text{in } \mathcal{L} \end{cases} \tag{J.1}$$

where

$$\tau = \frac{1}{a}\int_{-a/2}^{a/2}(w_y - \phi)\,dy, \quad \tau^b = 2\pi P\sin(2\pi\phi\, a),$$

and the first equation represents static balance of forces (balance of linear momentum), for the ansatz being considered here.

As can be seen from a comparison of (J.1) and (4.11), the governing equations of the screw dislocation model are exactly analogous to the disclination model.

Bibliography

[Ach01] Amit Acharya, *A model of crystal plasticity based on the theory of continuously distributed dislocations*, Journal of the Mechanics and Physics of Solids **49** (2001), no. 4, 761–784. 1.1, 2.2, 2.7.2, A

[Ach03] ———, *Driving forces and boundary conditions in continuum dislocation mechanics*, Proceedings of the Royal Society of London A: Mathematical, Physical and Engineering Sciences, vol. 459, The Royal Society, 2003, pp. 1343–1363. 1.1

[AD13] Amit Acharya and Kaushik Dayal, *Continuum mechanics of line defects in liquid crystals and liquid crystal elastomers*, Quarterly of Applied Mathematics **72** (2013), no. 1, 33–64. 1.2, 4.1, 4.5, 4.5.1, 5.3.2

[AD15] Vaibhav Agrawal and Kaushik Dayal, *A dynamic phase-field model for structural transformations and twinning: Regularized interfaces with transparent prescription of complex kinetics and nucleation. Part I: Formulation and one-dimensional characterization*, Journal of the Mechanics and Physics of Solids **85** (2015), 270–290. 2.2

[ADLGP14] Roberto Alicandro, Lucia De Luca, Adriana Garroni, and Marcello Ponsiglione, *Metastability and dynamics of discrete topological singularities in two dimensions: a Γ-convergence approach*, Archive for Rational Mechanics and Analysis **214** (2014), no. 1, 269–330. 4.8

[AF12] Amit Acharya and Claude Fressengeas, *Coupled phase transformations and plas-*

ticity as a field theory of deformation incompatibility, International Journal of Fracture **174** (2012), no. 1, 87–94. 1.1, 2.1, 2.4, 3.1, 3.3

[AF15] ———, *Continuum mechanics of the interaction of phase boundaries and dislocations in solids*, Differential Geometry and Continuum Mechanics, Springer Proceedings in Mathematics and Statistics; Ed: G. Q. Chen, M. Grinfeld, R. J. Knops **137** (2015), 125–168. (document), 1.1, 2.1, 2.4, 2.6, 2.6, 2.6, 2.6, 3, 2.6.1, 2.16, 3.1, 3.3, 3.7, E

[AMK17] Hillel Aharoni, Thomas Machon, and Randall Kamien, *Composite dislocations in smectic liquid crystals*, Physical review letters **118** (2017), no. 25, 257801. 3.5.7.1

[AR06] Amit Acharya and Anish Roy, *Size effects and idealized dislocation microstructure at small scales: predictions of a phenomenological model of mesoscopic field dislocation mechanics: Part i*, Journal of the Mechanics and Physics of Solids **54** (2006), no. 8, 1687–1710. 3.4.2, 3.4.2

[AZ15] Amit Acharya and Xiaohan Zhang, *From dislocation motion to an additive velocity gradient decomposition, and some simple models of dislocation dynamics*, Chinese Annals of Mathematics, Series B **36B** (2015), no. 5, 645–658. 3, 4.5.2.1, 4.5.2.1

[AZH08] S. Akarapu, H. Zbib, and J. P. Hirth, *Modeling and analysis of disconnections in tilt walls*, Scripta Materialia **59** (2008), no. 3, 265–267. 2.2

[BAC05] Robert W. Balluffi, Samuel M. Allen, and W. Craig Carter, *Kinetics of materials*, John Wiley & Sons, 2005. (document), 2.2, 2.4.4, 2.11, 3.12, 3.5.6.2

[BB56] R. Bullough and B. A. Bilby, *Continuous distributions of dislocations: Surface dislocations and the crystallography of martensitic transformations*, Proceedings of the Physical Society. Section B **69** (1956), no. 12, 1276. 2.2

[BB15] John M. Ball and S.J. Bedford, *Discontinuous order parameters in liquid crystal theories*, Molecular Crystals and Liquid Crystals **612** (2015), no. 1, 467–489. 1, 4.1

[BBCH92] F. Bethuel, Haim Brezis, B.D. Coleman, and F. Hélein, *Bifurcation analysis of minimizing harmonic maps describing the equilibrium of nematic phases between cylinders*, Archive for Rational Mechanics and Analysis **118** (1992), no. 2, 149–168. 2, 4.1

[BBS55] B. A. Bilby, R. Bullough, and E. Smith, *Continuous Distributions of Dislocations: A New Application of the Methods of Non-Riemannian Geometry*, Proceedings of the Royal Society of London A: Mathematical, Physical and Engineering Sciences **231** (1955), no. 1185, 263–273. 2.2

[BCF51] W.-K._ Burton, N. Cabrera, and F. C. Frank, *The growth of crystals and the equilibrium structure of their surfaces*, Philosophical Transactions of the Royal Society of London A: Mathematical, Physical and Engineering Sciences **243** (1951), no. 866, 299–358. 5.3.4

[BCG05] L. Berlyand, D. Cioranescu, and D. Golovaty, *Homogenization of a Ginzburg–Landau model for a nematic liquid crystal with inclusions*, Journal de Mathématiques Pures et Appliquées **84** (2005), no. 1, 97–136. 4.1

[BCSS94] Mark J. Bowick, L. Chandar, E. A. Schiff, and Ajit M. Srivastava, *The cosmological kibble mechanism in the laboratory: String formation in liquid crystals*, Science **263** (1994), no. 5149, 943–945. 5.1

[Bha03] Kaushik Bhattacharya, *Microstructure of martensite: why it forms and how it gives rise to the shape-memory effect*, vol. 2, Oxford University Press, 2003. 3.5.9.4, 3.5.12.2

[Bil55] B. A. Bilby, *In: Report of the conference on defects in crystalline solids*, Physical

Soc (1955), 124. 1.1

[BPP12] Patricia Bauman, Jinhae Park, and Daniel Phillips, *Analysis of nematic liquid crystals with disclination lines*, Archive for Rational Mechanics and Analysis **205** (2012), no. 3, 795–826. 4.1

[BS03] Paolo Biscari and Timothy J. Sluckin, *Expulsion of disclinations in nematic liquid crystals*, European Journal of Applied Mathematics **14** (2003), no. 01, 39–59. 4.1

[BS05] ———, *Field-induced motion of nematic disclinations*, SIAM Journal on Applied Mathematics **65** (2005), no. 6, 2141–2157. 4.1

[BV97] Paolo Biscari and Epifanio G. Virga, *Local stability of biaxial nematic phases between two cylinders*, International Journal of Non-linear Mechanics **32** (1997), no. 2, 337–351. 4.1

[BZ07] John M. Ball and Arghir Zarnescu, *Orientable and non-orientable director fields for liquid crystals*, PAMM **7** (2007), no. 1, 1050701–1050704. 1, 3

[BZB+12] Thomas R. Bieler, Bite Zhou, Lauren Blair, Amir Zamiri, Payam Darbandi, Farhang Pourboghrat, Tae-Kyu Lee, and Kuo-Chuan Liu, *The role of elastic and plastic anisotropy of sn in recrystallization and damage evolution during thermal cycling in sac305 solder joints*, Journal of Electronic Materials **41** (2012), no. 2, 283–301. 3.5.9.4

[Cah82] J.W. Cahn, *Transitions and phase equilibria among grain boundary structures*, Le Journal de Physique Colloques **43** (1982), no. C6, C6–199. 2.2

[Can13] Giacomo Canevari, *Biaxiality in the asymptotic analysis of a 2-D Landau-de Gennes model for liquid crystals*, arXiv preprint arXiv:1307.8065 (2013). 4.1

[Cas04] James Casey, *On volterra dislocations of finitely deforming continua*, Mathematics and mechanics of solids **9** (2004), no. 5, 473–492. 2.1

[CD+91] Isaac Chuang, Ruth Durrer, et al., *Cosmology in the laboratory: Defect dynamics in liquid crystals*, Science **251** (1991), no. 4999, 1336. 5.1

[CGH+15] Peter J. Collings, Joshua N. Goldstein, Elizabeth J. Hamilton, Benjamin R. Mercado, Kenneth J. Nieser, and Margaret H. Regan, *The nature of the assembly process in chromonic liquid crystals*, Liquid Crystals Reviews **3** (2015), no. 1, 1–27. 5.1

[che] *Chemdoodle*, `http://www.chemdoodle.com/`. (document), 2.6, 2.7

[CK72] P.E. Cladis and M. Kleman, *Non-singular disclinations of strength s=+1 in nematics*, Journal de Physique **33** (1972), no. 5-6, 591–598. 4.1

[CMB06] John D. Clayton, David L. McDowell, and Douglas J. Bammann, *Modeling dislocations and disclinations with finite micropolar elastoplasticity*, International Journal of Plasticity **22** (2006), no. 2, 210–256. 2.2

[CMS06] John W. Cahn, Yuri Mishin, and Akira Suzuki, *Coupling grain boundary motion to shear deformation*, Acta Materialia **54** (2006), no. 19, 4953–4975. 2.2

[DAZM13] Amit Das, Amit Acharya, Johannes Zimmer, and Karsten Matthies, *Can equations of equilibrium predict all physical equilibria? A case study from field dislocation mechanics*, Mathematics and Mechanics of Solids **18** (2013), no. 8, 803–822. 3, I

[DeW71] R. DeWit, *Relation between dislocations and disclinations*, Journal of Applied Physics **42** (1971), 3304–3308. 1.1, 2.1, 2.2, 2.4

[DeW72] R. DeWit, *Partial disclinations*, Journal of Physics C: Solid State Physics **5** (1972), no. 5, 529. (document), 2.2, 3.5.9.4, 3.5.10, 3.30

[DeW73a] R. DeWit, *Theory of disclinations. II- continuous and discrete disclinations in anisotropic elasticity*, Journal of Research **77** (1973), 49–100. 1.1, 2.1, 2.5, 3.1, 3.3.2, 3.6, 3.6, 3.7, H

[DeW73b] R. DeWit, *Theory of disclinations: IV. Straight disclinations*, J. Res. Natl Bureau Standards Sect. A, Phys. Chem. A **77** (1973), 607–658. 2.1, 2.2, 2.4, 2.5

[DeW73c] R. DeWit, *Theory of disclinations: Iv. straight disclinations*, J. Res. Natl Bureau Standards Sect. A, Phys. Chem. A **77** (1973), 607–658. 3.5.3

[DFRSZ14] G. Di Fratta, J.M. Robbins, V. Slastikov, and A. Zarnescu, *Half-integer point defects in the Q-Tensor theory of nematic liquid crystals*, Journal of Nonlinear Science (2014), 1–20. 4.1

[dGP95] Pierre-Gilles de Gennes and Jacques Prost, *The physics of liquid crystals (international series of monographs on physics)*, Oxford University Press, USA (1995), no. 0.10, 0–20. 4.1

[DSSS98] Liang Dong, Jurgen Schnitker, Richard W. Smith, and David J. Srolovitz, *Stress relaxation and misfit dislocation nucleation in the growth of misfitting films: A molecular dynamics simulation study*, Journal of Applied Physics **83** (1998), no. 1, 217–227. 2.2

[DXS13] Shuyang Dai, Yang Xiang, and David J. Srolovitz, *Structure and energy of (111) low-angle twist boundaries in Al, Cu and Ni*, Acta Materialia **61** (2013), no. 4, 1327–1337. 2.2

[DZ11] S. Derezin and L. Zubov, *Disclinations in nonlinear elasticity*, ZAMM-Journal of Applied Mathematics and Mechanics/Zeitschrift für Angewandte Mathematik und Mechanik **91** (2011), no. 6, 433–442. 2.1, 2.2

[Ede85] Dominic G. B. Edelen, *Applied Exterior Calculus*, Wiley-Interscience, Wiley, New York, 1985. A

[EES+09] Matt Elsey, Selim Esedog, Peter Smereka, et al., *Diffusion generated motion for grain growth in two and three dimensions*, Journal of Computational Physics **228** (2009), no. 21, 8015–8033. 2.2

[EL88] Dominic G. B. Edelen and Dimitris C. Lagoudas, *Dispersion relations for the linearized field equations of dislocation dynamics*, International journal of engineering science **26** (1988), no. 8, 837–846. A

[Eri61] Jerald .L Ericksen, *Conservation laws for liquid crystals*, Transactions of The Society of Rheology (1957-1977) **5** (1961), no. 1, 23–34. 2, 5.3.2

[Eri91] Jerald L. Ericksen, *Liquid crystals with variable degree of orientation*, Archive for Rational Mechanics and Analysis **113** (1991), no. 2, 97–120. 1, 2, 4.3, 5.1, 5.3.1, 5.3.3, 5.5

[Eri95] J. L. Ericksen, *Remarks concerning forces on line defects*, Theoretical, Experimental, and Numerical Contributions to the Mechanics of Fluids and Solids, Springer, 1995, pp. 247–271. 4.3, 4.6.3

[Esh56] J. D. Eshelby, *The continuum theory of lattice defects*, Solid state physics **3** (1956), 79–144. 3.5.1

[Esh57] John D. Eshelby, *The determination of the elastic field of an ellipsoidal inclusion, and related problems*, Proceedings of the Royal Society of London A: Mathematical, Physical and Engineering Sciences, vol. 241, The Royal Society, 1957, pp. 376–396. 3.5.1

[Esh80] J.D. Eshelby, *The force on a disclination in a liquid crystal*, Philosophical Magazine A **42** (1980), no. 3, 359–367. 4.6.3

[EV09] Nicholas M. Ercolani and S. C. Venkataramani, *A variational theory for point defects in patterns*, Journal of nonlinear science **19** (2009), no. 3, 267–300. 4.8

[Fra50] F. C. Frank, *The resultant content of dislocations in an arbitrary intercrystalline boundary*, Symposium on The Plastic Deformation of Crystalline Solids, Mellon Institute, Pittsburgh,(NAVEXOS-P-834), vol. 150, 1950. 1.1, 2.2

[Fra53] F. C. Frank, *Martensite*, Acta Metallurgica **1** (1953), no. 1, 15 – 21. 2.2

[Fra58] Frederick C. Frank, *I. Liquid crystals. On the theory of liquid crystals*, Discussions of the Faraday Society **25** (1958), 19–28. 1, 4.1, 4.3, 4.4, 4.4.4, 5.1

[FS09] Ibrahim Fatkullin and Valeriy Slastikov, *Vortices in two-dimensional nematics*, Communications in Mathematical Sciences **7** (2009), no. 4, 917–938. 4.1

[FTC11] C. Fressengeas, V. Taupin, and L. Capolungo, *An elasto-plastic theory of dislocation and disclination fields*, International Journal of Solids and Structures **48** (2011), no. 25, 3499–3509. 1.1, 2.1, 2.2

[FTC14] ———, *Continuous modeling of the structure of symmetric tilt boundaries*, International Journal of Solids and Structures **51** (2014), no. 6, 1434–1441. 1.1, 2.2

[GAdP03] Sylvain Grollau, N. L. Abbott, and J. J. de Pablo, *Spherical particle immersed in a nematic liquid crystal: Effects of confinement on the director field configurations*, Physical Review E **67** (2003), no. 1, 011702. 5.1

[GJ15] Eugene C. Gartland Jr, *Scalings and limits of the Landau-de Gennes model for liquid crystals: A comment on some recent analytical papers*, arXiv preprint arXiv:1512.08164 (2015). 3, 4.1

[GM14] Dmitry Golovaty and José Alberto Montero, *On minimizers of a Landau–de Gennes energy functional on planar domains*, Archive for Rational Mechanics and Analysis **213** (2014), no. 2, 447–490. 4.1

[GNR+89] V. Yu Gertsman, A. A. Nazarov, A. E. Romanov, R. Z. Valiev, and V. I. Vladimirov, *Disclination-structural unit model of grain boundaries*, Philosophical magazine A **59** (1989), no. 5, 1113–1118. 1.1

[GSJ+05] Y. Gao, L. Song, P. Jiang, L.F. Liu, X.Q. Yan, Z.P. Zhou, D.F. Liu, J.X. Wang, H.J. Yuan, Z.X. Zhang, et al., *Silver nanowires with five-fold symmetric cross-section*, Journal of crystal growth **276** (2005), no. 3, 606–612. 3.5.10

[GSV02] Eugene C. Gartland, Jr., André M. Sonnet, and Epifanio G. Virga, *Elastic forces on nematic point defects*, Continuum Mechanics and Thermodynamics **14** (2002), no. 3, 307–319. 4.1

[HES+95] J. A. Hurtado, B. R. Elliott, H. M. Shodja, D. V. Gorelikov, C. E. Campbell, H. E. Lippard, T. C. Isabell, and J. Weertman, *Disclination grain boundary model with plastic deformation by dislocations*, Materials Science and Engineering: A **190** (1995), no. 1-2, 1–7. 1.1

[HH98] J. P. Hirth and R. G. Hoagland, *Extended dislocation barriers in tilt boundaries in fcc crystals*, Material Research Innovations **1** (1998), no. 4, 235–237. 2.2

[HHM01] E. A. Holm, G. N. Hassold, and M. A. Miodownik, *On misorientation distribution evolution during anisotropic grain growth*, Acta Materialia **49** (2001), no. 15, 2981–2991. 2.2

[HKL86] Robert Hardt, David Kinderlehrer, and Fang-Hua Lin, *Existence and partial regularity of static liquid crystal configurations*, Communications in mathematical physics **105** (1986), no. 4, 547–570. 5.1

[HKL88] ———, *Stable defects of minimizers of constrained variational principles*, vol. 5, 1988, pp. 297–322. 1, 4.1

[HLL+12] Christopher M. Hefferan, Jonathan Lind, Shiu Fai Li, Ulrich Lienert, Anthony D. Rollett, and Robert M. Suter, *Observation of recovery and recrystallization in high-purity aluminum measured with forward modeling analysis of high-energy diffraction microscopy*, Acta Materialia **60** (2012), no. 10, 4311–4318. 3.5.9.4

[HM12] Duvan Henao and Apala Majumdar, *Symmetry of uniaxial global Landau–de Gennes minimizers in the theory of nematic liquid crystals*, SIAM Journal on Mathematical Analysis **44** (2012), no. 5, 3217–3241. 4.1

[HP96] J. P. Hirth and R. C. Pond, *Steps, dislocations and disconnections as interface defects relating to structure and phase transformations*, Acta Materialia **44** (1996), no. 12, 4749–4763. 2.2

[HP11] ———, *Compatibility and accommodation in displacive phase transformations*, Progress in Materials Science **56** (2011), no. 6, 586–636. 2.2

[HPH09] J. M. Howe, R. C. Pond, and J. P. Hirth, *The role of disconnections in phase transformations*, Progress in Materials Science **54** (2009), no. 6, 792–838. 2.2

[HPH+13] J. P. Hirth, R. C. Pond, R. G. Hoagland, X.-Y. Liu, and J. Wang, *Interface defects, reference spaces and the Frank–Bilby equation*, Progress in Materials Science **58** (2013), no. 5, 749–823. (document), 2.2, 3.15, 3.16, 3.5.7, 3.5.7, 3.18

[HPL06] J. P. Hirth, R. C. Pond, and J. Lothe, *Disconnections in tilt walls*, Acta Materialia **54** (2006), no. 16, 4237–4245. 2.1, 2.2, 3.5.7

[HPL07] ———, *Spacing defects and disconnections in grain boundaries*, Acta Materialia **55** (2007), no. 16, 5428–5437. 2.2

[INSZ13] Radu Ignat, Luc Nguyen, Valeriy Slastikov, and Arghir Zarnescu, *Stability of the vortex defect in the Landau–de Gennes theory for nematic liquid crystals*, Comptes Rendus Mathématique **351** (2013), no. 13, 533–537. 4.1

[INSZ14] ———, *Uniqueness results for an ODE related to a generalized Ginzburg–Landau model for liquid crystals*, SIAM Journal on Mathematical Analysis **46** (2014), no. 5, 3390–3425. 4.1

[INSZ15] ———, *Stability of the melting hedgehog in the Landau–de Gennes theory of nematic liquid crystals*, Archive for Rational Mechanics and Analysis **215** (2015), no. 2, 633–673. 4.1

[Jia98] B. Jiang, *The least-squares finite element method*, Springer, Berlin, 1998. 3.4

[JS98] Robert Leon Jerrard and Halil Mete Soner, *Dynamics of Ginzburg-Landau vor-*

tices, Archive for Rational Mechanics and Analysis **142** (1998), no. 2, 99–125. 4.8

[KF08] Maurice Kleman and Jacques Friedel, *Disclinations, dislocations, and continuous defects: A reappraisal*, Reviews of Modern Physics **80** (2008), no. 1, 61. 1.1, 2

[Kib76] T. W. B. Kibble, *Topology of cosmic domains and strings*, Journal of Physics A: Mathematical and General **9** (1976), no. 8, 1387. 5.1

[KKJ+03] S. V. Khare, S. Kodambaka, D. D. Johnson, I. Petrov, and J. E. Greene, *Determining absolute orientation-dependent step energies: a general theory for the Wulff-construction and for anisotropic two-dimensional island shape fluctuations*, Surface science **522** (2003), no. 1, 75–83. 5.3.4

[KL07] Maurice Kléman and Oleg D. Laverntovich, *Soft matter physics: an introduction*, Springer Science & Business Media, 2007. 1.2, 3, 5.1

[Klé73] M. Kléman, *Defect densities in directional media, mainly liquid crystals*, Philosophical Magazine **27** (1973), no. 5, 1057–1072. 4.1

[KLT06] David Kinderlehrer, Irene Livshits, and Shlomo Ta'Asan, *A variational approach to modeling and simulation of grain growth*, SIAM Journal on Scientific Computing **28** (2006), no. 5, 1694–1715. 2.2

[KMS15] Raz Kupferman, Michael Moshe, and Jake P. Solomon, *Metric description of singular defects in isotropic materials*, Archive for Rational Mechanics and Analysis **216** (2015), no. 3, 1009–1047. 2.2

[KNT+11] Stefan Kaufmann, Robert Niemann, Thomas Thersleff, Ulrich K. Rößler, Oleg Heczko, Jörg Buschbeck, Bernhard Holzapfel, Ludwig Schultz, and Sebastian Fähler, *Modulated martensite: why it forms and why it deforms easily*, New Journal of Physics **13** (2011), no. 5, 053029. 3.5.12.2

[Koh06] Robert V. Kohn, *Energy-driven pattern formation*, Proceedings of the International Congress of Mathematicians, vol. 1, 2006, pp. 359–384. 4.8

[Krö81] Ekkehart Kröner, *Continuum theory of defects*, Physics of Defects (Jean-Paul Poirier Roger Balian, Maurice Kléman, ed.), vol. 35, North-Holland, Amsterdam, 1981, pp. 217–315. 1.1, 2.4

[KRR06] Chang-Soo Kim, Anthony D. Rollett, and Gregory S. Rohrer, *Grain boundary planes: New dimensions in the grain boundary character distribution*, Scripta Materialia **54** (2006), no. 6, 1005–1009. 2.2

[KSL13] Young-Ki Kim, Sergij V. Shiyanovskii, and Oleg D. Lavrentovich, *Morphogenesis of defects and tactoids during isotropic–nematic phase transition in self-assembled lyotropic chromonic liquid crystals*, Journal of Physics: Condensed Matter **25** (2013), no. 40, 404202. (document), 1.2, 5.1, 5.1, 5.3.3, 5.3.3, 5.3.4, 5.3.4, 5.3.6

[KVŽ99] Samo Kralj, Epifanio G. Virga, and Slobodan Žumer, *Biaxial torus around nematic point defects*, Physical Review E **60** (1999), no. 2, 1858. 4.1

[KŽA91] Samo Kralj, Slobodan Žumer, and David W. Allender, *Nematic-isotropic phase transition in a liquid-crystal droplet*, Physical Review A **43** (1991), no. 6, 2943. 4.1

[Lav98] Oleg D. Lavrentovich, *Topological defects in dispersed words and worlds around liquid crystals, or liquid crystal drops*, Liquid crystals **24** (1998), no. 1, 117–126. 5.3.3

[Lav14] ———, *Transport of particles in liquid crystals*, Soft Matter **10** (2014), no. 9, 1264–1283. 1.2

[Les66] Frank M Leslie, *Some constitutive equations for anisotropic fluids*, The Quarterly Journal of Mechanics and Applied Mathematics **19** (1966), no. 3, 357–370.

2

[Les68] Frank M. Leslie, *Some constitutive equations for liquid crystals*, Archive for Rational Mechanics and Analysis **28** (1968), no. 4, 265–283. 2

[Les92] ———, *Continuum theory for nematic liquid crystals*, Continuum Mechanics and Thermodynamics **4** (1992), no. 3, 167–175. 5.3.2

[Li72] J. C. M. Li, *Disclination model of high angle grain boundaries*, Surface Science **31** (1972), 12–26. 1.1, 2.2, 2.4.4.1

[LIO98] V. I. Levitas, A. V. Idesman, and G. B. Olson, *Continuum modeling of strain-induced martensitic transformation at shear-band intersections*, Acta materialia **47** (1998), no. 1, 219–233. 3.5.12.2

[LL64] Lev Davidovich Landau and Evgenii Mikhailovich Lifshits, *Theoretical physics*, Statistical Physics (1964). 5.3.4

[LL95] Fang-Hua Lin and Chun Liu, *Nonparabolic dissipative systems modeling the flow of liquid crystals*, Communications on Pure and Applied Mathematics **48** (1995), no. 5, 501–537. 4.1

[LL00] ———, *Existence of solutions for the Ericksen-Leslie system*, Archive for Rational Mechanics and Analysis **154** (2000), no. 2, 135–156. 4.1

[Lyd11] John Lydon, *Chromonic liquid crystalline phases*, Liquid Crystals **38** (2011), no. 11-12, 1663–1681. 5.1

[MGJ00] S. Mkaddem and E.C. Gartland Jr, *Fine structure of defects in radial nematic droplets*, Physical Review E **62** (2000), no. 5, 6694. 4.1

[MMRN12] Craig S. MacDonald, John A. Mackenzie, Alison Ramage, and Christopher J.P. Newton, *Robust adaptive computation of a one-dimensional-tensor model of nematic liquid crystals*, Computers & Mathematics with Applications **64** (2012), no. 11, 3627–3640. 4.1

[MN14] Nigel J. Mottram and Christopher J.P. Newton, *Introduction to Q-tensor theory*, arXiv preprint arXiv:1409.3542 (2014). 3, 4.1, 4.3

[Mul56] William W. Mullins, *Two-Dimensional Motion of Idealized Grain Boundaries*, Journal of Applied Physics **27** (1956), no. 8, 900–904. 2.2

[MZ10] Apala Majumdar and Arghir Zarnescu, *Landau–de Gennes theory of nematic liquid crystals: the Oseen–Frank limit and beyond*, Archive for rational mechanics and analysis **196** (2010), no. 1, 227–280. 3

[Nab67] F. R. N. Nabarro, *Theory of Crystal Dislocations (Monographs on Physics)*, Oxford University Press, 1967. 3.1

[Nab85] ———, *The development of the idea of a crystal dislocation*, University of Tokyo Press, Tokyo, 1985. 2.4.1, 3.1

[Nab87] ———, *Theory of Crystal Dislocations*, Dover Pubns, 1987. (document), 2.1, 2.2, 2.2

[Naz13] Ayrat A. Nazarov, *Disclinations in bulk nanostructured materials: their origin, relaxation and role in material properties*, Advances in Natural Sciences. Nanoscience and Nanotechnology **4** (2013), no. 3, 033002–1. (document), 2.4.1, 2.3

[NBP+10] V. G. Nazarenko, O. P. Boiko, H.-S. Park, O. M. Brodyn, M. M. Omelchenko, L. Tortora, Yu A. Nastishin, and O. D. Lavrentovich, *Surface alignment and anchoring transitions in nematic lyotropic chromonic liquid crystal*, Physical review letters **105** (2010), no. 1, 017801. 5.1, 5.4.2

[New12] Alan C Newell, *Pattern quarks and leptons*, Applicable Analysis **91** (2012), no. 2, 213–223. 4.8

[NLS+04] Yu A. Nastishin, H. Liu, S. V. Shiyanovskii, O. D. Lavrentovich, A. F. Kostko, and M. A. Anisimov, *Pretransitional fluctuations in the isotropic phase of a*

lyotropic chromonic liquid crystal, Physical Review E **70** (2004), no. 5, 051706. 5.1

[NLS+05] Yu. A. Nastishin, H. Liu, T. Schneider, V. Nazarenko, R. Vasyuta, S. V. Shiyanovskii, and O. D. Lavrentovich, *Optical characterization of the nematic lyotropic chromonic liquid crystals: Light absorption, birefringence, and scalar order parameter*, Phys. Rev. E **72** (2005), 041711. 5.1

[Noz92] P. Nozières, *Shape and growth of crystals*, Solids far from equilibrium **56** (1992), no. 2, 1–154. 5.3.4

[NSB00] A. A. Nazarov, O. A. Shenderova, and D. W. Brenner, *On the disclination-structural unit model of grain boundaries*, Materials Science and Engineering: A **281** (2000), no. 1, 148–155. 2.2

[NZ10] Luc Nguyen and Arghir Zarnescu, *Refined approximation for a class of Landau-de Gennes energy minimizers*, arXiv preprint arXiv:1006.5689 (2010). 4.1

[OP05] Patrick Oswald and Pawel Pieranski, *Nematic and cholesteric liquid crystals: concepts and physical properties illustrated by experiments*, CRC press, 2005. 5.3.4

[Ose33] C.W. Oseen, *The theory of liquid crystals*, Transactions of the Faraday Society **29** (1933), no. 140, 883–899. 1, 4.3, 5.1

[PAD15] Hossein Pourmatin, Amit Acharya, and Kaushik Dayal, *A fundamental improvement to Ericksen-Leslie kinematics*, Quarterly of Applied Mathematics **LXXXIII** (2015), no. 3, 435–466. 1.2, 2, 4.1, 4.3, 4.3, 4.8

[PKT+11] Heung-Shik Park, Shin-Woong Kang, Luana Tortora, Satyendra Kumar, and Oleg D. Lavrentovich, *Condensation of self-assembled lyotropic chromonic liquid crystal sunset yellow in aqueous solutions crowded with polyethylene glycol and doped with salt*, Langmuir **27** (2011), no. 7, 4164–4175. 5.1

[PL12] H. S. Park and O. D. Lavrentovich, *Lyotropic chromonic liquid crystals: Emerging applications*, Chapter 14 in Liquid crystals beyond displays: chemistry, physics, and applications (ed Quan Li) (2012). 5.1

[PL13] Marcel Porta and Turab Lookman, *Heterogeneity and phase transformation in materials: Energy minimization, iterative methods and geometric nonlinearity*, Acta Materialia **61** (2013), no. 14, 5311–5340. 2.2

[PNS96] V. Popa-Nita and T. J. Sluckin, *Kinetics of the nematic-isotropic interface*, Journal de Physique II **6** (1996), no. 6, 873–884. 5.1

[Pur09] Saurabh Puri, *Modeling dislocation sources and plastic flow through grain boundaries in mesoscopic field dislocation mechanics*, Ph.D. thesis, Civil and Environmental Engineering, Carnegie Mellon University, 2009. 2, 3.4.2, 3.4.2

[QYC+15] Qingquan Qin, Sheng Yin, Guangming Cheng, Xiaoyan Li, Tzu-Hsuan Chang, Gunther Richter, Yong Zhu, and Huajian Gao, *Recoverable plasticity in penta-twinned metallic nanowires governed by dislocation nucleation and retraction*, Nature communications **6** (2015). (document), 3.5.10, 3.31

[RA05] Anish Roy and Amit Acharya, *Finite element approximation of field dislocation mechanics*, Journal of the Mechanics and Physics of Solids **53** (2005), no. 1, 143–170. 3.4

[RG17] Ayan Roychowdhury and Anurag Guptan, *Non-metric connection and metric anomalies in materially uniform elastic solids*, Journal of Elasticity **126** (2017), no. 14, 1–26. 2.2

[RK09] Alexey E. Romanov and Anna L. Kolesnikova, *Application of disclination concept to solid structures*, Progress in Materials Science **54** (2009), no. 6, 740–769. 2.1, 2.2, 2, 2.4.3

[Roh10] Gregory S. Rohrer, *Introduction to Grains, Phases, and Interfacesan Interpreta-*

tion of Microstructure, Trans. AIME, 1948, vol. 175, pp. 15–51, by C.S. Smith, Metallurgical and Materials Transactions A **41** (2010), no. 5, 1063–1100. 2.2

[Roh11] ———, *Grain boundary energy anisotropy: a review*, Journal of Materials Science **46** (2011), no. 18, 5881–5895. 2.2

[RP69] A. Rapini and M. Papoular, *Distorsion d'une lamelle nématique sous champ magnétique conditions d'ancrage aux parois*, Le Journal de Physique Colloques **30** (1969), no. C4, C4–54. 5.3.3

[RS50] W. T. Read and W. Shockley, *Dislocation models of crystal grain boundaries*, Physical Review **78** (1950), no. 3, 275. 2.2

[RV92] A. E. Romanov and V. I. Vladimirov, *Disclinations in Crystalline Solids*, Dislocation in Solids **9** (1992), 191–402. 2.2

[RŽ09] Miha Ravnik and Slobodan Žumer, *Landau–de Gennes modelling of nematic liquid crystal colloids*, Liquid Crystals **36** (2009), no. 10-11, 1201–1214. 4.1

[SAF+05] Tod Schneider, Kateryna Artyushkova, Julia E. Fulghum, Laurie Broadwater, Ashley Smith, and Oleg D. Lavrentovich, *Oriented monolayers prepared from lyotropic chromonic liquid crystal*, Langmuir **21** (2005), no. 6, 2300–2307. 5.1

[SB95] Adrian P. Sutton and Robert W. Balluffi, *Interfaces in crystalline materials*, Clarendon Press, 1995. 2.2

[SElDRR04] David M. Saylor, Bassem S. E. l. Dasher, Anthony D. Rollett, and Gregory S. Rohrer, *Distribution of grain boundaries in aluminum as a function of five macroscopic parameters*, Acta Materialia **52** (2004), no. 12, 3649–3655. 2.2

[SGL11] Hanu Seiner, Ondej Glatz, and Michal Landa, *A finite element analysis of the morphology of the twinned-to-detwinned interface observed in microstructure of the CuAlNi shape memory alloy*, International Journal of Solids and Structures **48** (2011), no. 13, 2005 – 2014. 3.5.12.2

[Shi73] R. T. Shield, *The rotation associated with large strains*, SIAM Journal on Applied Mathematics **25** (1973), no. 3, 483–491. 3.5.9.4

[SP86] T. J. Sluckin and A. Poniewierski, Fluid Interfacial phenomena (C.A. Croxton, ed.), John Wiley and Sons, Chichester, 1986. 5.4.2

[SS87] N. Schopohl and T.J. Sluckin, *Defect core structure in nematic liquid crystals*, Physical Review Letters **59** (1987), no. 22, 2582. 3, 4.1

[Ste04] Iain W. Stewart, *The static and dynamic continuum theory of liquid crystals: a mathematical introduction*, CRC Press, 2004. 1.2, 4.1, 5.3.2

[SV83a] A. P. Sutton and V. Vitek, *On the structure of tilt grain boundaries in cubic metals I. Symmetrical tilt boundaries*, Philosophical Transactions of the Royal Society of London A: Mathematical, Physical and Engineering Sciences **309** (1983), no. 1506, 1–36. 2.2

[SV83b] ———, *On the structure of tilt grain boundaries in cubic metals II. Asymmetrical tilt boundaries*, Philosophical Transactions of the Royal Society of London A: Mathematical, Physical and Engineering Sciences **309** (1983), no. 1506, 37–54. 2.2

[SV97] André M. Sonnet and Epifanio G. Virga, *Dynamics of nematic loop disclinations*, Physical Review E **56** (1997), no. 6, 6834. 4.1

[SV12] André M Sonnet and Epifanio G Virga, *Dissipative ordered fluids: theories for liquid crystals*, Springer Science & Business Media, 2012. 4.1

[SW+71] Gene Simmons, Herbert Wang, et al., *Single crystal elastic constants and calculated aggregate properties*. G

[TAS05] H. Tang, A. Acharya, and S. Saigal, *Directional dependence of crack growth along the interface of a bicrystal with symmetric tilt boundary in the presence of gradient effects*, Mechanics of materials **37** (2005), no. 5, 593–606. 3

[TCF+13] Vincent Taupin, L. Capolungo, Claude Fressengeas, A. Das, and M. Upadhyay, *Grain boundary modeling using an elasto-plastic theory of dislocation and disclination fields*, Journal of the Mechanics and Physics of Solids **61** (2013), no. 2, 370–384. 1.1

[TL11] Luana Tortora and Oleg D. Lavrentovich, *Chiral symmetry breaking by spatial confinement in tactoidal droplets of lyotropic chromonic liquid crystals*, Proceedings of the National Academy of Sciences **108** (2011), no. 13, 5163–5168. 5.1

[TPK+10a] Luana Tortora, Heung-Shik Park, Shin-Woong Kang, Victoria Savaryn, Seung-Ho Hong, Konstantine Kaznatcheev, Daniele Finotello, Samuel Sprunt, Satyendra Kumar, and Oleg D. Lavrentovich, *Self-assembly, condensation, and order in aqueous lyotropic chromonic liquid crystals crowded with additives*, Soft Matter **6** (2010), 4157–4167. 5.1

[TPK+10b] ———, *Self-assembly, condensation, and order in aqueous lyotropic chromonic liquid crystals crowded with additives*, Soft Matter **6** (2010), no. 17, 4157–4167. 5.1

[Vac91] Tanmay Vachaspati, *Formation of topological defects*, Physical Review D **44** (1991), no. 12, 3723. 5.1

[VAKD14] A. J. Vattré, N. Abdolrahim, K. Kolluri, and M. J. Demkowicz, *Computational design of patterned interfaces using reduced order models*, Scientific Reports **4** (2014). 2.2

[VD13] A. J. Vattré and M. J. Demkowicz, *Determining the Burgers vectors and elastic strain energies of interface dislocation arrays using anisotropic elasticity theory*, Acta Materialia **61** (2013), no. 14, 5172–5187. 2.2

[VD15] ———, *Partitioning of elastic distortions at a semicoherent heterophase inter-*

face between anisotropic crystals, Acta Materialia **82** (2015), 234–243. 2.2

[Vir95] Epifanio G Virga, *Variational theories for liquid crystals*, vol. 8, CRC Press, 1995. 2, 4.1, 5.1

[Vit68] V Vitek, *Intrinsic stacking faults in body-centred cubic crystals*, Philosophical Magazine **18** (1968), no. 154, 773–786. J

[VL83] G. E. Volovik and O. D. Lavrentovich, *Topological dynamics of defects: boojums in nematic drops*, Zh Eksp Teor Fiz **85** (1983), no. 6, 1997–2010, /Sov.Phys. JETP, v.58, p.1159-1167 (1983). 5.1

[Vol07] Vito Volterra, *Sur l'équilibre des corps élastiques multiplement connexes*, Annales scientifiques de l'École normale supérieure, vol. 24, Société mathématique de France, 1907, pp. 401–517. 1.1

[VPSL02] D. Voloschenko, Oleg P. Pishnyak, Sergij V. Shiyanovskii, and O.D. Lavrentovich, *Effect of director distortions on morphologies of phase separation in liquid crystals*, Physical Review E **65** (2002), no. 6, 060701. 1.2

[Wal11a] Noel J. Walkington, *Numerical approximation of nematic liquid crystal flows governed by the ericksen-leslie equations*, ESAIM: Mathematical Modelling and Numerical Analysis **45** (2011), no. 03, 523–540. 2, 5.3.3, 5.5

[Wal11b] ———, *Numerical approximation of nematic liquid crystal flows governed by the Ericksen-Leslie equations*, ESAIM Math. Model. Numer. Anal. **45** (2011), no. 3, 523–540. MR 2804649 (2012c:76009) 4.1

[WBH12] J. Wang, I. J. Beyerlein, and J. P. Hirth, *Nucleation of elementary and twinning dislocations at a twin boundary in hexagonal close-packed crystals*, Modelling and Simulation in Materials Science and Engineering **20** (2012), no. 2, 024001. 3.5.8

[Wei01] G. Weingarten, *Sulle superficie di discontinuità nella teoria della elasticità dei*

corpi solidi, Rend. Roma Acc. Linc **5** (1901), 57. 1.1

[Whe06] A. A. Wheeler, *Phase-field theory of edges in an anisotropic crystal*, Proceedings of the Royal Society of London A: Mathematical, Physical and Engineering Sciences, vol. 462, The Royal Society, 2006, pp. 3363–3384. 5.3.4

[Wil67] John R. Willis, *Second-order effects of dislocations in anisotropic crystals*, International Journal of Engineering Science **5** (1967), no. 2, 171–190. 2.4

[WIT70] D.E. WIT, *Linear theory of static disclinations(plastic deformation of disclination and dislocation density tensors)*, 1970. (1970), 651–673. 2.1, 2.2

[YG12] Arash Yavari and Alain Goriely, *Riemann–Cartan geometry of nonlinear disclination mechanics*, Mathematics and Mechanics of Solids (2012), 1081286511436137. 2.2

[ZAWB15] Xiaohan Zhang, Amit Acharya, Noel J. Walkington, and Jacobo Bielak, *A single theory for some quasi-static, supersonic, atomic, and tectonic scale applications of dislocations*, Journal of the Mechanics and Physics of Solids **84** (2015), 145–195. 3, 4.5.2.1, 4.6.3, I, J

[ZCL14] Shuang Zhou, A. J. Cervenka, and O. D. Lavrentovich, *Ionic-content dependence of viscoelasticity of the lyotropic chromonic liquid crystal sunset yellow*, Phys Rev E **90** (2014). 5.1, 5.4.1

[ZNN+14] S. Zhou, K. Neupane, Yu. A. Nastishin, A. R. Baldwin, S. V. Shiyanovskii, O. D. Lavrentovich, and S. N. Sprunt, *Elasticity, viscosity, and orientational fluctuations of a lyotropic chromonic nematic liquid crystal disodium cromoglycate*, Soft Matter **10** (2014), 6571–6581. 5.1

[ZNO+12] Shuang Zhou, Yu A. Nastishin, M. M. Omelchenko, L. Tortora, V. G. Nazarenko, O. P. Boiko, T. Ostapenko, T. Hu, C. C. Almasan, S. N. Sprunt, et al., *Elasticity of lyotropic chromonic liquid crystals probed by director reori-*

entation in a magnetic field, Physical review letters **109** (2012), no. 3, 037801. 5.1

[ZSPL17] Shuang Zhou, Sergij V. Shiyanovskii, Heung-Shik Park, and Oleg D. Lavrentovich, *Fine structure of the topological defect cores studied for disclinations in lyotropic chromonic liquid crystals*, Nature Communications **8** (2017). 5.1

[Zub97] Leonid M. Zubov, *Nonlinear theory of dislocations and disclinations in elastic bodies*, vol. 47, Springer Science & Business Media, 1997. 2.1, 2.2

[ZZA+16] Chiqun Zhang, Xiaohan Zhang, Amit Acharya, Dmitry Golovaty, and Noel Walkington, *A non-traditional view on the modeling of nematic disclination dynamics*, Quarterly of Applied Mathematics (2016), no. LXXV, 309–357. 3